Universidade do Minho
Escola de Ciências

Pedro Manuel Abreu Martins

New generation of photocatalytic nanocomposites: production, characterization and environmental application

dezembro de 2018

New generation of photocatalytic nanocomposites: production, characterization and environmental application
Pedro Manuel Abreu Martins
UMinho | 2018

FCT
Fundação para a Ciência e a Tecnologia
MINISTÉRIO DA EDUCAÇÃO E CIÊNCIA
POPH QUALIFICAR É CRESCER.
QREN QUADRO DE REFERÊNCIA ESTRATÉGICO NACIONAL PORTUGAL 2007.2013
Governo da República Portuguesa
UNIÃO EUROPEIA Fundo Social Europeu

Universidade do Minho
Escola de Ciências

Pedro Manuel Abreu Martins

New generation of photocatalytic nanocomposites: production, characterization and environmental application

Tese de Doutoramento em Ciências
Especialidade em Física

Trabalho efetuado sob a orientação da
Professora Doutora Maria Madalena dos Santos Alves
e do
Professor Doutor Senentxu Lanceros-Méndez

dezembro de 2018

STATEMENT OF INTEGRITY

I hereby declare having conducted my thesis with integrity. I confirm that I have not used plagiarism or any form of falsification of results in the process of the thesis elaboration.

I further declare that I have fully acknowledged the Code of Ethical Conduct of the University of Minho.

University of Minho, Braga, 12 December 2018

Full name: Pedro Manuel Abreu Matias

Signature: _____

Acknowledgments

This document constitutes the last step in a unique and thrilling journey; I must acknowledge many people that helped me during this adventure.

Firstly, to the Foundation for Science and Technology (FCT) (grant: SFRH/BD/98616/2013) for the financial support of this project.

I have, and I want to thank Professor Senentxu, for basically everything! He made me as I am now, he believed my capabilities, he gave me the proper tools and advice. He allowed me to learn and evolve every day with his lessons (which keep happening). He was the perfect scientific tutor, but above all, he was a psychologist during all these years – there he was at the good and the bad moments - using the right words in the right time. He provides, to everyone in the group, a scaffold made of optimism and ambition that allows us to grow sustainably and fulfil all our potential. I will never be able to retribute all the good things I received from him.

I have to thank Prof. Madalena Alves, for in the very beginning accept to be my supervisor without even knowing me, and for open the doors of her lab. Equally, a gratitude word to Luciana Pereira for her time.

Many thanks to all the ESM group members as a whole. Many thanks to all the ESM group members. Among them, I want to address a particular thank to a former member, Vitor Sencadas because he had a paramount role in the development of my potential and skills in the laboratory. Also, a big thank you to Carlos Costa because he always has nice and positive words to everyone and for always being available to help.

I must express thanks to Professor Gabriela Botelho for her sympathy and willingness to help in any situation. Besides, she's probably one of the most educated people I've ever met in academia.

I want to thank professor Carlos Tavares and to Juliana Marques for their help during the measurements.

I am also very grateful to all the students that I tutored during my Ph.D. It was a pleasure to work with all them, and in some way, they also taught me something and contributed to the outcome of my thesis. Thank you to Clarisse and Sylvie Ribeiro for the help with formatting the thesis.

I want to thank some friends that helped me in very different ways: Gabriel Mendes, João Pereira, Manuel Sarmento, Dina Silva, Laelba Baptista, Susana, and especially Sara Teixeira, because besides being a friend she was also the bridge in the most fruitful collaboration during my thesis. A word to Daniela Correia, with whom I lived great moments that I will keep in my memories forever. Finally, I address the warmer thank you to my family. Without their education, concern, support, and encouragement I am sure that this journey would have been tougher and lonely. Daddy, this one is all for you – the silent fighter!!

Abstract

Photocatalysis has obtained considerable attention, and a variety of materials have been applied in different areas, in particular in the environmental field. Photocatalysis consists of the use of radiation (UV or sunlight) to generate highly oxidizing species, which will destroy environmental contaminants into innocuous compounds. Catalysts are required to this process, and due to its significant oxidizing properties under UV irradiation, superhydrophilicity, chemical stability in a broad pH range, low-cost, and extended durability, titanium dioxide (TiO_2) are one of the most used photocatalysts with increasing interest for environmental applications.

Despite the advantages of TiO_2 as a photocatalyst, there are still two main issues concerning the use of TiO_2 nanoparticles for practical applications. First, the reusability of TiO_2 nanoparticles is time-consuming and requires expensive separation/filtering processes. Second, the reduced spectral activation of TiO_2 that has a wide band gap (3.2 eV, for anatase), being only activated by UV radiation (< 387 nm). The proposed work will address those relevant issues.

In this way, TiO_2 nanoparticles were immobilized into a poly(vinylidenefluoride-trifluoroethylene) (P(VDF-TrFE)) membrane, and the comparative study of their photocatalytic performance with dispersed TiO_2 nanoparticles was performed. The membrane shows a highly porous structure (≈75 %) with controlled wettability, achieved by the inclusion of zeolites (NaY). These properties are critical to achieving a methylene blue degradation efficiency of 96 % in 40 min under ultraviolet (UV) irradiation, corresponding to an efficiency loss of just 3 % regarding the corresponding suspended TiO_2 nanoparticles assay. The same nanocomposite was also tested in the degradation of tartrazine in a solar photoreactor, and the results show that the TiO_2/PVDF-TrFE nanocomposite exhibits a remarkable sunlight photocatalytic activity, with 78% of tartrazine being degraded.

The same polymer matrix was used to immobilize TiO_2 nanoparticles doped with erbium (Er) and codoped with erbium and praseodymium (Pr), produced by a microwave-assisted technique. The results reveal that the low band gap (2.63 eV) and high surface area of these TiO_2 modified nanoparticles, coupled with the highly porous structure of the membrane, synergistically envisages the best photocatalytic performance by degrading 98 % of methylene blue after 100 min exposed to UV radiation.

To enhance the photocatalytic activity of TiO_2 both under UV and visible radiation, an Au/TiO_2 nanocomposite was produced, characterized and applied to the degradation of ciprofloxacin (CIP). A homogeneous distribution of Au nanoparticles over the TiO_2 nanoparticles surface has been achieved, with an effective band gap of 2.84 eV for the nanocomposite. These results allowed to foresee the enhanced degradation of CIP, 13 and 145 % under UV and simulated visible light radiation, respectively. The gold nanoislands play a critical role, working as electron receptor and endowing the nanocomposite with the ability to absorb the visible radiation. Additionally, the separation of the electron-hole pair, and the surface plasmon of resonance can promote the photocatalytic efficiency of the nanocomposite

In the same scope, a TiO_2/G and TiO_2/GO nanocomposites were produced to reduce the electron-hole pair recombination and enhance the photocatalytic activity under visible radiation. Computational models indicate potentially improved photocatalytic activity due to lower band gaps and charge carrier segregation at the interfaces. Regarding methylene blue degradation, show that TiO_2/G and TiO_2/GO nanocomposites were more efficient than pure TiO_2 under UV light. In contrast, the same nanocomposites were less efficient than pristine TiO_2 in ciprofloxacin degradation. These nanocomposites were also immobilized in electrospun fiber mats, and the results show that even 3% wt. % of TiO_2/GO in the fibers yields excellent photocatalytic performance by degrading ≈100% of MB after 90 min of visible light exposure.

A new hybrid photocatalytic material was produced to address polluted water in sites deprived of light (e.g., deep water and turbid water). TiO_2 nanoparticles immobilized in a poly(vinylidene difluoride) matrix were coated onto polymeric optical fibers. The photocatalytic efficiency tests revealed that the 50 w/w % of TiO_2 P25 in the coating lead to a degradation of 95 % of ciprofloxacin after 72 hours under artificial sunlight and that reusability of 3 times led to a loss of activity lower than 11 %.

Thus, the present work shows a set of different approaches that tackle the main issues related to photocatalysis. Different photocatalytic materials were produced, characterized and applied. Similarly, to improve reusability of the photocatalyst, different support materials (PVDF and PVDF-TrFE) were used as well as different morphologies (membrane, fiber membrane, and coating). All the produced photocatalysts show enhanced activity when compared to pristine TiO_2 and all the immobilized systems have also displayed an efficient functional performance and suitable reusability.

Resumo

A fotocatálise tem atraído muitas atenções, e nesse sentido, muitos materiais têm sido aplicados em diversas áreas, em particular no ambiente. A fotocatálise consiste na utilização da radiação (ultravioleta ou solar) para produzir espécies oxidativas, que serão responsáveis pela destruição dos contaminantes aquáticos, originando compostos inofensivos. Os catalisadores são necessários para este processo e devido as suas propriedades oxidativas sob irradiação UV, superhidrofilicidade, estabilidade química a diferentes gamas de pH, baixo custo e elevada durabilidade, o dióxido de titânio (TiO_2) é um dos fotocatalisadores mais utilizados em aplicações ambientais.

Apesar das vantagens do TiO_2 como fotocatalisador, existem alguns problemas associados à sua utilização prática. A reutilização destas nanopartículas é morosa e que requer processos de separação/filtração dispendiosos. Além disso, outra limitação é a reduzida ativação espectral do TiO_2, que possui um elevado *band gap* e por isso é ativado apenas por radiação UV (<387 nm). O trabalho aqui apresentado foca-se no desenvolvimento de materiais alternativos capazes de superar estes problemas.

Neste sentido, as nanopartículas de TiO_2 foram imobilizadas numa membrana de poli(fluoreto de vinilideno) trifluoretileno (PVDF-TrFE), e testada a sua performance fotocatalíticas, comparando-a com as nanopartículas em suspensão. Estas membranas possuem uma estrutura porosa (≈75 %) e a molhabilidade foi controlada pela incorporação de zeólitos (NaY). Estas propriedades foram fundamentais para obter uma degradação de 96% de azul de metilenos sob radiação UV durante 40 min. Correspondendo a uma perda de apenas 3% de eficiência relativamente ao ensaio com TiO_2 em suspensão. O mesmo nanocompósito foi também testado na degradação de tartrazina, num fotoreactor solar, e os resultados mostraram que após 5 horas de irradiação, ≈ 78% da tartrazina foi degradada. A mesma matriz polimérica foi utilizada para imobilizar nanopartículas de TiO_2 dopadas com erbium (Er) e co-dopadas com Er e prasiodímio (Pr) produzidas pelo método de micro-ondas. Os resultados mostram que o *band gap* (2.63eV) mais baixo e a elevada área de superfície das nanopartículas de TiO_2, juntamente com a elevada porosidade da membrana, contribuíram para a melhor eficiência fotocatalítica, degradando 98 % de azul de metileno após 100 min de exposição a radiação UV.

Para melhorar a atividade fotocatalítica do TiO_2, foi produzido, caracterizado e aplicado o nanocompósito de Au/TiO_2 na degradação de ciprofloxacina (CIP). A caracterização revelou uma distribuição homogénea de nanopartículas de Au na superfície das nanopartículas de TiO_2, bem como um *band gap* efetivo de 2.84 eV. O nanocompósito revelou um aumento na degradação da CIP, cerca de 13 e 145 % em UV e radiação visível, respetivamente. As nanoilhas de ouro funcionam como recetores de eletrões, dotando o nanocompósito da capacidade de absorver radiação visível. Além disso, a separação do par eletrão-lacuna, bem como a ressonância de plasmão de superfície podem promover maior eficiência fotocatalítica do nanocompósito.

Adicionalmente, nanocompósitos de grafeno (TiO_2/G) e óxido de grafeno (TiO_2/GO) foram produzidos para também reduzir a recombinação do par eletrão-lacuna e aumentar a atividade fotocatalítica usando radiação visível. Os modelos computacionais indicaram um potencial aumento da atividade fotocatlítica com base no menor *band gap* e na presença de transportadores de carga nas interfaces. Os resultados experimentais mostram que os nanocompósitos de TiO_2/G e TiO_2/GO foram mais eficientes que TiO_2 puro na deagradação de azul ed metileno sob radiação UV. Os mesmos nanocompósitos foram menos eficientes na degradação da CIP do que o TiO_2 puro. Os nanocompósitos TiO_2/GO foram ainda imobilizados em membrana de fibras de PVDF-TrFE produzidas por *electrospinning*, e os resultados mostram que com apenas 3 wt. % TiO_2/GO, este compósito degradou ≈100% do AM após 90 min de exposição a radiação visível.

Um novo material hibrido foi também produzido, de forma a possibilitar o tratamento de aguas contaminadas em locais desprovidos de radiação (e.g., aguas profundas e aguas turvas). Nanopartículas de TiO_2 foram imobilizadas numa matriz de poli(fluoreto de vinilideno) (PVDF) para revestimento de fibras óticas poliméricas. Os testes fotocatalícos mostraram que foi possível degradar 95% da CIP após 72 horas de radiação visível, e que após 3 reutilizações a perda de eficiência foi de apenas 11%.

Em resumo, o presente trabalho apresenta uma série de abordagens focadas na resolução das principais limitações da fotocatálise – aumento da atividade no visível e reutilização. Similarmente, para aumentar a reutilização do fotocatalisador, diferentes substratos foram usados (PVDF e PVDF-TrFE) bem como diferentes morfologias (membranas, membranas de fibras, e revestimento). Todos os fotocatalisadores produzidos possuem maior atividade fotocatalítica do que o TiO_2 puro. Por outro lado, os sistemas de imobilização também demonstraram uma eficaz performance e possibilidade de serem reutilizados.

Table of contents

List of figures

List of tables

List of symbols

θ_0	Contact angle
C_t	Concentration after a certain reaction time t
θ	Diffraction angle
β	Full width at half-maximum
Co	Initial concentration
K_L	Langmuir adsorption constant
h	Planck constant
ε	Porosity
wt. %	Percentage by weight
k_r	Reaction rate constant
R_∞	Reflectance of the sample
γp	Surface free energy
λ	Wavelength of the incident X-ray radiation
ζ	Zeta potential

List of abbreviations

A	
AOP	Advanced oxidation processes
ATR	Attenuated total reflectance
B	
BET	Brunauer–Emmett–Teller
BJH	Barrett-Joyner-Halenda
C	
CVD	Chemical vapor deposition
CIP	Ciprofloxcain
D	
DFT	Density functional theory
DLS	Dynamic Light Scattering
DMF	N, N-dimethylformamide
DMA	Dimethylacetamide
DSO	Density of states
DRS	Diffuse reflectance spectroscopy
E	
EDX	X-ray spectroscopy
Eq.	Equation
F	
FTIR	Fourier transformed infrared spectroscopy
G	
G	Graphene
GO	Graphene oxide
I	
IEP	Isoelectric point
L	
L-H	Langmuir-Hinshelwood
M	
MB	Methylene blue
UV	Ultraviolet

WWO	World health organization
WWTP	Wastewater treatment plant
P	
PTFE	Polytetrafluoroethylene
PDI	Polydispersity index
PMMA	Poly(methyl methacrylate)
POF	Polymeric optical fibre
PVDF	Poly(vinylidene fluoride)
PVDF-TrFE	Polyvinylidene difluoride-co-trifluoroethylene
Q	
QOF	Quartz optical fibers
S	
SEM	Scanning electron microscopy
T	
TEM	Transmission electron micrsocopy
U	
UNICEF	United Nations Children's Fund
X	
XRD	X-ray diffraction

1. Introduction

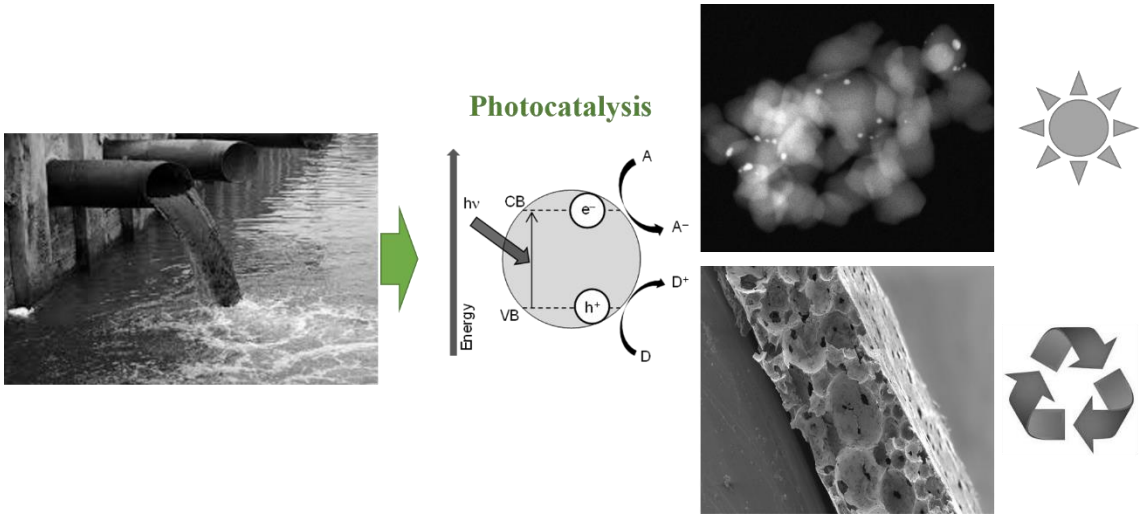

Water pollution is a growing problem, and many efforts were made in the last decades to tackle it. Among many solutions, photocatalysis arises as an exciting technique to destroy a wide range of pollutants present in water. The current chapter presents a state of art of the central concepts of photocatalysis and photocatalytic materials used in the current work. This chapter also indicates the primary objectives of the study and the structure of this document.

1.1. Motivation

Nowadays a significant part of the worldwide population has no access to drinking water. The records provided by UNICEF and the world health organization (WWO), show that around 663 million people - almost a tenth of the global population, in particular in underdeveloped countries, have no access to drinking water (Figure 1.1)[1].

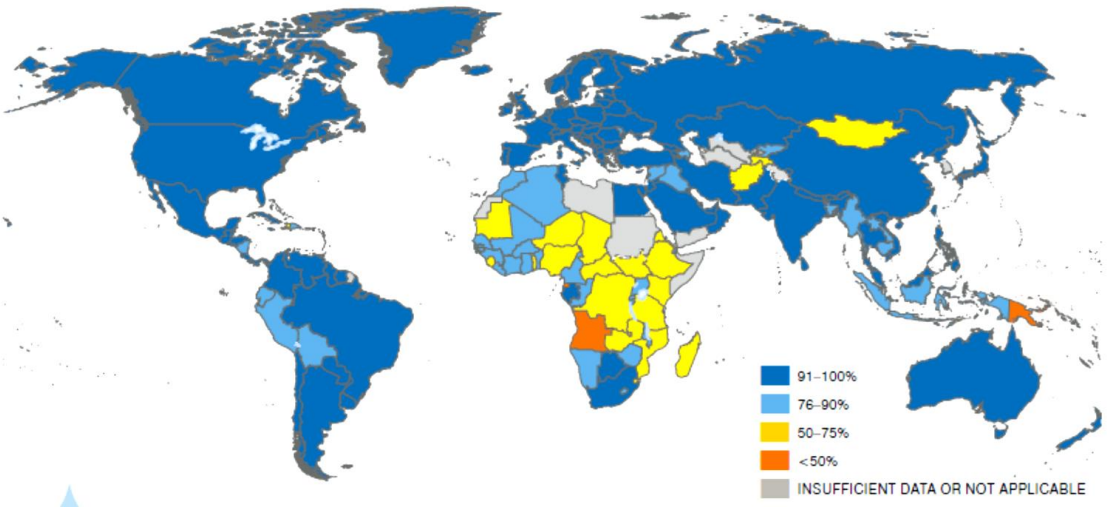

Figure 1.1. Scheme of worldwide distribution of drinking water in 2015 according to the assessment of UNICEF and WWO (adapted from [1]).

The aggravation of the water scarcity problem is in part caused by the increasing pollution of water resources all over the world. Humankind activities are responsible for the continuous and growing discharge of hazardous pollutants into water. Among the leading aquatic contaminants, micropollutants have recently received considerable attention from the scientific community. Micropollutants are organic substances that occur in water in concentrations of a few nanograms/micrograms per liter and, even at such low levels, can affect fundamental biochemical processes in ecosystems. Micropollutants include different compounds such as heavy metals, dyes and pharmaceuticals (mainly antibiotics), fertilizers and pesticides, and also personal care health products (e.g., body creams, and sun-creams), among others. Despite the high toxicity of these pollutants, the classical techniques for wastewater treatment, such as ponds and activated sludges, together with other technologies involving adsorption, coagulation, and filtration have proved to be ineffective in their removal.

In this context, the scientific community pursues the development of efficient, economical, and sustainable approaches to address these environmental issues. Consequently, significant efforts in developing suitable treatment processes to destroy these organic contaminants have been carried out, with emphasis on Advanced Oxidation Processes (AOPs).

Among the AOPs, photocatalysis arises as a simple alternative to degrade organic pollutants into carbon dioxide, water, and inorganic compounds.

The work herein presented focus on overcoming the principal limitations of photocatalysis by developing a new generation of materials and solutions that bring more efficiency, enhanced reusability, scalability and novel application areas.

1.2. Water remediation

The wastewater produced in agricultural and industrial activities and treated by wastewater treatment plants constitute one of the most significant possible water resources, as its reuse could counterweight the problem with water scarcity. Recycling wastewater is usually associated with the presence of suspended solids, health-threat coliforms, and soluble refractory organic compounds, becoming difficult and expensive to treat [2]. Thus, it is necessary to further research on the removal of traced contaminants to minimize their accumulation [3]. The remediation of water resources contamination is a huge concern, and many approaches able to degrade/remove micropollutants have been investigated [4]. The methods used in wastewater treatment plants have received particular attention since some resilient pollutants are discharged after secondary treatment, requiring subsequent treatment stages [5].

Processes such as filtration and coagulation/flocculation/sedimentation are the most used in conventional wastewater treatment plants (WWTPs). These techniques require following treatments to remove the pollutants from the effluents. Due to the low efficiency of these methodologies and the occasional inability of their use, new strategies have appeared [4, 6, 7]. Nowadays, available wastewater treatment technologies include activated carbon adsorption and chemical coagulation, membrane filtration, sedimentation and ion exchange on synthetic adsorbent resins, which do not entirely degrade water contaminants [2, 8, 9]. These technologies have high operating costs and could generate toxic by-products during treatment [10], demanding additional time

consuming and expensive steps [2, 3]. Other techniques include chemical oxidation and biodegradation, liquid extraction and membrane techniques, among others. The application of these methods heavily depends on the pollutant concentration in the effluent and cost of the process [4].

Adsorption is extensively used in industry for the removal of organic pollutants, but the pollutant is not eliminated, it passes from a liquid to a solid phase, producing a new solid waste with the contaminant, which again requires further treatments [11]. In filtration processes, the contaminants are retained in the pressurized side of the membrane while the clean effluent passes through to the other side. This process shows the same disadvantage that adsorption processes: generation of new waste. Ion exchange has been used to improve water quality, especially concerning heavy metals, boron, uranium and other elements. However, this is an expensive technique and requires pretreatment and the use of chemicals for resins maintenance and disinfection [4, 11, 12]. Chlorination is commonly used as a disinfectant, but it generates mutagenic and carcinogenic by-products [4]. The synergetic combination of different processes for higher or total mineralization of the pollutant may also be a strategy to deal with the main disadvantages of each method.

The lack of a robust method has led to the rapid research and development in the field of AOP as an innovative water treatment technology [4, 13, 14].

1.3. Advanced oxidation processes

Advanced Oxidation Processes are efficient environmental friendly processes based on the production of reactive free radicals with potent oxidizing properties such as $O2^{\bullet-}$ and, in particular, $OH^{\bullet}$ [15]. As it allows the oxidation of chemical pollutants as well as microorganisms inactivation, it can be a suitable process towards wastewater treatment and disinfection [16-18]. The AOP include techniques such as ozonation, photolysis, electrochemical oxidation, Fenton oxidation, ultrasound irradiation, and photocatalysis, among others [5, 19].

Ozonation has proven to be capable of efficiently oxidize a wide range of pollutants [20-22]. In this process, ozone is decomposed in water to form OH·, which is a stronger oxidizing agent than ozone itself. This technique has the advantage of allowing the application even at unstable flow rates. Additionally, to enhance its efficiency, the

treatment can be complemented with hydrogen peroxide, light irradiation, or iron copper complexes [4, 22]. As for disadvantages, the main ones are mass transfer limitations, low solubility, and temperature and pH-dependence. Moreover, the process demands high costs of equipment and energy [5].

Photolysis is the decomposition of any compound through photochemical reactions induced by natural or artificial light [4, 5]. The process efficiency depends on the absorption spectrum of the pollutant, radiation intensity and frequency, the oxygen and hydrogen peroxide concentration, and the water mass. This method is relatively ineffective in the removal of recalcitrant contaminants in effluents towards other treatments. It is typically used in wastewater with photo-sensitive compounds and with low chemical oxygen demand (COD) [2, 5, 23].

Another AOP is Fenton oxidation, which occurs in acidic medium with hydrogen peroxide solution and an iron salt catalyst (ferrous or ferric ions). The mechanism is based on the decomposition of ferric ions by the hydrogen peroxide in the aqueous phase, yielding the hydroxyl radicals [2, 4, 24]. To increase the process efficiency, it is possible the combination with UV radiation, the so-called photo-Fenton [24]. However, similarly to ozonation, Fenton oxidation is also highly dependent on the pH's and requires a time-consuming process to recover the precipitates [11]. Additionally, some compounds ($\mathrm{e.g.,Cl^-}$, SO_4^{2-}, $H_2PO_4/H_2PO_4^{2-}$) eventually present in the wastewater may interfere with the process and reduce its efficiency [25].

In electrochemical oxidation processes, the oxidation process takes place on the surface of the anodes. Typically, graphite (C), platinum (Pt), titanium dioxide (TiO_2), Ti-based alloys, iridium oxide (IrO_2), plumbic oxide (PbO_2), and more recently boron-doped diamond, are used in the presence of an appropriate electrolyte. In this way, the pollutants are adsorbed onto the anode's surface and then broken down through an anodic electron transfer reaction [4, 26].

Ultrasound irradiation is a relatively recent process in water treatment, where high-intensity acoustic radiation induces sonochemical reactions, which produces cavitation. These reactions originate OH·, which will ultimately oxidize the pollutants. This process is efficient for organics with low solubility and high volatility since they tend to accumulate inside the gas-liquid interface [26].

It is in this context that semiconductor photocatalysis upsurge as an emerging technology. It just requires a photocatalyst, a source of photon energy and an oxidizing agent (pollutant). The photocatalytic treatment has as main advantages the operation at ambient

conditions, photochemical stability, being economical and commercially available [4, 5, 24, 27]. Further, this treatment process gains a particular relevance due to its remarkable degradation efficiency, non-selectiveness and potential for the treatment of effluents with low loads of organic matter (river, groundwater, and drinking water) [28]. This work will focus on heterogeneous photocatalysis.

1.4. Heterogeneous photocatalysis

The expression catalysis was initially used in 1835 by Jöns Jacob Berzelius to describe the increasing rate of a chemical reaction using compounds that remained intact during the reaction, the so-called catalyst [29]. The term "photocatalysis" was mentioned for the first time in 1910 by Plotnikow when referring to catalytic process induced by radiation absorption (ultraviolet, visible, or infrared), using a photocatalyst [30]. Later, in 1960's, Fujishima and Honda published a work dedicated to water splitting under visible radiation with a titanium dioxide (TiO_2) electrode and without external voltage [31, 32]. In 1977, Frank and Bard reported the degradation of cyanide and sulfite with different photocatalysts [33]. This work proved that photocatalysis was an effective wastewater treatment method as it allowed the degradation of organic contaminants into innocuous compounds such as CO_2 and H_2O [34], [35, 36]. The heterogeneous photocatalytic oxidation is usually merely called photocatalysis. Among the above mentioned AOP, photocatalysis is one of the most promising techniques. Mainly because when compared with other technologies, it only requires a source of radiation (UV or sunlight) and a photocatalyst, making it a straightforward and a cost-effective process [34, 37]. Many materials, usually semiconductors (e.g., TiO_2 and ZnO), can be used in heterogeneous photocatalysis - this issue will be discussed in detail in the following sections.

1.4.1. Reaction pathways and kinetics of heterogeneous photocatalysis

The photocatalytic process, represented in Figure 1.2, begins irradiating a semiconductor with equal or higher energy than its bandgap. The absorption of such radiation will allow the transition of an electron (e^-) from the valence band to the conduction band, which will also create a hole (h^+) in the valence band. This newly formed electron-hole pair can recombine again in the semiconductor, producing heat, or be a part of redox reactions with the species adsorbed onto the photocatalyst surface [38, 39].

Holes possess positive charge that reacts with water producing hydroxyl radicals (OH•) and hydrogen ions (H^+). On the other hand, under aerobic conditions, electrons react with the dissolved oxygen in the water and form superoxide anions ($O2^-$•), which react with water molecules to produce hydroxide ions (OH^-) and peroxide radicals (•OOH) [34, 40, 41].

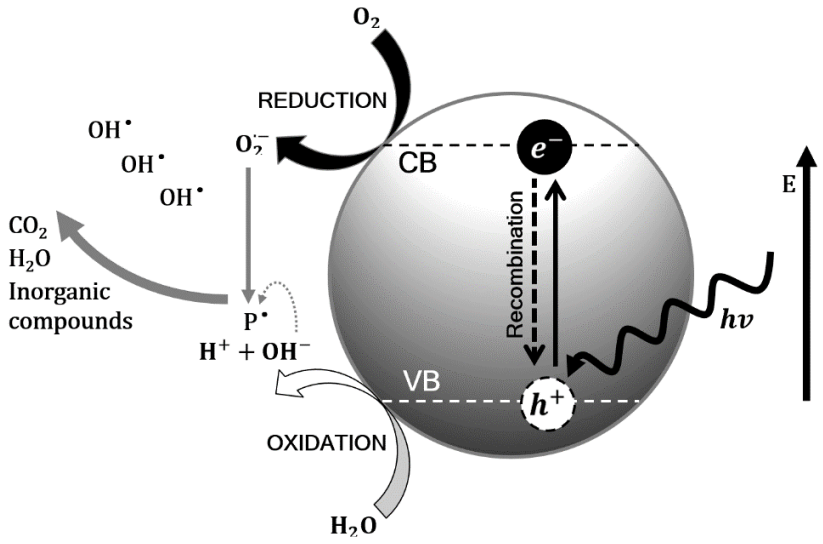

Figure 1.2. Schematic representation of the photocatalytic mechanism on a semiconductor nanoparticle in the presence of a water pollutant (P) and with light irradiation (hυ).

The produced peroxide radicals combine with H^+ ions to form OH• and OH^-, while the holes can oxidize OH^- to OH• and then oxidize organic pollutants. Subsequently, all species contribute to the production of OH•, which is the primarily responsible species in the degradation of contaminant molecules present in aqueous solution [42-44].

As mentioned, the principle of photocatalysis lies in the activation of the semiconductor by an energy source (ultraviolet (UV) or visible range radiation), represented in Eq.1.1 [5, 45].

$$Catalyst \xrightarrow{h\nu} Catalyst\ (e^- + h^+) \qquad \text{Eq. 1.1}$$

The photogenerated holes have a high oxidation potential, yielding OH trough water molecules oxidation. The conduction band electrons have now no holes to recombine with (because they oxidized the water molecules Eq.1.2). Consequently, they reduce the dissolved oxygen, producing a superoxide radical anion (O2–•) (Eq.1.3). These can

subsequently react with water to form hydroxyl radicals (Eq.1.4), which later are transformed into H_2O_2 (Eq.1.5) [46-48]:

$$Catalyst\ (h^+) + H_2O_{ads} \rightarrow Catalyst + \ OH\bullet\ + H^+ \qquad \text{Eq. 1. 2}$$

$$Catalyst\ (e^-) + O_2 \rightarrow Catalyst + O_2^-\bullet \qquad \text{Eq. 1.3}$$

$$O_2^-\bullet + H_2O \rightarrow HO_2\bullet + OH^- \qquad \text{Eq. 1.4}$$

$$2HO_2\bullet \rightarrow H_2O_2 + O_2 \qquad \text{Eq. 1.5}$$

Additionally, hydrogen peroxide (H_2O_2) may act as an electron receptor and generate other hydroxyl radicals (Eq.1.6) [46-48]:

$$Catalyst\ (e^-) + H_2O_2 \rightarrow Catalyst + OH^- + OH\bullet \qquad \text{Eq. 1.6}$$

It may also react with the $O^{2-}\bullet$ and originate further OH•:

$$H_2O_2\ +\ O_2^-\bullet \rightarrow OH^- + OH\bullet \qquad \text{Eq. 1.7}$$

The adsorbed compounds (C_{ads}) can be directly oxidized by the holes at the surface of the photocatalyst [4, 49]:

$$Catalyst\ (h^+) + C_{ads} \rightarrow Catalyst + C_{ads}^{\circ+} \qquad \text{Eq. 1.8}$$

These reaction pathways show that organic species can be oxidized by the radicals or by the holes, after adsorption to the photocatalyst surface, and produce carbon dioxide (CO_2), water, and inorganic compounds [50-52]. The weakly adsorbed contaminants are oxidized by OH• radicals. On the other hand, the pollutants that are strongly adsorbed are oxidized at the surface of the photocatalyst by the photo-induced holes [53].

Another relevant and widely discussed issue about the photocatalytic degradation of water contaminants is the kinetics [54]. Many studies state that these photocatalytic reactions typically obey to the classical Langmuir-Hinshelwood kinetics (L-H model) that is simplified to pseudo-first order kinetics or zero-order kinetics, depending on the experimental conditions [55, 40, 42]. For instance, the initial concentration of the contaminant is a paramount variable, as it directly affects the surface of the catalyst. If the contaminant completely covers the catalyst surface, the surface will be saturated, and

the Langmuir-type kinetic rate is the zero-order type, which implies that the overall rate does not depend on external mass transfer. Conversely, if the initial concentration of the pollutant is low, the kinetic rate is a pseudo-first order. In this case, the kinetics depends on mass transfer regardless the initial concentration [56].

This classical L-H model is typically used to estimate the kinetics of heterogeneous photocatalytic materials, on the assumption of the adsorption/desorption equilibrium of the reactants to the catalyst [57-59]:

$$r = -\frac{dC}{dt} = \frac{k_r K_L C}{1 + K_L C} \qquad \text{Eq. 1.9}$$

Herein, r is the reaction rate, k_r is the reaction rate constant, K_L is the Langmuir adsorption constant, and C corresponds to the reactant concentration.

If the reactant concentration is low ($K_L C < 1$), in the mM order, it is possible to simplify to an "apparent" pseudo-first-order kinetic law (Eq.1.10) [57, 2]:

$$r = -\frac{dC}{dt} = kC \qquad \text{Eq. 1.10}$$

Here, $k = k_r K_L$ is the pseudo-first-order reaction rate constant. From this previous equation, reordering and integrating it into a typical pseudo-first order [2], Eq.1.11 is obtained:

$$C = C_o e^{-kt} \qquad \text{Eq. 1.11}$$

It is important to highlight that this model lies on the amount of contaminant that adsorbs onto catalyst surface, and therefore it is not adequate to explain the photocatalytic degradation if the contaminant does not adsorb to the catalyst surface. Furthermore, it is capable of defining the relationship between the reaction rate (dC/dt) and the intensity of the photon flux. This model assumes that the reaction of the adsorbed molecules controls the reaction rate and that the adsorption/desorption equilibrium is reached [40, 60].

Therefore, although the L-H model is used in the general situation of heterogeneous photocatalytic reactions, it disregards several steps of the process such as [60]:

1) generation of free holes in the valence band and free electrons in the conduction band;
2) charge carriers recombination;
3) trapping of the photogenerated holes in surface states;
4) reduction of the dissolved oxygen by the photogenerated electrons process.

In spite of the cited restrictions of the L-H model, a significant number of works continue to use the Langmuir model, mainly because the majority of these studies deal with low contaminants concentration (avoiding catalyst saturation), following the L-H kinetics [42].

1.4.2. Photocatalytic materials

As previously mentioned, a photocatalyst absorbs photons with energy equal or higher than its band gap, and an electron is excited from the valence to the conduction band, generating a hole in the valence band [4]. Several materials have been studied for photocatalysis (Table 1.1).

Table 1.1. List of photocatalytic materials and representative references with their use in photocatalysis.

Material	References
Titanium dioxide | TiO_2	[61-65]
Zinc oxide | ZnO	[61-63, 65, 66]
Cadmium sulfide | CdS	[62, 63, 66-68]
Gallium phosphide | GaP	[62, 63, 66, 67]
Zinc sulfide | ZnS	[62, 63, 68-70]
Niobium oxide | Nb_2O_3	[69]
Tin oxide | SnO_2	[63, 65, 68, 69, 71]
Molybdenium disulfide | MoS_2	[72]
Strontium titanate | $SrTiO_3$	[63, 68]
Cerium oxide | CeO_2	[73]
Copper oxidde | CuO Calcium oxide | CaO	[74]
Tungstenium trioxide | WO_3	[63, 68, 69, 71, 75]
Zirconium dioxide | ZrO_2	[67, 72]
Aluminum oxide | Al_2O_3	[67]
Magnetite | Fe_2O_3	[62, 63, 66, 68, 69]

Titanium dioxide (TiO_2), Zinc oxide (ZnO) and Cadmium sulfide (CdS) are the three most used in wastewater decontamination - usually in suspension systems. They possess unique optical properties, low cost, availability, high activity, chemical and thermal stability, chemical resistance to breakdown and robust mechanical properties [5].

Among the materials used in photocatalysis, TiO_2 is the most used and studied regarding photocatalytic applications.

TiO_2 is part of the family of transient metal oxides and appears mostly in the crystalline phases anatase, rutile or brookite. Both anatase and rutile show a tetragonal structure, with rutile being a high-temperature stable phase, and having an optical energy band gap of 3.2 eV (380 nm) and 3.0 eV (415 nm) for anatase and rutile, respectively [76-78]. The photocatalytic efficiency of each phase is different, with the anatase demonstrating a better photocatalytic activity [38, 79, 80].

The first evidence of the photocatalytic effect of TiO_2 arose in 1921 when Carl Renz [81] observed that this material, when illuminated by sunlight, and in the presence of organic compounds, was partially reduced by changing color. At this point, the mechanism was still unknown. In 1938, Goodeve and Kitchener [82, 83] performed the photocatalytic degradation of a dye using TiO_2 and stated that this semiconductor acted as a catalyst for the oxidation reactions involving the absorption of light. In 1965 McLintock and Ritchie [84] used titanium dioxide as a photocatalyst and showed the total degradation of ethylene and propylene, obtaining as natural products, carbon dioxide, and water. In spite of those advances, it was only in 1972, with the construction of the first photoelectrochemical cell for water electrolysis by Fujishima and Honda [32], containing a TiO_2 anode and a platinum cathode, that the photocatalysis using titanium dioxide began to assume more significant expression [51, 53].

The properties of TiO_2 also contributed to its increasing importance in photocatalysis. TiO_2 is the most active photocatalyst under the photon energy of $300\ \text{nm} < \lambda < 390\ nm$, it remains stable even after the repeated catalytic cycles, unlike Cds and ZnO, which are degraded along to produce toxic by-products [4, 85]. Nonetheless, TiO_2 has a few drawbacks, such as the difficulty and high cost for post-separation of the used nanoparticles from the treated effluent, low UV utilization efficiency, especially in a slurry reactor system, and high recombination rate of the electron/hole pairs [50, 52]. Table 1.2 summarizes the main advantages and disadvantages of TiO_2 nanoparticles as photocatalytic material.

Table 1.2. Main advantages and disadvantages of TiO_2 nanoparticles as a photocatalytic material.

Advantage	Reference	Disadvantage	Reference
Low price	[62, 64, 86-88]	Limited to UV	[89-91]
High photocatalytic activity	[86, 92-95]	High recombination of electron-hole pairs	[89, 91, 92, 96, 97]
Good performance in atmospheric condition	[5, 62]	Aggregation due to its small size	[90]
Environmental friendly	[5, 64, 86-88]		
Good chemical stability	[66, 86, 93, 98, 99]		
Good biological stability	[75, 89, 95, 99, 100]		
Thermal stability	[66, 94]		
Strong mechanical properties	[66]		
Biocompatibility	[71, 101]		
Corrosion resistance			
Strong oxidizing power	[89, 100]		
Self-cleaning properties	[89]		
Antibacterial properties	[89, 102]		
High specific area	[89, 103-106]		
Availability	[92, 101, 107, 108]		
Unique electronic and optical properties	[106]		

Besides photocatalysis, TiO_2 has been used as capacitors, pigments, antimicrobial materials [90, 109, 110], self-sterilizing devices [90], medical implants, biosensors [111], cancer therapy [90, 111], thin film solar cells [90, 109], air purification, sensing, electrochromic, photochromics, toothpaste and UV protection sunscreens [90].

Nowadays, Degussa P25 TiO_2 is the most widely applied commercial photocatalyst in the experimental research of water treatment. P25 contains ≈ 75% of anatase and ≈ 25% of rutile phases with a specific Brunauer, Emmett, and Teller (BET) surface area of 50 m^2g^{-1} and a primary particle size of 20 nm [2, 3, 5]. This catalyst is used as a standard reference under different photo activity conditions [2]. The photocatalytic activity of Degussa P25 was reported to be higher than other photocatalysts because it prevents the fast recombination between electrons and holes [3]. Although nanoscale TiO_2 shows considerable improvement regarding physical and chemical properties compared to the

bulk TiO_2 catalysts, its smaller particle size and morphology remains the main problem when applied in larger scale water treatment systems. The main difficulty is to build an efficient UV reactor system with well-controlled conditions to properly disperse and recover the nanocatalyst [112].

ZnO is also very used for the photocatalytic process, mainly because it presents unique characteristics that make it widely used, such as its wide band gap (3.4 eV) and good optoelectronic, catalytic and photochemical properties. On the other hand, it possesses a fast recombination rate of photogenerated electrons/holes pairs [2]. Overall, ZnO shows excellent photocatalytic activity, decomposing different organic contaminants more efficiently than TiO_2 in an aqueous solution [85]. CdS is also popular due to its shorter excitation wavelength ($\simeq$ 495 nm) and excellent absorption of sunlight because of its smaller band-gap (2.4 eV) [78]. However, ZnO and CdS present photo-dissolution when in water, causing them to decompose into hazardous by-products, which is considered the primary limitation - lowering its photocatalytic efficiency and application [113].

In short, TiO_2 nanoparticles continue to possess the most advantageous catalyst material for photocatalytic applications when compared with others photocatalyst. For all the mentioned reasons, TiO_2 was the photocatalyst used in this work.

1.4.3. Operational parameter influencing photocatalysis

To properly employ and interpret photocatalysis it is essential to understand the process (section 1.4.1) and also the main factors that can affect it. Several works have studied these parameters [52, 114-117]. In slurry photocatalysis some crucial factors influence photocatalytic process efficiency. For instance, the photocatalyst concentration, the initial concentration of the contaminant (presence of other chemicals), the dissolved oxygen concentrations, pH and temperature, and the illumination conditions play essential roles on the photocatalytic process [42, 118, 119]. For easy readability and comprehension, the different parameters are presented separately.

- *Photocatalyst concentration*

The concentration of the photocatalyst is among one of the most critical factors affecting the photocatalytic process. Different authors reported a wide range of concentration (mg L^{-1} to g L^{-1}) [58, 120, 121].

In good agreement with L-H model, below hundreds mg L^{-1} the reaction rate increases with increasing the concentration of the catalyst due to its larger total surface area [122-124] and improved radiation harvesting. Above a specific concentration, the reaction rate constant decreases with increasing the photocatalyst concentration [121, 123, 124]. This decreased efficiency usually happens in the range of mg L^{-1} to g L^{-1} and can be explained by the high turbidity caused by suspended particles, which mitigates the penetration of radiation [125, 126]. Additionally, the agglomeration of the particles will also reduce the number of active sites for adsorption. In short, increasing the catalyst concentration above an optimum plateau will not improve the photocatalytic efficiency [127-129]. It is also important to state that the optimum amount of catalyst depends on the types of contaminants, and the experimental conditions [114, 130, 131].

- *Illumination conditions*

The light wavelength and intensity are also critical parameters to consider because the photocatalytic activity is highly related to the energy of the incident photons [114, 132, 133].

Typically, under low intensities (< 20 mW/cm^2), the dependence between the reaction rate and light intensity is linear, which means that the reaction rate increases with the light intensity until it reaches a certain limit [49, 135, 136]. At medium intensities (≈ 25 mW/cm^2) [98], the reaction rate becomes square root dependent because the rate of e^-/h^+ pairs formation competes with the photocatalytic rate [114, 136]. Concerning high intensities, it is observed a zero order dependency because there is a predominance of e^-/h^+ recombination over formation [49, 136, 137]. It is important to underline that the recombination is an exothermic process. Consequently, high intensities should be avoided, as the catalyst can overheat reducing its reusability. The influence of temperature will be discussed later.

- *pH*

As previously mentioned, the photocatalytic process strongly relies on the generation of hydroxyl radicals that strongly depends on the pH of the solution [29], [89]. All the reactions occur on the surface of the catalyst, and the pH of the solution influences its surface charge [138, 139]. The *isoelectric point* (IEP) represents the point of zero charged

surface, *i.e.*, there is a low interaction between the photocatalyst particles and the charged water contaminants, because there are no electrostatic forces [66, 127].
When the pH of a suspension is equal to the IEP, the photocatalyst tends to agglomerate (limiting radiation penetration) and precipitate as the electrostatic surface potentials are zero [140]. Above the IEP value, the surface of the catalysts becomes negatively charged, while below this pH, it becomes positively charged. In practice, cations can adsorb on the surface of the catalyst above IEP value, and repelled from the positively charged surface at pH below the IEP value [2, 127]. In this way, the nature of the electrostatic forces between the catalyst surface and the pollutant, attraction or repulsion, may respectively enhance or inhibit the photocatalytic process efficiency [66, 127].
The relevance of the pH is such that some works state that the position of conduction and valence bands of photocatalysts depends on the pH, suggesting that the band gap also changes [141, 142].

- *Reaction temperature*

Like any chemical reaction, the photocatalytic process depends on temperature [143]. Additionally, the adsorption of contaminants to the photocatalyst surface is equally influenced by the reaction temperature [66, 144]. At low temperatures, the adsorption of reactants, by-products, and final products is promoted and restrains the product desorption. Conversely, at high temperatures, the adsorption process rate is not favored and becomes the rate-limiting step of the photocatalytic process [127, 145, 146].
Usually, the photocatalytic process occurs at ambient temperature, and the optimum temperature ranges between 20 °C and 80 °C [147, 148]. When temperature increases, the reaction rate increases because of the collision of the pollutant molecules [147]. At extreme temperatures (-40 °C – 0 °C and above 80 °C) the photoactivity process decreases, although low temperatures favor reactants adsorption whereas high temperatures disfavor it [149, 150]. Additionally, it should be emphasized that the increase in temperature results in a decrease of the dissolved oxygen, which is also a crucial parameter affecting the photocatalytic process [148].

- *Dissolved oxygen*

The dissolved oxygen is one of the possible electron acceptors alongside with hydrogen peroxide or ozone [39, 134, 151]. The dissolved oxygen does not affect the adsorption of the reactive species on the surface of the catalyst since oxidation occurs at different sites from those of reduction [2, 128, 140]. Oxygen plays as an electron scavenger, being reduced by the excited electrons avoiding them from recombination with the photogenerated hole. Moreover, it is involved in the formation of other reactive oxygen species, such as the superoxide radical [129,134].

A very high amount of electron acceptors will completely cover the surface of the photocatalyst, and compete for the adsorption of the organic pollutants, having an undeniable effect on the photocatalytic process.

- *The initial concentration of the contaminant*

The adsorption process, as the ratio between the amount of photocatalyst and the concentration of organic pollutants, is affected by the initial concentration of the organic substances [130]. In the absence of organic compounds, the hydroxyl radicals accumulated on the photocatalyst surface are not consumed. In this context, the photocatalytic process only takes places in the presence of organic substances [152]. On the other hand, increased concentration causes mass transfer limitations. Organic compounds, intermediates, and products obstruct the active reaction sites at the TiO_2 surface [127,130]. However, below a specific concentration of the photocatalyst, the mass transport is negligible [153, 154].

The shielding effect of organic substances can also occur because depending on the organic molecules properties, they can absorb UV or visible radiation. Usually, for colored dye substances at high concentrations, more photons are absorbed by the dye molecules instead of the catalyst surface, which will negatively affect the photocatalytic process efficiency [155-159].

- *Morphology of photocatalysts*

Many techniques can be used to characterize photocatalytic materials, and some of them are focused on the morphology of nanoparticles. Due to the synthetic process of

nanocatalysts, one rarely finds them as primary particles. In its place, it is usually obtained as the so-called aggregate and agglomerate structures [160], which properties differ from the primary particles. Optical properties such as scattering or the degree of photon diffusion depend on the aggregate size and structure.

Particle size and morphology determine optical properties of the system [161, 162]. It was demonstrated that particle size also affects the lifetime of electrons and holes, and their recombination [163, 164]. Also, shape and structure of photocatalysts affect the internal diffusion of light and organic concentration inter-particles [153, 165, 166]. Experimentally, the reactivity of photocatalysts reduces as the aggregates become larger and denser [167-169]. Lastly, size also affects the distribution and sedimentation of photocatalysts in suspension, as well as influences the operation of post-treatment [149, 170].

1.5. Strategies to improve the photocatalytic process

As previously discussed in detail, TiO_2 is very promising because of its photocatalytic efficiency, biological inertness, and its commercial availability, among other characteristics [2, 171]. However, the broad bandgap requiring UV irradiation for the activation is the main disadvantage. Regarding the excitation of TiO_2 nanoparticles, an energy of 3.0 – 3.2 eV or, accordingly, wavelengths shorter than $\approx$ 410 – 387 nm are required [38, 53, 172]. Due to the reduced amount of UV-radiation in the sunlight spectrum [173, 174], TiO_2 can absorb only 2−5 % of the incoming solar energy.

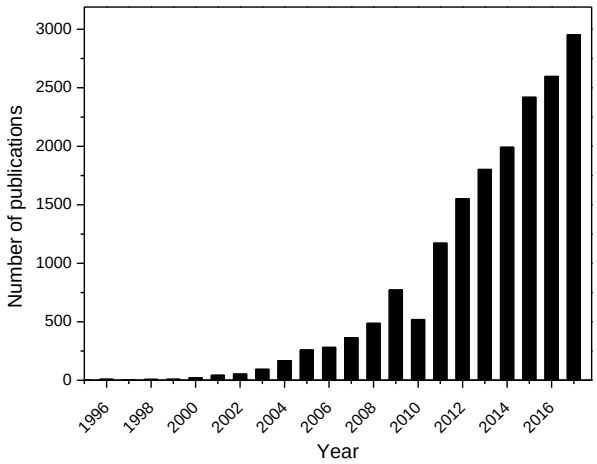

Figure 1.3. The number of scientific papers with the keywords "photocatalysis" and "visible" (Source: Scopus in March of 2018).

This paramount limitation of TiO_2 has compelled scientists to pursue new solutions. to endow TiO_2 nanoparticles with the ability to absorb visible radiation, leading to an increasing number of publications (Figure 1.3)[38].

Alongside with the low visible activation of the photocatalysts, other hindrances are the recovery of the particles after water treatment. In this way, the main advantage of the use of the immobilized form towards the suspension form is that the costly and extra final filtration or sedimentation process can be avoided [42, 175, 176]. Additionally, immobilizing the photocatalyst favors its reusability.

The following sections will address both, the modification of photocatalyst towards visible absorbance, as well as the immobilization of photocatalysts to improve reusability, eco-friendliness, and economics of photocatalytic materials.

1.5.1. Modified photocatalyst

Doping is one of the main techniques employed to achieve photocatalytic materials active under visible radiation. Photocatalysts can be doped with different types of metals (including rare earth elements) or nonmetals [2, 177, 178]. The non-metallic dopants (nitrogen [179, 180], carbon [181]) may localize electronic states above the valence band of the photocatalyst, thus narrowing the band gap energy and extending the light absorption of photocatalysts to the visible range [178, 179] and, therefore, it increases the photocatalytic response or photoresponse of the materials. The presence of metals can also narrow the band gap of photocatalysts, becoming active with lower photon energy than pristine photocatalysts [178]. Moreover, metallic ion dopants extend the lifetime of the charge carriers by trapping electrons. Hence, the counter carrier can reach the surface of the photocatalyst [182, 49, 50]. Various metals have been used such as silver [183], platinum [184], gold [185], iron [186], copper [187], chromium [188], magnesium [189] and tin [190]. Doping can also be performed using rare earth elements, which belong to the f-block in the periodic table including lanthanides, as well as scandium and yttrium. Doping with this elements will inhibit the phase transformation of titania photocatalysts from anatase to rutile [191, 192], being anatase is claimed to be the most active for photocatalytic uses. Besides, rare earth doped photocatalysts show an improved photocatalytic activity as lanthanide ions play a role of an electron acceptor and accelerate the electron-hole separation [193-195]. Attributed to a charge transfer transition between f-electrons and the conduction/valence band of titania, the bandgap of the photocatalyst

is narrower [188, 193]. The redshift to longer wavelength excites the catalyst, in the visible light, and allows more efficient utilization of the spectra.

Another modified photocatalyst group is nanocomposites [196, 197]. The materials consist of photocatalyst domains in contact with inert or photoactive compounds. Different strategies have been applied. Nanocomposites can be produced by depositing metals (Ag [198], Au [199]) on photocatalysts. Similar to the mechanism of metallic doped photocatalysts, the Fermi level of metals shift closer to the conduction band of the photocatalyst, which indicates a better separation of electrons and holes [200]. Composites composed of photocatalysts and some carbonaceous materials with high conductivity (like graphene [201], carbon nanotubes [202]) also show this property. Another strategy is coupling. TiO_2 can be coupled with different semiconductors (SnO_2 [203], WO_3 [204], ZnO and CdS [205]). Their bandgap is similar to TiO_2, which possesses a conduction band with lower energy state and the valence band is either similar or lower, acting as an electrons and holes storages. Consequently, interparticle electron transfer from TiO_2 to the other materials occurs and expands the lifetime of electrons and holes.

Surface modification is the other form to improve photocatalytic activity [197]. Sol-gel preparation of silica or zirconia allows controlling the crystallinity and help to achieve purer anatase [197, 206]. The surface roughness of photocatalysts is related to their reflectivity, and the efficiency of light absorbance [43] can be altered by doping photocatalysts with silver [76]. Adsorption capacity is one of the most dominant parameters affecting photodegradation [43]. The deposition of nanoporous materials such as fractal-type morphology [207], nanofibrous architecture [148], nano hollow [208] structured may enlarge the surface area of photocatalysts. In additions, increasing the adsorption of dissolved oxygen enhances the charge carriers separation [197]. As polytetrafluoroethylene (PTFE) has an affinity toward O_2, it can be selected to produce the composite film to increase the local concentration of oxygen [209]. Other properties such as surface charge, surface hydrophilicity, and specificities (selectivity of specific toxic compounds) can be altered as well [197].

1.5.2. Immobilization of photocatalytic nanoparticles

As previously mentioned, another drawback of photocatalytic slurry systems lies on the recovery of the suspended nanoparticles from the treated water stream [75, 87, 98], which

is also the critical obstacle towards the applications in industrial scale [66]. Additionally, such difficulty is associated with secondary pollution of the effluent [65, 210], the loss of catalyst [65, 210], increasing the overall cost of the treatment – hindering its reuse [65, 210].

The immobilization of photocatalysts is the right path to endow a photocatalytic system with reusability and to avoid the discharge of suspended nanocatalyst in the treated effluents. The efficient immobilization of catalytic nanoparticles requires some critical conditions. For instance, the support/substrate should allow a durable adherence to the catalyst, high specific surface area, high adsorption and affinity to the pollutants, and the catalytic properties of the catalyst should not be negatively affected by the immobilization process [4, 211]. Despite resulting in a considerable reduction of surface area and mass transfer limitations, and consequent loss of photocatalytic efficiency [4, 5, 212] this methodology seems to be promising in the efficient removal of micropollutants from effluents. Immobilising photocatalysts, on the other hand, also reduces the amount of catalyst active sites and hinders light harvesting [4, 5, 212].

Over the last few decades, significant advances were made in the scope of immobilized catalysts. However, this technology has never been used in real water/wastewater treatment [4, 213]. There are also several restrictions to find the suitable and an efficient immobilization procedure, in particular, at economic levels, regarding the immobilization method, the light source (artificial [214, 215] or solar [216, 217]) and micropollutant type (organics [218, 219] or dyes [215, 220]). This context demands the design and fabrication of robust and stable immobilized photocatalytic system [1].

Many immobilization techniques such as chemical vapor deposition (CVD), dip coating, sol-gel, and electrospinning have been employed to achieve photocatalyst immobilization [221, 222]. For instance, gas-phase methods (e.g., CVD) are typically used for the catalyst deposition on glass and metals substrates, while liquid phase methods (e.g., dip coating) are usually used for deposition onto polymeric and heat sensitive substrates [223]. Dip coating requires simple equipment and mild conditions is difficult to achieve by gas-phase methods [224]. Electrospinning seems to be a suitable immobilization method because it is a simple, low-cost approach used to produce electrospun membranes with low intramolecular defects [225-227]. Spray pyrolysis is also used to prepare photocatalyst thin films because it is an inexpensive and eco-friendly technique [228]. The electrophoretic deposition also allows the production of thin films but with complex geometry and even multilayer structure [229]. Besides the mentioned approaches, other

techniques have been used; such as cold plasma discharge, polymer assisted hydrothermal decomposition, and photo etching among others [230].

Concerning the materials, similarly to the used techniques, many attempts have been made to find the perfect substrate for immobilization of photocatalytic nanoparticles [231], Table 1.3 summarizing some of the tested materials.

Table 1.3. List of some materials used as a substrate for photocatalyst immobilization.

Material	References
SiO_2	[93, 100, 232, 233]
Carbon Fibers	[100, 234]
Activated carbon	[232, 235]
Gibbsite	[236]
Glass	[100, 106]
Alumina	[237]
Zeolite	[93, 99, 106, 232]
Quartz/Polymeric Optical Fibers	[100, 238]
Sand	[100, 106]
Wool	[239]
Pyrex Stainless Steel	[240]
Ceramic	[241]
Polystyrene	[236, 242]
Cellulose	[243]
Polythene	[244]
Polyvinylidene Fluoride	[245]
Polyethylene Terephthalate	[246]

The performance of the immobilized nanoparticles is related to the support type, pore size and blockage, regeneration or back-washing and, in some cases, fouling [66]. A study that used different substrates and methods for TiO_2 nanoparticles immobilization was carried out [112]. The results show that the use of nanofibers, nanowires or nanorods solves the mass transfer limitation due to their thin longitudinal morphology. These fiber membranes show high pollutant removal rate. However, the use of less mechanical resistant materials such as glass or woven cloths may lead to low durability, with the attached nanoparticles peeling-off, and loss of photocatalytic efficiency over time.

Despite the many materials and techniques tested, the immobilization of photocatalytic nanoparticles remains a challenge. Many of the mentioned substrates lack the conditions required for photocatalytic applications, such as adequate adhesion of the nanoparticles

to the substrate and catalyst reactivity after its attachment [221]. Among all the materials, the attention seems to be growing towards polymers such as polyester, polyamide-12, cellulose, high-density polyethylene, chitosan and poly(vinylidene fluoride) (PVDF) [247-252].The reason behind the attention over polymers is in part related with the polymer chains that are flexible and may contain a variety of functional groups that easily immobilize nanoparticles by van der Waals, electrostatic, hydrogen, or covalent bonds. Moreover, the extensive use of polymers is because they are inert, inexpensive, mechanically stable, and durable, which matches the ideal support material [252-256].
In particular, PVDF and its copolymers exhibit excellent chemical, mechanical, thermal, and UV resistance [13, 85].

1.5.3. Poly(vinylidene fluoride) and its copolymers

During this thesis, poly(vinylidene fluoride) (PVDF) and its copolymer polyvinylidene difluoride-co-trifluoroethylene (P(VDF/TrFE)), will be used as a substrate to immobilize different photocatalytic nanomaterials. In this sense, an introduction to these fluoropolymers will be outlined.
Fluoropolymers are characterized by high chemical inertness, very low surface tension, thermal stability and electrical insulating properties [257]. PVDF is a semi-crystalline fluoropolymer of the repeat unit (CH2-CF2-) [257, 258]. Many of the exciting properties of PVDF are related to the strong electrical dipole moment of the PVDF monomer unit, of $5 - 8 \times 10^{-30}$ Cm, due to the electronegativity of fluorine atoms about those of hydrogen and carbon atoms. In this way, each monomer possesses a dipole moment perpendicular to the polymer chain [259].

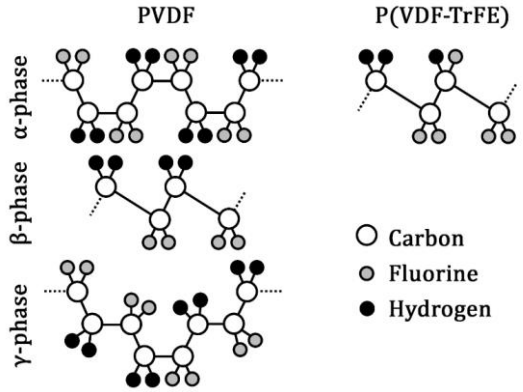

Figure 1.4. A schematic representation of the chain conformation of α, β, and γ-phases of PVDF and P(VDF-TrFE). Adapted from [227].

PVDF and vinylidene copolymers show a complex structure and possess five crystalline phases, corresponding to different chain conformations [258, 260]. The three most studied and used PVDF phases are shown in Figure 1.4.

Among the three most investigated PVDF phases, the α-phase presents a nonpolar structure with a TGTG′ chain conformation, while the β- and γ-phases present a polar structure with all-trans planar zigzag TTT and T3GT3G′ chain conformation, respectively. The β -phase presents the highest dipolar moment per unit cell (8×10^{-30} C m) when compared to the other two phases [258, 259].

Several co-polymers of PVDF have been developed to enhance certain properties and adjust them to the increasing technological needs. These include (P(VDF-TrFE)), poly(trifluoroethylene chloride) (P(PDF-CTFE)), poly(vinylidene fluoride-co-hexafluoropropene) (P(VDF-HFP)) and poly(vinylidene fluoride-trifluoroethylene-chlorofluoroethylene) (P(VDF-TrFE-CTFE)) [259]. P(VDF-TrFE) is among the most studied copolymers, and its chain conformation is shown in Figure .4. Polymer crystalline phase is highly affected by the processing technique and conditions or the inclusion of nanomaterials, yet PVDF−TrFE (70:30) crystallizes in the β-phase regardless the conditions employed [262]. This copolymer possesses a high degree of crystallinity and a high remnant polarization ($\simeq$ 110 mC m^{-2}) when compared to PVDF, allowing a larger electromechanical coupling factor, k, which translates into higher piezoelectric properties. P(VDF-TrFE) can be produced either in the form of films [260], fibers [263] [263] and membranes with a controlled microporosity [264, 265]. The physicochemical properties of this fluorinated co-polymer make it suitable for the photocatalytic application, as it shows excellent chemical, mechanical, thermal and UV radiation resistance, related to the stable C–F bonds of the polymer chain [258, 265].

It is important to emphasize that when using polymeric membranes, the photocatalytic reaction can take place, not only at the surface of the membrane but also inside their interconnected pores, enabling the treated water to be continuously discharged without the loss of photocatalyst particles [66, 258]. There is, however, always the risk of problems such as the deterioration of the membrane structure, low photocatalytic activity and the loss of the attached TiO_2 nanoparticles over time/use [2].

1.5.3.1. Production techniques

Numerous techniques have been proposed and employed for the immobilization of photocatalytic nanoparticles onto polymeric support [213]. Some of these techniques are listed in Table1.4.

Table 1.4. List of methods for the fabrication of supports for the immobilization of TiO_2 nanoparticles.

Technique	Type	References
Electrospinning	• Fibrous membrane	[227, 259, 263, 267, 268]
Spin and dip coating	• Film • Fibers and membranes	[269-272]
Deposition and sputtering	• Film	[273-275]
Solvent Casting	• Film • Porous membrane	[74][259] [238, 248, 276]

Thin films have the disadvantage of a low surface area and the fact that proper fixation of the nanoparticles is not guaranteed [266]. Fibers present a high surface area and porosity. However, their mechanical properties and practicability are poor. Membrane technology has dramatically grown in the last 30 years, not just for water treatment applications, but also for food processing and medical applications [277-279].

This work will focus on the solvent evaporation method, also known as solvent cast, as it enables the production of membranes with a controlled degree of porosity and pore size. In this way, it is possible to adjust the microstructure of the polymer for the desired application and to rapidly recover and reutilize the immobilized catalyst [258, 261]. One of the disadvantages of using P(VDF–TrFE) is its low wettability [280], as a result of its low surface tension, which restricts the interaction between the pollutant and the polymeric substrate, where the TiO_2 nanoparticles are immobilized [257]. A hydrophilic surface can be obtained using several techniques such as coating with nanoparticles, UV irradiation, and electron irradiation [281-284].

1.6. Objectives

The primary goals of this work are to produce, characterize and test photocatalytic nanoparticles and nanocomposites aiming to tackle the main problems of photocatalytic systems: enable reuse/recycling, increase photocatalytic efficiency and broaden photocatalytic activity to the visible range.

Thus, several specific objectives of this work are:

- Production of TiO_2/PVDF-TrFE nanocomposites, tailoring of wettability and comparison of degradation efficiencies with suspension systems;
- Use of TiO_2/PVDF-TrFE nanocomposite membrane in a solar photoreactor;
- Synthesis of pristine, doped, and codoped TiO_2 nanoparticles and immobilization on PVDF-TrFE membranes;
- Optimization and study of the influence of synthesis conditions of Au/TiO_2 nanocomposites on photocatalytic degradation performance;
- Processing of G/TiO_2 and GO/TiO_2 nanocomposites with different ratios of (G and GO) for photocatalytic degradation under UV and visible radiation;
- Production of PVDF-TrFE electrospun membranes for immobilization of GO/TiO_2 for photocatalytic activity studies;
- Development and optimization of a PVDF/TiO_2 coating for polymeric optical fibers and application in ciprofloxacin degradation;

1.7. Outline of the thesis

The herein presented thesis is composed of seven chapters, five of them are being based on published or submitted scientific papers. The arrangement of the chapters obeys a sequential order; the first one exploring several thematics related to water remediation and photocatalytic materials and process. The identification of the most critical

limitations of photocatalysis is emphasized in the first chapter, and the following chapters are devoted to the development of strategies and materials that allow overcoming those limitations efficiently. Two materials can be highlighted in this work, namely TiO_2 (pristine, doped, codoped, and nanocomposite) as the elected catalyst, and PVDF and PVDF-TrFE, as substrates for photocatalyst immobilization. The polymers are used in several chapters in different morphologies such as porous membranes (Chapter 2 and 3), fibers (Chapter 5), and coating (Chapter 6). Similarly, TiO_2 is present in all the chapters with different modifications, Er/TiO_2 and $Er/Pr/TiO_2$ (Chapter 3), Au/TiO_2 nanocomposite (Chapter 4), G/TiO_2 and GO/TiO_2 nanocomposites (Chapter 5), and pristine TiO_2 (Chapter 2 and 6).
In the following, a summary of the covered work in each chapter is briefly described.

Chapter 1 presents a general overview on photocatalysis and, specifically, its mechanism, kinetics, parameters limitations and strategies for enhanced efficiency. It is to notice that the specific state of the art on the different issues related to the present work are provided in the various chapters. The primary objectives and the structure of the document are described in this chapter

Chapter 2 reports on the development of photocatalytic membranes based on TiO_2 nanoparticles immobilized into a poly(vinylidenefluoride-trifluoroethylene) (P(VDF-TrFE)) membrane. Additionally, to change the wettability of the nanocomposites, NaY zeolites were added to the polymer matrix. This work also compared the photocatalytic performance of all the produced membranes with the equivalent amount of TiO_2 nanoparticles in suspension, in the degradation of methylene blue. Moreover, the TiO_2/PVDF-TrFE membrane was tested in the degradation of tartrazine. The dependence of tartrazine concentration, flow and light intensity on photocatalysis efficiency was addressed, as well as the reusability of the membrane.

Chapter 3 focus on the production of rare earth metals doped (erbium – Er) and codoped (erbium and praseodymium – Er:Pr) TiO_2 nanoparticles immobilized in poly(vinylidenefluoride - trifluoroethylene) (PVDF-TrFE) copolymer membrane. Both the nanocatalyst and the nanocomposite were physical-chemical characterized, and the efficiency of the different nanocomposites on the degradation of methylene blue, under UV radiation, was studied and related to their properties.

Chapter 4 is dedicated to the production of Au/TiO_2 trough nanoprecipitation method and under different synthesis conditions (e.g., temperature). The characterization of the nanocomposites was performed and the Au nanoparticles size and loading influence on the photocatalytic degradation of ciprofloxacin, under UV and simulated visible radiation, was assessed. All the photocatalytic efficiencies of the nanocomposites were compared with pristine TiO_2.

Chapter 5 comprises the synthesis of G/TiO_2 and GO/TiO_2 nanocomposites for degradation of methylene blue and ciprofloxacin, and a computational study focused on the nanocomposites interface. This chapter also addresses production, characterization and photocatalytic application of GO/TiO_2 immobilized in PVDF-TrFE electrospun. The photocatalytic efficiency was tested using different GO/TiO_2 loading and compared with electrospun membranes with bare TiO_2, under UV and visible radiation.

Chapter 6 shows the immobilization of the photocatalytic titanium dioxide (TiO_2) nanoparticles in a PVDF onto the surface of PMMA optical fibers by dip coating. The catalyst and polymer concentration, as well as the number of dips, were studied. Furthermore, the photocatalytic efficiency of the TiO_2/PVDF/MMA was tested for ciprofloxacin degradation under visible radiation.

Finally, **chapter 7** presents the main results, conclusions, and suggestions for future work.

1.8. References

1. Supply, W.U.J.W., et al., Progress on sanitation and drinking water. 2015.

2. Chong, M.N., et al., Recent developments in photocatalytic water treatment technology: A review. Water Research, 2010. 44(10): p. 2997-3027.

3. Ahmed, S., et al., Heterogeneous photocatalytic degradation of phenols in wastewater: A review on current status and developments. Desalination, 2010. 261(1): p. 3-18.

4. Homem, V. and L. Santos, Degradation and removal methods of antibiotics from aqueous matrices – A review. Journal of Environmental Management, 2011. 92(10): p. 2304-2347.

5. Klavarioti, M., D. Mantzavinos, and D. Kassinos, Removal of residual pharmaceuticals from aqueous systems by advanced oxidation processes. Environment international, 2009. 35(2): p. 402-417.

6. Arikan, O.A., The Fate of Chlortetracycline During the Anaerobic Digestion of Manure from Medicated Calves, in Survival and Sustainability: Environmental concerns in the 21st Century, H. Gökçekus, U. Türker, and J.W. LaMoreaux, Editors. 2011, Springer Berlin Heidelberg: Berlin, Heidelberg. p. 1087-1096.

7. Adams, C., et al., Removal of Antibiotics from Surface and Distilled Water in Conventional Water Treatment Processes. Journal of Environmental Engineering, 2002. 128(3): p. 253-260.

8. Wintgens, T., et al., Emerging contaminants and treatment options in water recycling for indirect potable use. Water Sci Technol, 2008. 57(1): p. 99-107.

9. Padmanabhan, P.V.A., et al., Nano-crystalline titanium dioxide formed by reactive plasma synthesis. Vacuum, 2006. 80(11): p. 1252-1255.

10. Gaya, U.I. and A.H. Abdullah, Heterogeneous photocatalytic degradation of organic contaminants over titanium dioxide: A review of fundamentals, progress and problems. Journal of Photochemistry and Photobiology C: Photochemistry Reviews, 2008. 9(1): p. 1-12.

11. Jiménez, S., et al., State of the art of produced water treatment. Chemosphere, 2018. 192: p. 186-208.

12. Nadav, N., Boron removal from seawater reverse osmosis permeate utilizing selective ion exchange resin. Desalination, 1999. 124(1): p. 131-135.

13. Andreozzi, R., et al., Advanced oxidation processes (AOP) for water purification and recovery. Catalysis Today, 1999. 53(1): p. 51-59.

14. Oturan, M.A., Electrochemical advanced oxidation technologies for removal of organic pollutants from water. Environmental Science and Pollution Research, 2014. 21(14): p. 8333-8335.

15. Leistner, G., Hazardous Waste Treatment Technologies. Von A. P. Jackman und R. L. Powell. Noyes Data Corp., Park Ridge 1991. IX, 276 S., zahlr. Abb. u. Tab., geb.–. Chemie Ingenieur Technik, 1993. 65(1): p. 96-96.

16. Lofrano, G., et al., An integrated chemical and ecotoxicological assessment for the photocatalytic degradation of vancomycin. Environmental Technology, 2014. 35(10): p. 1234-1242.

17. An, T., et al., Kinetics and mechanism of advanced oxidation processes (AOPs) in degradation of ciprofloxacin in water. Applied Catalysis B: Environmental, 2010. 94(3): p. 288-294.

18. Yang, H., et al., Photocatalytic degradation kinetics and mechanism of environmental pharmaceuticals in aqueous suspension of TiO_2: A case of β-blockers. Journal of Hazardous Materials, 2010. 179(1): p. 834-839.

19. Wang, J.L. and L.J. Xu, Advanced Oxidation Processes for Wastewater Treatment: Formation of Hydroxyl Radical and Application. Critical Reviews in Environmental Science and Technology, 2012. 42(3): p. 251-325.

20. Sui, M., et al., Heterogeneous catalytic ozonation of ciprofloxacin in water with carbon nanotube supported manganese oxides as catalyst. Journal of Hazardous Materials, 2012. 227-228: p. 227-236.

21. Liu, C., et al., Spectroscopic study of degradation products of ciprofloxacin, norfloxacin and lomefloxacin formed in ozonated wastewater. Water Research, 2012. 46(16): p. 5235-5246.

22. Mehrjouei, M., S. Müller, and D. Möller, A review on photocatalytic ozonation used for the treatment of water and wastewater. Chemical Engineering Journal, 2015. 263: p. 209-219.

23. De Bel, E., et al., Influence of pH on the sonolysis of ciprofloxacin: Biodegradability, ecotoxicity and antibiotic activity of its degradation products. Chemosphere, 2009. 77(2): p. 291-295.

24. Prihod'ko, R.V. and N.M. Soboleva, Photocatalysis: Oxidative Processes in Water Treatment. Journal of Chemistry, 2013. 2013: p. 8.

25. De Laat, J., G. Truong Le, and B. Legube, A comparative study of the effects of chloride, sulfate and nitrate ions on the rates of decomposition of H_2O_2 and organic compounds by Fe(II)/H_2O_2 and Fe(III)/H_2O_2. Chemosphere, 2004. 55(5): p. 715-723.

26. Mahamuni, N.N. and Y.G. Adewuyi, Advanced oxidation processes (AOPs) involving ultrasound for waste water treatment: A review with emphasis on cost estimation. Ultrasonics Sonochemistry, 2010. 17(6): p. 990-1003.

27. Philippopoulos, C. and M. Nikolaki, Photocatalytic processes on the oxidation of organic compounds in water, in New trends in technologies. 2010, InTech.

28. World Health, O., Pharmaceuticals in drinking-water. 2012.

29. Davis, M.E. and R.J. Davis, Fundamentals of chemical reaction engineering. 2012: Courier Corporation.

30. New and Future Developments in Catalysis A2 - Suib, Steven L, in New and Future Developments in Catalysis. 2013, Elsevier: Amsterdam. p. iii.

31. Coronado, J., et al., Design of advanced photocatalytic materials for energy and environmental applications. 2015.

32. Fujishima, A. and K. Honda, Electrochemical Photolysis of Water at a Semiconductor Electrode. Nature, 1972. 238: p. 37.

33. Frank, S.N. and A.J. Bard, Heterogeneous photocatalytic oxidation of cyanide and sulfite in aqueous solutions at semiconductor powders. The Journal of Physical Chemistry, 1977. 81(15): p. 1484-1488.

34. Kazuhito, H., I. Hiroshi, and F. Akira, TiO_2 Photocatalysis: A Historical Overview and Future Prospects. Japanese Journal of Applied Physics, 2005. 44(12R): p. 8269.

35. Hosseini, S.N., et al., Immobilization of TiO_2 on perlite granules for photocatalytic degradation of phenol. Applied Catalysis B: Environmental, 2007. 74(1): p. 53-62.

36. Malato Rodríguez, S., et al., Engineering of solar photocatalytic collectors. Solar Energy, 2004. 77(5): p. 513-524.

37. Liu, H.-L. and T.C.K. Yang, Photocatalytic inactivation of Escherichia coli and Lactobacillus helveticus by ZnO and TiO_2 activated with ultraviolet light. Process Biochemistry, 2003. 39(4): p. 475-481.

38. Linsebigler, A.L., G. Lu, and J.T. Yates, Photocatalysis on TiO_2 Surfaces: Principles, Mechanisms, and Selected Results. Chemical Reviews, 1995. 95(3): p. 735-758.

39. Hoffmann, M.R., et al., Environmental Applications of Semiconductor Photocatalysis. Chemical Reviews, 1995. 95(1): p. 69-96.

40. Minero, C., Kinetic analysis of photoinduced reactions at the water semiconductor interface. Catalysis Today, 1999. 54(2): p. 205-216.

41. Bahnemann, D., Photocatalytic water treatment: solar energy applications. Solar Energy, 2004. 77(5): p. 445-459.

42. Nair, M.L.S.V.S., Photocatalytic Water Treatment by Titanium Dioxide: Recent Updates. 2012.

43. Loutfy, R.O. and L.F. McIntyre, Photoelectrochemical solar energy conversion by polycrystalline films of phthalocyanine. Solar Energy Materials, 1982. 6(4): p. 467-479.

44. Augugliaro, V., et al., Photocatalytic degradation of phenol in aqueous titanium dioxide dispersions. Toxicological & Environmental Chemistry, 1988. 16(2): p. 89-109.

45. Sirés, I. and E. Brillas, Remediation of water pollution caused by pharmaceutical residues based on electrochemical separation and degradation technologies: A review. Environment International, 2012. 40: p. 212-229.

46. Kabra, K., R. Chaudhary, and R.L. Sawhney, Treatment of Hazardous Organic and Inorganic Compounds through Aqueous-Phase Photocatalysis: A Review. Industrial & Engineering Chemistry Research, 2004. 43(24): p. 7683-7696.

47. Böer, K.W., Survey of Semiconductor Physics. 1990, Boston, MA: Springer US.

48. Palominos, R.A., et al., Photocatalytic oxidation of the antibiotic tetracycline on TiO_2 and ZnO suspensions. Catalysis Today, 2009. 144(1): p. 100-105.

49. Fujishima, A., T.N. Rao, and D.A. Tryk, Titanium dioxide photocatalysis. Journal of Photochemistry and Photobiology C: Photochemistry Reviews, 2000. 1(1): p. 1-21.

50. Hoffmann, M., et al., Environmental applications of semiconductor photocatalysis. Chemical Reviews, 1995. 95: p. 69-96.

51. Mills, A. and S. Le Hunte, An overview of semiconductor photocatalysis. Journal of Photochemistry and Photobiology A: Chemistry, 1997. 108(1): p. 1-35.

52. Herrmann, J.-M., Heterogeneous photocatalysis: fundamentals and applications to the removal of various types of aqueous pollutants. Catalysis Today, 1999. 53(1): p. 115-129.

53. Fujishima, A., X. Zhang, and D.A. Tryk, TiO_2 photocatalysis and related surface phenomena. Surface Science Reports, 2008. 63(12): p. 515-582.

54. Montoya, J.F., J.A. Velásquez, and P. Salvador, The direct–indirect kinetic model in photocatalysis: A reanalysis of phenol and formic acid degradation rate dependence on photon flow and concentration in TiO_2 aqueous dispersions. Applied Catalysis B: Environmental, 2009. 88(1): p. 50-58.

55. Faramarzpour, M., M. Vossoughi, and M. Borghei, Photocatalytic degradation of furfural by titania nanoparticles in a floating-bed photoreactor. Chemical Engineering Journal, 2009. 146(1): p. 79-85.

56. Lin, H. and K.T. Valsaraj, Development of an optical fiber monolith reactor for photocatalytic wastewater Treatment. Journal of Applied Electrochemistry, 2005. 35(7): p. 699-708.

57. Yang, H., et al., Photocatalytic degradation kinetics and mechanism of environmental pharmaceuticals in aqueous suspension of TiO_2: A case of sulfa drugs. Catalysis Today, 2010. 153(3): p. 200-207.

58. Hapeshi, E., et al., Drugs degrading photocatalytically: Kinetics and mechanisms of ofloxacin and atenolol removal on titania suspensions. Water Research, 2010. 44(6): p. 1737-1746.

59. Mascolo, G., et al., Photocatalytic degradation of methyl red by TiO_2: Comparison of the efficiency of immobilized nanoparticles versus conventional suspended catalyst. Journal of Hazardous Materials, 2007. 142(1): p. 130-137.

60. Valencia, S., et al., A new kinetic model for heterogeneous photocatalysis with titanium dioxide: Case of non-specific adsorption considering back reaction. Applied Catalysis B: Environmental, 2011. 104(3): p. 300-304.

61. Wu, C.Y., et al., Photocatalyst coated magnetic composite particle. 2002, Google Patents.

62. Eydivand, S. and M. Nikazar, Degradation of 1, 2-Dichloroethane in Simulated Wastewater Solution: A Comprehensive Study by Photocatalysis Using TiO_2 and ZnO Nanoparticles. Chemical Engineering Communications, 2015. 202(1): p. 102-111.

63. Stoller, M., et al., Membrane process enhancement of 2-phase and 3-phase olive mill wastewater treatment plants by photocatalysis with magnetic-core titanium dioxide nanoparticles. Journal of Industrial and Engineering Chemistry, 2015. 30: p. 147-152.

64. Altın, İ., M. Sökmen, and Z. Bıyıklıoğlu, Quaternized zinc (II) phthalocyanine-sensitized TiO_2: surfactant-modified sol–gel synthesis, characterization and photocatalytic applications. Desalination and Water Treatment, 2016. 57(34): p. 16196-16207.

65. Wang, J., et al., Preparation and photocatalytic properties of magnetically reusable Fe 3 O 4@ ZnO core/shell nanoparticles. Physica E: Low-dimensional Systems and Nanostructures, 2016. 75: p. 66-71.

66. Chong, M.N., et al., Recent developments in photocatalytic water treatment technology: a review. Water research, 2010. 44(10): p. 2997-3027.

67. Kalaivani, G.J. and S. Suja, TiO_2 (rutile) embedded inulin—A versatile bio-nanocomposite for photocatalytic degradation of methylene blue. Carbohydrate polymers, 2016. 143: p. 51-60.

68. Prihod'ko, R.V. and N.M. Soboleva, Photocatalysis: oxidative processes in water treatment. Journal of Chemistry, 2013. 2013.

69. Dong, H., et al., An overview on limitations of TiO_2-based particles for photocatalytic degradation of organic pollutants and the corresponding countermeasures. water research, 2015. 79: p. 128-146.

70. Zou, X.-X., et al., Light-Driven Preparation, Microstructure, and Visible-Light Photocatalytic Property of Porous Carbon-Doped TiO_2. International Journal of Photoenergy, 2012. 2012.

71. Karuppuchamy, S. and R.D. Kumar, Synthesis and Characterization of Visible Light Active Titanium Dioxide Nanomaterials for Photocatalytic Applications. Synthesis, 2015. 8(7): p. 278-283.

72. Reddy, P.A.K., et al., Recent advances in photocatalytic treatment of pollutants in aqueous media. Environment international, 2016. 91: p. 94-103.

73. Khan, M.M., et al., Electrochemically active biofilm assisted synthesis of Ag@CeO2 nanocomposites for antimicrobial activity, photocatalysis and photoelectrodes. Journal of Colloid and Interface Science, 2014. 431: p. 255-263.

74. Bhaskar, N.S., et al., Removal of Rhodamine 6G from wastewater using solar irradiations in the presence of different additives. Desalination and Water Treatment, 2015: p. 1-11.

75. Yao, H., et al., Magnetic titanium dioxide based nanomaterials: synthesis, characteristics, and photocatalytic application in pollutant degradation. Journal of Materials Chemistry A, 2015. 3(34): p. 17511-17524.

76. Chiang, K., et al., Photocatalytic degradation and mineralization of bisphenol A by TiO2 and platinized TiO_2. Applied Catalysis A: General, 2004. 261(2): p. 225-237.

77. Thamaphat, K., P. Limsuwan, and B. Ngotawornchai, Phase characterization of TiO_2 powder by XRD and TEM. Kasetsart J.(Nat. Sci.), 2008. 42(5): p. 357-361.

78. Zhou, P., et al., Studies on facile synthesis and properties of mesoporous CdS/TiO2 composite for photocatalysis applications. Journal of Alloys and Compounds, 2017. 692: p. 170-177.

79. Carp, O., C.L. Huisman, and A. Reller, Photoinduced reactivity of titanium dioxide. Progress in Solid State Chemistry, 2004. 32(1): p. 33-177.

80. Kato, S.-i. and F. Mashio, Titanium Dioxide-Photocatalyzed Liquid Phase Oxidation of Tetralin. The Journal of the Society of Chemical Industry, Japan, 1964. 67(8): p. 1136-1140.

81. Renz, C., Lichtreaktionen der Oxyde des Titans, Cers und der Erdsäuren. Helvetica Chimica Acta, 1921. 4(1): p. 961-968.

82. Goodeve, C.F. and J.A. Kitchener, Photosensitisation by titanium dioxide. Transactions of the Faraday Society, 1938. 34(0): p. 570-579.

83. Goodeve, C.F. and J.A. Kitchener, The mechanism of photosensitisation by solids. Transactions of the Faraday Society, 1938. 34(0): p. 902-908.

84. McLintock, I.S. and M. Ritchie, Reactions on titanium dioxide; photo-adsorption and oxidation of ethylene and propylene. Transactions of the Faraday Society, 1965. 61: p. 1007-1016.

85. Akkari, M., et al., ZnO/clay nanoarchitectures: Synthesis, characterization and evaluation as photocatalysts. Applied Clay Science, 2016. 131: p. 131-139.

86. Ye, M., et al., Magnetically recoverable core–shell nanocomposites with enhanced photocatalytic activity. Chemistry–A European Journal, 2010. 16(21): p. 6243-6250.

87. Rashid, J., et al., $Fe_3O_4/SiO_2/TiO_2$ nanoparticles for photocatalytic degradation of 2-chlorophenol in simulated wastewater. Environmental Science and Pollution Research, 2015. 22(4): p. 3149-3157.

88. Shokri, M., et al., A comparative study of photocatalytic degradation of the antibiotic cefazolin by suspended and immobilized TiO_2 nanoparticles. Desalination and Water Treatment, 2015: p. 1-8.

89. Cui, B., et al., Magnetically recoverable core–shell nanocomposites γ-Fe_2O_3@ SiO_2@TiO_2–Ag with enhanced photocatalytic activity and antibacterial activity. Separation and Purification Technology, 2013. 103: p. 251-257.

90. Mahlambi, M.M., C.J. Ngila, and B.B. Mamba, Recent developments in environmental photocatalytic degradation of organic pollutants: the case of titanium dioxide nanoparticles—a review. Journal of Nanomaterials, 2015. 2015: p. 5.

91. Zhang, W., B. Yang, and J. Chen, Effects of calcination temperature on preparation of boron-doped TiO_2 by sol-gel method. International Journal of Photoenergy, 2012. 2012.

92. Ahmed, S., et al., Advances in heterogeneous photocatalytic degradation of phenols and dyes in wastewater: a review. Water, Air, & Soil Pollution, 2011. 215(1-4): p. 3-29.

93. Heredia, C.L., Tartrazine degradation by supported TiO_2 on magnetic particles. Matéria (Rio de Janeiro), 2015. 20(3): p. 668-675.

94. Yao, Y., et al., Highly water-dispersible and easily recyclable anatase nanoparticles for photocatalysis. Ceramics International, 2015. 41(10): p. 14740-14747.

95. Yu, J. and B. Wang, Effect of calcination temperature on morphology and photoelectrochemical properties of anodized titanium dioxide nanotube arrays. Applied Catalysis B: Environmental, 2010. 94(3): p. 295-302.

96. Jeevagan, A.J., et al., Photocatalytic Activity of Pd-Au Alloy Nanoparticle Co-Catalyst/TiO_2 for Acetic Acid Decomposition. ECS Transactions, 2015. 64(25): p. 9-16.

97. Momeni, M.M. and Y. Ghayeb, Fabrication and characterization of zinc oxide-decorated titania nanoporous by electrochemical anodizing-chemical bath deposition techniques: visible light active photocatalysts with good stability. Journal of the Iranian Chemical Society, 2016. 13(3): p. 481-488.

98. Shih, Y.-J., et al., Synthesis of magnetically recoverable ferrite (MFe_2O_4, M Co, Ni and Fe)-supported TiO_2 photocatalysts for decolorization of methylene blue. Catalysis Communications, 2015. 72: p. 127-132.

99. Yu, X., S. Liu, and J. Yu, Superparamagnetic γ-Fe2O3@SiO2@TiO2 composite microspheres with superior photocatalytic properties. Applied Catalysis B: Environmental, 2011. 104(1–2): p. 12-20.

100. Hamad, H., et al., Synthesis and characterization of core–shell–shell magnetic ($CoFe_2O_4$–SiO_2–TiO_2) nanocomposites and TiO_2 nanoparticles for the evaluation of photocatalytic activity under UV and visible irradiation. New Journal of Chemistry, 2015. 39(4): p. 3116-3128.

101. Santhi, K., et al., Synthesis of nanocrystalline titanium dioxide for photodegradation treatment of remazol brown dye. Applied Nanoscience, 2015. 5(3): p. 373-378.

102. Hanus, M.J. and A.T. Harris, Nanotechnology innovations for the construction industry. Progress in Materials Science, 2013. 58(7): p. 1056-1102.

103. Hu, J., et al., Doped titanium dioxide films prepared by pulsed laser deposition method. International Journal of Photoenergy, 2012. 2012.

104. Kumar, R., J. Rashid, and M. Barakat, Zero valent Ag deposited TiO_2 for the efficient photocatalysis of methylene blue under UV-C light irradiation. Colloids and Interface Science Communications, 2015. 5: p. 1-4.

105. Verhovšek, D., et al., The synthesis of anatase nanoparticles and the preparation of photocatalytically active coatings based on wet chemical methods for self-cleaning applications. International Journal of Photoenergy, 2012. 2012.

106. Yuan, Q., et al., Preparation of magnetically recoverable Fe_3O_4@SiO_2@ meso-TiO_2 nanocomposites with enhanced photocatalytic ability. Materials Research Bulletin, 2012. 47(9): p. 2396-2402.

107. Amalraj, A. and A. Pius, Photocatalytic degradation of monocrotophos and chlorpyrifos in aqueous solution using TiO_2 under UV radiation. Journal of Water Process Engineering, 2015. 7: p. 94-101.

108. Liu, J., et al., Photocatalytic degradation of commercially sourced naphthenic acids by TiO2-graphene composite nanomaterial. Chemosphere, 2016. 149: p. 328-335.

109. Chaturvedi, S., P.N. Dave, and N. Shah, Applications of nano-catalyst in new era. Journal of Saudi Chemical Society, 2012. 16(3): p. 307-325.

110. Campoccia, D., L. Montanaro, and C.R. Arciola, A review of the biomaterials technologies for infection-resistant surfaces. Biomaterials, 2013. 34(34): p. 8533-8554.

111. Treccani, L., et al., Functionalized ceramics for biomedical, biotechnological and environmental applications. Acta biomaterialia, 2013. 9(7): p. 7115-7150.

112. Yu, J.C., J. Yu, and J. Zhao, Enhanced photocatalytic activity of mesoporous and ordinary TiO2 thin films by sulfuric acid treatment. Applied Catalysis B: Environmental, 2002. 36(1): p. 31-43.

113. Comparelli, R., et al., UV-induced photocatalytic degradation of azo dyes by organic-capped ZnO nanocrystals immobilized onto substrates. Applied Catalysis B: Environmental, 2005. 60(1): p. 1-11.

114. Minero, C., et al., Large solar plant photocatalytic water decontamination: Effect of operational parameters. Solar Energy, 1996. 56(5): p. 421-428.

115. Thakur, R.S., R. Chaudhary, and C. Singh, Fundamentals and applications of the photocatalytic treatment for the removal of industrial organic pollutants and effects of operational parameters: A review. Journal of Renewable and Sustainable Energy, 2010. 2(4): p. 042701.

116. Akpan, U.G. and B.H. Hameed, Parameters affecting the photocatalytic degradation of dyes using TiO_2-based photocatalysts: A review. Journal of Hazardous Materials, 2009. 170(2): p. 520-529.

117. Tanveer, M. and G. Tezcanli Guyer, Solar assisted photo degradation of wastewater by compound parabolic collectors: Review of design and operational parameters. Renewable and Sustainable Energy Reviews, 2013. 24: p. 534-543.

118. Herrmann, J.-M., Photocatalysis fundamentals revisited to avoid several misconceptions. Applied Catalysis B: Environmental, 2010. 99(3-4): p. 461-468.

119. Lin, Y., et al., Photocatalytic degradation of methylparaben by TiO_2: Multivariable experimental design and mechanism. Applied Catalysis B: Environmental, 2009. 88(1): p. 32-41.

120. Vild, A., et al., Orthogonal experimental design of titanium dioxide—Poly(methyl methacrylate) electrospun nanocomposite membranes for photocatalytic applications. Journal of Environmental Chemical Engineering, 2016. 4(3): p. 3151-3158.

121. Cantarella, M., et al., Immobilization of nanomaterials in PMMA composites for photocatalytic removal of dyes, phenols and bacteria from water. Journal of Photochemistry and Photobiology A: Chemistry, 2016. 321: p. 1-11.

122. Thevenet, F., et al., Photocatalytic degradation of acetylene over various titanium dioxide-based photocatalysts. Applied Catalysis B: Environmental, 2005. 61(1): p. 58-68.

123. Sivlim, T., et al., TiO_2 Immobilized Biodegradable Polymer for Photocatalytic Removal of Chlorophenol. Water, Air, & Soil Pollution, 2012. 223(7): p. 3955-3964.

124. Matsuzawa, S., et al., Immobilization of TiO_2 nanoparticles on polymeric substrates by using electrostatic interaction in the aqueous phase. Applied Catalysis B: Environmental, 2008. 83(1): p. 39-45.

125. Ghaly, M.Y., J.Y. Farah, and A.M. Fathy, Enhancement of decolorization rate and COD removal from dyes containing wastewater by the addition of hydrogen peroxide under solar photocatalytic oxidation. Desalination, 2007. 217(1): p. 74-84.

126. Guillard, C., et al., Why inorganic salts decrease the TiO_2 photocatalytic efficiency. International Journal of Photoenergy, 2005. 7(1): p. 1-9.

127. Evgenidou, E., K. Fytianos, and I. Poulios, Semiconductor-sensitized photodegradation of dichlorvos in water using TiO_2 and ZnO as catalysts. Applied Catalysis B: Environmental, 2005. 59(1): p. 81-89.

128. Spasiano, D., et al., Solar photocatalysis: Materials, reactors, some commercial, and pre-industrialized applications. A comprehensive approach. Applied Catalysis B: Environmental, 2015. 170-171: p. 90-123.

129. Hoffman, A.J., E.R. Carraway, and M.R. Hoffmann, Photocatalytic Production of H_2O_2 and Organic Peroxides on Quantum-Sized Semiconductor Colloids. Environmental Science & Technology, 1994. 28(5): p. 776-785.

130. Emeline, A.V., V. Ryabchuk, and N. Serpone, Factors affecting the efficiency of a photocatalyzed process in aqueous metal-oxide dispersions: Prospect of distinguishing between two kinetic models. Journal of Photochemistry and Photobiology A: Chemistry, 2000. 133(1): p. 89-97.

131. Cunningham, V.L., S.P. Binks, and M.J. Olson, Human health risk assessment from the presence of human pharmaceuticals in the aquatic environment. Regulatory Toxicology and Pharmacology, 2009. 53(1): p. 39-45.

132. Kansal, S.K., N. Kaur, and S. Singh, Photocatalytic Degradation of Two Commercial Reactive Dyes in Aqueous Phase Using Nanophotocatalysts. Nanoscale Research Letters, 2009. 4(7): p. 709.

133. Alfano Orlando, M., et al., A Methodology for Modeling Slurry Photocatalytic Reactors for Degradation of an Organic Pollutant in Water.

134. Kormann, C., D.W. Bahnemann, and M.R. Hoffmann, Photolysis of chloroform and other organic molecules in aqueous titanium dioxide suspensions. Environmental Science & Technology, 1991. 25(3): p. 494-500.

135. Ollis, D.F., E. Pelizzetti, and N. Serpone, Photocatalyzed destruction of water contaminants. Environmental Science & Technology, 1991. 25(9): p. 1522-1529.

136. Herrmann, J.M., Heterogeneous photocatalysis: state of the art and present applications In honor of Pr. R.L. Burwell Jr. (1912–2003), Former Head of Ipatieff Laboratories, Northwestern University, Evanston (Ill). Topics in Catalysis, 2005. 34(1): p. 49-65.

137. Sun, R.-D., et al., TiO_2-coated optical fiber bundles used as a photocatalytic filter for decomposition of gaseous organic compounds. Journal of Photochemistry and Photobiology A: Chemistry, 2000. 136(1): p. 111-116.

138. Sakthivel, S., et al., Solar photocatalytic degradation of azo dye: comparison of photocatalytic efficiency of ZnO and TiO_2. Solar Energy Materials and Solar Cells, 2003. 77(1): p. 65-82.

139. Kormann, C., D.W. Bahnemann, and M.R. Hoffmann, Preparation and characterization of quantum-size titanium dioxide. The Journal of Physical Chemistry, 1988. 92(18): p. 5196-5201.

140. Plataforma Solar de Almería - Cientro de Investigaciones Energéticas Medioambientales y Tecnológicas, "Solar Photocatalysis," Unesco - Encyclopedia of life support system - Sample chapters. Available from: www.eolss.net/sample-chapters/c08.

141. Masamichi, F., S. Yoshiharu, and O. Tetsuo, Heterogeneous Photocatalytic Reactions on Semiconductor Materials. III. Effect of pH and Cu2+ Ions on the Photo-Fenton Type Reaction. Bulletin of the Chemical Society of Japan, 1982. 55(3): p. 666-671.

142. Bolts, J.M. and M.S. Wrighton, Correlation of photocurrent-voltage curves with flat-band potential for stable photoelectrodes for the photoelectrolysis of water. The Journal of Physical Chemistry, 1976. 80(24): p. 2641-2645.

143. Herrmann, J.-M., Fundamentals and misconceptions in photocatalysis. Journal of Photochemistry and Photobiology A: Chemistry, 2010. 216(2): p. 85-93.

144. Malato, S., et al., Decontamination and disinfection of water by solar photocatalysis: The pilot plants of the Plataforma Solar de Almeria. Materials Science in Semiconductor Processing, 2016. 42: p. 15-23.

145. Fu, X., et al., Effects of reaction temperature and water vapor content on the heterogeneous photocatalytic oxidation of ethylene. Journal of Photochemistry and Photobiology A: Chemistry, 1996. 97(3): p. 181-186.

146. Jain, R., et al., Removal of the hazardous dye rhodamine B through photocatalytic and adsorption treatments. Journal of Environmental Management, 2007. 85(4): p. 956-964.

147. Ollis, D.F., Kinetics of Liquid Phase Photocatalyzed Reactions: An Illuminating Approach. The Journal of Physical Chemistry B, 2005. 109(6): p. 2439-2444.

148. Fonzo, F.D., et al., Hierarchically organized nanostructured TiO_2 for photocatalysis applications. Nanotechnology, 2009. 20(1): p. 015604.

149. Samhaber, W.M. and M.T. Nguyen, Applicability and costs of nanofiltration in combination with photocatalysis for the treatment of dye house effluents. Beilstein Journal of Nanotechnology, 2014. 5: p. 476-484.

150. Ochiai, T., et al., Development of a hybrid environmental purification unit by using of excimer VUV lamps with TiO_2 coated titanium mesh filter. Chemical Engineering Journal, 2013. 218: p. 327-332.

151. Identification and Roles of the Active Species Generated on Various Photocatalysts, in Photocatalysis and Water Purification.

152. Photocatalytic Treatment of Water: Irradiance Influences, in Photocatalysis and Water Purification.

153. Ballari, M.d.l.M., et al., Mass transfer limitations in photocatalytic reactors employing titanium dioxide suspensions: I. Concentration profiles in the bulk. Chemical Engineering Journal, 2008. 136(1): p. 50-65.

154. Ballari, M.d.l.M., O.M. Alfano, and A.E. Cassano, Mass transfer limitations in slurry photocatalytic reactors: Experimental validation. Chemical Engineering Science, 2010. 65(17): p. 4931-4942.

155. Neppolian, B., et al., Solar light induced and TiO_2 assisted degradation of textile dye reactive blue 4. Chemosphere, 2002. 46(8): p. 1173-1181.

156. Mahmoodi, N.M., et al., Kinetics of heterogeneous photocatalytic degradation of reactive dyes in an immobilized TiO2 photocatalytic reactor. Journal of Colloid and Interface Science, 2006. 295(1): p. 159-164.

157. Konstantinou, I.K. and T.A. Albanis, TiO_2-assisted photocatalytic degradation of azo dyes in aqueous solution: kinetic and mechanistic investigations: A review. Applied Catalysis B: Environmental, 2004. 49(1): p. 1-14.

158. AE Ghaly, R.A., M Alhattab and VV Ramakrishnan, Identification and Roles of the Active Species Generated on Various Photocatalysts, in Photocatalysis and Water Purification.

159. Farah Maria Drumond, C., et al., Textile Dyes: Dyeing Process and Environmental Impact. 2013: INTECH Open Access Publisher.

160. Nickel, C., et al., Dynamic light-scattering measurement comparability of nanomaterial suspensions. Journal of Nanoparticle Research, 2014. 16(2): p. 2260.

161. Zhang, H., et al., Enhanced Adsorption of Molecules on Surfaces of Nanocrystalline Particles. The Journal of Physical Chemistry B, 1999. 103(22): p. 4656-4662.

162. Kočí, K., et al., Effect of TiO_2 particle size on the photocatalytic reduction of CO_2. Applied Catalysis B: Environmental, 2009. 89(3): p. 494-502.

163. Neppolian, B., et al., Solar/UV-induced photocatalytic degradation of three commercial textile dyes. Journal of Hazardous Materials, 2002. 89(2): p. 303-317.

164. Matthews, R.W., Purification of water with near—u.v. illuminated suspensions of titanium dioxide. Water Research, 1990. 24(5): p. 653-660.

165. Ballari, M.d.l.M., et al., Mass transfer limitations in photocatalytic reactors employing titanium dioxide suspensions: II. External and internal particle constrains for the reaction. Chemical Engineering Journal, 2008. 136(2): p. 242-255.

166. Amano, F., E. Ishinaga, and A. Yamakata, Effect of Particle Size on the Photocatalytic Activity of WO_3 Particles for Water Oxidation. The Journal of Physical Chemistry C, 2013. 117(44): p. 22584-22590.

167. Jassby, D., J. Farner Budarz, and M. Wiesner, Impact of Aggregate Size and Structure on the Photocatalytic Properties of TiO_2 and ZnO Nanoparticles. Environmental Science & Technology, 2012. 46(13): p. 6934-6941.

168. Maira, A.J., et al., Size Effects in Gas-Phase Photo-oxidation of Trichloroethylene Using Nanometer-Sized TiO_2 Catalysts. Journal of Catalysis, 2000. 192(1): p. 185-196.

169. Bitenc, M., et al., The impact of ZnO load, stability and morphology on the kinetics of the photocatalytic degradation of caffeine and resazurin. Applied Catalysis B: Environmental, 2013. 136-137: p. 202-209.

170. Erdei, L., N. Arecrachakul, and S. Vigneswaran, A combined photocatalytic slurry reactor–immersed membrane module system for advanced wastewater treatment. Separation and Purification Technology, 2008. 62(2): p. 382-388.

171. Bodzek, M. and M. Rajca, Photocatalysis in the treatment and disinfection of water. Part I. Theoretical backgrounds. ECOLOGICAL CHEMISTRY AND ENGINEERING S, 2012. 19(4): p. 489-512.

172. Herrmann, J.-M., Heterogeneous photocatalysis: state of the art and present applications In honor of Pr. R.L. Burwell Jr. (1912–2003), Former Head of Ipatieff Laboratories, Northwestern University, Evanston (Ill). Topics in Catalysis, 2005. 34(1): p. 49-65.

173. Ochiai, T. and A. Fujishima, Photoelectrochemical properties of TiO_2 photocatalyst and its applications for environmental purification. Journal of Photochemistry and Photobiology C: Photochemistry Reviews, 2012. 13(4): p. 247-262.

174. Malato, S., et al., Solar Photocatalytic Pilot Plants: Commercially Available Reactors. 2013: p. 377-397.

175. Ji, Z., et al., Development and characterization of a titanosilicate ETS-10-coated optical fiber reactor towards the photodegradation of methylene blue. Journal of Photochemistry and Photobiology A: Chemistry, 2011. 217(1): p. 22-28.

176. Wastewater Treatment Using Highly Functional Immobilized TiO_2 Thin-Film Photocatalysts, in Photocatalysis and Water Purification.

177. Rehman, S., et al., Strategies of making TiO_2 and ZnO visible light active. Journal of Hazardous Materials, 2009. 170(2): p. 560-569.

178. Daghrir, R., P. Drogui, and D. Robert, Modified TiO_2 For Environmental Photocatalytic Applications: A Review. Industrial & Engineering Chemistry Research, 2013. 52(10): p. 3581-3599.

179. Di Valentin, C., et al., Characterization of Paramagnetic Species in N-Doped TiO_2 Powders by EPR Spectroscopy and DFT Calculations. The Journal of Physical Chemistry B, 2005. 109(23): p. 11414-11419.

180. Zhang, J., et al., Development of modified N doped TiO_2 photocatalyst with metals, nonmetals and metal oxides. Energy & Environmental Science, 2010. 3(6): p. 715-726.

181. Shen, M., et al., Carbon-doped anatase TiO_2 obtained from TiC for photocatalysis under visible light irradiation. Materials Letters, 2006. 60(5): p. 693-697.

182. Kumar, A. and N. Mathur, Photocatalytic oxidation of aniline using Ag^+-loaded TiO2 suspensions. Applied Catalysis A: General, 2004. 275(1): p. 189-197.

183. Seery, M.K., et al., Silver doped titanium dioxide nanomaterials for enhanced visible light photocatalysis. Journal of Photochemistry and Photobiology A: Chemistry, 2007. 189(2): p. 258-263.

184. Li, F.B. and X.Z. Li, The enhancement of photodegradation efficiency using Pt–TiO2 catalyst. Chemosphere, 2002. 48(10): p. 1103-1111.

185. Li, X.Z. and F.B. Li, Study of Au/Au^{3+}-TiO_2 Photocatalysts toward Visible Photooxidation for Water and Wastewater Treatment. Environmental Science & Technology, 2001. 35(11): p. 2381-2387.

186. Wang, C.-y., et al., A comparative study of nanometer sized Fe(III)-doped TiO_2 photocatalysts: synthesis, characterization and activity. Journal of Materials Chemistry, 2003. 13(9): p. 2322-2329.

187. Colón, G., et al., Cu-doped TiO_2 systems with improved photocatalytic activity. Applied Catalysis B: Environmental, 2006. 67(1): p. 41-51.

188. Borgarello, E., et al., Visible light induced water cleavage in colloidal solutions of chromium-doped titanium dioxide particles. Journal of the American Chemical Society, 1982. 104(11): p. 2996-3002.

189. Ullah, R. and J. Dutta, Photocatalytic degradation of organic dyes with manganese-doped ZnO nanoparticles. Journal of Hazardous Materials, 2008. 156(1): p. 194-200.

190. Arpaç, E., et al., Photocatalytic performance of Sn-doped and undoped TiO2 nanostructured thin films under UV and vis-lights. Journal of Hazardous Materials, 2007. 140(1): p. 69-74.

191. El-Bahy, Z.M., A.A. Ismail, and R.M. Mohamed, Enhancement of titania by doping rare earth for photodegradation of organic dye (Direct Blue). Journal of Hazardous Materials, 2009. 166(1): p. 138-143.

192. Yan, X., et al., Preparation, characterization and photocatalytic activity of Si-doped and rare earth-doped TiO_2 from mesoporous precursors. Applied Catalysis B: Environmental, 2005. 55(4): p. 243-252.

193. Hassan, M.S., et al., TiO_2 nanofibers doped with rare earth elements and their photocatalytic activity. Ceramics International, 2012. 38(7): p. 5925-5930.

194. Shi, H., et al., Enhancement of photocatalytic activity of nano-scale TiO_2 particles co-doped by rare earth elements and heteropolyacids. Journal of Colloid and Interface Science, 2012. 380(1): p. 121-127.

195. Štengl, V., S. Bakardjieva, and N. Murafa, Preparation and photocatalytic activity of rare earth doped TiO2 nanoparticles. Materials Chemistry and Physics, 2009. 114(1): p. 217-226.

196. Titanium Dioxide Nanocomposites, in Nanotechnologies for the Life Sciences.

197. Pichat, P., Photocatalysis and Water Purification: From Fundamentals to Recent Applications. 2013.

198. Hirakawa, T. and P.V. Kamat, Charge Separation and Catalytic Activity of Ag@TiO_2 Core−Shell Composite Clusters under UV−Irradiation. Journal of the American Chemical Society, 2005. 127(11): p. 3928-3934.

199. Liu, Y., et al., TiO_2 Nanoflakes Modified with Gold Nanoparticles as Photocatalysts with High Activity and Durability under near UV Irradiation. The Journal of Physical Chemistry C, 2010. 114(3): p. 1641-1645.

200. Kumar, S.G. and L.G. Devi, Review on Modified TiO_2 Photocatalysis under UV/Visible Light: Selected Results and Related Mechanisms on Interfacial Charge

Carrier Transfer Dynamics. The Journal of Physical Chemistry A, 2011. 115(46): p. 13211-13241.

201. Zhao, D., et al., Enhanced photocatalytic degradation of methylene blue under visible irradiation on graphene@TiO_2 dyade structure. Applied Catalysis B: Environmental, 2012. 111-112: p. 303-308.

202. Scalese, S., et al., Photocatalytic properties of carbon nanotubes/titania nanoparticles composite layers deposited by electrophoresis. Materials Science in Semiconductor Processing, 2016. 42: p. 45-49.

203. Vinodgopal, K. and P.V. Kamat, Enhanced Rates of Photocatalytic Degradation of an Azo Dye Using SnO_2/TiO_2 Coupled Semiconductor Thin Films. Environmental Science & Technology, 1995. 29(3): p. 841-845.

204. Higashimoto, S., M. Sakiyama, and M. Azuma, Photoelectrochemical properties of hybrid WO_3/TiO_2 electrode. Effect of structures of WO_3 on charge separation behavior. Thin Solid Films, 2006. 503(1): p. 201-206.

205. Serpone, N., et al., Exploiting the interparticle electron transfer process in the photocatalysed oxidation of phenol, 2-chlorophenol and pentachlorophenol: chemical evidence for electron and hole transfer between coupled semiconductors. Journal of Photochemistry and Photobiology A: Chemistry, 1995. 85(3): p. 247-255.

206. Fu, X., et al., Enhanced Photocatalytic Performance of Titania-Based Binary Metal Oxides: TiO_2/SiO_2 and TiO_2/ZrO_2. Environmental Science & Technology, 1996. 30(2): p. 647-653.

207. Goossens, A., E.L. Maloney, and J. Schoonman, Gas-Phase Synthesis of Nanostructured Anatase TiO_2. Chemical Vapor Deposition, 1998. 4(3): p. 109-114.

208. Eiden-Assmann, S., J. Widoniak, and G. Maret, Synthesis and Characterization of Hollow and Non-Hollow Monodisperse Colloidal TiO_2 Particles. Journal of Dispersion Science and Technology, 2005. 25(4): p. 535-545.

209. Uchida, H., S. Katoh, and M. Watanabe, Photocatalytic degradation of trichlorobenzene using immobilized TiO_2 films containing poly(tetrafluoroethylene) and platinum metal catalyst. Electrochimica Acta, 1998. 43(14): p. 2111-2116.

210. Asha, R.C., et al., Livestock Wastewater Treatment in Batch and Continuous Photocatalytic Systems: Performance and Economic Analyses. Water, Air, & Soil Pollution, 2015. 226(5): p. 1-13.

211. Ao, Y., et al., Preparation of porous titania thin film and its photocatalytic activity. Applied Surface Science, 2008. 255(5, Part 2): p. 3137-3140.

212. Yu, C., et al., Design and fabrication of microsphere photocatalysts for environmental purification and energy conversion. Chemical Engineering Journal, 2016. 287: p. 117-129.

213. Lim, L.L.P., R.J. Lynch, and S.I. In, Comparison of simple and economical photocatalyst immobilisation procedures. Applied Catalysis A: General, 2009. 365(2): p. 214-221.

214. Wang, R., et al., Photocatalytic degradation of Bisphenol A (BPA) using immobilized TiO_2 and UV illumination in a horizontal circulating bed photocatalytic reactor (HCBPR). Journal of Hazardous Materials, 2009. 169(1): p. 926-932.

215. da Motta, M., et al., UV/TiO_2 photocatalytic reactor for real textile wastewaters treatment. Water Sci Technol, 2014. 70(10): p. 1670-6.

216. Kaneco, S., et al., Optimization of solar photocatalytic degradation conditions of bisphenol A in water using titanium dioxide. Journal of Photochemistry and Photobiology A: Chemistry, 2004. 163(3): p. 419-424.

217. Malato, S., et al., Decontamination and disinfection of water by solar photocatalysis: Recent overview and trends. Catalysis Today, 2009. 147(1): p. 1-59.

218. Pereira, L., et al., UV/TiO_2 Photocatalytic Degradation of Xanthene Dyes. Photochemistry and Photobiology, 2013. 89(1): p. 33-39.

219. Silva, A.R., et al., Ciprofloxacin wastewater treated by UVA photocatalysis: contribution of irradiated TiO_2 and ZnO nanoparticles on the final toxicity as assessed by Vibrio fischeri. RSC Advances, 2016. 6(98): p. 95494-95503.

220. Saquib, M. and M. Muneer, TiO_2-mediated photocatalytic degradation of a triphenylmethane dye (gentian violet), in aqueous suspensions. Dyes and Pigments, 2003. 56(1): p. 37-49.

221. Shan, A.Y., T.I.M. Ghazi, and S.A. Rashid, Immobilisation of titanium dioxide onto supporting materials in heterogeneous photocatalysis: A review. Applied Catalysis A: General, 2010. 389(1): p. 1-8.

222. Ma, D., et al., RGO/$InVO_4$ hollowed-out nanofibers: Electrospinning synthesis and its application in photocatalysis. Applied Surface Science, 2015. 353: p. 118-126.

223. Faure, B., et al., Dispersion and surface functionalization of oxide nanoparticles for transparent photocatalytic and UV-protecting coatings and sunscreens. Science and Technology of Advanced Materials, 2013. 14(2): p. 023001.

224. Sonawane, R.S., S.G. Hegde, and M.K. Dongare, Preparation of titanium(IV) oxide thin film photocatalyst by sol–gel dip coating. Materials Chemistry and Physics, 2003. 77(3): p. 744-750.

225. Nurfaizey, A.H., et al., 12 - Functional nanofibers in clothing for protection against chemical and biological hazards A2 - Wei, Qufu, in Functional Nanofibers and their Applications. 2012, Woodhead Publishing. p. 236-261.

226. Bhardwaj, N. and S.C. Kundu, Electrospinning: A fascinating fiber fabrication technique. Biotechnology Advances, 2010. 28(3): p. 325-347.

227. Cossich, E., et al., Development of electrospun photocatalytic TiO_2-polyamide-12 nanocomposites. Materials Chemistry and Physics, 2015. 164: p. 91-97.

228. Mahadik, M.A., et al., Visible light catalysis of rhodamine B using nanostructured Fe_2O_3, TiO_2 and TiO_2/Fe_2O_3 thin films. Journal of Photochemistry and Photobiology B: Biology, 2014. 133: p. 90-98.

229. Djošić, M.S., et al., Electrophoretic deposition and characterization of boehmite coatings on titanium substrate. Colloids and Surfaces A: Physicochemical and Engineering Aspects, 2006. 274(1): p. 185-191.

230. Srikanth, B., et al., Recent advancements in supporting materials for immobilised photocatalytic applications in waste water treatment. Journal of Environmental Management, 2017. 200: p. 60-78.

231. Ma, J.-Q., et al., Liquid-phase deposition of TiO_2 nanoparticles on core–shell Fe3O4@SiO2 spheres: preparation, characterization, and photocatalytic activity. Journal of Nanoparticle Research, 2015. 17(7): p. 1-11.

232. Salameh, C., et al., Dispersion of colloidal TiO_2 nanoparticles on mesoporous materials targeting photocatalysis applications. Catalysis Today, 2015. 257: p. 35-40.

233. Hu, X., J. Yang, and J. Zhang, Magnetic loading of $TiO_2/SiO_2/Fe_3O_4$ nanoparticles on electrode surface for photoelectrocatalytic degradation of diclofenac. Journal of hazardous materials, 2011. 196: p. 220-227.

234. Yuan, R., et al., Surface characteristics and photocatalytic activity of TiO_2 loaded on activated carbon fibers. Colloids and Surfaces A: Physicochemical and Engineering Aspects, 2005. 254(1): p. 131-136.

235. Torimoto, T., et al., Effect of activated carbon content in TiO_2-loaded activated carbon on photodegradation behaviors of dichloromethane. Journal of Photochemistry and Photobiology A: Chemistry, 1997. 103(1): p. 153-157.

236. Demirörs, A.F., A. van Blaaderen, and A. Imhof, A General Method to Coat Colloidal Particles with Titania. Langmuir, 2010. 26(12): p. 9297-9303.

237. Anderson, C. and A.J. Bard, Improved photocatalytic activity and characterization of mixed TiO2/SiO2 and TiO_2/Al2O3 materials. The Journal of Physical Chemistry B, 1997. 101(14): p. 2611-2616.

238. Teixeira, S., et al., Reusable Photocatalytic Optical Fibers for Underground, Deep-Sea, and Turbid Water Remediation. Global Challenges, 2018. 2(3): p. 1700124.

239. Matthews, R.W., Solar-electric water purification using photocatalytic oxidation with TiO2 as a stationary phase. Solar energy, 1987. 38(6): p. 405-413.

240. Gao, Y., et al., Preparation and photocatalytic properties of titanium (IV) oxide films. Materials research bulletin, 1992. 27(9): p. 1023-1030.

241. Sabate, J., et al., A kinetic study of the photocatalytic degradation of 3-chlorosalicylic acid over TiO_2 membranes supported on glass. Journal of Catalysis, 1991. 127(1): p. 167-177.

242. Fabiyi, M. and R. Skelton, Photocatalytic mineralisation of methylene blue using buoyant TiO_2 -coated polystyrene beads. Journal of Photochemistry and Photobiology A: Chemistry, 2000. 132(1): p. 121-128.

243. Bellobono, I.R., et al., Degradation of some chloro-aliphatic water contaminants by photocatalytic membranes immobilizing titanium dioxide. Journal of Photochemistry and Photobiology A: Chemistry, 1992. 67(1): p. 109-115.

244. Tennakone, K., C.T.K. Tilakaratne, and I.R.M. Kottegoda, Photocatalytic degradation of organic contaminants in water with TiO_2 supported on polythene films. Journal of Photochemistry and Photobiology A: Chemistry, 1995. 87(2): p. 177-179.

245. Damodar, R.A., S.-J. You, and H.-H. Chou, Study the self cleaning, antibacterial and photocatalytic properties of TiO_2 entrapped PVDF membranes. Journal of hazardous materials, 2009. 172(2): p. 1321-1328.

246. Fostier, A.H., et al., Arsenic removal from water employing heterogeneous photocatalysis with TiO_2 immobilized in PET bottles. Chemosphere, 2008. 72(2): p. 319-324.

247. Hosseini, M. and A.S.H. Makhlouf, Industrial Applications for Intelligent Polymers and Coatings. 2016.

248. Li, G., et al., Laccase-immobilized bacterial cellulose/TiO_2 functionalized composite membranes: Evaluation for photo- and bio-catalytic dye degradation. Journal of Membrane Science, 2017. 525: p. 89-98.

249. Xiao, G., H. Su, and T. Tan, Synthesis of core–shell bioaffinity chitosan–TiO_2 composite and its environmental applications. Journal of Hazardous Materials, 2015. 283: p. 888-896.

250. Vatanpour, V., A. Karami, and M. Sheydaei, Central composite design optimization of Rhodamine B degradation using TiO_2 nanoparticles/UV/PVDF process in continuous submerged membrane photoreactor. Chemical Engineering and Processing: Process Intensification, 2017. 116: p. 68-75.

251. Du, Z., et al., Enhanced photocatalytic activity of Bi_2WO_6/TiO_2 composite coated polyester fabric under visible light irradiation. Applied Surface Science, 2018. 435: p. 626-634.

252. Application of titanium dioxide photocatalysis to construction materials. 2013, [Place of publication not identified]: Springer.

253. Wang, B., et al., Photocatalysis: A novel approach to efficient demulsification. Catalysis Communications, 2016. 75: p. 83-86.

254. Halmann, M.M., Photodegradation of water pollutants. 1996, Boca Raton: CRC.

255. Peng, W.-c., Y. Chen, and X.-y. Li, MoS2/reduced graphene oxide hybrid with CdS nanoparticles as a visible light-driven photocatalyst for the reduction of 4-nitrophenol. Journal of Hazardous Materials, 2016. 309: p. 173-179.

256. Singh, S., H. Mahalingam, and P.K. Singh, Polymer-supported titanium dioxide photocatalysts for environmental remediation: A review. Applied Catalysis A: General, 2013. 462-463: p. 178-195.

257. Duca, M.D., C.L. Plosceanu, and T. Pop, Surface modifications of polyvinylidene fluoride (PVDF) under rf Ar plasma. Polymer Degradation and Stability, 1998. 61(1): p. 65-72.

258. Martins, P., A.C. Lopes, and S. Lanceros-Mendez, Electroactive phases of poly(vinylidene fluoride): Determination, processing and applications. Progress in Polymer Science, 2014. 39(4): p. 683-706.

259. Salimi, A. and A.A. Yousefi, Analysis Method: FTIR studies of β-phase crystal formation in stretched PVDF films. Polymer Testing, 2003. 22(6): p. 699-704.

260. Gregorio, R., Determination of the α, β, and γ crystalline phases of poly(vinylidene fluoride) films prepared at different conditions. Journal of Applied Polymer Science, 2006. 100(4): p. 3272-3279.

261. Ferreira, A., et al., Poly[(vinylidene fluoride)-co-trifluoroethylene] Membranes Obtained by Isothermal Crystallization from Solution. Macromolecular Materials and Engineering, 2010. 295(6): p. 523-528.

262. Ramakrishna, S., An introduction to electrospinning and nanofibers. 2005.

263. Zheng, J., et al., Polymorphism Control of Poly(vinylidene fluoride) through Electrospinning. Macromolecular Rapid Communications, 2007. 28(22): p. 2159-2162.

264. Liu, F., et al., Progress in the production and modification of PVDF membranes. Journal of Membrane Science, 2011. 375(1): p. 1-27.

265. Teixeira, S., et al., Reusability of photocatalytic TiO2 and ZnO nanoparticles immobilized in poly(vinylidene difluoride)-co-trifluoroethylene. Applied Surface Science, 2016. 384: p. 497-504.

266. Yousef, A., et al., Encapsulation of CdO/ZnO NPs in PU electrospun nanofibers as novel strategy for effective immobilization of the photocatalysts. Colloids and Surfaces A: Physicochemical and Engineering Aspects, 2012. 401: p. 8-16.

267. Kenawy, E.-R., et al., Processing of polymer nanofibers through electrospinning as drug delivery systems. Materials Chemistry and Physics, 2009. 113(1): p. 296-302.

268. An, N., et al., Preparation and electroactive properties of a PVDF/nano-TiO_2 composite film. Applied Surface Science, 2011. 257(9): p. 3831-3835.

269. Zeng, J., et al., TiO_2 Immobilized in Cellulose Matrix for Photocatalytic Degradation of Phenol under Weak UV Light Irradiation. The Journal of Physical Chemistry C, 2010. 114(17): p. 7806-7811.

270. Costa, A.L., et al., TiO_2 based photocatalytic coatings: From nanostructure to functional properties. Chemical Engineering Journal, 2013. 225: p. 880-886.

271. Erjavec, B., et al., Glass fiber-supported TiO_2 photocatalyst: Efficient mineralization and removal of toxicity/estrogenicity of bisphenol A and its analogs. Applied Catalysis B: Environmental, 2016. 183: p. 149-158.

272. Tang, H., et al., Electrical and optical properties of TiO_2 anatase thin films. Journal of Applied Physics, 1994. 75(4): p. 2042-2047.

273. Yu, J.-G., et al., The Effect of Calcination Temperature on the Surface Microstructure and Photocatalytic Activity of TiO_2 Thin Films Prepared by Liquid Phase Deposition. The Journal of Physical Chemistry B, 2003. 107(50): p. 13871-13879.

274. Collins, R.J., et al., Low temperature deposition of patterned TiO_2 thin films using photopatterned self-assembled monolayers. Applied Physics Letters, 1996. 69(6): p. 860-862.

275. Martins, P.M., et al., Improving Photocatalytic Performance and Recyclability by Development of Er-Doped and Er/Pr-Codoped TiO_2/Poly(vinylidene difluoride)–Trifluoroethylene Composite Membranes. The Journal of Physical Chemistry C, 2014. 118(48): p. 27944-27953.

276. Martins, P.M., et al., Comparative efficiency of TiO_2 nanoparticles in suspension vs. immobilization into P(VDF-TrFE) porous membranes. RSC Advances, 2016. 6(15): p. 12708-12716.

277. Wang, Y., et al., A review of polymer electrolyte membrane fuel cells: Technology, applications, and needs on fundamental research. Applied Energy, 2011. 88(4): p. 981-1007.

278. Jeon, G., S.Y. Yang, and J.K. Kim, Functional nanoporous membranes for drug delivery. Journal of Materials Chemistry, 2012. 22(30): p. 14814-14834.

279. Mokhtari, B. and K. Pourabdollah, Inclusion desalination of alkali metal cations by emulsion liquid membranes and nano-baskets of p-tert-calix[4]arene bearing di-[N-(X)sulfonyl carboxamide] and di-(1-propoxy) in para-cone conformation. Desalination, 2012. 292: p. 1-8.

280. Gören, A., et al., Effect of the degree of porosity on the performance of poly(vinylidene fluoride-trifluoroethylene)/poly(ethylene oxide) blend membranes for lithium-ion battery separators. Solid State Ionics, 2015. 280: p. 1-9.

281. Zeolite characterization and catalysis: a tutorial. 2014, [Place of publication not identified]: Springer.

282. Gu, H., et al., Investigation on contact angle measurement methods and wettability transition of porous surfaces. Surface and Coatings Technology, 2016. 292: p. 72-77.

283. Du, Q., et al., Tailoring the surface wettability of polyimide by UV laser direct texturing in different gas atmospheres. Materials & Design, 2016. 104: p. 134-140.

284. Balaur, E., et al., Tailoring the wettability of TiO_2 nanotube layers. Electrochemistry Communications, 2005. 7(10): p. 1066-1070.

2. TiO_2 nanoparticles in suspension vs. TiO_2 immobilization in poly(vinylidenefluoride-co-trifluoroethylene) membranes and scale-up.

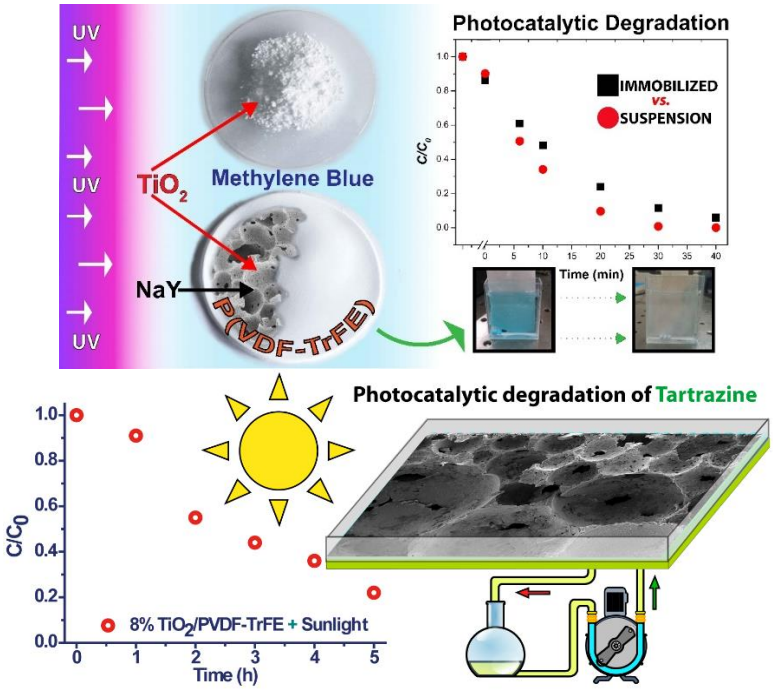

This work reports on the development of photocatalytic membranes based on TiO_2 nanoparticles immobilized into a poly(vinylidenefluoride-trifluoroethylene) (P(VDF-TrFE)) membrane and the comparative study of their photocatalytic performance with dispersed TiO_2 nanoparticles. Additionally, the membrane was tested in a solar photoreactor for tartrazine degradation.

This chapter is based on the following publications: Martins, P.M., et al., *Comparative efficiency of* TiO_2 *nanoparticles in suspension vs. immobilization into P(VDF-TrFE) porous membranes*. RSC Advances, 2016. 6(15): p. 12708-12716. Aoudjit, L., et al., *Photocatalytic reusable membranes for the effective degradation of tartrazine with a solar photoreactor*. Journal of Hazardous Materials, 2018. 344: p. 408-416.

2.1. Introduction

Photocatalysis has become an attractive process to remove contaminants from aquatic environments [1]. Photocatalysis occurs when a catalyst is irradiated with UV light and produces electron-hole pairs which react with H_2O, OH^-, and O_2 to generate highly oxidizing species, usually the hydroxyl radical (•OH), superoxide radical anions ($O_2•^-$) and hydrogen peroxide (H_2O_2). These species will subsequently begin a cascade of redox reactions leading to decomposition of organics into CO_2, H_2O, among other harmless compounds [2, 3]. Several photocatalysts such as Si, BiOBr, $BiFeO_3$, CuS, WSe_2, WO_3, Fe_2O_3, ZnO, and TiO_2 have been tested with this objective [4, 5]. Among these materials, titanium dioxide (TiO_2) is the most widely used one for degradation of organic pollutants, mainly due to its physical and chemical stability, non-toxicity, superhydrophilicity, abundance, low cost, and remarkable reactivity under UV light irradiation ($\lambda > 390$ nm)[6-8]. The application of TiO_2 as a photocatalyst usually occurs in two forms: in suspension and immobilized on solid materials.

The increasing use of TiO_2 powder in suspension and its efficiency is mainly related to the nanoparticles large surface area, porosity and proximity between nanoparticle surface and pollutant species, promoting a large mass transfer process [9].

Despite the advantages of the photocatalytic process with TiO_2 nanoparticles in suspension, some important problems arise, namely the recuperation of these nanoparticles from the suspension before treated water is reused. This separation is a time-consuming step and demands an expensive downstream filtering post-treatment, preventing widespread use of this system [10, 11]. In this way, several approaches have been tested to overcome these hindrances, namely the immobilization of TiO_2 nanoparticles into solid substrates [2]. The problems to be overcome with this possible solution are the loss of surface area, partial loss of TiO_2 and mass transfer limitations linked to this configuration [12]. Several substrates have been tested as TiO_2 support for degradation of water pollutants. Materials such as sand, paper, quartz, wool, pyrex, cement beads and steel mesh have been thus coated or functionalized with TiO_2 [13]. Alternatively, more complex structures such as glass fiber/beads, ceramic membranes, pumice stones, zeolites, and alumina clays were also tested [13, 14]. Recently, some attention has been paid to polymers such as nylon-6, polyester, polyamide-6, cellulose, high-density polyethylene, chitosan and polyvinylidene fluoride [14-16]. Conversely,

several techniques such as dip coating [17], chemical vapor deposition [18], electrospinning [19] and electrophoretic deposition [20] have been employed for the immobilization of TiO_2 nanoparticles. Many of these photocatalytic substrates lack to satisfy some criteria required for photocatalytic applications such as strong adhesion of nanoparticles to the substrate, catalyst reactivity after attachment process, high surface area and strong adsorption affinity to the pollutant [14]. In this connection, in spite of the many materials and techniques evaluated, with some encouraging results, the immobilization of TiO_2 nanoparticles remains a challenge as the hurdles above are not completely overcome and the main application requirements are not satisfied. Additionally, such drawbacks become even more important regarding large-scale applications (*e.g.,* photocatalytic reactors) [21]. With this respect, we propose poly(vinylidene fluoride-trifluoroethylene) (P(VDF-TrFE)) as a substrate to immobilize TiO_2 nanoparticles. This fluorinated copolymer allows the production of membranes with controlled porosity and pore size [22, 23]. Moreover, physicochemical properties of fluorinated polymers are suitable for the intended application as they show excellent UV radiation, chemical, mechanical and thermal resistance, related to the stable C−F bonds of the polymer chain [24-26]. Furthermore, TiO_2/P(VDF-TrFE) nanocomposite membranes have been successfully produced with demonstrated photocatalytic activity in the degradation of methylene blue (MB). One of the problems associated with P(VDF-TrFE) is its low hydrophilicity [27]. To tailor nanocomposite membranes wettability, zeolites (NaY) can be incorporated into the P(VDF-TrFE) matrix. Zeolites are classified as highly hydrophilic and porous structures, which makes them good adsorbents [28, 29]. These properties are essential to allow a proper interaction between the pollutant and the polymeric substrate where TiO_2 nanoparticles are immobilized.

This work is centered in two main goals, the first one is to compare and quantify the efficiency of photocatalytic TiO_2 nanoparticles in suspension and immobilized into a P(VDF-TrFE) porous membrane. Additionally, it is also shown how the inclusion of NaY to tailor the wettability of the membrane influences its photocatalytic performance. The other goal of this work, is to demonstrate the suitability and reusability of photocatalytic TiO_2 nanoparticles immobilized on a P(VDF–TrFE) porous membrane in the degradation of tartrazine in a solar photoreactor. Tartrazine is an azoic dye widely used in the textile, cosmetics, pharmaceutical and food industry [30-31]. Several studies have reported about

tartrazine photocatalytic degradation [32-33]. However, few of them focus on the solar radiation and using immobilized catalysts.

2.2. Experimental

2.2.1. Membranes production

Poly(vinylidenefluoride-co-trifluoroethylene), P(VDF-TrFE) (Solvay 70:30) composite membranes with 3, 5 and 8 wt. % of both TiO_2 (P25, supplied by EVONIK industries) nanoparticles and zeolites (NaY, Zeolyst International) were prepared by solvent casting (Table 2.1).

Table 2.1. Nanocomposite membranes identification and TiO_2 and NaY contents.

P(VDF-TrFE) membranes	m (NaY) (g)	m (TiO_2) (g)
P(VDF-TrFE)	-	-
3 %TiO_2	-	0.030
5 %TiO_2	-	0.052
8 %TiO_2	-	0.087
3 %NaY:8 %TiO_2	0.030	0.087
5 %NaY:8 %TiO_2	0.052	0.087
8 %NaY:8 %TiO_2	0.087	0.087

The filler contents were selected in a range of concentration that avoids nanoparticles agglomeration, detachment and preserves a homogenous microstructure with the mechanical properties required for this application.

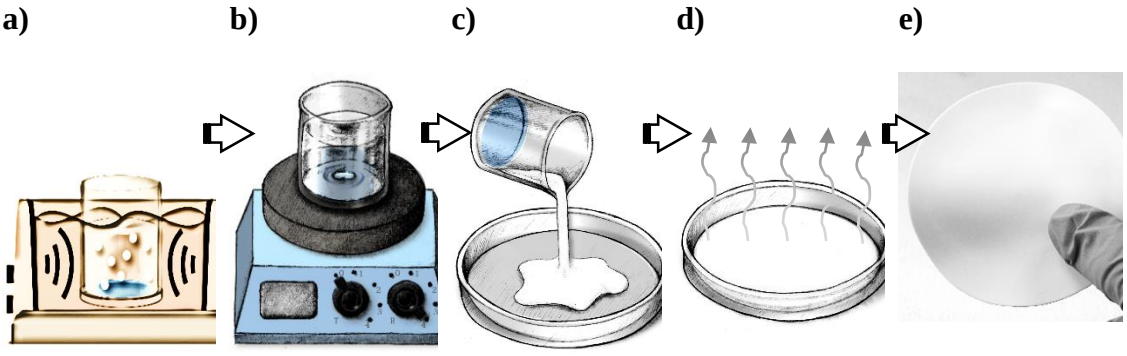

Figure 2.1. Schematic representation of the production of the 8 wt. % TiO_2/PVDF-TrFE nanocomposite membranes by solvent casting; a) ultrasonic bath of DMF and TiO_2 nanoparticles; b) magnetic stirring of DMF, TiO_2 nanoparticles, and the added PVDF-TrFE; c) pouring the

solution on a glass support; d) solvent evaporation at room temperature; e) membrane after complete evaporation of the solvent.

The nanocomposite membranes were produced (Figure 2.1) adding zeolites and nanoparticles in the desired amount to 9.5 mL of N, N-dimethylformamide (DMF, from Merck). The solution was placed in an ultrasonication bath for 4 hours to achieve good dispersion. Afterward, 1g of the copolymer was added to the solution, to obtain a polymer concentration of 10 % wt., and kept under magnetic stirring until complete polymer dissolution. Later, the solution was placed in a glass Petri dish, and the DMF solvent evaporated at room temperature, to produce a highly porous structure [23].

2.2.2. Nanoparticle and membrane characterization

The crystal structure, purity, and degree of crystallinity of the commercial nanoparticles was evaluated by X-ray diffraction, XRD, measurements in a Rygaku/Max System RU 300.

The optical properties of the nanoparticle powder were measured by UV–vis absorption spectroscopy with a Jasco V-670 spectrophotometer coupled with an integrating sphere.

The average hydrodynamic diameter and zeta potentials of the nanoparticles were measured by Dynamic Light Scattering (DLS) in a Zetasizer NANO ZS-ZEN3600, Malvern (Malvern Instruments Limited, UK), equipped with a He–Ne laser (wavelength 633 nm) and a detection angle of 173° (backscatter detection). Hydrodynamic diameter was assessed by 6 measurements performed at 25 °C dispersing TiO_2 nanoparticles in ultra-pure water (0.1 mg L^{-1}) to avoid multi scattering events. The zeta (ζ) potential of TiO_2 nanoparticles was evaluated at different pHs (2, 4, 7, 9 and 12). Solutions of HCl (1 M) and NaOH (1M) were added to adjust the pH. The average value and standard deviation for each sample were obtained from 10 measurements, at 25 °C. The results were obtained using the approximation of Smoluchowski theory. Zetasizer 6.20 software was used to estimate particle mean diameter from the intensity distributions (Zeta-average), the polydispersity index (PDI) and ζ-potential values.

The porosity of the nanocomposite membranes was estimated with a pycnometer, using equation (2.1). In a first step, the weight of the pycnometer, filled with ethanol, was measured and labeled *W1*; the sample, whose weight was *Ws*, was then immersed in ethanol. After the sample was saturated with ethanol, additional ethanol was added to

complete the volume of the pycnometer, weighted and labeled as *W2*. Then, the sample filled with ethanol was taken out of the pycnometer, and the residual weight of the ethanol was labeled as *W3*.

$$\boldsymbol{\varepsilon} = \frac{W2 - W3 - Ws}{W1 - W3} \qquad (2.1)$$

This procedure was repeated three times for each sample, and the obtained values correspond to the average.

The morphology of the TiO_2/P(VDF-TrFE) samples were evaluated by scanning electron microscopy (SEM) with a Quanta 650 from FEI Scanning Electron Microscope at a measured voltage of 10 kV. Before examination, the samples were coated with a thin gold layer by using a Fisons Instruments SC502 sputter coater.

The polymer phase content was obtained from the infrared spectra obtained by Fourier transformed infrared spectroscopy (FTIR) in attenuated total reflectance mode (ATR) in an FTIR Alpha - Bruker apparatus over a range of 650 – 4000 cm^{-1} using 64 scans and a resolution of 4 cm^{-1}.

The wettability of the samples was assessed by measuring the contact angle of distilled water at 22 °C, using an OCA15 Dataphysics contact angle analyzer. Five measurements were carried out for each sample at different places. Surface free energy (γp) values were estimated using an adaptation of Young-Dupre, Eq. 2.2:

$$\gamma p = \frac{\gamma w}{4}(1 + \cos\theta_0)^2 \qquad (2.2)$$

where θo is the contact angle at equilibrium and γw is the water surface energy, (73 mJ/m^2) [30, 31].

2.2.3. Photocatalytic activity

Photocatalytic oxidation of an MB solution by TiO_2 nanoparticles in suspension and immobilized into P(VDF-TrFE) membranes, under UV irradiation, was used to evaluate the photocatalytic efficiency of both systems.

For the sake of comparison of the obtained efficiency, the same MB aqueous solution of 10^{-5} M at pH = 6.8 was used for assays with suspended and immobilized TiO_2

nanoparticles. Additionally, before the degradation tests, suspended TiO_2 nanoparticles and membranes with immobilized nanoparticles and zeolites were first immersed in the MB aqueous solution for 30 min in the dark, to allow the complete dye adsorption-desorption. The suspension tests were performed in a 100 mL beaker with 3.3 mm thickness and 5 cm in diameter. Tests with 5, 10, 20, 40 and 60 mg of TiO_2 nanoparticles were performed. The degradation experiments were carried out placing nanoparticles in the MB solution under magnetic stirring and UV-A radiation. The beaker was positioned at 10 cm from 6 lamps (Phillips 8W), with an excitation peak at 365 nm. The UV intensity ranged from 3.6 to 3.8 mW/cm^2, as measured with a UV34 Lux meter. To analyze the MB degradation, aliquots were withdrawn at different times during the assay. All the samples were centrifuged using an EBA 21 from Hettich, for 30 min at 36220 rcf/s, and then analyzed with a UV - Vis Shimadzu 2501 PC. Degradation of MB was assessed by monitoring the decrease of the 663 nm absorption peak [32].

Concerning immobilized TiO_2 nanoparticles, 12 cm^2 samples of the photocatalytic TiO_2/P(VDF-TrFE) and NaY/TiO_2/P(VDF-TrFE) nanocomposites were immersed in a quartz cuvette (1 cm path optical) with 13 mL of MB solution (10^{-5} M). The quartz cell was then irradiated with a high-power LED source (Thorlabs, 700 mA) with an excitation peak at 365 nm (UV-A). The incident radiation over the sample was measured with a Delta Ohm irradiance meter, and the average values were around 4 $mW \cdot cm^{-2}$ [33]. The absorbance of the MB was monitored at intervals of 2 min using a spectrophotometer (ScanSpecUV-Vis, ScanSci) in the range of 300–900 nm. The rate of photodegradation of MB was analyzed by monitoring the intensity variation of the main absorption peak at 663 nm.

The MB degradation in aqueous solution fits a pseudo-first-order reaction, Langmuir–Hinshelwood model, which can be expressed by Eq. 2.3[34]:

$$ln\left(\frac{C}{C_0}\right) = -kt \qquad (2.3)$$

where C_0 and C represents the initial concentration of the dye at time *t*, respectively and k is the first-order rate constant of the reaction.

2.2.4. Photocatalytic activity in sunlight photoreactor

The photocatalytic degradation of tartrazine was carried out in a solar photoreactor located in northern Algeria (latitude 36°.39´; longitude 2°.42´ at sea level), from August to September, using natural solar irradiation. The intensity of solar UV radiation was measured with a Pyranometer CMP 11 (Kipp & Zonen) with a spectral range between 285 and 2800 nm. All the assays performed in this study presented sunlight similar intensities profiles.

The reactor was developed at the Solar Equipment Development Unit (UDES) in Algeria. The adequate volume of the photoreactor is 1 L (38 cm length × 12 cm wide × 8.5 cm high). The photoreactor tank was fabricated from Pyrex glass, where the produced TiO_2/PVDF-TrFE nanocomposite membrane was placed at the bottom (Figure 2.2). The flow rate used for tartrazine solution recirculation was 28 mL s^{-1}; allowing to cover the entire surface of the nanocomposite membrane with the tartrazine solution. The photoreactor was wholly covered with glass to avoid evaporation during the photocatalytic experiments.

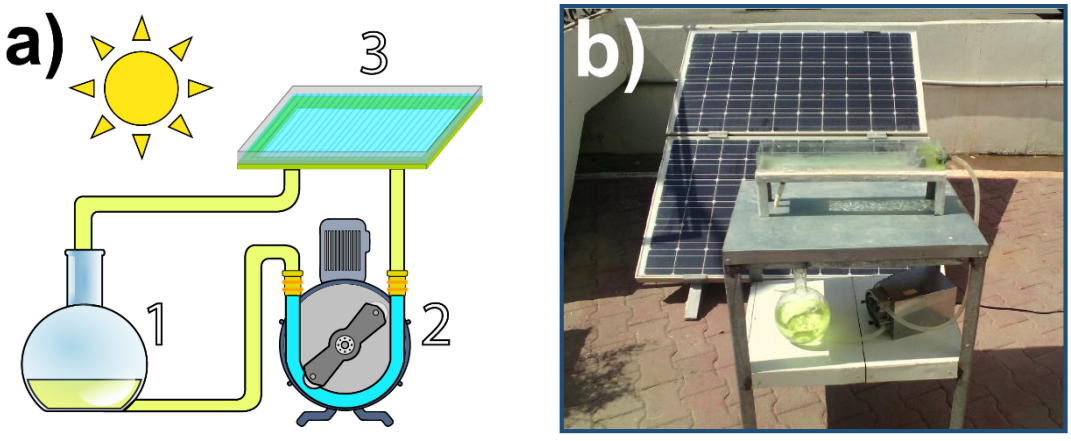

Figure 2.2. Schematic representation of the solar photoreactor: 1- tartrazine solution flask; 2- peristaltic pump; 3 – photoreactor tank with the 8 wt. % TiO_2/PVDF-TrFE photocatalytic membrane (a); picture of the photoreactor during the photocatalytic degradation of tartrazine under sunlight irradiation (b).

For the photocatalytic assays, one liter of tartrazine solution was added to the photoreactor tank containing the 8 wt. % TiO_2/P(VDF-TrFE) porous membrane and illuminated with solar light for five hours. The pH of the solution was not adjusted (initial pH ≈ 6.2 and

final pH ≈ 4.3), and the temperature was not controlled, varying from 25 to 36°C. These conditions were selected to evaluate the potential applicability of the system. Tartrazine solutions of 10, 20, and 30 mg L^{-1} were prepared to study the effect of initial concentrations on the photocatalytic degradation. A 5 mL sample was withdrawn at one-hour intervals. The influence of flow rate was investigated using a flow rate of 28 mL s^{-1} and 9.8 mL s^{-1} under the same experimental conditions (C_0=10 mg L^{-1} under UV for five hours).

To assess the reusability of the produced 8 wt. % TiO_2/P(VDF-TrFE) nanocomposite, after the first use the membrane and the photoreactor were washed with distilled water under continuous flow and dried at ambient conditions. Afterward, a new tartrazine solution (same concentration - 10 mg L^{-1}) was added, and the same procedure was adopted.

Different UV intensities were used in the photocatalytic process; it was used a UV lamp from Phillips (PL-L 24W/10/4P) - with a maximum wavelength peak at 365 nm and an intensity of ≈ 6 mW/cm^2. The lamp was used to irradiate the photoreactor (15 cm distance) with the nanocomposite and the tartrazine solution (10 mg L^{-1}), for five hours. The results were compared with the sunlight photocatalytic degradation.

All the withdrawn samples were analyzed with a UV–visible spectrophotometer (Shimadzu-1800), and the peak at 427 nm was used to monitor tartrazine absorbance over irradiation time. The percentage of degradation was estimated using the following Eq. 2.4 [45].

$$Degradation\ (\%) = \frac{C_0 - C_t}{C_0} \times 100 \qquad \text{(Eq.2.4)}$$

where C_o is the initial dye concentration and C_t is the dye concentration after a specific reaction time t (min).

2.3. Results and discussion

2.3.1. Nanoparticle characterization

The P25-TiO_2 commercial nanoparticles were analyzed by SEM. The images (not shown) allowed to estimate a particle size of ≈ 30 nm from a statistic of 50 nanoparticles per

micrograph. The crystal structure and purity of the nanoparticles were studied by X-ray diffraction (not shown). The samples show diffraction peaks at 25.3, 37.8, 48.0, 53.9, 55.1, and 62.7°, which are ascribed to the anatase crystalline structure. Further, the diffractogram also shows 2θ values of rutile phase, for instance of 27.4, 36.1 and 41.2° [35]. SEM and XRD results agree with the data sheet provided by the manufacturer.

Regarding TiO_2 nanoparticles hydrodynamic size, results obtained by DLS show a Z-average diameter of 430 ± 28 nm (Figure 2.3) and average PDI of 0.45 ± 0.040. In related work, hydrodynamic sizes around 600 nm were obtained through DLS measurements [9]. The difference between DLS and SEM nanoparticles sizes can be explained by the agglomeration of the nanoparticles in aqueous media and due to the presence of clusters with different sizes. Agglomerated nanoparticles show a smaller diffusion rate than isolated particles, and thus the diameter of the nanoparticles obtained by DLS is larger than the one assessed by other techniques [36].

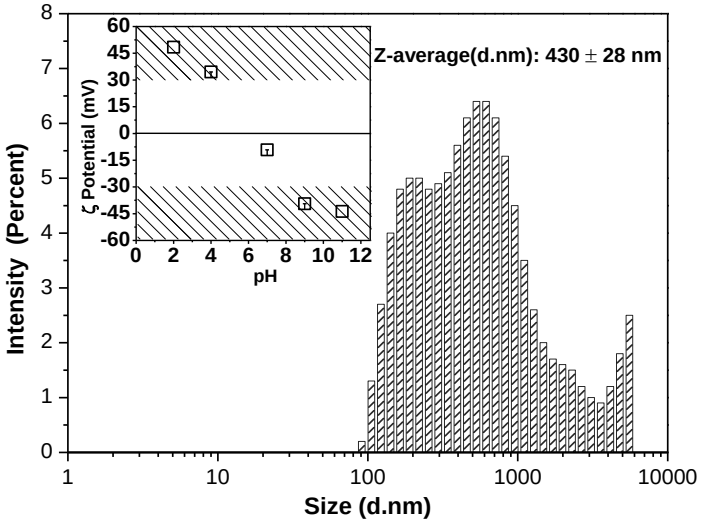

Figure 2.3. Dynamic light scattering (DLS) size distribution of P25-TiO_2 nanoparticles at room temperature; inset room temperature ζ - potential of TiO_2 nanoparticles at pH of 2; 4; 7; 9 and 11.

Concerning ζ –potential measurements (Figure 2.3 inset), the results show that TiO_2 nanoparticles are more stable at pH above 8 or below 4. In these pH ranges, ζ –potential values are higher than |30| mV, which means that nanoparticles show higher peripheral charge values, contributing for nanoparticle repulsion and thus higher stability, preventing aggregation and precipitation. Furthermore, these results are in agreement with previous works [37, 38], which indicates that at pH= 6.8 the TiO_2 net charge is 0, at

pH < 6.8 TiO_2 is positively charged and at pH > 6.8 TiO_2 is negatively charged. Zeta potential measurements are relevant for the intended application as the adsorption of molecules into nanoparticles surface is pH dependent [39]. If TiO_2 nanoparticles and the pollutant/dye exhibit opposite charges, the favorable electrostatic interaction will promote adsorption and enhanced photocatalytic activity.

2.3.2. Nanocomposites characterization

TiO_2 nanoparticles were successfully immobilized in the P(VDF-TrFE) porous membranes produced by solvent evaporation at room temperature. SEM cross-section images (Figure 2.4) show the polymer microstructure of the produced membranes, all presenting spherical pores independently of the TiO_2 content. Further, TiO_2 nanoparticles are well dispersed within the porous structure of the membrane, just with few aggregates in the inner pore walls.

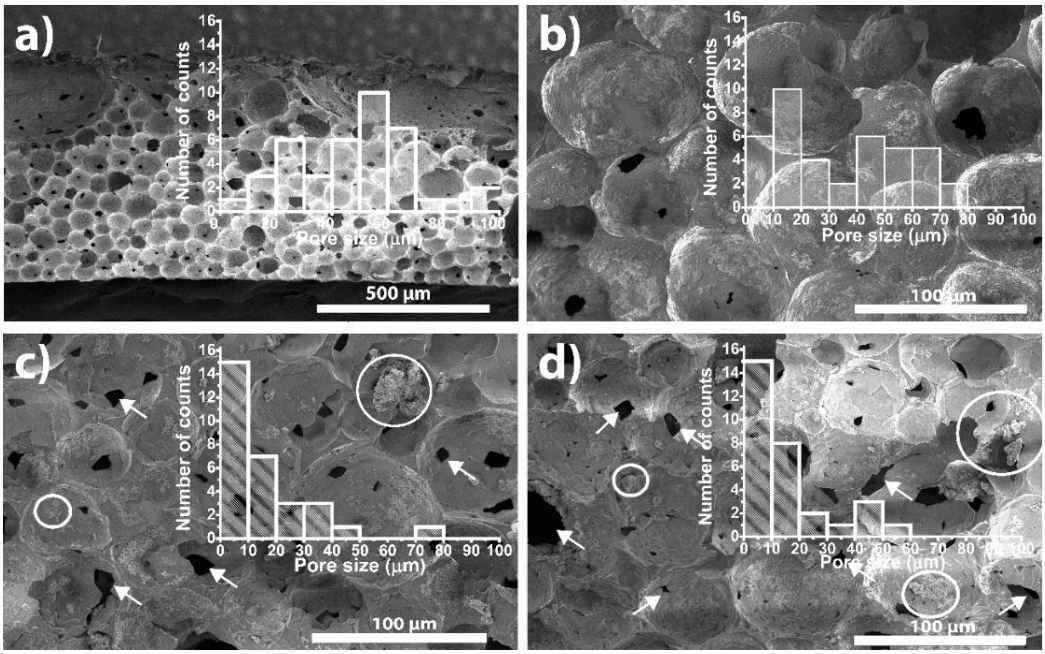

Figure 2.4. Cross-section SEM images of P(VDF-TrFE) membranes. a) Pristine P(VDF-TrFE); b) 8 % TiO_2/P(VDF-TrFE) membranes; c) and d) 8 % TiO_2/P(VDF-TrFE) with and 5 and 8 % NaY, respectively. Inset, the histograms of the pore diameter distribution for the respective SEM image.

The TiO_2/P(VDF-TrFE) nanocomposites functionalized with varying zeolite content (Figure 2.4c and d) also reveals a microporous structure similar to the pristine and TiO_2 nanocomposite samples. Noticeably, pore interconnectivity seems to increase through small pores within the walls of the larger pores, as depicted with the arrows in the micrographs. Regarding the filler dispersion, only the sample with 3 % NaY (supplementary information) shows a good dispersion of the zeolites along the pores, in contrast with samples loaded with 5 and 8 % zeolite content that exhibit a large amount of aggregates over the pore walls. This is in good agreement with previous studies indicating that zeolites remain in the pore walls instead of being integrated into the polymer structure, which is attributed to their porous structure, leading to solvent absorption and influencing the phase separation process [22].

Furthermore, the pores within the membranes with zeolites show a more heterogeneous microstructure with less defined forms (less spherical). These findings indicate that the incorporation of zeolites into the solution influence the phase diagram and crystallization dynamic of the polymer, which is mainly dictated by polymer/solvent initial ratio and solvent evaporation temperature [23].

The main parameters quantifying the porous microstructure of the membranes are shown in Figure 2.5. Thus, pore size and degree of porosity depend on TiO_2 and NaY contents differently. Regarding pore size for natural polymer and samples containing TiO_2 nanoparticles, no significant differences were observed, with pores ranging from 51 to 62 µm. However, when zeolites are added to the samples, the pore size strongly decreases to 24, 18 and 13 µm for samples with 3, 5 and 8% NaY content, respectively. Furthermore, the degree of porosity remains also nearly constant with the inclusion of the TiO_2 nanoparticles, in the range of 73-79 %. On the other hand, when zeolites are added to the membrane, the degree of porosity strongly increases to 89 and 97 %, for 3 % and 8 % NaY filler contents, respectively. It is important to notice that, in samples with zeolites, porosity measurements do not represent only membrane porosity, but also includes the contribution of the porosity of the zeolites. The decrease of the average pore size and the increase of the overall porosity are indicative of strong influence of the zeolites on the phase diagram and the crystallization process, acting as nucleation elements for crystallization and hindering barriers for the phase separation process, thus leading to a higher number of smaller pores (arrows Figure 2.4c and d). The histograms of Figure 2.4, show a shift regarding the prevalence of pores size. In histogram from Figure 2.4b, one

can observe a predominance of larger pores and instead, on Figure 2.4c and d) we realize a predominance of smaller pores.

Figure 2.5. Estimated pore size (○) and average porosity (□) for pristine and nanocomposite membranes of P(VDF-TrFE) with different amounts of TiO_2 and NaY.

For the intended application, connectivity of pores enhances light penetration and increases mass transfer of pollutants for photocatalysis [40]. On the other hand, it should be noted that the small size of the TiO_2 nanofillers leads to no significant effect on the phase separation process and therefore on the final membrane microstructure.

Finally, it is worth noticing that the produced samples show a suitable porous structure appropriateate for pollutant diffusion onto the TiO_2 nanoparticles within pore walls [41]. Infrared spectroscopy (FTIR) was used to determine polymer phase content and the possible chemical interaction between fillers and polymer matrix. In Figure 2.6, FTIR spectra show that TiO_2/P(VDF-TrFE) composites show unchanged polymer structure concerning the pristine polymer, independently of the filler content. In particular, bands at 840, 1288 and 1400 cm^{-1} show that the polymer crystallizes in the all-trans piezoelectric β-phase [42, 43]. The polymer phase remains unchanged when TiO_2 and zeolite are present in the membranes (Figure 2.6). Further, a new band around 900-1100 cm^{-1}, assigned to the stretching vibration of the Si-O bond, appears and increases with increasing zeolite content, indicative of the presence of zeolite in the membrane [44, 45]. In this way, filler content and type do not change the crystallization phase of the polymer, which crystallizes in the all-trans β-phase, and no chemical bonds are detected between polymer and fillers.

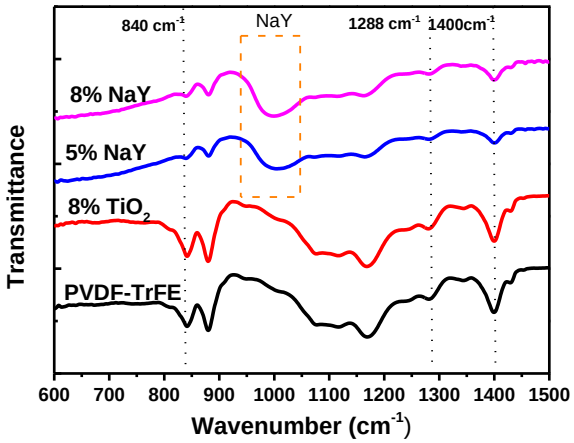

Figure 2.6. FTIR spectra of pristine P(VDF-TrFE) membrane, and nanocomposite membranes with 8 %TiO_2 and 8 %TiO_2 with 5 and 8 % NaY.

The wettability of the membranes was assessed by contact angle measurements. Figure 2.7 shows the variation of the contact angle and surface energy with TiO_2 and NaY filler content in the polymer membrane.

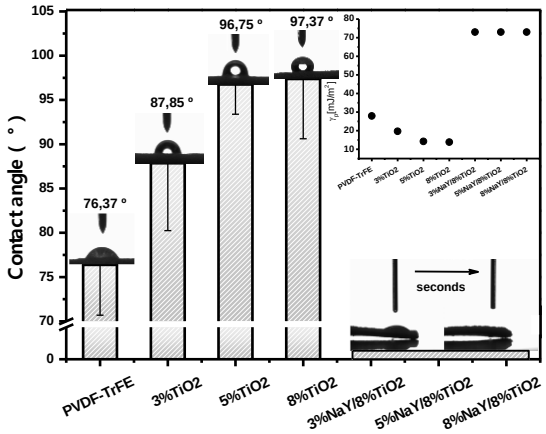

Figure 2.7. Contact angle measurements and inset the estimated surface free energy (γp) of P(VDF-TrFE) with different amounts of TiO_2 and NaY.

Pristine polymer and samples with 3, 5 and 8 % of TiO_2 nanoparticles present a contact angle 76, 88, 96 and 97°, respectively, showing an apparent increase of the contact angle with increasing amount of TiO_2 nanoparticles. Regarding the estimated surface energy, values decrease from 27.9 mJ/m^2 for the pristine PVDF-TrFE membrane to 13.87 mJ/m^2 for the membrane containing 8 % TiO_2. These values are in the range of hydrophobic

materials, with the characteristic low surface energy and low wettability [27]. Contrarily, all the samples containing NaY present high surface energy, 73 mJ/m^2, which is typical of hydrophilic materials. Previous works already reported the hydrophobic nature of polymer nanocomposites containing TiO_2 nanoparticles, as these particles only display hydrophilic behavior when irradiated with UV irradiation [46, 47]. On the other hand, the inclusion of zeolites into the membrane yields hydrophilic properties to the membrane and the water droplet completely spread in the membrane surface and is rapidly absorbed. The hydrophilic properties of these samples is attributed exclusively to the microporosity and capillary effect of the zeolites [48]. Additionally, the increased irregularity on membrane surface caused by zeolites may also contribute for hydrophilicity of the membrane [49] although this effect certainly plays a secondary role as the variation among membranes is not as significant as the water absorption capability introduced by the zeolites. Materials with increased wettability promote the contact between the pollutant and the surface of the TiO_2 nanoparticles which is a key issue for improved photocatalytic performance.

2.3.3. Photocatalytic Activity Evaluation

To compare the photocatalytic efficiency of TiO_2 nanoparticles in suspension and immobilized into P(VDF-TrFE) the evaluation of the maximum absorbance of MB, at 63 nm, was assessed.

The photocatalytic assays in suspension were performed with different amounts of TiO_2 nanoparticles in a constant volume of MB aqueous solution (Figure 2.8).

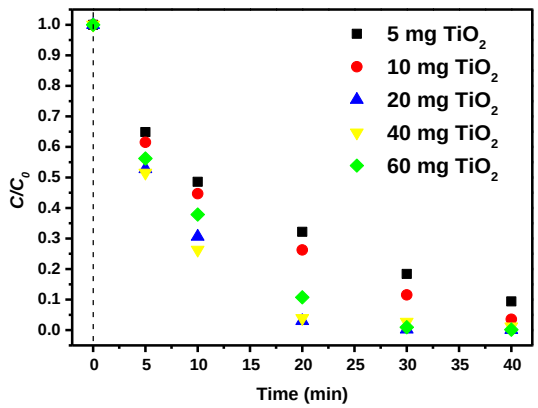

Figure 2.8. Methylene blue photocatalytic degradation performance as a function of time for different amounts of TiO_2 nanoparticles in suspension.

The trials with 5, 10 and 20 mg of nanoparticles in suspension show MB degradation efficiencies of 91.6, 96.8 and 99.9 %, respectively (Table 2.2). Similarly, the 1st order rate constant values show estimated values of 0.056, 0.079 and 0.184 min^{-1} for assays with 5, 10 and 20 mg of nanoparticles, respectively.

Table 2.2. Amount of TiO_2 nanoparticles used in suspension assays, first-order rate constant (*k*) and degradation efficiency (%) of MB (10^{-5} M), at 40 minutes of irradiation.

m(mg)	**Reaction Rate (min^{-1})**	**Degradation (%)**
5	0.056	92
10	0.079	97
20	0.184	100
40	0.114	99
60	0.168	100

When higher amounts of TiO_2 nanoparticles are used, the trend above no longer occurs. Using 40 and 60 mg of nanoparticles yields similar MB degradation efficiencies (99.8 to 99 %), however, the reaction rates decrease to 0.114 and 0.168 min^{-1}, respectively. A significant amount of nanoparticles speeds up nanoparticles aggregation process resulting in a loss of surface area, which is in good agreement with hydrodynamic size measurements performed by DLS, showing the formation of large agglomerates. Thus, the obtained results indicate that for the given conditions, 20 mg of nanoparticles is the optimum amount to achieve the highest photocatalytic degradation efficiency.

For the study of the photocatalytic activity for immobilized TiO_2 nanoparticles, two sets of measurements were performed. First, the photocatalytic activity of different amounts of immobilized nanoparticles (3, 5 and 8 %) was tested. The results, shown in Figure 2.9a and quantified in Table 2.3, indicate that the pristine P(VDF-TrFE) membrane does not show any photocatalytic activity, being the small absorbance decrease addressed to MB photodegradation and absorbance to the membrane. Additionally, for the same experimental conditions, the reaction rate and photocatalytic degradation efficiency of MB increases with increasing amount of TiO_2 nanoparticles. The degradation efficiency reaches 77 and 98 %, for the membranes with 3 and 8 % TiO_2 nanoparticles, respectively.

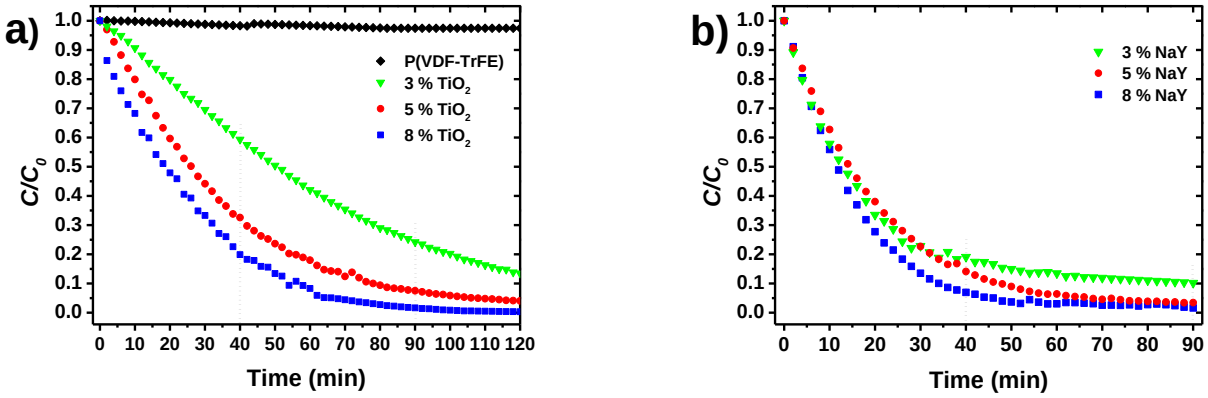

Figure 2.9. Methylene blue photocatalytic degradation performance as a function of time for pristine PVDF-TrFE membranes and membranes containing different amounts of TiO_2 nanoparticles (a), and containing 8 wt. % TiO_2 nanoparticles and different amounts of zeolites (b).

Once the nanocomposite membrane with the highest photocatalytic performance has been assessed, the potential effect of improvement of membrane wettability was addressed with the addition of different amounts of zeolites (3, 5 and 8 %). The obtained results (Figure 2.9b) indicate that the incorporation of zeolites into the nanocomposite slightly accelerate the initial adsorption of MB during the first 30 minutes under dark conditions for all the samples when compared with the sample of P(VDF-TrFE) with 8 % TiO_2.

Table 2.3. Amount of TiO_2 nanoparticles and NaY immobilized in P(VDF-TrFE), first-order rate constant (k) and degradation efficiency (%) of MB (10^{-5} M) at 40 and 90 minutes.

Samples		***k*** **(min^{-1})**		**Degradation (%)**	
		40 min	**90 min**	**40 min**	**90 min**
3 %TiO_2		0.029	0.018	49	77
5 %TiO_2		0.013	0.026	76	93
8 %TiO_2		0.037	0.037	86	99
8 %TiO_2	3 %NaY	0.049	0.023	86	91
	5 %NaY	0.045	0.04	91	99
	8 %NaY	0.069	0.033	96	96

Regarding 90 minutes of degradation, only the membranes with 5 % NaY show better reaction rate and slightly higher degradation efficiency (99 %) than the membrane with 8 % TiO_2. The remainder samples with zeolites show lower degradation values of MB and

lower reaction rates than the sample with 8 % TiO_2. On the other hand, after 40 min of UV irradiation, the influence of zeolite loading shows more significant impact on the reaction rate and MB degradation efficiencies than at 90 min. Thus, for 40 minutes of UV irradiation, all the samples with zeolites present higher reaction rates, 0.049 up to 0.069 min^{-1}, and higher degradation efficiencies, 86 up to 95.7 %, regarding the sample of 8 %TiO_2 (0.037 min^{-1} and 85.7 %). It is noteworthy to mention that for 90 minutes of degradation the rate constant and MB removal efficiency for the sample with 8 % NaY are lower than the values for 5 % NaY, indicating that for higher amounts of NaY particles agglomeration, well supported by SEM images. Particles agglomeration cause surface area loss, leading to lower photocatalytic activity efficiencies. Analysis of the results at both intervals of UV irradiation indicates that the zeolites main role is to accelerate the photocatalytic process through the improved interaction of the aqueous MB solution with the nanoparticles exposed on the polymer matrix. This acceleration is in good agreement with the wettability results, which show the hydrophilic behavior of samples with zeolites by opposition to the hydrophobic one in samples without zeolite. In general, hydrophilic materials allow for increased permeability to water [50, 51]. In this respect, hydrophilicity together with a highly interconnected porous structure, are responsible for a good diffusion of MB in the catalyst surface, allowing for a faster adsorption process to take place.

The use of MB to assess the photocatalytic activity of materials is a standard procedure as it allows to evaluate and easily compare our results with the literature. Table 2.4 shows some results obtained using different polymeric membranes with TiO_2 used in MB photocatalytic degradation.

Table 2.4. Summary of reporting on MB removal using polymeric membranes and the main experimental conditions.

Type of membrane	TiO_2 (%)	UV irradiation	Removal efficiency (%)	k (min^{-1})	Ref.
TiO_2/PEI	6	300 mW/cm^2	100 % after 60 min	-	[54]
TiO_2/PA-12	20	5 mW/cm^2	100 % after 120 min	0.012	[55]
TiO_2/PVDF	18.65	15 W	≈100 % after 150 min	-	[56]
TiO_2/PVDF-TrFE	8	4 mW/cm^2	≈100 % after 90 min	0.04	This study

To compare the results from various works, the different conditions used should be considered.

Concerning the comparison between suspended and immobilized TiO_2 nanoparticles, it is important to refer that membranes with 3, 5 and 8 wt. % TiO_2 were estimated to correspond to the assays with 20, 40 and 60 mg of TiO_2 nanoparticles in suspension, respectively. As expected, the produced membranes do not show higher degradation efficiencies or reaction rates when compared with the suspension experiments. Thus, after 40 min of UV irradiation, membranes with TiO_2 show degradation efficiencies from 49.1 (3 % TiO_2) to 85.7 % (5 wt. % TiO_2), when compared with efficiencies around 99 % for the corresponding suspension trials. These results indicate an efficiency loss in the range of ≈ 50 % for the membrane with 3 % TiO_2 to 13 % in the sample with 8 % TiO_2, comparatively to the 20 and 60 mg suspension trials. As mentioned before, the immobilization of nanoparticles may tackle some of the mainstream problems of photocatalysis application, but this configuration also hosts some undesirable features, which synergistically explain the obtained results. Therefore, one of the main problems relies on nanoparticles surface area loss and mass transfer limitations, caused by nanoparticles adherence to the substrate [52]. Additionally, decrease in water permeability, and inappropriate light harvesting may also hinder the photocatalytic performance. These drawbacks were already mitigated by the development of membranes with highly porous structure, good nanoparticles dispersion, attachment and non-degradation of catalyst properties during immobilization process [14]. In this connection, membrane wettability was improved incorporating zeolites into the polymeric matrix to allow MB enhanced adsorption. The comparison of photocatalytic performance at 40 min between suspension and immobilized configuration, with zeolite incorporated, indicate that 8 % NaY/8 % TiO_2/P(VDF-TrFE) best degradation efficiency (95.7 %) presents a degradation loss efficiency of only 3.3 %, relative to the 60 mg TiO_2 result. This result shows that with proper tailoring, an immobilized photocatalytic configuration may achieve degradation performances very close to the suspension ones. In this sense, the recuperation of nanoparticles in suspension is overcome, and the accelerated corrosion of TiO_2 nanoparticles is prevented, as the exposed area is lower than in the suspension configuration [53].

2.3.4. Photocatalytic evaluation in a solar photoreactor

The photocatalytic activity of the 8% TiO_2/P(VDF–TrFE) membrane [37, 40] was also used in this work to assess the degradation of tartrazine. Figure 2.10 shows the degradation profile of tartrazine (10 mg L^{-1}) after 5 h (300 min) of sunlight irradiation indicating that approximately 78% of the dye was degraded, at a reaction rate constant of 0.30 min^{-1}.

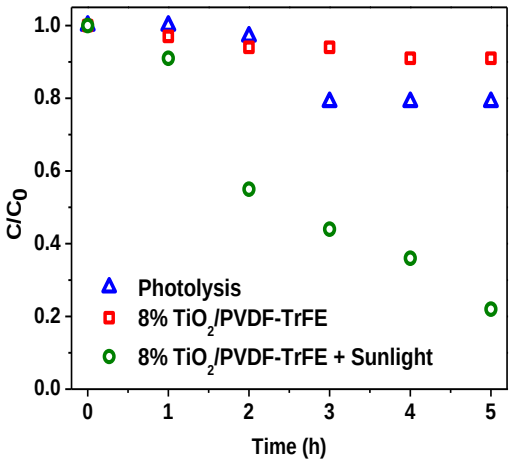

Figure 2.10. Photocatalytic degradation of tartrazine (10 mg L^{-1} with the 8 wt. % TiO_2/PVDF–TrFE nanocomposite, over 5 hours of sunlight irradiation. Controls: irradiation of tartrazine solution without the nanocomposite (photolysis); the nanocomposite in tartrazine solution with no radiation (adsorption).

As a control, the same experiment was carried out without the 8% TiO_2/P(VDF–TrFE) membrane and, under this condition, just 2% of degradation was observed after sunlight irradiation of the tartrazine solution for 5 h. This result shows that this dye is stable under sunlight irradiation, presenting low photolysis, which agrees with [47, 48]. In the presence of the produced membrane but the absence of sunlight, 9% of tartrazine removal was observed after 5 h (Figure 2.7), which can be addressed to adsorption of dye into the 8 wt. % TiO_2/PVDF-TrFE nanocomposite membrane.

As previously mentioned, few works have reported on tartrazine degradation in immobilized systems [42, 49, 50] using different approaches like the one presented in this work. Thus, given the different set-ups and experimental conditions of these works, is not possible to make a direct comparison of the results. The utmost similar work also using a solar photoreactor, was based on TiO_2 (P25) impregnated on the photoreactor surface to

degrade tartrazine [49]. The results show that 99% of the dye was degraded after 5 hours of sunlight radiation. The system mentioned above is based on particles fixed to the photoreactor surface, but the nanoparticles are not embedded into any substrate or matrix - reducing the surface area loss when compared to our system. Additionally, this work employs a significantly larger photoreactor (1×0.5 m), and the estimated amount of TiO_2 nanoparticles was almost 2-fold (1.8 ×) the amount used in our study. Furthermore, the impregnation of the nanocatalyst directly into the photoreactor surface will require a laborious process to clean and re-impregnate it with a new TiO_2 layer for eventual further reuse, a task that was not addressed. On the other hand, our system allows a fast and straightforward monitorization/substitution of the photocatalytic nanocomposite for the proper recycling of the remaining residues. TiO_2 nanoparticles have also been immobilized by sol-gel on calcinated sewage sludge and ≈ 80% of tartrazine was degraded under visible radiation (82 Lm W^{-1}) for 120 min [50]. The drawback of this system is the same presented by slurry systems, which require sedimentation and decantation processes that are time-consuming and expensive.

Other works, where the UV lamps were used instead of sunlight radiation also serve as a reference but not for straightforward comparison; for instance, nanocomposites based on TiO_2 and activated carbon were able to degrade 80% of tartrazine in 3 hours (UV - 4.7 mW/cm^2) [42]. The authors mentioned that the obtained efficiency is owed to the adsorptive properties of the activated carbon that transfers the adsorbed organic compounds to the active catalytic sites on the TiO_2 surface. Moreover, despite the promising results, this suspension system does not avoid the time-consuming and expensive recuperation processes, which is a hindrance concerning the reusability of photocatalytic materials.

Effect of initial dye concentration

The effect of initial tartrazine concentration on the photocatalytic activity was studied by degrading tartrazine solutions of 10, 20 and 30 mg L^{-1}. It was found that degradation percentage is strongly dependent on the initial dye concentration and decreased from ≈ 78 to 46 % with increasing concentration of the dye, from 10 to 30 mg L^{-1} (Figure 2.11).

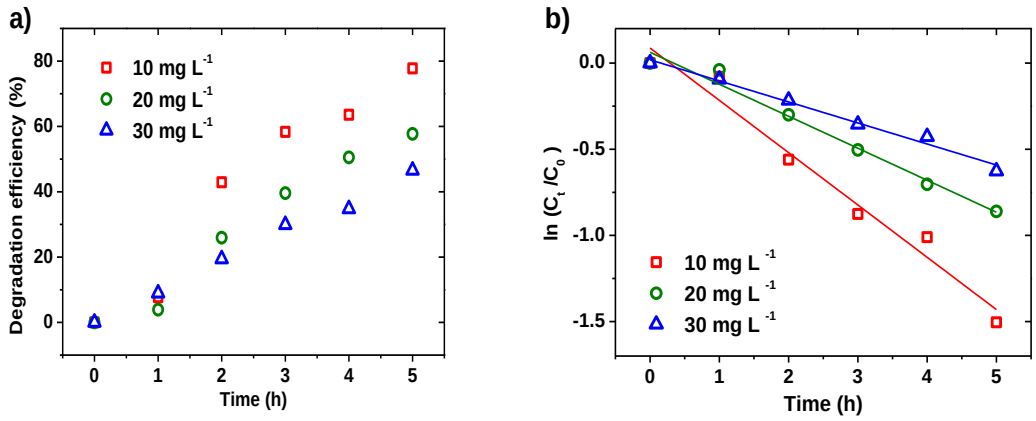

Figure 2.11. Degradation efficiency (%) (a) and ln (C_t/C_0) *vs*. time (b) for different initial dye concentration (10, 20 and 30 mg L^{-1}), using 8 wt. % TiO_2/PVDF-TrFE nanocomposites under sunlight irradiation over 5 hours.

The rate of degradation is related to the available catalyst surface for the generation of electron-hole pairs, which in turn generates hydroxyl radicals. In this case, the amount of catalyst is kept constant, and the number of hydroxyl radicals generated remains the same, while dye concentration increases. Therefore, the ratio of *hydroxyl radical/tartrazine molecules* decreases with higher concentrations [50], leading to lower photodegradation efficiencies. Additionally, higher tartrazine concentrations will also reduce the UV light absorbance by TiO_2 nanoparticles surface, which will also contribute to decreasing the amount of hydroxyl radicals formed [44]. In this context, the photocatalytic efficiency reduces in high concentrated tartrazine solutions.

The kinetics of photocatalytic degradation of tartrazine can be described by the first-order Eq. 2.3 [51]. Figure 6b shows the plot of ln (C_t/C_0) vs. time at different initial dye concentrations. Linear plots were observed (with R^2 values higher than 0.9), which confirms that the photocatalytic degradation of tartrazine obeys pseudo-first-order kinetics. The estimated pseudo-first order rate constant and corresponding R^2 values are presented in Table 2.5. With increasing dye concentration from 10 to 30 mg L^{-1}, the degradation rate constant decreases from 0.30 to 0.12 min^{-1}. Other works reporting on the effect of initial tartrazine concentration on the photocatalytic process also confirm a similar trend: higher initial concentrations yield lower degradation constants [49, 52].

Table 2.5. Effect of initial dye concentration (C_0) on photocatalytic degradation efficiency (%) and apparent reaction rate (K_{app}) of tartrazine.

C_0 (mg L^{-1})	Degradation (%)	K_{app} (min^{-1})	R^2
10	77.77	0.30	0.96
20	57.72	0.18	0.97
30	46.57	0.12	0.98

The Langmuir–Hinshelwood model has also been used to evaluate the heterogeneous photocatalytic reaction of organic compounds in aqueous solutions [53]. The experimental data were then represented concerning the Langmuir–Hinshelwood model to accommodate reactions taking place at the solid-liquid interface, Eqs. (2.5) and (2.6) [54].

$$r_0 = -\frac{dC}{dt} = \frac{K_1 K_2\, C}{(1+K_2 C_0)} = K_{app}\, C \qquad \text{(Eq.2.5)}$$

$$\frac{1}{K_{app}} = \frac{1}{K_1 K_2} + \frac{C_0}{K_1} \qquad \text{(Eq.2.6)}$$

Where r_o is the rate of degradation of the dye, K_1 is the surface reaction rate constant ($molL^{-1}min^{-1}$), and K_2 is the Langmuir-Hinshelwood adsorption equilibrium constant ($Lmol^{-1}$). The plot of $1/K_{app}$ *vs*. C_o for the photocatalytic degradation of tartrazine is shown in Figure 2.12.

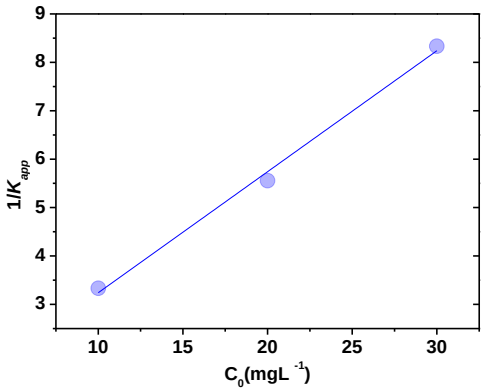

Figure 2.12. Plot of $1/K_{app}$ as a function of the initial concentration (C_0) of tartrazine.

The linear relationship between $1/K_{app}$ and C_o (R^2=0.995) indicates the validity and applicability of the Langmuir - Hinshelwood model for photocatalytic degradation of tartrazine by the 8 wt. % TiO_2/P(VDF–TrFE) membrane suggesting that tartrazine degradation occurs mostly on nanoparticles surface, in good agreement with other works [50]. The values of K_1 and K_2 were found to be 5.4 mol $L^{-1}min^{-1}$ and 4 $Lmol^{-1}$, respectively.

Effect of Flow rate

The effect of tartrazine solution flow rate in the photocatalytic degradation was investigated by testing two different flow rates: 9.78 mL s^{-1} and 28 mL s^{-1}. Figure 2.13 shows that the degradation of tartrazine increases almost linearly with time for both flow rates tested. After 5 hours of UV irradiation, the percent degradation of tartrazine was 37% and 77% for 9.78 mL s^{-1} and 28 mL s^{-1}, respectively.

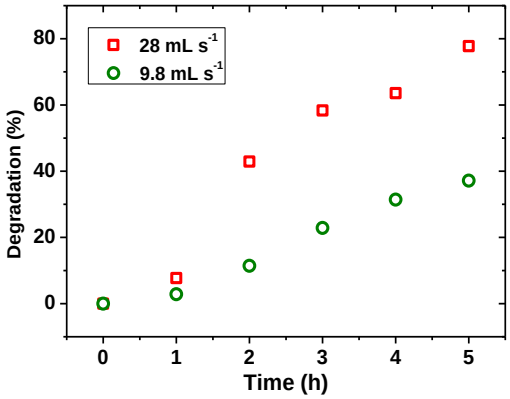

Figure 2.13. Degradation of tartrazine (C_0= 10 mg L^{-1}) at different circulation flowrates with an 8 %wt TiO_2/PVDF–TrFE nanocomposite and free pH (6.2) under 5 hours of solar irradiation.

The increase in degradation efficiency at a higher flow rate is ascribed to a larger turbulence in the solution, which promotes the external mass transfer from the bulk solution to TiO_2/PVDF–TrFE nanocomposite surface. This conditions will indirectly increase the global rate of reaction between the TiO_2/PVDF–TrFE nanocomposite and tartrazine and in turn will result in higher percent degradation of tartrazine. In fact, Amid Amiri and co-workers also found that increasing the flow rate throughout membranes coated with zinc oxide nanoparticles promoted higher Reactive Yellow degradation rates, caused by enhanced mass transfer [55].

Reusability of the TiO_2/P(VDF-TrFE) nanocomposite membrane

The reusability of the nanocomposite was also assessed, and two uses were performed. Between the first and the second uses the nanocomposite membrane was rinsed with distilled water and dried at room temperature. Afterward, a new tartrazine solution was added to the photoreactor and a second use performed, under the same experimental conditions. The results presented in Figure 2.14 show that ≈ 78% of tartrazine was degraded after 5 h of sunlight exposure. For a second use, ≈ 67% of tartrazine was degraded, which corresponds to ≈ 10% of efficiency loss. No further reuses were performed, as it has been demonstrated that most nanoparticles inefficiently attached to the polymer matrix detach during the first use and cleaning step [46, 56, 57].

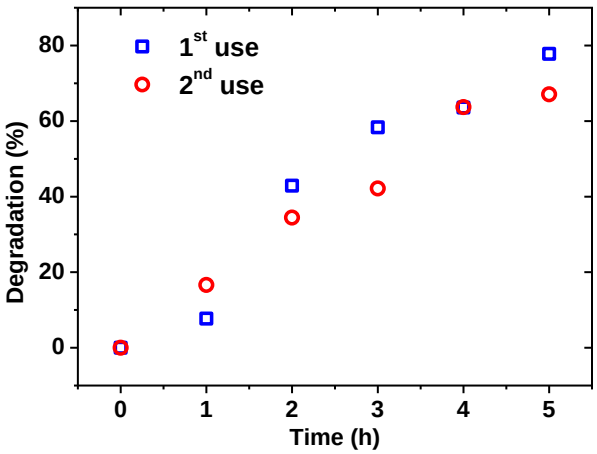

Figure 2.14. Photocatalytic degradation of tartrazine (C_0= 10 mg L^{-1}) with an 8 %wt TiO_2/PVDF–TrFE nanocomposite in two consecutive uses, under 5 hours of sunlight exposure.

This loss of photocatalytic efficiency is explained by the washing out of TiO_2 nanoparticles from the surface of the PVDF-TrFE membrane, during the first use and posterior cleaning step. The second use corresponds to the photocatalytic process involving the TiO_2 nanoparticles more efficiently retained on the microporous structure, in good agreement with the SEM and EDX mapping images – where high amounts of nanoparticles are distributed inside the pores. Previous reports on the recyclability of the nanocomposite indicate similar efficiencies losses (16 % after 3 cycles) for a 10 wt. % TiO_2 PVDF-TrFE nanocomposite used for methylene blue degradation [46]. This efficiency loss is in the order of the losses observed in related immobilization strategies. Thus, a TiO_2-RGO/nylon-6 nanocomposite produced by electrospinning and

hydrothermal treatment revealed a slight photocatalytic efficiency loss (< 10 %) after 4 cycles of methylene blue degradation [58]; a sol-gel membrane containing TiO_2, silicon dioxide (SiO_2) and silicon carbide (SiC) was used to degrade methylene blue and for some of the produced membranes, the efficiency decreased 2.3, 3 and 5 times during the second use [59]. Finally, pluronic-based TiO_2 hybrid photocatalytic membranes suffered a reduction of ≈ 9% after 5 cycles for Rhodamine B degradation [60]. In all these works, the efficiency loss was explained by the loss of nanoparticles from the substrate, which is one of the larger hurdles immobilized systems [21]. Additionally, the efficiency loss can also be related to the high amount of accumulated dye (after the consecutive uses) on the membrane surface and the consequent diminishing specific photo catalytically active sites [60]. Thus, considering the literature and the obtained results, the produced photocatalytic nanocomposites demonstrate a suitable reusability.

Effect of irradiation intensity

The influence of irradiation intensity on the degradation efficiency of the 8 wt. % TiO_2/PVDF-TrFE nanocomposite was assessed exposing the nanocomposite and tartrazine solution to a UV lamp or sunlight irradiation (Figure 2.15).

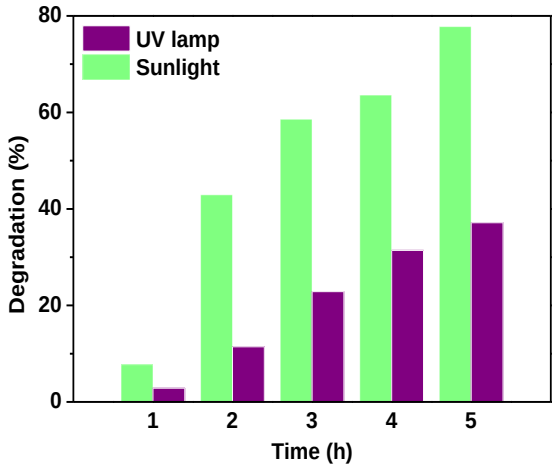

Figure 2.15. Comparative degradation of tartrazine (C_0= 10 mg L^{-1}) with an 8 %wt TiO_2/PVDF–TrFE nanocomposite under 5 hours of solar or UV lamp irradiation.

As mentioned before, during 5 h of sunlight exposure, the 8 %wt TiO_2/PVDF–TrFE nanocomposite placed on the photoreactor could degrade ≈ 78% of tartrazine. In comparison using a UV lamp, under the same experimental conditions, there was a significant photocatalytic efficiency decrease, and just ≈ 37% of tartrazine was degraded. These results indicate a remarkable photocatalytic activity under sunlight radiation, especially because TiO_2 requires UV radiation (< 387 nm) to be photocatalytic active, which corresponds to only ≈5% of the radiation provided by the sun [61]. The different intensity of the UV lamp and UV from sunlight during the photocatalytic experiments, respectively 6 mW/cm^2 and 60-100 mW/cm^2, explains the differences observed in the photocatalytic degradation. However, higher light intensities do not always guarantee higher photocatalytic efficiencies, and studies with different compounds have shown the nonlinear relationship between these two variables, due to the higher electron-hole recombination rate that may occur under high light intensities [51, 53]. However, our results show that a significant increase in light intensity (≥ 10×) yielded an enhanced tartrazine degradation efficiency. These results are consistent with the results obtained by Salam K. Al-Dawery, which demonstrated the linear relationship between the light intensity and degradation rate and identified light intensity as the main factor in the tartrazine degradation kinetic [44]. The work developed by Chekir and co-workers also shows that tartrazine was more efficiently degraded by TiO_2 under solar radiation than with UV lamp radiation [49].

2.4. Conclusions

Nanocomposite membranes with different amounts of immobilized TiO_2 nanoparticles with/without NaY zeolite were successfully produced and characterized. All the produced samples presented good nanoparticles dispersion regardless of TiO_2 content as well as a highly porous structure with degrees of porosity between 73 and 79 %. The photocatalytic activity is due to the TiO_2 nanoparticles, while the NaY zeolites lead to the hydrophilic behavior of the membranes. Photocatalytic assays were performed with TiO_2 nanoparticles in suspension and immobilized in P(VDF-TrFE) membranes, monitoring MB degradation. Photocatalytic assays in suspension revealed an optimum amount of nanoparticles (20 to 30 mg) leading to the best MB degradation performance (100 % degradation in approximately 30 min of UV irradiation). Afterward, the photocatalytic

activity of nanocomposite membranes was assessed. Results show that, nanocomposites with TiO_2 increase degradation rates and efficiency with increasing nanoparticles content. However, the membrane with the best performance (85.7 % of MB degradation after 40 minutes of UV irradiation) corresponds to an efficiency loss of 13 % comparatively to the respective assay with nanoparticles in suspension. To mitigate the limitations caused by immobilization (lower surface area, mass transfer limitations, and reduced light harvesting), zeolites were added to the nanocomposites. Zeolites play a vital role in the first minutes, favoring higher MB solution permeability and percolation through the porous structure. With this configuration, an efficiency loss of only 3 % was achieved regarding the best performance assay with suspended nanoparticles.

The degradation of Tartrazine solutions of 10, 20 and 30 mg L^{-1}, in a sunlight photoreactor, presented degradation efficiencies of 78, 58 and 47 % respectively, after 5h of solar irradiation. The results show that the photocatalytic degradation of tartrazine obeys pseudo-first-order kinetics and that degradation occurs mainly on nanoparticles surface. Decreasing the UV radiation intensity (UV lamp) reduces the photocatalytic degradation of tartrazine to 37 %. The reusability assays were performed, and the nanocomposite proved to be effective, as the nanoparticles efficiently attached/retained in the polymeric porous structure allow for an efficient photocatalytic performance.

After the production and optimization of the TiO_2/PVDF-TrFE nanocomposite, and final application in a solar photoreactor, the results herein presented indicate the suitability of the produced membranes for photocatalytic applications.

2.5. References

1. Lu, S.-y., et al., Photocatalytic decomposition on nano-TiO_2: Destruction of chloroaromatic compounds. Chemosphere, 2011. 82(9): p. 1215-1224.

2. Uddin, M.N., et al., An experimental and first-principles study of the effect of B/N doping in TiO_2 thin films for visible light photo-catalysis. J. Photochem. Photobiol., A, 2013. 254(0): p. 25-34.

3. Kabra, K., R. Chaudhary, and R.L. Sawhney, Treatment of Hazardous Organic and Inorganic Compounds through Aqueous-Phase Photocatalysis: A Review. Ind. Eng. Chem. Res., 2004. 43(24): p. 7683-7696.

4. Leong, S., et al., TiO_2 based photocatalytic membranes: A review. J. Membr. Sci., 2014. 472(0): p. 167-184.

5. Lu, S.-y., et al., Photocatalytic decomposition on nano-TiO_2: Destruction of chloroaromatic compounds. Chemosphere. Vol. 82. 2011: Wiley. 1215-1224.

6. Linsebigler, A.L., G. Lu, and J.T. Yates, Photocatalysis on TiO_2 Surfaces: Principles, Mechanisms, and Selected Results. Chem. Rev., 1995. 95(3): p. 735-758.

7. Wu, X., et al., UV, visible and near-infrared lights induced NOx destruction activity of (Yb, Er)-NaYF4/C-TiO_2 composite. Sci. Rep., 2013. 3.

8. Ahmed, M.H., et al., 1 - Characteristics and applications of titanium oxide as a biomaterial for medical implants, in The Design and Manufacture of Medical Devices, J.P. Davim, Editor. 2012, Woodhead Publishing. p. 1-57.

9. Simonsen, M.E., Chapter 4 - Heterogeneous Photocatalysis, in Chemistry of Advanced Environmental Purification Processes of Water, E.G. Søgaard, Editor. 2014, Elsevier: Amsterdam. p. 135-170.

10. Gumy, D., et al., Solar photocatalysis for detoxification and disinfection of water: Different types of suspended and fixed TiO_2 catalysts study. Solar Energy, 2006. 80(10): p. 1376-1381.

11. Guillard, C., et al., Influence of chemical structure of dyes, of pH and of inorganic salts on their photocatalytic degradation by TiO_2 comparison of the efficiency of powder and supported TiO_2. Journal of Photochemistry and Photobiology A: Chemistry, 2003. 158(1): p. 27-36.

12. Choi, H., S.R. Al-Abed, and D.D. Dionysiou, Chapter 3 - Nanostructured Titanium Oxide Film- and Membrane-Based Photocatalysis for Water Treatment, in Nanotechnology Applications for Clean Water, N.S.D.D.S. Sustich, Editor. 2009, William Andrew Publishing: Boston. p. 39-46.

13. Pozzo, R.L., M.A. Baltanás, and A.E. Cassano, Supported titanium oxide as photocatalyst in water decontamination: State of the art. Catal. Today, 1997. 39(3): p. 219-231.

14. Shan, A.Y., T.I.M. Ghazi, and S.A. Rashid, Immobilisation of titanium dioxide onto supporting materials in heterogeneous photocatalysis: A review. Appl. Catal., A, 2010. 389(1–2): p. 1-8.

15. Damodar, R.A., S.-J. You, and H.-H. Chou, Study the self cleaning, antibacterial and photocatalytic properties of TiO_2 entrapped PVDF membranes. J. Hazard. Mater., 2009. 172(2–3): p. 1321-1328.

16. Daels, N., et al., Functionalisation of electrospun polymer nanofibre membranes with TiO_2 nanoparticles in view of dissolved organic matter photodegradation. Sep. Purif. Technol., 2014. 133(0): p. 282-290.

17. Ortelli, S., et al., TiO_2 based nano-photocatalysis immobilized on cellulose substrates. J. Photochem. Photobiol., A, 2014. 276(0): p. 58-64.

18. Ding, Z., et al., Synthesis of anatase TiO_2 supported on porous solids by chemical vapor deposition. Catal. Today, 2001. 68(1–3): p. 173-182.

19. Pang, Z., et al., Fabrication of PA6/TiO_2/PANI composite nanofibers by electrospinning–electrospraying for ammonia sensor. Colloids Surf., A, 2014. 461(0): p. 113-118.

20. Zhang, Y., J. Wan, and Y. Ke, A novel approach of preparing TiO_2 films at low temperature and its application in photocatalytic degradation of methyl orange. J. Hazard. Mater., 2010. 177(1–3): p. 750-754.

21. Choi, H., et al., Chapter 8 - Nanostructured Titanium Oxide Film- and Membrane-Based Photocatalysis for Water Treatment, in Nanotechnology Applications for Clean Water (Second Edition), A.S.S.D. Savage, Editor. 2014, William Andrew Publishing: Oxford. p. 123-132.

22. Nunes-Pereira, J., et al., Microporous membranes of NaY zeolite/poly(vinylidene fluoride–trifluoroethylene) for Li-ion battery separators. J. Electroanal. Chem., 2013. 689(0): p. 223-232.

23. Ferreira, A., et al., Poly(vinylidene fluoride-trifluoroethylene) (72/28) interconnected porous membranes obtained by crystallization from solution. MRS Online Proc. Libr., 2011. 1312: p. null-null.

24. Brown, L.F., Design considerations for piezoelectric polymer ultrasound transducers. IEEE Trans. Sonics Ultrason., 2000. 47(6): p. 1377-1396.

25. Botelho, G., et al., Performance of electroactive poly(vinylidene fluoride) against UV radiation. Polym. Test., 2008. 27(7): p. 818-822.

26. Martins, P., A.C. Lopes, and S. Lanceros-Mendez, Electroactive phases of poly(vinylidene fluoride): Determination, processing and applications. Prog. Polym. Sci., 2014. 39(4): p. 683-706.

27. Dahan, R.M., et al., Surface Modification of Polyvinylidenefluoride-Trifluoroethylene Film Using Argon Gas Plasma. Adv. Mat. Res., 2012. 626: p. 317-323.

28. Lee, D., et al., Aluminum Silicate Nanotube Modification of Cotton-Like Siloxane-poly(L-lactic acid)-vaterite Composites. Adv. Mater. Sci. Eng., 2013. 2013: p. 6.

29. Chester, A.W. and E.G. Derouane, Zeolite Chemistry and Catalysis : an integrated Approach and Tutorial. 2009, Berlin: Springer Netherland.

30. Tanaka, T., Reproductive and neurobehavioural toxicity study of tartrazine administered to mice in the diet. Food and Chemical Toxicology, 2006. 44(2): p. 179-187.

31. Moutinho, I., L. Bertges, and R. Assis, Prolonged use of the food dye tartrazine (FD&C yellow n° 5) and its effects on the gastric mucosa of Wistar rats. Brazilian Journal of Biology, 2007. 67: p. 141-145.

32. Rao, K.V.S., B. Lavédrine, and P. Boule, Influence of metallic species on TiO_2 for the photocatalytic degradation of dyes and dye intermediates. Journal of Photochemistry and Photobiology A: Chemistry, 2003. 154(2): p. 189-193.

33. Al-Dawery, S.K., Enhanced dynamics characterization of photocatalytic decolorization of hazardous dye Tartrazine using titanium dioxide. Desalination and Water Treatment, 2016. 57(19): p. 8851-8859.

34. Braswell, E., Evidence for trimerization in aqueous solutions of methylene blue. J. Phys. Chem., 1968. 72(7): p. 2477-2483.

35. Marques, J., et al., Release of Volatile Compounds from Polymeric Microcapsules Mediated by Photocatalytic Nanoparticles. Int. J. Photoenergy, 2013. 2013: p. 9.

36. Yu, J., et al., Effects of hydrothermal temperature and time on the photocatalytic activity and microstructures of bimodal mesoporous TiO_2 powders. Appl. Catal. B, 2007. 69(3–4): p. 171-180.

37. Jin, Z., et al., Fabrication of efficient visible light activated Cu–P25–graphene ternary composite for photocatalytic degradation of methyl blue. Applied Surface Science, 2015. 356: p. 707-718.

38. Bradbury, A., S. Menear, and R.W. Chantrell, A Monte Carlo calculation of the magnetic properties of a ferrofluid containing interacting polydispersed particles. J. Magn. Magn. Mater., 1986. 54–57, Part 2(0): p. 745-746.

39. Okte, A.N. and O. Yilmaz, Photodecolorization of methyl orange by yttrium incorporated TiO_2 supported ZSM-5. Appl. Catal. B, 2008. 85(1-2): p. 92-102.

40. Sentein, C., et al., Dispersion and stability of TiO_2 nanoparticles synthesized by laser pyrolysis in aqueous suspensions. J. Phys. Conf. Ser. , 2009. 170.

41. El-Bahy, Z.M., A.A. Ismail, and R.M. Mohamed, Enhancement of titania by doping rare earth for photodegradation of organic dye (Direct Blue). J. Hazard. Mater., 2009. 166(1): p. 138-143.

42. Chen, Y. and D.D. Dionysiou, A comparative study on physicochemical properties and photocatalytic behavior of macroporous TiO_2-P25 composite films and macroporous TiO_2 films coated on stainless steel substrate. Appl. Catal., A, 2007. 317(1): p. 129-137.

43. Dong, L., et al., Structuring porous “sponge-like” BiVO4 film for efficient photocatalysis under visible light illumination. J. Colloid Interface Sci., 2013. 393(0): p. 126-129.

44. Prabu, A.A., et al., Infrared spectroscopic studies on crystallization and Curie transition behavior of ultrathin films of P(VDF/TrFE) (72/28). Vib. Spectrosc., 2006. 41(1): p. 1-13.

45. Reynolds, N.M., et al., Spectroscopic analysis of the electric field induced structural changes in vinylidene fluoride/trifluoroethylene copolymers. Macromolecules, 1989. 22(3): p. 1092-1100.

46. Shikunov, B.I., et al., Infrared spectra of synthetic zeolites. Bull. Acad. Sci. USSR, Div. Chem. Sci., 1972. 21(1): p. 201-203.

47. Auerbach, S.M., K.A. Carrado, and P.K. Dutta, Handbook of zeolite science and technology. 2003, New York: M. Dekker.

48. Nakata, K., et al., UV/Thermally Driven Rewritable Wettability Patterns on TiO_2−PDMS Composite Films. ACS Appl. Mater. Interfaces, 2010. 2(9): p. 2485-2488.

49. Wang, R., et al., Photogeneration of Highly Amphiphilic TiO_2 Surfaces. Adv. Mater., 1998. 10(2): p. 135-138.

50. Nosrati, R., A. Olad, and K. Nofouzi, A self-cleaning coating based on commercial grade polyacrylic latex modified by TiO_2/Ag-exchanged-zeolite-A nanocomposite. Appl. Surf. Sci., 2015. 346(0): p. 543-553.

51. Carneiro, C., et al., Nanocomposite acrylic paint with self-cleaning action. J. Coat. Technol. Res., 2012. 9(6): p. 687-693.

52. Dong, H., et al., High-flux reverse osmosis membranes incorporated with NaY zeolite nanoparticles for brackish water desalination. J. Membr. Sci., 2015. 476(0): p. 373-383.

53. Liao, C., et al., Preparation and characterization of NaY/PVDF hybrid ultrafiltration membranes containing silver ions as antibacterial materials. Desalination, 2011. 272(1–3): p. 59-65.

54. Lu, M. and P. Pichat, Photocatalysis and water purification: from fundamentals to recent applications. 2013: John Wiley & Sons.

55. Ryu, S.Y., et al., Photocatalytic Production of Hydrogen from Water with Visible Light Using Hybrid Catalysts of CdS Attached to Microporous and Mesoporous Silicas. J. Phys. Chem. C, 2007. 111(49): p. 18195-18203.

56. Martins, P.M., et al., Improving Photocatalytic Performance and Recyclability by Development of Er-Doped and Er/Pr-Codoped TiO_2/Poly(vinylidene difluoride)–Trifluoroethylene Composite Membranes. The Journal of Physical Chemistry C, 2014. 118(48): p. 27944-27953.

57. Martins, P.M., et al., Comparative efficiency of TiO_2 nanoparticles in suspension vs. immobilization into P(VDF-TrFE) porous membranes. RSC Advances, 2016. 6(15): p. 12708-12716.

58. dos Santos, T.C., et al., Assessment of the breakdown products of solar/UV induced photolytic degradation of food dye tartrazine. Food and Chemical Toxicology, 2014. 68: p. 307-315.

59. Tanaka, K., K. Padermpole, and T. Hisanaga, Photocatalytic degradation of commercial azo dyes. Water Research, 2000. 34(1): p. 327-333.

60. Chekir, N., et al., A comparative study of tartrazine degradation using UV and solar fixed bed reactors. International Journal of Hydrogen Energy, 2017. 42(13): p. 8948-8954.

61. Jamil, T.S. and S.E.A. Sharaf El-Deen, Removal of persistent tartrazine dye by photodegradation on TiO_2 nanoparticles enhanced by immobilized calcinated sewage sludge under visible light. Separation Science and Technology, 2016. 51(10): p. 1744-1756.

62. Andriantsiferana, C., E.F. Mohamed, and H. Delmas, Photocatalytic degradation of an azo-dye on TiO_2/activated carbon composite material. Environmental Technology, 2014. 35(3): p. 355-363.

63. Ahmed, S., et al., Influence of parameters on the heterogeneous photocatalytic degradation of pesticides and phenolic contaminants in wastewater: A short review. Journal of Environmental Management, 2011. 92(3): p. 311-330.

64. Heredia, C.L., d.L. Sham, and l.M. Farfán-Torres, Tartrazine degradation by supported TiO_2 on magnetic particles. Matéria (Rio de Janeiro), 2015. 20: p. 668-675.

65. Hoffmann, M.R., et al., Environmental Applications of Semiconductor Photocatalysis. Chemical Reviews, 1995. 95(1): p. 69-96.

66. Yang, L.-Y., et al., Microwave-assisted preparation, characterization and photocatalytic properties of a dumbbell-shaped ZnO photocatalyst. Journal of Hazardous Materials, 2010. 179(1–3): p. 438-443.

67. Amiri, H., B. Ayati, and H. Ganjidoust, Mass transfer phenomenon in photocatalytic cascade disc reactor: Effects of artificial roughness and flow rate. Chemical Engineering and Processing: Process Intensification, 2017. 116(Supplement C): p. 48-59.

68. Teixeira, S., et al., Reusability of photocatalytic TiO_2 and ZnO nanoparticles immobilized in poly(vinylidene difluoride)-co-trifluoroethylene. Applied Surface Science, 2016. 384: p. 497-504.

69. Snyder, A., et al., Reusable photocatalytic titanium dioxide–cellulose nanofiber films. Journal of Colloid and Interface Science, 2013. 399: p. 92-98.

70. Harifi, T. and M. Montazer, A novel magnetic reusable nanocomposite with enhanced photocatalytic activities for dye degradation. Separation and Purification Technology, 2014. 134: p. 210-219.

71. Pant, H.R., et al., Photocatalytic TiO_2–RGO/nylon-6 spider-wave-like nano-nets via electrospinning and hydrothermal treatment. Journal of Membrane Science, 2013. 429: p. 225-234.

72. Huertas, R.M., et al., Sol-gel membrane modification for enhanced photocatalytic activity. Separation and Purification Technology, 2017. 180: p. 69-81.

73. Goei, R., Z. Dong, and T.-T. Lim, High-permeability pluronic-based TiO_2 hybrid photocatalytic membrane with hierarchical porosity: Fabrication, characterizations and performances. Chemical Engineering Journal, 2013. 228: p. 1030-1039.

74. Shan, A.Y., T.I.M. Ghazi, and S.A. Rashid, Immobilisation of titanium dioxide onto supporting materials in heterogeneous photocatalysis: A review. Applied Catalysis A: General, 2010. 389(1–2): p. 1-8.

75. Gurkan, Y.Y., E. Kasapbasi, and Z. Cinar, Enhanced solar photocatalytic activity of TiO_2 by selenium(IV) ion-doping: Characterization and DFT modeling of the surface. Chemical Engineering Journal, 2013. 214: p. 34-44.

76. Zhang, T., et al., Hollow TiO_2 containing multilayer nanofibers with enhanced photocatalytic activity. Polymer, 2008. 49(12): p. 2898-2902.

77. Cossich, E., et al., Development of electrospun photocatalytic TiO_2-polyamide-12 nanocomposites. Materials Chemistry and Physics, 2015. 164: p. 91-97.

78. He, T., et al., Preparation and photocatalysis of TiO_2–fluoropolymer electrospun fiber nanocomposites. Polymer, 2009. 50(13): p. 3031-3036.

3. Erbium-doped and Erbium/Praseodymium codoped TiO_2/poly(vinylidenefluoride-co-trifluoroethylene) nanocomposite membranes for photocatalysis.

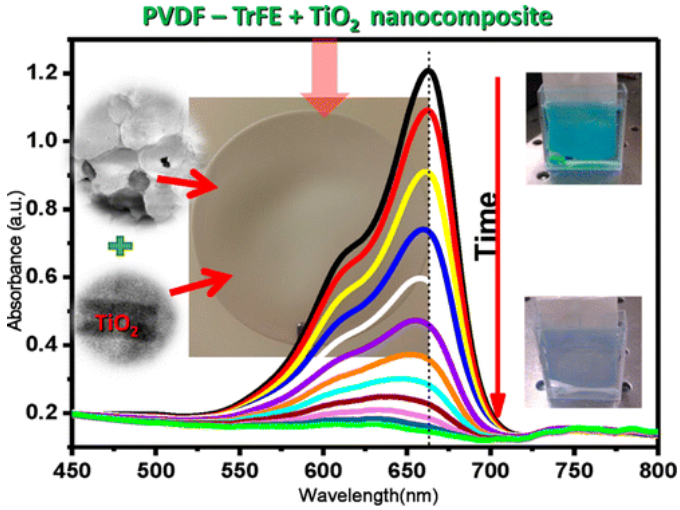

This work reports on the photocatalytic activity of rare earth metals doped (erbium – Er) and codoped (Erbium and Praseodymium – Er:Pr) TiO_2 nanoparticles immobilized in poly(vinylidenefluoride - trifluoroethylene) (PVDF-TrFE) copolymer porous membrane as a suitable strategy to overcome the reduced photocatalytic activity under visible radiation.

This chapter is based on the following publication: Martins, P.M., et al., Improving Photocatalytic Performance and Recyclability by Development of Er-Doped and Er/Pr-Codoped TiO_2/Poly(vinylidene difluoride)–Trifluoroethylene Composite Membranes. The Journal of Physical Chemistry C, 2014. **118(48)**: p. 27944-27953.

3.1. Introduction

Water pollution is becoming a serious concern and complex issue, as so many and different contaminants are released into the water environment disregarding their fate [1, 2]. Environmental concern is thus focusing on uprising micropollutants such as pharmaceuticals, personal care products, antibiotics, and pathogens, which are present in increasing amounts in the water environment [3]. Many of these chemicals are potentially harmful to human life and are unable to be treated by conventional biological processes [4]. In this sense, it is essential to develop energy efficient and sustainable methods, such as photocatalysis [5-7], to decompose or mitigate such environmental pollutants [8]. Photocatalysis has thus received considerable attention, and a variety of products and materials have been applied in water purification [9] [10]. Titanium dioxide (TiO_2) is one of the most widely used photocatalysts [11]. There are three main crystal phases of titania (anatase, brookite, and rutile) presenting different photocatalytic activities, being anatase the more interesting one for photocatalytic applications [7].

There are nevertheless some drawbacks regarding the photocatalytic applications of bare TiO_2 powders in suspension [7]. The use of TiO_2 nanoparticles with sizes from 4 to 30 nm leads to the formation of aggregates, with the consequent loss of surface area and photocatalytic efficiency [12]. Additionally, the non-porous structure of TiO_2 nanoparticles leads to lower adsorption of organics on its surface [13]. Other known drawbacks associated with the use of these catalysts are: on the one hand, the re-utilization/recycling of TiO_2 nanoparticles, which is time-consuming and requires expensive separation/filtering processes [14]. On the other hand, the recombination between photogenerated electrons and holes, which is often the largest hindrance in photocatalytic efficiency [15].

To overcome the inability to recuperate, recycle and reuse catalysts, immobilization arises as a possible solution [16], and it was already discussed in the previous chapter. In short, the immobilization implies a significant decrease in photocatalytic activity and selectivity occurs due to a substantial reduction of active surface area-to-volume ratios, plus an inefficient light harvesting related to the high content of inactive matrixes [17]. We have proposed the use of poly(vinylidene fluoride-Trifluoroethylene), P(VDF-TrFE) as a substrate to immobilize TiO_2 nanopowders, due to the already mentioned advantages of this polymer.

In this work, the focus is the reduced spectral activation of TiO_2, which is characterized by a wide band gap (3.2 eV, for anatase) and is only photocatalytically active under UV irradiation (< 387 nm) – corresponding only to 3 - 5% of the solar spectrum [18]. Large efforts are being dedicated to improving the spectral sensitivity of photocatalysts to visible light, being the main approaches by the doping of TiO_2 with metal [19, 20], nonmetal [21, 22] and rare earth metals [18, 23]. Doping TiO_2 with rare earth metals, has been reported to be one of the most efficient methods to improve photocatalytic activity. Which is related to the vacant f-orbitals of the rare earth metal ions that allow for intermediate energy states, reducing the band gap and enhancing pollutant adsorption onto the nanoparticles surface and thus enhancing the photoactivity [23, 24]. Herein, two rare-earth metals, erbium (Er) and praseodymium (Pr), were chosen as TiO_2 nanoparticles dopants, for being able to form complexes with several molecules, such as thiols, alcohols, amines and aldehydes via functional groups and f-orbitals. Thus, the transitions of 4f electrons of Er^{3+}/Pr^{3+}, the enhanced adsorption and the redshift of the absorption edge, together with the inhibition of the increase of the TiO_2 crystallite size justifies the dopants selection [25, 26]. Furthermore, co-doping is also a practical approach to improve the photocatalytic activity of the catalyst due to the synergetic action of the doping species [27, 28].

Up to our best knowledge, there are no photocatalytic nanocomposites produced with PVDF-TrFE and TiO_2 doped (Er) or codoped (Er/Pr) nanoparticles. This work allows tackling the drawbacks above of photocatalytic systems towards an improved photocatalytic activity: immobilization for proper recycling and improved photocatalytic performance.

3.2. Experimental

3.2.1. Microwave-assisted synthesis of doped TiO2 nanoparticles

Pristine, doped (Erbium (Er)) and codoped (Er and Praseodymium (Pr)) TiO_2 nanoparticles were prepared according to the microwave-assisted method [23]. In short, 2 mL titanium (IV) isopropoxide (Sigma–Aldrich, 97%) and 30 mL of absolute ethanol (Panreac, analytical grade) were mixed under magnetic stirring after which 3 mL of acetic acid (Panreac) were added. Different amounts of Erbium (III) nitrate pentahydrate

(Sigma-Aldrich) was then added to obtain Er/TiO_2 atomic ratios of 0.005, 0.01 and 0.03 (respectively 0.5, 1 and 3 % of Er). Similarly, the codoped TiO_2 nanoparticles were produced adding praseodymium (III) nitrate hexahydrate (Sigma–Aldrich) and erbium (III) nitrate pentahydrate, both with 0.005 atomic ratios (0.5/0.5% Er/Pr). After 5 minutes under magnetic stirring, 5 mL of deionized water was added and finally the mixture was poured into a Teflon lined steel autoclave that was then sealed and heated up in a microwave oven for 15 minutes at 120 °C. After synthesized, the nanoparticle suspension was centrifuged at 9000 rpm, the supernatant discarded and the nanoparticles re-suspended in ethanol under 3 minutes sonication. This procedure was repeated twice before the particles were finally dried overnight in an oven at 80 ºC.

3.2.2. Er-TiO_2/PVDF-TrFE and Er:Pr-TiO_2/PVDF-TrFE nanocomposite production

Poly(vinylidenefluoride-co-trifluoroethylene), P(VDF-TrFE) (Solvay 70:30) composite membranes with 5 % wt. of the synthesized nanoparticles were prepared by solvent casting as described in section 2.2.2. of the previous chapter.

3.2.3. Nanoparticle and membranes characterization

The crystal structure, purity, and degree of crystallinity of the nanoparticles was evaluated by XRD (as described in the previous chapter, 2.2.3). Size and crystalline structure of nanoparticles were also analyzed by transmission electron microscopy, TEM (Tecnai T20). Moreover, the porosity of the as-synthesized nanoparticles was measured by nitrogen adsorption at 77 K in a Micromeritics TriStar analyzer (Micromeritics, Norcross GA). Samples (0.5 g) were outgassed at 26.7 Pa and 350 ◦C for 6 h before performing the adsorption experiments. Surface area was determined using the Brunauer–Emmett–Teller (BET) equation [29]. Pore size distribution was determined using the Barrett-Joyner-Halenda (BJH) data reduction scheme in the desorption branch of the isotherms [30].
The optical properties of the nanoparticle powder were measured by UV–vis absorption spectroscopy with a Jasco V-670 spectrophotometer coupled with a solid sampling system (integrating sphere). To estimate the indirect band gap, the spectra were obtained

in reflectance (R) mode and the absorbance calculated through the Kubelka-Munk Eq. (3.1):

$$F(R) = \frac{(1-R_\infty)^2}{2R_\infty} \quad (3.1)$$

where R∞ (=Rsample/RBaSo4) is the reflectance of the sample and F(R) the absorbance. The average hydrodynamic diameters and zeta potentials of the nanoparticles were measured using the Zetasizer NANO ZS-ZEN3600, Malvern (Malvern Instruments Limited, UK), equipped with a He–Ne laser (wavelength 633 nm) and a detection angle of 173° (backscatter detection). Measurements were performed at 25 °C using the appropriate sample dilution in ultra-pure water to hinder multiscattering events. Zetasizer 6.20 software was used to estimate particle mean diameters from the intensity-weighted distributions (Zeta-average), the polydispersity index (PDI) and Zeta-potentials values.
The porosity of the nanocomposite membranes was estimated with a pycnometer (2), according to the method described in 2.2.3.
The morphology and chemical stability of the TiO_2/PVDF-TrFE samples were evaluated by SEM and FTIR, respectively (according to the characterization performed in 2.2.3).

3.2.4. Photocatalytic activity

Photocatalytic oxidation of MB solution by the doped and codoped TiO_2/PVDF-TrFE nanocomposite membranes under UV irradiation was recurred to evaluate the photocatalytic activity of the membranes with different nanoparticle types (TiO_2:Er 0.5%; TiO_2:Er 1%; TiO_2:Er:Pr 0.5/0.5%)
The membranes were first immersed in the MB aqueous solution for 30 min in the dark, to ensure complete adsorption of the dye. Later, a 3 cm^2 sample of photocatalytic TiO_2/PVDF-TrFE nanocomposite was immersed in the MB solution (10^{-5} M) placed in a quartz cell (40mm × 40mm × 10 mm) at pH 6.8. The quartz cell was then irradiated with a high power LED source (Thorlabs, 700 mA) with an excitation peak at 365 nm (UV-A). The incident radiation over the sample was measured with a lux meter, and the average values were around 4mW·cm^{-2} [31].
The absorbance of the MB was monitored at intervals of 3 min using a spectrophotometer (ScanSpecUV-Vis, ScanSci) in the range of 300–900 nm. The rate of photodegradation

of MB was analyzed by monitoring the intensity variation of the main absorption peak at 663 nm.

The MB degradation in aqueous solution fits to a pseudo-first-order reaction, Langmuir–Hinshelwood model, which can be expressed by Eq. 2.3 (previous chapter) [32].

3.3. Results and discussion

3.3.1. Nanoparticle characterization

The pristine, doped and codoped TiO_2 nanoparticles produced by a microwave-assisted method were analyzed by TEM. The images in Figure 3.1 allowed to estimate of a particle size of ≈ 10 nm (from a statistics of 100 nanoparticles in each micrograph), with a polyhedral shape for all pristine, Er-doped (0.5; 1 and 3%) and codoped Er:Pr-TiO_2 nanoparticles.

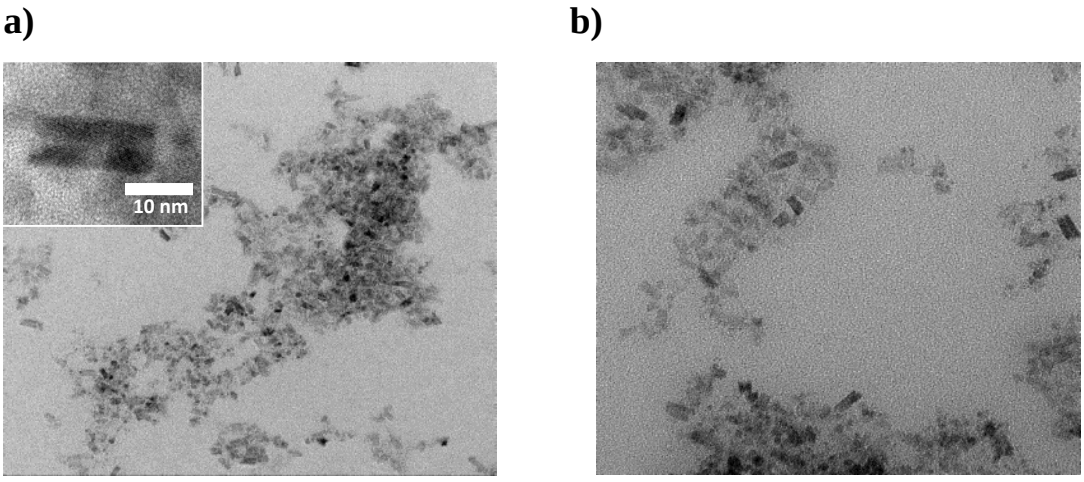

Figure 3.1. TEM micrographs of (a) pristine TiO_2 nanoparticles and inset a single nanoparticle; (b) Er3%-TiO_2 nanoparticles.

According to the TEM images, the doping or co-doping did not significantly change the nanoparticle size or morphology.

The degree of crystallinity, crystal structure, and purity of the nanoparticles was studied by X-ray diffraction (XRD). The XRD diffraction patterns of pristine TiO_2, doped Er0.5%-TiO_2; Er1%-TiO_2; Er3%-TiO_2 and codoped Er:Pr 0.5:0.5%-TiO_2 samples are shown in Figure 3.2 All the analyzed samples showed diffraction peaks at 25.3, 37.8, 48.0, 53.9, 55.1, and 62.7°, which are ascribed to the characteristic titania anatase

crystalline structure (JCPDS N 2000), the more reactive polymorph of TiO_2. There is not much difference in the intensity and position of the diffraction peaks amongst the pristine, doped or codoped samples. Interestingly, no diffraction peaks for Er or Pr species were detected, which is ascribed to the low dopant loading and crystal size below the detection limit of the technique.

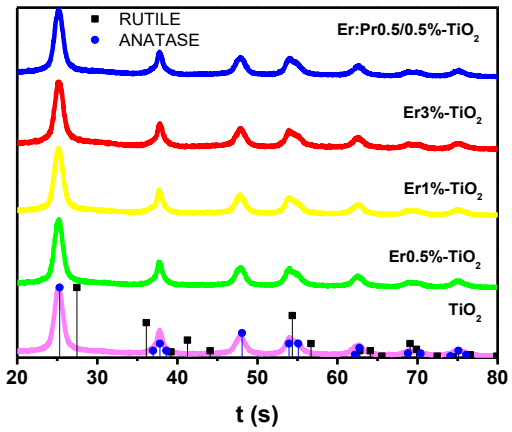

Figure 3.2. XRD patterns of (a) TiO_2; (b) Er 0.5%-TiO_2; (c) Er 1%-TiO_2; (d) Er 3%-TiO_2. Main diffraction lines for anatase (blue dots) and rutile (black squares) phases are indicated.

The crystal size was estimated from the XRD diffractograms by monitoring the (101) diffraction peak and applying the Scherrer Eq. 3.2:

$$D = \frac{0.89\lambda}{\beta \cos\theta} \qquad (3.2)$$

where D corresponds to the crystal size, λ is the wavelength of the incident X-ray radiation (CuKα; λ=0.154056 nm), θ is the diffraction angle, and β is the full width at half-maximum [33]. The estimated average size values (listed in Table 3.1) agree with the ones estimated from the TEM images: pristine TiO_2 nanoparticles show a higher crystal size (≅ 7.0 nm) than the doped (6.4; 6.5 and 6.3 nm) and codoped (6.42 nm) samples.

In spite of small differences between the produced nanoparticles, the results indicate that the higher the amount of dopant smaller is the nanoparticle, which is in agreement with previous reports addressing such trend to the hindrance on the growth of titanium dioxide crystallites imposed by the dopant [34, 35].

The as-synthesized nanoparticles show a hydrodynamic diameter ranging from 13 to 28 nm (Figure 3.3) and average PDI values from 0.32 to 0.21, as measured by DLS (Table 3.1).

All the samples show similar diameters, supporting the reproducibility of the microwave assisted method for TiO_2 nanoparticle synthesis [23].

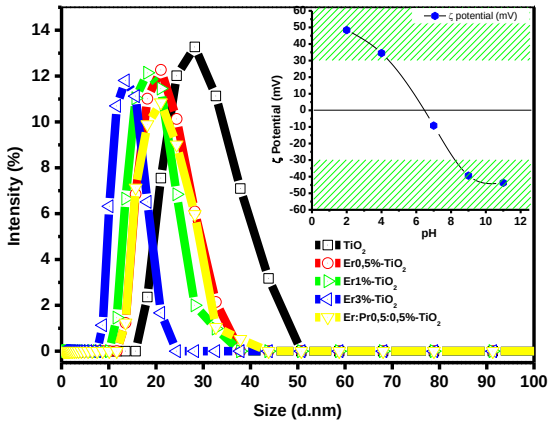

Figure 3.3. Dynamic light scattering (DLS) of Er0.5%-TiO_2, Er1%-TiO_2, Er3%-TiO_2 and Er:Pr/0.5:0.5%-TiO_2 nanoparticles at room temperature; inset room temperature zeta (ζ)- potential of synthesized Er3%/TiO_2 nanoparticles at pH =2; 4; 7; 9; 11.

It should be noted that the sizes estimated by TEM images (ranging from 10 to 18 nm, for pristine TiO_2 and doped/codoped nanoparticles) and calculated from the XRD diffractograms indicate smaller nanoparticles, which is explained by nanoparticles agglomeration in the aqueous media. Agglomerated nanoparticles show a lower diffusion rate than isolated particles. The diameter obtained by DLS is higher than the size of the nanoparticles when assessed by other techniques [36]. However, it is noticeable that XRD and DLS data present a similar trend (despite the significant standard deviation associated with DLS measurements). As for XRD calculated sizes, the pristine nanoparticles also show higher sizes than the doped ones and the size of the particle also diminishes with increasing the amount of dopant (0.5% > 1% > 3 %), supporting the interpretation of doping hindering TiO_2 crystal growth. Concerning the codoped sample, the size is similar to the Er0.5%/TiO_2 indicating that dopant content is more relevant than dopant type in determining nanoparticle size.

Table 3.1. Nanoparticle sizes, estimated by Scherrer equation and size intensity by DLS backscattering (173 º) at 25 ºC.

Sample	XRD	DLS	
	Crystallite size (nm)*	Size (d.nm)	PDI
TiO_2	7	28±5	0.32±0.01
Er0.5%-TiO_2	6.5	21±3	0.35±0.03
Er1%-TiO_2	6.4	18±6	0.31±0.04
Er3%-TiO_2	6.3	13±4	0.21±0.01
Er:Pr0.5:0.5%-TiO_2	6.4	21±5	0.28±0.04

Regarding the zeta potential (ζ) data (inset in Figure 3.3), the produced nanoparticles are more stable at pH above 8 or below 4, in which the zeta potential values are below -30 and above +30, respectively. Within the mentioned zeta potential range, the peripheral charge values of nanoparticles are higher, contributing to nanoparticles repulsion and thus larger stability, avoiding aggregation and precipitation. Additionally, the results are consistent with the literature [37], which indicates that at pH= 6.8 the TiO_2 net charge is 0, at pH < 6.8 TiO_2 is positively charged and at pH > 6.8 TiO_2 is negatively charged. Noticeably, pristine, doped and codoped TiO_2 nanoparticles do not show a different zeta potential behavior, which is attributed to the similar charge of the ionic species involved Ti^{4+}, Er^{3+}, and Pr^{3+}. Zeta potential measurements are relevant for the intended applications as the adsorption of molecules is pH dependent [38,39]: if TiO_2 nanoparticles and the pollutant/dye exhibit opposite charges they will attract each other, promoting the adsorption and enhanced photoactivity.

The specific surface area is one of the most important properties concerning photocatalytic activity, as photocatalytic reactions occur on the surface of the nanocatalyst [27]. In this sense, when surface area increases, the number of active sites increases proportionally and therefore a high surface area of the nanocatalyst is required for photocatalytic purposes. Table 3.2 shows that high specific surface areas are obtained for all nanoparticles. Several works reporting on different methods to produce pristine and doped TiO_2 nanoparticles present surface areas below 200 m^2/g [23]. In this work, the microwave assisted method enables the production of bare TiO_2 nanoparticles with larger surface areas: 239 m^2/g.

Table 3.2. Dopant content, BET surface area and BJH of pore size for all the produced nanoparticles.

Sample	Dopant content (real)	Nitrogen adsorption	Pore Size
	(mg)	BET Surface area (m^2/g)	BJH (nm)
TiO_2	-	239	3.8
Er0.5%-TiO_2	14.7	164	3.6
Er1%-TiO_2	29.4	159	4.8
Er3%-TiO_2	88.2	127	5.6
Er:Pr0.5:0.5%-TiO_2	14.7:14.7	273	2.8

Low dopant loadings have the benefit of increasing largely the surface area of the as-synthesized TiO_2 nanoparticles. This probably occurs due to the change in the anatase structure, caused by the substitution of Ti^{4+} for a larger ionic radius (Er^{3+} or Pr^{3+}). However, the Er-doped nanoparticles show a smaller surface area than the as-synthesized pristine or Er/Pr-codoped TiO_2 nanoparticles. A plausible explanation may be assigned to the high ionic radius of Er^{3+}, which blocks some of the TiO_2 pores yielding a surface area reduction. These results are different from reports on similar particles using different dopants [23, 40]. Although, it is worthy of notice that, in the latter case, the method used by those authors for nanoparticle synthesis is different and the microwave-assisted method, used in the present work, is tailored to optimize the surface area of the pure TiO_2 nanoparticles. Nevertheless, the surface area of the 0.5 (164 m^2/g); 1 (159 m^2/g) and 3% (127m^2/g) Er doped nanoparticles is higher than that of commercial P25® TiO_2 nanoparticles (50 m^2/g) [41].

Regarding pore size distribution, determined using the BJH data reduction scheme, the results indicate values of 2.8, 3.6, 4.8 and 5.6 nm for Pr0.5/Er0.5% -TiO_2, Er0.5%-TiO_2, Er1%-TiO_2 and Er3%-TiO_2 respectively, resulting in a significant modification of the surface area of TiO_2 nanoparticles depending on the dopant loading, as reported by other authors in the literature for cerium and neodymium doping [42, 43]. Additionally, such results are in good agreement with the BET surface area results above, as lower pore sizes contribute the higher surface area.

The as-produced powder was analyzed by UV-vis absorption spectroscopy. The bare TiO_2 nanoparticles revealed low light absorbance in the visible region (Figure 3.4.a) related to the low band gap (3.11eV). Conversely, the doped and codoped samples revealed absorption peaks in the visible region. The three characteristic Er peaks located

at 490, 523 and 654 nm correspond to the transitions from $^4I_{15/2}$ to $^4F_{7/2}$, $^2H_{11/2}$ and $^4F_{9/2}$, respectively [26]. Particularly, the 4f electron transitions on Er^{3+} promotes the separation of photogenerated electron-hole pairs, which in turn yield a higher photocatalytic activity of the catalyst.

Concerning the Pr absorption peaks, the results show a spectral band from 400 to 500 nm, associated with the f→f transition, and an absorption peak at 600 nm due to the $^1D_2 \rightarrow {}^3H_4$ transition [44]. Furthermore, the peaks intensity, namely the 523 and 654 nm peaks - assigned to Er - are also proportional to the dopant concentration used (Figure 3.4.b).

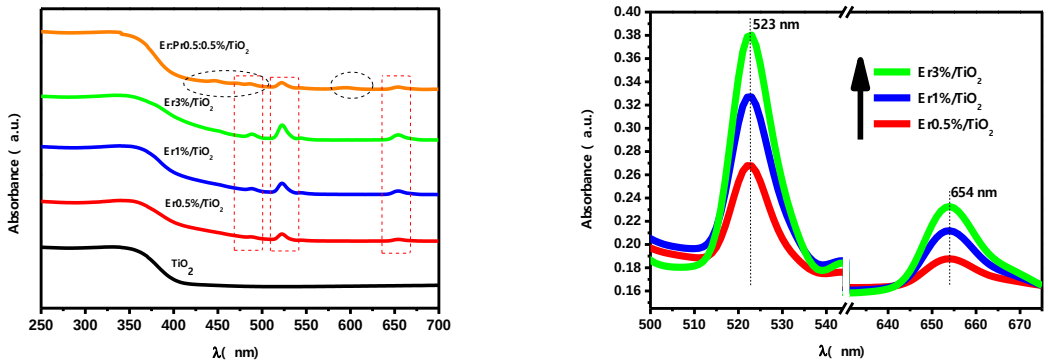

Figure 3.4. a) UV–visible spectra for TiO_2 and Er-doped and Er:Pr-TiO_2 samples. Dotted Red rectangles and black circles identify the absorbance peaks in the visible region of Erbium (Er^{3+}) and Praseodymium (Pr^{3+}), respectively; b) Absorption peaks for TiO_2 doped with Er at different concentrations.

Beyond the aforementioned peaks in the visible spectrum, the doped and codoped samples show a red-shift (towards visible region) near the UV to visible transition (around 400 nm) (Figure 3.5). This results show that the Er and Pr rare earth metals dopants modified the overall absorption spectra of the NP allowing absorbance enhancement in the visible region and therefore an enhanced photocatalytic performance of the doped and codoped TiO_2 nanoparticles when irradiated with visible light [25]. It is to notice that similar results have been obtained with Fe^{3+} doped TiO_2 [45], silver and nitrogen [46] and cerium and neodymium co-doping [34].

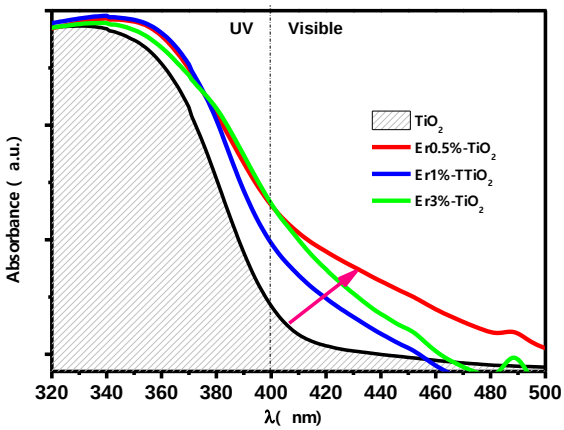

Figure 3.5. UV–vis spectra for the TiO_2 (a), TiO_2/Er0,5% (d), TiO_2/Er1% (b) and TiO_2/Er 3% (c) samples in the transition of UV to visible radiation range.

The indirect band gap was determined from the Kubelka-Munk equation by plotting $[F(R)h\upsilon]^{1/2}$ *vs.* hv (Figure 3.6) [47].

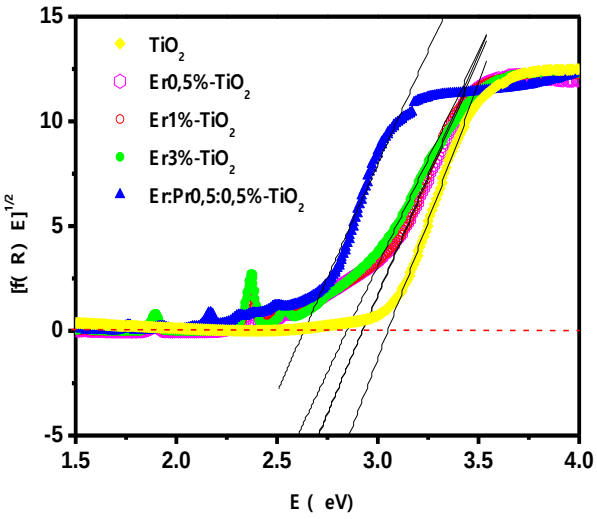

Figure 3.6. Determination of band gap of pristine TiO_2, Er doped and Er/Pr codoped TiO_2 nanoparticles at [F(R)]1/2 = 0.

All the doped and codoped samples present lower band gap values than the pristine TiO_2 nanoparticles (3.05 eV); the Er doped particles are showing similar band gaps 2.92 eV for the 0.5%Er and 1%Er and 2.85 eV for the 3%Er. As previously reported [23, 48], a significant reduction of the band gap values is observed with increasing amounts of dopant in the samples, in agreement with the obtained results. The band gap reduction is

related to the red-shift observed in Er-doped samples as compared to absorbance limit of pristine TiO_2 in the visible region as mentioned

Table 3.3. Band gap values for all the produced nanoparticles at [F(R)]1/2 = 0.

Sample	Bandgap (eV)
TiO_2	3.05
Er0,5%-TiO_2	2.92
Er1%-TiO_2	2.92
Er3%-TiO_2	2.85
Er:Pr/0.5:0.5%-TiO_2	2.63

Noticeably, through the microwave assisted technique, even the as-produced pristine TiO_2 nanoparticles show lower band gap values than Evonik P25 nanoparticles (Eg = 3.2 eV) (Table 3.3) [24].

It is interesting to note that the co-doping with two rare earth metals (Er and Pr) resulted in a further reduction of bandgap values (Eg = 2.63 eV), supporting the synergetic effect of the two dopants in the band gap reduction. The presented results suggest the presence of intermediate states between the valence band and the conduction band due to the presence of the dopant species [18, 49].

3.3.2. Nanocomposites characterization

Nanocomposite membranes of PVDF-TrFE incorporating TiO_2 nanoparticles were produced by solvent evaporation at room temperature from a homogeneous solution in DMF. SEM surface and cross-section images (Figure 3.7) show the polymer microstructure of the Er0.5%/TiO_2/PVDF-TrFE sample. The pore size distribution is shown in the inset of Figure 3.7 b), where it can be observed in pore sizes between 30 and 110 µm, with prevalence in the range of 50 to 80 µm. All produced nanocomposites show similar spherical pores and size, independently of the chosen nanoparticle filler. Regarding the filler nanoparticles, a good dispersion is achieved within the polymer matrix, with few nanoparticles aggregates inside inside the walls of the pores of the nanocomposite.

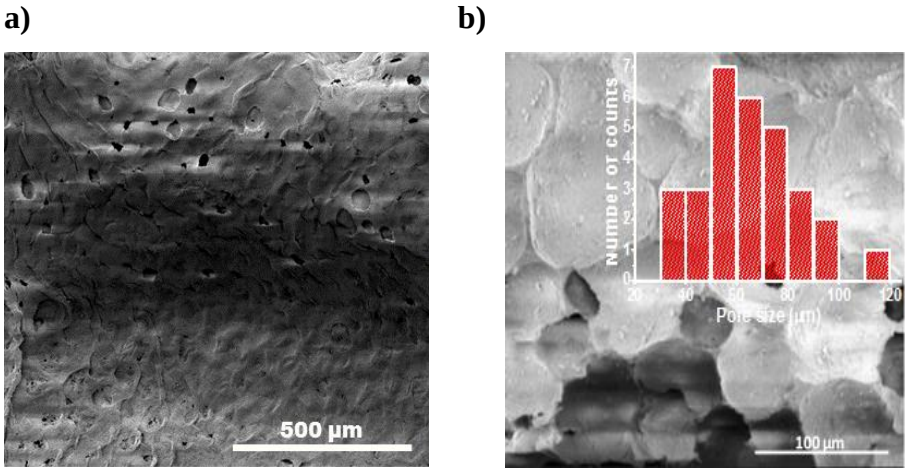

Figure 3.7. Surface a) and cross-section b) SEM images of the porous Er0.5%-TiO_2/PVDF-TrFE nanocomposite membranes.

The degree of porosity, around 74%, of the produced samples is summarized in Table 4, showing that there is no significant difference in them, being the variations within the experimental error. This data indicates that the presence of the nanoparticle filler type and content has no influence on the phase diagram and crystallization dynamic of the polymer, and is mainly governed by the polymer/solvent initial ratio and solvent evaporation temperature [50]. Additionally, the pore interconnectivity, which is an essential factor for the mass transfer across the membrane, is rendered by the spaces between the polymer microspheres that form the pore walls [50]. It has been already enlightened that a large pore channel enhances light utilization and the increase of mass transfer of reactants for photocatalysis applications [41]. These facts prove the importance of the porous structure of the polymer for the photocatalytic activity of the nanocomposite, as the efficiency depends on how they allow for a decent interaction of the dye with the TiO_2 surface, a crucial step for the photocatalysis as mentioned above. PVDF and co-polymer can appear in different phases related to different chain conformations, each with different characteristics, including polarity and piezoelectric activity [51].

Table 3.4. Degree of porosity of the nanocomposites with the pristine, doped and codoped TiO_2 nanoparticles.

Sample	**Pycnometer**
	Degree of porosity (%)
TiO_2/PVDF-(TrFE)	73 ± 6.2
Er0.5%- TiO_2/PVDF-(TrFE)	72 ± 7.5
Er1%- TiO_2/PVDF-(TrFE)	73 ± 8.0
Er3%- TiO_2/PVDF-(TrFE)	75 ± 6.1
Er:Pr0.5:0.5%- TiO_2/PVDF-(TrFE)	74 ± 5.4

The α-phase presents a non-polar structure with a TGTG' chain conformation, while the β-phase and γ-phase present a polar structure with all trans (TTT) planar zigzag and T3GT3G' chain conformation, respectively. The phase of the polymer is determined by the processing conditions of the membrane, including solution casting or melting conditions or the fillers, such as nanoparticles or clays [51].

Thus, FTIR-ATR measurements were performed for all the prepared sample composites (Figure 3.8).

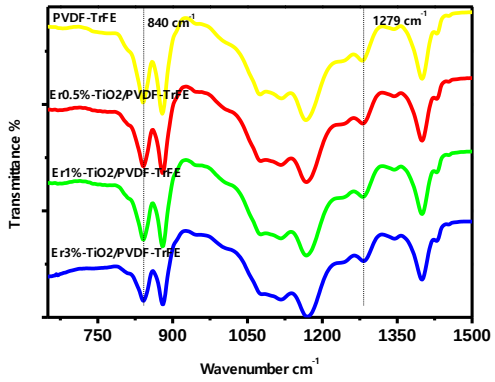

Figure 3.8. FTIR spectra of the TiO_2/PVDF-TrFE composites with TiO_2 nanoparticles with different dopant content.

The FTIR-ATR bands confirm the presence of the characteristic bands of the piezoelectric -phase of PVDF (840 and 1279 cm^{-1}) independently on the filler type and content. No trace of the non-polar α-phase, characterized, among others, by the FTIR band at 766 cm^{-1}, or any other polymorph, is found in the composites. This fact broadens the range of applicability of these membranes as the photocatalytic performance can be, hereafter, associated with the use of the membranes as sensors and actuators [51, 52].

3.3.3. Photocatalytic activity evaluation

To study the photocatalytic activity of the produced nanocomposites, the room temperature degradation of Methylene Blue (MB) in aqueous solution under UV irradiation was evaluated. These results are shown in Figure 3.9.

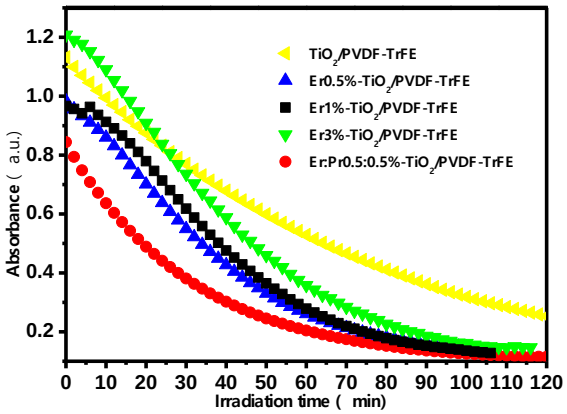

Figure 3.9. UV-vis absorption variation at 663 nm of an MB (10^{-5} M) aqueous solution as a function of time for the nanocomposite membranes.

All nanocomposites could degrade the MB molecule, as indicated by the decrease of the absorbance characteristic peak (663 nm) with increasing UV irradiation time. The initial absorbance (at t=0) is different for the tested samples due to the initial experimental conditions: samples were placed for 30 min in the MB solution in the dark without UV irradiation. Such data agree with the reported importance of the pollutants adsorption for the photocatalytic activity. Not only the dopant concentration affects the MB adsorption but also the choice of dopant [53]. In fact, the paramount role of adsorption is to overcome the fast (nano-seconds) recombination of an electron-hole pair and generally optimum adsorption results in enhanced photocatalytic activity. Moreover, for better adsorption of the substances to the catalyst surface (where photocatalysis take place), an improved interfacial charge transfer occurs [24, 53]. Hence, the data indicates that the codoped Er:Pr 0,5:0,5%/TiO_2/PVDF-TrFE nanocomposite is more efficient in adsorbing MB at the surface of the nanoparticles than the other samples, as it will be discussed later. Some works show the relevance of adsorption for the photocatalysis using rare earth elements

as dopants, sustaining that adsorption is deeply committed to the type of dopant for specific molecules [38, 54, 55]

The results depicted in Figure 3.9 show that the nanocomposites with incorporated doped or codoped nanoparticles present enhanced photocatalytic activities when compared to the nanocomposite containing the bare TiO_2 nanocatalyst. The pure PVDF-TrFE membrane was also tested and did not reveal any photocatalytic activity (results not shown). The obtained results correlated with the enhanced BET surface area of the doped and codoped nanoparticles concerning the pristine ones, and to the adsorption rates of MB to the TiO_2 nanoparticle surface. The three nanocomposites containing Er-doped nanoparticles show slightly similar photocatalytic performance, although it is apparent that the sample with the higher amount of Er (3%) has a lower reaction rate and degradation efficiency of MB after 100 min (Table 3.5), when compared to the ones with lower Er concentration (0.5 and 1%).

Table 3.5. First-order rate constant (k) and degradation level of the MB aqueous solution (10^{-5} M, pH 6.8) for all the produced nanocomposites.

Sample	Reaction rate (min^{-1})	Degradation (%) of MB solution after 100 min
TiO_2/PVDF-TrFE	0.012	81
Er0.5%-TiO_2/PVDF-TrFE	0.023	96
Er1%-TiO_2/PVDF-TrFE	0.023	97
Er3%-TiO_2/PVDF-TrFE	0.021	95
Er:Pr0.5:0.5%-TiO_2/PVDF-TrFE	0.023	98

This can be ascribed to the existence of an optimum amount of dopant; larger amounts lead to an increase of intermediate states in the band gap, which inevitably acts as recombination centers and thus decreases of the photocatalytic efficiency of the TiO_2 nanoparticles. Similar findings have been reported for the Ag-doping when exceeding 0.25 mol% covers the surface of TiO_2, decreasing the amount of photogenerated charge carriers and reducing photocatalytic activity [56]. Similarly, a high dopant level of selenium diminishes the photocatalytic activity of the catalyst [18]. This fact is attributed to the increase of the recombination rate of the charge carriers due to a decrease in the average distance between trap sites caused by an increasing amount of dopant in a single particle [57].

Additionally, from the tested nanocomposites, the codoped sample reveals a higher adsorption rate at t=0, a high reaction rate (k= 0.023 min^{-1}) and the highest BET surface area (273 m^2/g). Moreover, in 100 minutes under UV irradiation, the MB degradation is approximately 98%, which represents the highest degradation value among the tested samples. These results correlated well with those from the presented surface area data, indicating that the codoped sample possesses the highest value of trapping sites, promoting high adsorption rate and photocatalytic activity. These results are consistent with other works employing B and N codoped nanoparticles in MB photocatalysis [58] and support the synergetic effect of co-doping in the photocatalytic performance. Moreover, considering the reports on photocatalyst activity in suspension, it is worthy of notice that the photocatalytic performance herein reported in immobilized systems is comparable to systems employing nano/microparticles in suspension [23], representing a further step for photocatalytic applications due to the simpler removing and recycling. This efficiency is also profoundly related to the nanocomposite microstructure with degrees of porosity ranging from 72 to 75% and the macroporous structure of the polymer that enables a good mass transfer, promoting interaction between the MB and the porous inside wall loaded with nanoparticles and a proper light harvesting, suitable for photocatalysis.

Figure 10 shows the evolution of the absorbance spectra during 110 minutes at 10 min steps for the Er3%-TiO_2/PVDF-TrFE sample, indicating that the degradation of MB occurs with a small peak shift to values below the monitored 663 nm peak.

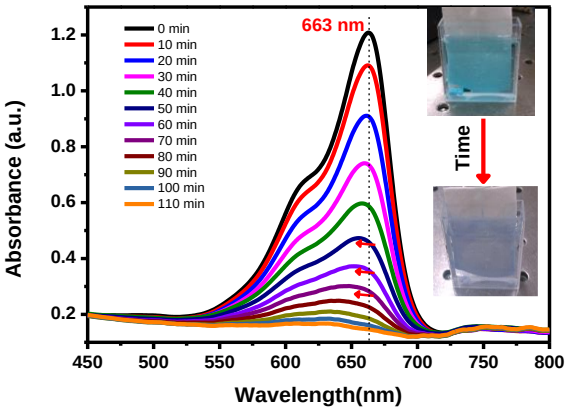

Figure 3.10. Degradation of 10^{-5} M of methylene blue in aqueous solution by Er3%-TiO_2/PVDF-TrFE nanocomposites.

This shift is perhaps associated with N-demethylation of MB by TiO_2 nanoparticles or the formation of N-demethylated intermediates [59]. Additionally, there are no MB byproduct peaks that interfere with the photocatalytic activity probes at 663 nm. Moreover, it is observed that the MB solution has become colorless after 90 minutes of irradiation. All the tested nanocomposites present similar spectra during the irradiation time and similar transparency at the end of the assays.

3.4. Conclusions

Doped and codoped nanoparticles (≈10 nm in size) were synthesized and proved to enable a crystallite size reduction, enhanced adsorption rate of MB to the photocatalyst, separation of the electron-hole pair and a red-shift in the absorbance spectra, which allows a visible light utilization. Afterward, novel photocatalytic nanocomposites with controlled porous microstructure were also successfully produced. From all the tested nanocomposites, the one with codoped Er-Pr nanoparticles showed the highest photocatalytic activity in the degradation of MB. These results can be ascribed to a favorable combination of physical-chemical properties of the nanoparticles, such as high adsorption rate of MB by the dopants (Er and Pr) in the catalyst surface, the high surface area (273 m^2/g) and the effective prevention of the electron-hole pair recombination promoted by the dopant species. Furthermore, the polymer membrane also plays a crucial role in the efficient photocatalytic performance, allowing for a highly porous structure (74%) and macropore architecture, suitable for a good radiation harvesting and interaction between the MB solution and the immobilized nanoparticles in the inside wall of the pores. The proposed system proved to be suitable for photocatalytic applications, as it allows to overcome the major hindrances of the suspension systems (recuperation and visible light utilization). Regardless the catalyst immobilization, the photocatalytic activity of the nanocomposites, in the MB degradation, exhibit remarkable reaction rates, close to the values presented for suspension system.

3.5. References

1. Muñoz, I., et al., Ranking potential impacts of priority and emerging pollutants in urban wastewater through life cycle impact assessment. Chemosphere, 2008. 74(1): p. 37-44.

2. Park, H., et al., Surface modification of TiO_2 photocatalyst for environmental applications. J. Photochem. Photobiol. C, 2013. 15(0): p. 1-20.

3. Schwarzenbach, R.P., et al., The challenge of micropollutants in aquatic systems. Science, 2006. 313(5790): p. 1072-7.

4. Kanki, T., et al., Water purification in a fluidized bed photocatalytic reactor using TiO_2-coated ceramic particles. Chem. Eng. J., 2005. 108(1–2): p. 155-160.

5. Britto, J.M. and M.d.C. Rangel, Processos avançados de oxidação de compostos fenólicos em efluentes industriais. Quim. Nova, 2008. 31: p. 114-122.

6. Gültekin, I. and N.H. Ince, Synthetic endocrine disruptors in the environment and water remediation by advanced oxidation processes. J. Environ. Manage., 2007. 85(4): p. 816-832.

7. Hoffmann, M.R., et al., Environmental Applications of Semiconductor Photocatalysis. Chem. Rev., 1995. 95(1): p. 69-96.

8. Liu, N., et al., A review on TiO_2-based nanotubes synthesized via hydrothermal method: Formation mechanism, structure modification, and photocatalytic applications. Catal. Today, 2014. 225(0): p. 34-51.

9. Ochiai, T. and A. Fujishima, Photoelectrochemical properties of TiO_2 photocatalyst and its applications for environmental purification. J. Photochem. Photobiol. C, 2012. 13(4): p. 247-262.

10. Tryba, B., A.W. Morawski, and M. Inagaki, A new route for preparation of TiO_2-mounted activated carbon. Appl. Catal. B, 2003. 46(1): p. 203-208.

11. Fujishima, A., T.N. Rao, and D.A. Tryk, TiO_2 photocatalysts and diamond electrodes. Electrochim. Acta, 2000. 45(28): p. 4683-4690.

12. Bhattacharyya, A., S. Kawi, and M.B. Ray, Photocatalytic degradation of orange II by TiO_2 catalysts supported on adsorbents. Catal. Today, 2004. 98(3): p. 431-439.

13. Lepore, G.P., L. Persaud, and C.H. Langford, Supporting titanium dioxide photocatalysts on silica gel and hydrophobically modified silica gel. J. Photochem. Photobiol. A, 1996. 98(1–2): p. 103-111.

14. Uddin, M.N., et al., An experimental and first-principles study of the effect of B/N doping in TiO_2 thin films for visible light photo-catalysis. J. Photochem. Photobiol. A, 2013. 254(0): p. 25-34.

15. An, T.-C., X.-H. Zhu, and Y. Xiong, Feasibility study of photoelectrochemical degradation of methylene blue with three-dimensional electrode-photocatalytic reactor. Chemosphere, 2002. 46(6): p. 897-903.

16. Fernandez, J., et al., Efficient photo-assisted Fenton catalysis mediated by Fe ions on Nafion membranes active in the abatement of non-biodegradable azo-dye. Chem. Commun., 1998(14): p. 1493-1494.

17. Álvarez, P.M., et al., Preparation and characterization of magnetic TiO_2 nanoparticles and their utilization for the degradation of emerging pollutants in water. Appl. Catal. B, 2010. 100(1–2): p. 338-345.

18. Gurkan, Y.Y., E. Kasapbasi, and Z. Cinar, Enhanced solar photocatalytic activity of TiO_2 by selenium(IV) ion-doping: Characterization and DFT modeling of the surface. Chem. Eng. J., 2013. 214(0): p. 34-44.

19. Chand, R., et al., Effect of transition metal doping under reducing calcination atmosphere on photocatalytic property of TiO_2 immobilized on SiO2 beads. J. Environ. Sci., 2013. 25(7): p. 1419-1423.

20. Rosario, A.V. and E.C. Pereira, The role of Pt addition on the photocatalytic activity of TiO_2 nanoparticles: The limit between doping and metallization. Appl. Catal. B, 2014. 144(0): p. 840-845.

21. Di Valentin, C. and G. Pacchioni, Trends in non-metal doping of anatase TiO_2: B, C, N and F. Catal. Today, 2013. 206(0): p. 12-18.

22. Marschall, R. and L. Wang, Non-metal doping of transition metal oxides for visible-light photocatalysis. Catal. Today, 2014. 225(0): p. 111-135.

23. Gomez, V., et al., Microwave-assisted mild-temperature preparation of neodymium-doped titania for the improved photodegradation of water contaminants. Appl. Catal. A, 2012. 441–442(0): p. 47-53.

24. Bingham, S. and W.A. Daoud, Recent advances in making nano-sized TiO_2 visible-light active through rare-earth metal doping. J. Mater. Chem., 2011. 21(7): p. 2041-2050.

25. Liang, C., et al., The effect of Praseodymium on the adsorption and photocatalytic degradation of azo dye in aqueous Pr^{3+}-TiO_2 suspension. Chem. Eng. J., 2009. 147(2–3): p. 219-225.

26. Liang, C.-H., et al., The effect of erbium on the adsorption and photodegradation of orange I in aqueous Er^{3+}-TiO_2 suspension. J. Hazard. Mater., 2006. 138(3): p. 471-478.

27. Shen, X.-Z., et al., Degradation of nitrobenzene using titania photocatalyst co-doped with nitrogen and cerium under visible light illumination. J. Hazard. Mater., 2009. 162(2–3): p. 1193-1198.

28. Shi, H., et al., Enhancement of photocatalytic activity of nano-scale TiO_2 particles co-doped by rare earth elements and heteropolyacids. J. Colloid Interface Sci., 2012. 380(1): p. 121-127.

29. Brunauer, S., P.H. Emmett, and E. Teller, Adsorption of Gases in Multimolecular Layers. J. Am. Chem. Soc., 1938. 60(2): p. 309-319.

30. Barrett, E.P., L.G. Joyner, and P.P. Halenda, The Determination of Pore Volume and Area Distributions in Porous Substances. I. Computations from Nitrogen Isotherms. J. Am. Chem. Soc., 1951. 73(1): p. 373-380.

31. Marques, J., et al., Release of Volatile Compounds from Polymeric Microcapsules Mediated by Photocatalytic Nanoparticles. Int. J. Photoenergy, 2013. 2013: p. 9.

32. Yu, J., et al., Effects of hydrothermal temperature and time on the photocatalytic activity and microstructures of bimodal mesoporous TiO_2 powders. Appl. Catal. B, 2007. 69(3–4): p. 171-180.

33. Deng, F., et al., Preparation of conductive polypyrrole/TiO_2 nanocomposite via surface molecular imprinting technique and its photocatalytic activity under simulated solar light irradiation. Colloids Surf. A, 2012. 395(0): p. 183-189.

34. Choudhury, B., B. Borah, and A. Choudhury, Ce–Nd codoping effect on the structural and optical properties of TiO_2 nanoparticles. Mat. Sci. Eng. B, 2013. 178(4): p. 239-247.

35. Wang, C., et al., Preparation, characterization and photocatalytic activity of the neodymium-doped TiO_2 hollow spheres. Appl. Surf. Sci., 2010. 257(1): p. 227-231.

36. Bradbury, A., S. Menear, and R.W. Chantrell, A Monte Carlo calculation of the magnetic properties of a ferrofluid containing interacting polydispersed particles. J. Magn. Magn. Mater., 1986. 54–57, Part 2(0): p. 745-746.

37. Okte, A.N. and O. Yilmaz, Photodecolorization of methyl orange by yttrium incorporated TiO_2 supported ZSM-5. Appl. Catal. B, 2008. 85(1-2): p. 92-102.

38. El-Bahy, Z.M., A.A. Ismail, and R.M. Mohamed, Enhancement of titania by doping rare earth for photodegradation of organic dye (Direct Blue). J. Hazard. Mater., 2009. 166(1): p. 138-143.

39. Parida, K.M. and N. Sahu, Visible light induced photocatalytic activity of rare earth titania nanocomposites. J. Mol. Catal. A, 2008. 287(1–2): p. 151-158.

40. Zhang, Y., et al., Significant effect of lanthanide doping on the texture and properties of nanocrystalline mesoporous TiO_2. J. Solid State Chem., 2004. 177(10): p. 3490-3498.

41. Chen, Y. and D.D. Dionysiou, A comparative study on physicochemical properties and photocatalytic behavior of macroporous TiO_2-P25 composite films and macroporous TiO_2 films coated on stainless steel substrate. Appl. Catal. A., 2007. 317(1): p. 129-137.

42. Li, H., J. Li, and Y. Huo, Highly Active TiO_2N Photocatalysts Prepared by Treating TiO_2 Precursors in NH3/Ethanol Fluid under Supercritical Conditions. J. Phys. Chem. B, 2006. 110(4): p. 1559-1565.

43. Xu, Y.-h., et al., Investigation on mechanism of photocatalytic activity enhancement of nanometer cerium-doped titania. Appl. Surf. Sci., 2006. 252(24): p. 8565-8570.

44. Hou, M., et al., Mechanisms of enhancement of photocatalytic properties and activity of Nd^{3+}-doped TiO_2 for methyl orange degradation. J. Rare Earths, 2004. 22(4): p. 542-546.

45. Lin, H.-J., et al., Optical and photocatalytic properties of Fe^{3+}-doped TiO_2 thin films prepared by a sol–gel spin coating. Ceram. Int., (0).

46. Ashkarran, A.A., et al., Double-doped TiO_2 nanoparticles as an efficient visible-light-active photocatalyst and antibacterial agent under solar simulated light. Appl. Surf. Sci., 2014. 301(0): p. 338-345.

47. Madhusudan Reddy, K., S.V. Manorama, and A. Ramachandra Reddy, Bandgap studies on anatase titanium dioxide nanoparticles. Mater. Chem. Phys., 2003. 78(1): p. 239-245.

48. Lin, H.-J., et al., Optical and photocatalytic properties of Fe^{3+}-doped TiO_2 thin films prepared by a sol–gel spin coating. Ceram. Int., 2014. 40(7, Part B): p. 10633-10640.

49. Ma, Y., et al., Synthesis and characterization of thermally stable Sm,N co-doped TiO_2 with highly visible light activity. J. Hazard. Mater., 2010. 182(1–3): p. 386-393.

50. Ferreira, A., et al., Poly(vinylidene fluoride-trifluoroethylene) (72/28) interconnected porous membranes obtained by crystallization from solution. MRS Online Proceedings Library, 2011. 1312: p. null-null.

51. Martins, P., A.C. Lopes, and S. Lanceros-Mendez, Electroactive phases of poly(vinylidene fluoride): Determination, processing and applications. Prog. Polym. Sci., 2014. 39(4): p. 683-706.

52. Tavares, C.J., et al., PVD-Grown photocatalytic TiO_2 thin films on PVDF substrates for sensors and actuators applications. Thin Solid Films, 2008. 517(3): p. 1161-1166.

53. Hung, W.-C., et al., Study on photocatalytic degradation of gaseous dichloromethane using pure and iron ion-doped TiO_2 prepared by the sol–gel method. Chemosphere, 2007. 66(11): p. 2142-2151.

54. Saif, M. and M.S.A. Abdel-Mottaleb, Titanium dioxide nanomaterial doped with trivalent lanthanide ions of Tb, Eu and Sm: Preparation, characterization and potential applications. Inorg. Chim. Acta, 2007. 360(9): p. 2863-2874.

55. Xu, A.-W., Y. Gao, and H.-Q. Liu, The Preparation, Characterization, and their Photocatalytic Activities of Rare-Earth-Doped TiO_2 Nanoparticles. J. Catal., 2002. 207(2): p. 151-157.

56. Suwarnkar, M.B., et al., Enhanced photocatalytic activity of Ag doped TiO_2 nanoparticles synthesized by a microwave assisted method. Ceram. Int., 2014. 40(4): p. 5489-5496.

57. Choi, W., A. Termin, and M.R. Hoffmann, The Role of Metal Ion Dopants in Quantum-Sized TiO_2: Correlation between Photoreactivity and Charge Carrier Recombination Dynamics. The Journal of Physical Chemistry, 1994. 98(51): p. 13669-13679.

58. Ling, Q., J. Sun, and Q. Zhou, Preparation and characterization of visible-light-driven titania photocatalyst co-doped with boron and nitrogen. Appl. Surf. Sci., 2008. 254(10): p. 3236-3241.

59. Zhang, T., et al., Photooxidative N-demethylation of methylene blue in aqueous TiO_2 dispersions under UV irradiation. J. Photoch. Photobio. A, 2001. 140(2): p. 163-172.

4. TiO_2 nanoparticles decorated with gold nanoislands for enhanced photocatalytic activity

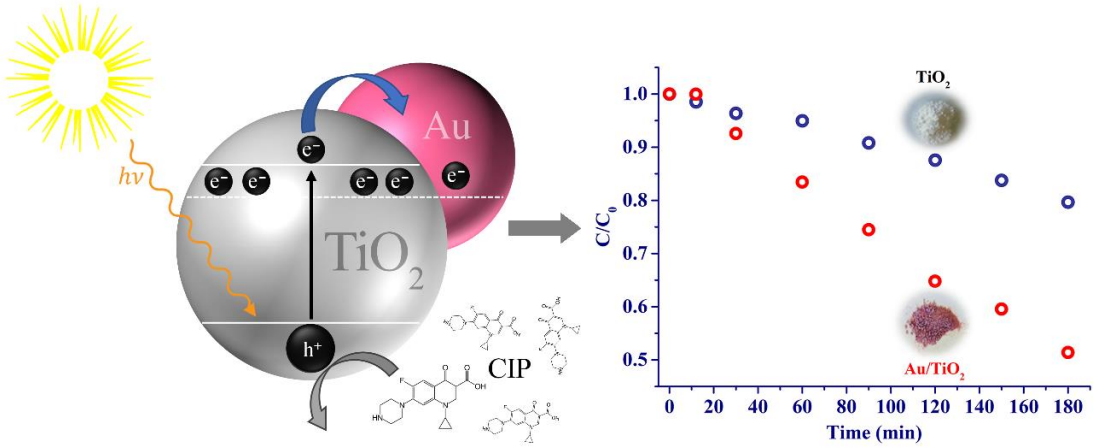

This work reports on the development of TiO_2 nanoparticles decorated with gold (Au) nanoislands, under different synthesis conditions. The produced Au/TiO_2 nanocomposites were characterized as well as their photocatalytic degradation efficiency with a ciprofloxacin solution.

4.1. Introduction

The resilience of specific emerging pollutants such as pharmaceuticals to the traditional wastewater treatments makes them end up discharged in the effluents [1]. Among these compounds, antibiotics are one of the most significant concerns as they affect biological metabolism and may induce bacterial resistance [2]. Ciprofloxacin (CIP) is a fluoroquinolone, a class of synthetic broad-spectrum antibiotics [3], which is mostly used in medicine (*e.g.,* tuberculosis, pneumonia or digestive disorders). It is also one of the most prescribed fluoroquinolones in the world and studies has shown its presence in potable water, wastewater effluents as well as in the sewage sludges [3, 4, 5]. In the last decades, photocatalysis has gathered considerable attention from the scientific community as a possible solution to tackle these environmental problems [6, 7].

Typically, the photocatalytic process takes place when a catalyst is UV irradiated and electron-hole pairs are created that will react with H_2O, OH^- and O_2 to generate oxidizing species such as the hydroxyl radical ($OH^\bullet$), superoxide radical anions ($O_2^{\bullet-}$), and hydrogen peroxide (H_2O_2). These species will initiate a series of reactions that will degrade pollutants into harmless compounds (*e.g.*, CO_2 and H_2O_2).

Photocatalysis presents several advantages when compared with other methods, for instance, the low-cost, the eco-friendly, and easy processing conditions [8-10]. Many photocatalysts have been reported in the last decades [11, 12]. Among all, titanium dioxide (TiO_2) is the most studied and applied in photocatalysis, mainly because of its remarkable optical and oxidizing properties, superhydrophilicity, chemical stability, and durability [13, 14]. Despite the compelling advantages of TiO_2, there are also some drawbacks. One of the main hurdles is the low spectral activation of TiO_2, caused by its wide band gap (3.0–3.2 eV) excitation that only occurs under radiation in the UV or near UV region (410–387 nm) [15]. For this reason, the solar radiation cannot be efficiently used because only less than 5 % of the radiation corresponds to UV [3]. Additionally, the process becomes less cost-effective as the UV lamps are required to provide the radiation. Another drawback is the electron-hole pair recombination that decreases the photocatalytic efficiency [16, 17].

The research developed in the last few decades is mainly devoted to surpass those limitations by producing new and more efficient photocatalytic materials. Strategies for metallic and non-metallic doping, co-doping, dye sensitization, semiconductor

combination, co-catalyst loading and nanocomposite materials were used and tested [18-22]. These approaches allow to reduce the electron-hole recombination rate and enhance the absorption of visible radiation of TiO_2, by introducing intermediate energy levels inside the band gap [23]. In this scope, several works have reported the functionalization of TiO_2 nanoparticles surfaces with noble metals such as Au, Pt, Pd, Co, and Ag [24-27]. When irradiated, noble metals nanoparticles at TiO_2 surface can receive electrons and prevent the recombination of the photogenerated electron–hole pairs [28, 29].

Among these materials, metals such as Au and Ag can increase visible light absorption owing to the surface plasmon of resonance effect [30, 31]. Gold (Au) nanoparticles have attracted considerable attention, mainly because they possess exceptional stability, non-toxicity, and biocompatibility [6]. Their properties are highly dependent on the nanoparticles size and shape allowing a broad range of applications [32-34]. For instance, the literature shows that gold nanoparticles in the range of 5 to 10 nm present an enhanced catalytic activity [35-37]. In this sense, some works focused in the photocatalytic activity of Au/TiO_2 nanocomposite have been published, including interesting review articles [6, 36, 38].

Different physical and chemical techniques have been exploited to produce Au/TiO_2 nanocomposites with enhanced catalytic properties. For instance, chemical vapor deposition [39], sol-gel [40], spray pyrolysis [41], electrophoretic approach [42], deposition-precipitation [43], impregnation [44] and surface functionalization [45], among others. However, many of these techniques are rather time-consuming and only few of them have focused on the optimization of synthesis parameters (e.g., synthesis temperature, Au loading), together with photocatalytic degradation conditions (e.g., photocatalyst and pollutant concentration).

This work will focus on the development and optimization of a simple, cost-effective, and fast precipitation synthesis to produce Au/TiO_2 nanocomposites with enhanced photocatalytic activity, under UV and visible radiation. The method optimization envisages the cost reduction, using the lowest Au loading that endows visible photocatalytic activity to the nanocomposite.

Degradation of CIP under UV and visible illumination was performed for the study on the photocatalytic efficiency. To the best of our knowledge, this is the first work that combines an optimization process of Au/TiO_2 nanocomposite, photocatalytic experiments, and theoretical simulation.

4.2. Materials and methods

4.2.1. Materials

P25 TiO_2 nanoparticles were kindly provided by Evonik®. Gold(III) chloride solution, 99.9% trace metals, 30 wt. % in dilute HCl, CAS: 16903-35-8 was purchased from Sigma-Aldrich. Sodium hydroxide (NaOH) was obtained from VWR. Millipore Milli-Q-system ultra-pure (UP) water was used in all the experiments.

4.2.2. Nanocomposite production

The Au/TiO_2 nanocomposites were produced, as illustrated in Figure 4.1, dispersing 200 mg of TiO_2-P25 nanoparticles in 40 mL of UP water in a sonication bath for 30 min. Afterward, this solution was placed under agitation in a water bath at different temperatures (25, 60, and 80 °C), using a thermostat to precisely control and stabilize the temperature – avoiding thermal gradients.

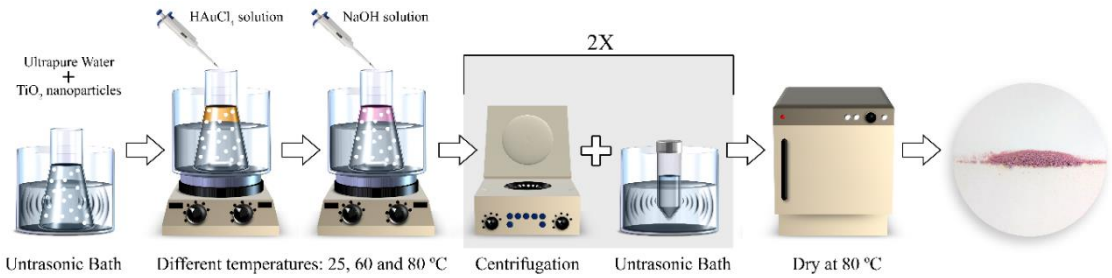

Figure 4.1. Schematic representation of the synthesis method for of Au/TiO_2 nanocomposites.

When the dispersion solution reached the desired temperature, different volumes from the chloroauric solution (10 µL of Gold(III) chloride trihydrate in 100 mL of UP water) were added, to achieve the Au loadings of 0.025, 0.05. 0.1, 0.25, and 0.5 wt.%. The solution was then stirred for 10 minutes to achieve a homogeneous distribution of gold precursor solution. Later, several volumes of a 0.1 M sodium hydroxide solution (NaOH) were added dropwise and mixed for 10 minutes, to obtain a pH = 9. The solution was then centrifuged at 23 000 rpm, the supernatant discarded and the nanocomposite pellet redispersed in UP water with the US for 1 minute, and this washing procedure was

repeated one more time. The last step was to dry the nanocomposite at 80 °C in an oven overnight and ground it with a pestle and mortar.

4.2.3. Characterization

The morphology of the nanocomposites was assessed by transmission electron microscopy (TEM), a Tecnai T20 from FEI. For the analysis, the nanocomposite samples were sonicated for 5 minutes to achieve good dispersion and afterward, a drop of the suspension was placed on a copper grid and dried at room temperature for the analysis. Particle size histograms were obtained after measuring at least 200 nanoparticles using Image J 1.50i software. Aberration-corrected scanning transmission electron microscopy (Cs-corrected STEM) images were acquired using a high angle annular dark field detector in an FEI XFEG TITAN electron microscope operated at 300 kV equipped with a CETCOR Cs-probe corrector from CEOS Company allowing the formation of an electron probe of 0.08 nm. Elemental analysis was carried out with an EDS (EDAX) detector which allows performing EDS experiments in the scanning mode.

The crystallographic phases of the pure TiO_2 and the Au/TiO_2 nanocomposite was evaluated by X-ray diffraction using a Bruker D8 Discover diffractometer with incident Cu Kα (40 kV and 30 mA).

The average hydrodynamic diameter was assessed by Dynamic Light Scattering (DLS) in a Zetasizer NANO ZS-ZEN3600, Malvern (Malvern Instruments Limited, UK), equipped with a He–Ne laser (wavelength 633 nm) and backscatter detection (173°). The samples were dispersed (0.1 mg L^{-1}) in ultrasonication bath at 22 °C for 30 minutes to avoid aggregates, and each sample was measured ten times. The zeta (ζ) potential was measured in the same device, and TiO_2 nanoparticles were equally suspended in ultra-pure water and solutions at different pHs (2, 4, 7, 9 and 12) were prepared with HCl (1M) and NaOH (1M) solutions. The results were obtained using the *Smoluchowski* theory approximation, and each sample was measured 10 times at 22 °C. The manufacturer software (Zetasizer 7.12) was used to assess particles diameter (intensity distribution), the PDI, and ζ-potential values.

The optical properties of the pristine TiO_2 and the Au/TiO_2 nanocomposite were assessed by Diffuse reflectance spectroscopy (DRS), using a Shimadzu UV-2501-PC equipped with an integrating sphere. The spectra were acquired in reflectance mode, and the

bandgap was estimated via the Kubelka-Munk Eq. (4.1) and the Tauc plot represented by Eq. (4.2).

$$F(R) = (1 - R_\infty)^2/(2R_\infty) \quad (1)$$

where R∞ (R_{Sample}/R_{BaSO4}) corresponds to the reflectance of the sample and F(R) is the absorbance.

$$[F(R)h\upsilon]^{1/n} \text{ versus } h\upsilon \quad (4.2)$$

where h is the Planck constant (6.626 $\times 10^{-19}$ J), n is the frequency and n is the sample transition (indirect transition, n = 2) [46].

4.2.4. Photocatalytic degradation

The photocatalytic activity of all the produced samples and pristine TiO_2 was tested by performing (CIP) degradation tests, under artificial ultraviolet (UV) or visible illumination. First, a solution of 5 mg L^{-1} of CIP was prepared. The CIP solution was adjusted to pH=3, to ensure the solubility, by using 0.1 mL hydrochloric acid (HCl) 1 M. Before all the degradation assays (UV or visible radiation), the Au/TiO_2 or P25 nanoparticles were stirred in the dark for 30 min to achieve an adsorption-desorption equilibrium.

The UV degradation of CIP was performed in a chamber with six Philips 8 W mercury fluorescent lamps with the mode wavelength of 365 nm. The suspensions of photocatalysts and CIP were kept stirred in a container under the illumination from the top. The distance between the beaker and the lamp was 13.5 cm, and the intensity coming to the system was 15−17 W/m². The samples were irradiated for 30 min.

The visible light tests were performed in a visible chamber fabricated by Ingenieurbüro Mencke & Tegtmeyer GmbH©, Germany. According to the manufacturer, the visible light spectrum is equivalent to that of the natural solar light. The light source has the intensity of 98 W/m². The visible light test was performed similarly to the UV test. Here, the container was placed at 21 cm from the light source, and the samples were irradiated continuously for 180 minutes.

The first photocatalytic activity tests were performed to determine the optimal ratio of CIP/catalyst. For this purpose 5, 15, 45 and 60 mg of Au/TiO_2 nanocomposite were

dispersed in a borosilicate beakers of 80 mL with 45 mL of CIP solution (5mg L^{-1}). The effect of Au loading on the photocatalytic efficiency was also assessed, under UV and simulated visible radiation. The impact of the synthesis temperature (25, 60, and 80 °C) on CIP photocatalytic degradation was equally evaluated using both types of illumination. The photocatalytic reproducibility tests were performed using nanocomposites produced in different batches but under the same synthesis conditions.

The bare TiO_2-P25 nanoparticles were used as controls in all the assays. Additionally, to prove the relevance of the Au/TiO_2 nanocomposites structure and interface, the photocatalytic degradation of CIP was assessed using the same amounts of Au and TiO_2 nanoparticles but not as a nanocomposite, these nanoparticles were separately added to the solution.

The photocatalytic efficiencies were tested by degrading CIP in aqueous solution under UV and Visible radiation and monitoring the maximum absorption peak (277 nm) using a Shimadzu UV-2501PC UV/Vis spectrophotometer. The degradation fits the Langmuir–Hinshelwood model, expressed by Eq. 2.3, in chapter 2.

4.3. Results

4.3.1. Nanocomposite characterization

The Au/TiO_2 nanocomposites were produced by nanoprecipitation method, and different temperatures (25, 60, and 80 °C) and Au loadings (ranging from 0.025 to 0.5 wt. %) were tried in order to understand how these parameters affect the morphology of the nanocomposites - and to relate this to the photocatalytic efficiency. In this sense, STEM-HAADF analysis was performed, and the micrographs of the different nanocomposites are displayed in Figure 4.2.

The Au loading study (Figure 4.2 a-c) was assessed by producing different nanocomposites with different gold content– from 0.025 to 0.5 wt.% with the same experimental conditions (temperature = 60 °C) . The STEM-HAADF micrographs show that for the sample with 0.025 wt. % of Au (Figure 4.2a), the presence of Au nanoparticles over the TiO_2 nanoparticles surface is almost inexistent (Figure 4.2a). After increasing the Au loading to 0.05 wt. % (Figure 4.2b), it is possible to observe a homogeneous distribution of predominantly small Au nanoparticles (bright contrast nanoparticles below

5 nm do diameter) over the TiO_2 nanoparticles, similar results were obtained for 0.1 wt. % (data not shown).

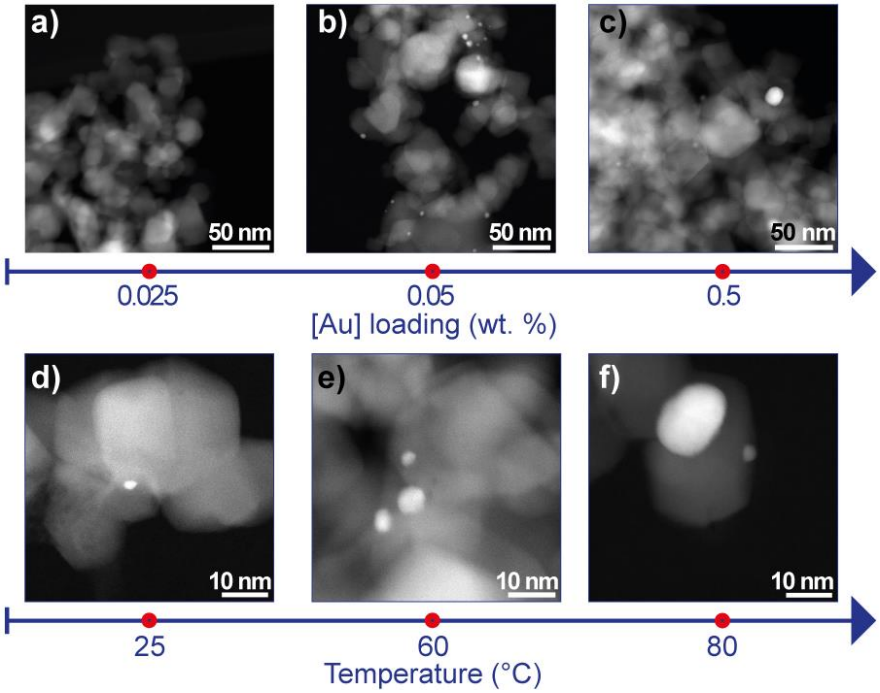

Figure 4.2. STEM-HAADF micrographs of Au/TiO_2 nanocomposites synthesized with different Au loadings at 60 °C – a) - c), and Au/TiO_2 nanocomposites obtained at different temperatures with an Au loading of 0.05 wt. % – d) to f).

For the concentrations of 0.25 and 0.5 wt. % (Figure 4.2c), agglomerates of Au over the TiO_2 nanoparticles (brightest areas of the micrograph) were identified, as well as large Au nanoparticles. Analogously, the effect of temperature on the synthesis product was also performed maintaining all the synthesis parameters (Au loading = 0.05 wt. % - yielded a homogeneous distribution and size of Au nanoparticles) and changing the temperature of the different samples. STEM-HAADF images (Figure 4.2d-f) indicate that although the used Au loading is the same in the three temperatures tested, when the nanocomposite is synthesized at 80 °C, larger Au nanoparticles on the nanocomposite are observed more frequently (Figure 4.2f). Conversely, at lower temperatures (25 and 60 °C), the Au nanoparticles sizes are lower (Figure 4.2d and e).

The study of the effect of Au loading and temperature in the nanocomposites morphology indicates that the samples produced at 60 °C and with an Au loading of 0.05 wt.% possess the more homogeneous distribution and size of Au nanoparticles. This sample was selected for a, more detailed, TEM analysis (Figure 4.3), revealing a homogeneous dispersion of Au nanoparticles (white arrows) over the surface of TiO_2 nanoparticles,

Figure 4.3a and b. The representation of the sphere-like shape of Au nanoparticles in Figure 4.3c shows that single crystal nanoparticles with high crystallinity were produced by the proposed method.

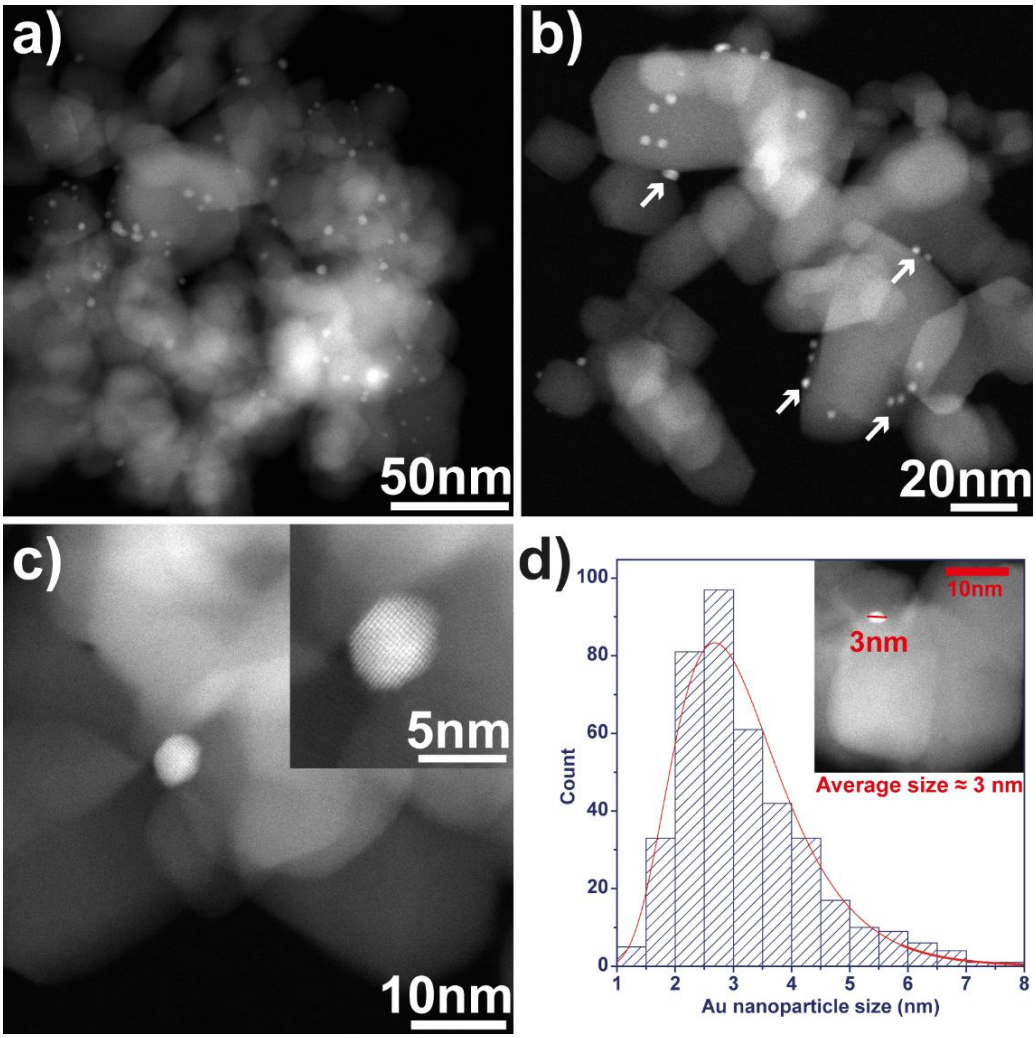

Figure 4.3. STEM-HAADF micrographs of Au/TiO_2 nanocomposites (produced at 60 °C and Au loading of 0.05 wt.%) at two different scales: a) 50 and b) 20 nm; c) detail of Au nanoparticle over TiO_2 nanoparticles surface and single Au nanoparticle amplification (inset); d) size distribution of 400 Au nanoparticles with the respective average size.

The Au nanoparticles size distribution, ranging from 1 to 7nm, and an average size of 3.2 ± 1.1 nm (Figure 4.3d) was estimated using Image J software by measuring 400 nanoparticles. All the images show Au nanoparticles with similar sizes, and in good agreement with the size distribution histogram that presents a sharp size distribution.

The STEM-HAADF- EDX measurements allowed to identify the elements present in the Au/TiO_2 sample in two different points, 1 and 2 (signaled in Figure 4.4a). STEM-HAADF-EDX spectra in Figure 4.4b in point 1, indicates the presence of Au and Cu (copper), which can be respectively ascribed to Au nanoparticles and the copper grid. In point 2, the signatures of Ti (titanium) and O (oxygen) were identified, corresponding to TiO_2 nanoparticles. Thus, EDX measurements confirm the presence of all the elements of the Au/TiO_2 nanocomposite.

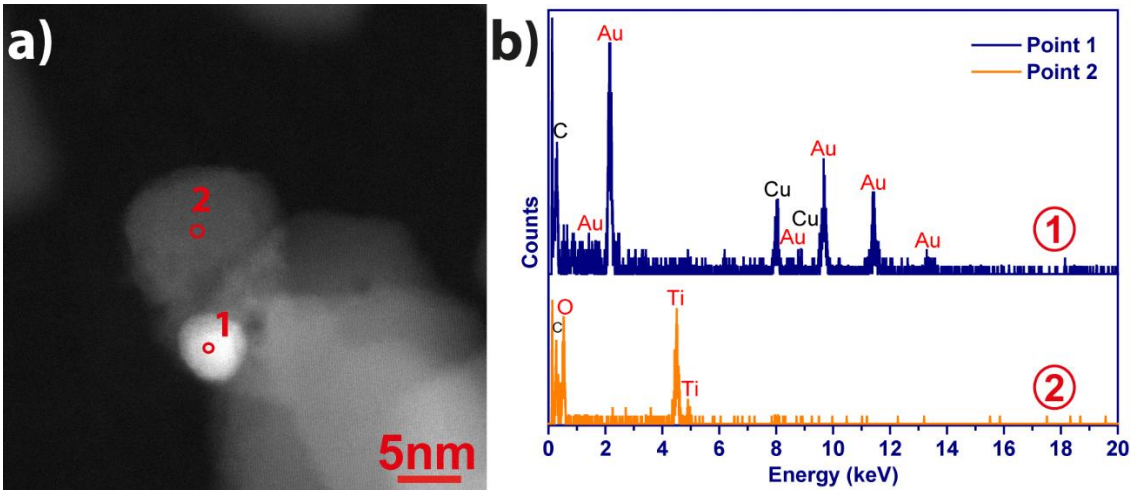

Figure 4.4. The STEM-HAADF-EDX image of Au/TiO_2 nanocomposites with the identification of the measured points: Au (1) and TiO_2 (2) a); EDX spectra with elemental identification (Au, Ti, O, and C) for points 1 and 2 b).

X-ray diffraction, Figure 4.5a evaluated the crystal structure of the pure TiO_2 nanoparticles and the Au/TiO_2 nanocomposite. Both samples show the typical reflexes from anatase (25.3°, 37.8°, and 48.0°) and rutile (27.49°). There is no significant difference between the intensities or positions of the reflexes from both samples. Moreover, no reflexes of Au were detected, which can be explained by the low amount of Au present in the nanocomposite (below detection limit). Figure 4.5b shows the study of hydrodynamic size for TiO_2 and Au/TiO_2 nanocomposites obtained by DLS. The results indicate nanoparticles diameters of 1023 nm and 342 nm, for the pristine TiO_2 and the Au/TiO_2 nanocomposites, respectively. The results suggest that the presence of Au nanoparticles over TiO_2 nanoparticles surface may prevent the formation of nanoparticles aggregates. On the other hand, the size distribution is broader for the nanocomposites regarding the pristine TiO_2. Previous work has equally shown that the presence of Erbium

(Er) on TiO_2 nanoparticles contributed to reducing the hydrodynamic size when compared with bare TiO_2 [22].

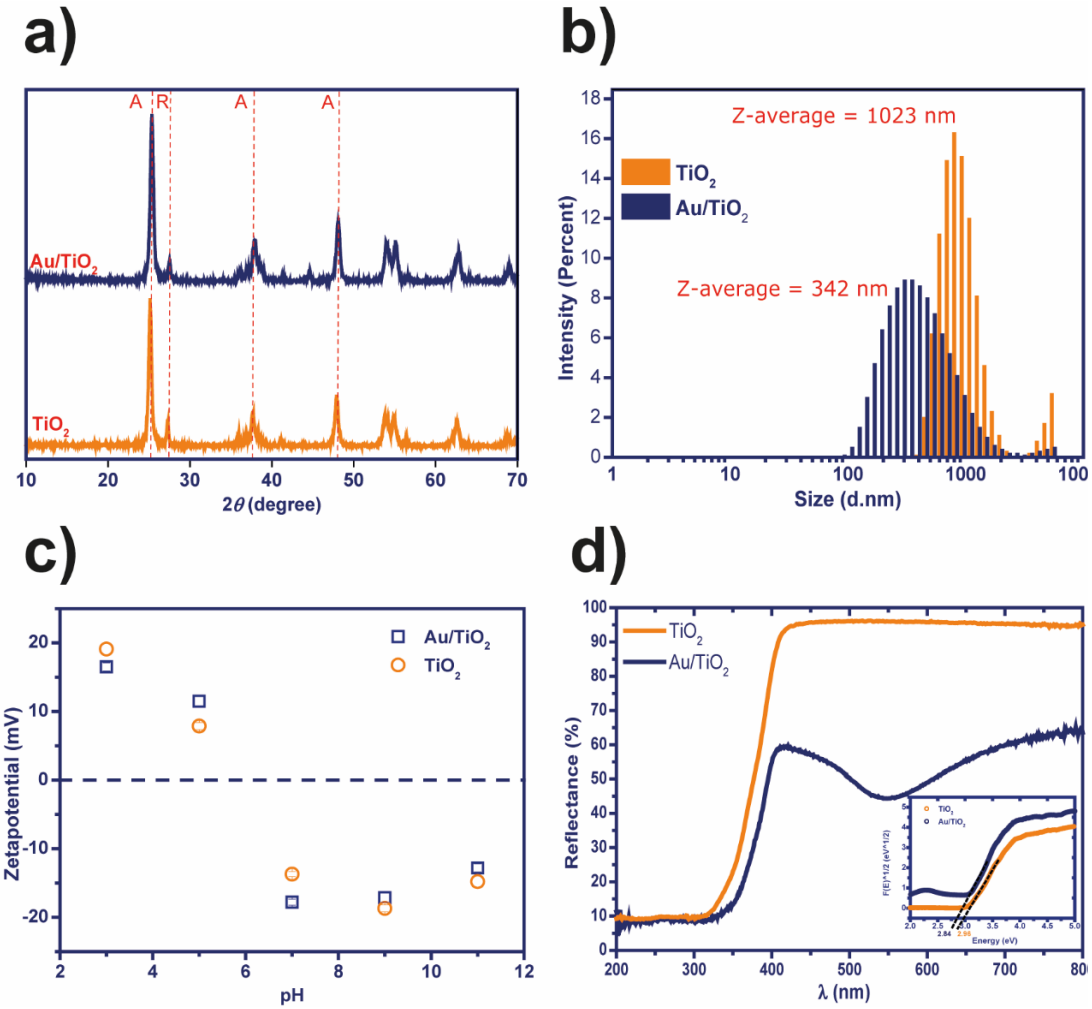

Figure 4.5. X-ray diffraction reflexes of pristine TiO_2 and Au/TiO_2 nanocomposite and identification of the representative peaks for anatase (A) and rutile (R) phases a); Dynamic light scattering, intensity size distribution of the pristine TiO_2 nanoparticles and the Au/TiO_2 nanocomposite and respective Z-average hydrodynamic size b); Zeta potential measurements, performed at different pH's (3, 5, 7, 9, and 11) for pristine TiO_2 nanoparticles and Au/TiO_2 nanocomposite c); UV–vis reflectance spectra of pristine TiO_2 and Au/TiO_2 and inset the estimation of the band gap for both samples at $[F(R)]^{1/2} = 0$ d).

The zeta potential was studied at different pH values (3, 5, 7, 9 and 11) for TiO_2 and Au/TiO_2 samples and the results are displayed in Figure 4.5c). The pristine and the Au/TiO_2 present very similar profiles, with higher zeta potential values ≈ |20| mV for pH below 3 and above 8. These data are in good agreement with the literature [47], with

positive zeta potential values for acidic conditions and negative values for basic pH which imply that at acidic conditions the TiO_2 and Au/TiO_2 are probably protonated and consequently have positive charges, and that at basic pH they are negatively charged.The more significant difference between the two samples occurred at pH=7, with the nanocomposite presenting higher zeta potential values than the pure TiO_2. Higher zeta potential values mean that nanoparticles possess higher periphery surface charge, which promotes nanoparticles repulsions avoiding aggregates formation, and enhanced stability [48]. In this context, and relating it with DLS obtained results, the lower hydrodynamic size is probably obtained for the Au/TiO_2 because repulsions endowed by Au on TiO_2 nanoparticles surface may help prevent aggregation.

To understand the differences in the photocatalytic performance of TiO_2 and Au/TiO_2 nanocomposite, the optical properties of these materials were studied by UV–Visible diffuse reflectance spectra (DRS), depicted in Figure 4.5d. In the visible range (400-800 nm) the pure TiO_2 nanoparticles almost reflect the incident radiation (≈ 95%) entirely. However, the nanocomposite displays reflectance's below 64% for the same range. Additionally, a minimum reflectance (≈ 44%) was obtained at 545 nm, indicating a maximum of the absorbance band that can be ascribed to the surface plasmon of Au nanoparticles – typically in the wavelength range between 520 and 560 nm [49, 50]. These results show that the nanocomposite presents a broad absorbance spectrum when compared to the pristine TiO_2 nanoparticles, which is also consistent with the purple/pink color exhibited by the produced nanocomposite powder, Figure 1. In the ultraviolet range (200-400 nm) both samples show similar behavior.

The band gap (inset graph of Figure 4d) of pure and Au/TiO_2 nanocomposite was estimated from DRS spectra, converting the reflectance to Kubelka-Munk units through equation (1) and (2). The obtained values show that the nanocomposites possess a slightly lower band gap (2.84 eV) than the pristine TiO_2 nanoparticles (2.96 eV). The decrease of the band gap in Au/TiO_2 is related to the shift absorption to longer wavelengths, similar results have been reported in the literature [51, 52].

4.3.2. Photocatalytic activity evaluation of Au/TiO_2

The photocatalytic activity of all the produced Au/TiO_2 nanocomposites was assessed by monitoring the degradation of CIP under artificial UV and visible irradiations. Process conditions were varied depending on the studying purposes.

- *Effect of photocatalyst concentration*

The optimal photocatalyst concentration was assessed through degradation of CIP with the different amounts of Au/TiO_2 nanocomposites - from 5 to 60 mg, which corresponds to a photocatalyst concentration of 0.1 and 1.3 g L^{-1}, respectively, Figure 4.6.

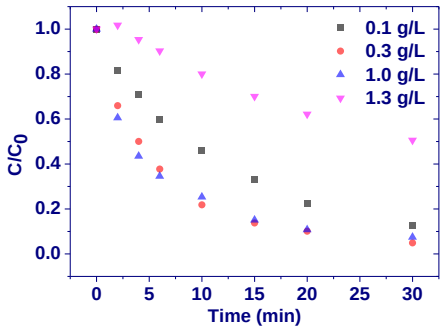

Figure 4.6. Photocatalytic degradation of ciprofloxacin (5 mg L^{-1}) in 45 mL of aqueous solution with different Au/TiO_2 concentrations (0.1, 0.3, 1.0 and 1.3 g L^{-1}). The Au/TiO_2 nanocomposite synthesized at 60 °C and with an Au loading of 0.05 wt. %. was used. The tests were performed over 30 minutes under UV irradiation.

Interestingly, with the photocatalytic concentrations of 0.1-1.0 g L^{-1}, ≈ 90 % of the CIP in solution was degraded, while with the high concentration of 1.3 g L^{-1}, only 50 % CIP was degraded after exposure to the same UV irradiation time. With the lower photocatalytic concentrations, 0.1–0.3 g L^{-1}, the photocatalytic degradation increased with the amount of nanocomposite. Mechanistically, it is expected that the increased amount of photocatalysts in solution will result in higher surface coverage, owing to the highest number of available active sites [53]. However, when increasing the concentration to 1.0 g L^{-1}, the degradation rate remained unchanged. And, with the highest concentration of Au/TiO_2, 1.3 g L^{-1}, the degradation was the slowest. This was due to the excess turbidity of the CIP solution [54], that strongly affects the penetration length of the light in the suspension, and consequently unabling the activation of photocatalytic particles in the inner region of the solution. The finding is in agreement with other reports [53], [55]. For this reason, the second lowest concentration tried, 0.3 g L^{-1} (15 mg in 45 mL), which yielded the highest photocatalytic efficiency, was chosen for the following photocatalytic activity assays.

- Effect of initial ciprofloxacin concentration

The rate of photocatalytic degradation depends on the availability of catalyst surface for the photo-generation of electron-hole pairs that produce hydroxyl radicals. Thus, in these experiments, the amount of catalyst is kept constant, while CIP concentration increases. The influence of CIP initial concentration of 5, 10 and 25 mg L^{-1} was studied under visible irradiation. It is observed that different CIP concentration affected the photocatalytic degradation rate and efficiency (Figure 4.7). With the lowest CIP concentration, 40 % of CIP degradation was obtained after 30 min. With the increase of concentrations by 2 and 5-times, the efficiencies achieved were 22 and 8 %, respectively. In these tests, with photocatalyst concentrations of 0.3 g L^{-1}, the adsorption of the CIP on the Au/TiO_2 nanoparticles surface might reach saturation. Additionally, the presence of other organic compounds, like intermediates and/or products from the CIP degradation will compete with CIP for adsorption onto the photocatalyst surface [56, 60]. This competition causes, in turn, lower reaction rates for higher CIP concentrations which accounts for the lower efficiency. The following assays focused on the photocatalytic activity of the produced nanocomposites with the lowest CIP concentration - 5 mg L^{-1}.

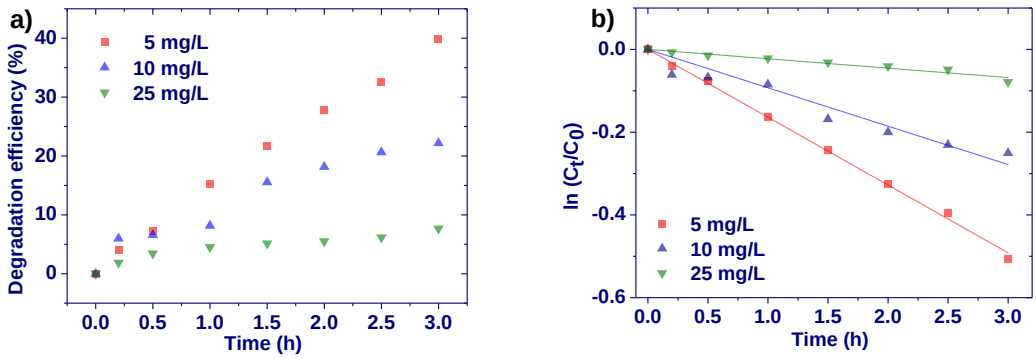

Figure 4.7. Degradation efficiency (%) (a) and ln (C_t/C_0) *vs.* time (b) for different initial ciprofloxacin concentrations (5, 10 and 25 mg L^{-1}), using Au/TiO_2 nanocomposites produced at 60 °C and with an Au loading of 0.05 wt. %, under 3 hours of simulated visible radiation.

In short, the ratio between hydroxyl radical/CIP molecules decreases with higher concentrations, causing slower degradation lower photocatalytic activity. Moreover, higher CIP concentrations may also reduce radiation harvesting by TiO_2 nanoparticles surface, which will also contribute to decreasing the number of hydroxyl radicals formed. Figure 4.7b displays the plot of ln (C_t/C_0) vs. time at different initial CIP concentrations.

Linear plots were observed, and the R^2 values are higher than 0.9, confirming that the photocatalytic degradation of CIP obeys pseudo-first-order kinetics.

- *Effect of the Au loading*

As gold is a noble metal; cost-effectiveness should be considered, and the total amount of gold used in the nanocomposite is one of the most paramount parameters. In this study, Au loading was varied by using different concentrations of the gold precursor. The tested Au loadings are 0.025, 0.05, 0.1, 0.25, and 0.5 wt.%. These nanocomposites were employed for the photocatalytic degradation of CIP under, both UV and simulated visible radiation.

Figure 4.8 shows the data of photocatalytic experiments under UV light. Accordingly, all produced samples, together with the pristine TiO_2 used as a control, showed photocatalytic activity, proved by the decrease of ciprofloxacin concentration along with the irradiation time. As confirmed by diffuse reflectance spectroscopy (section 3.1), the bandgap of the nanocomposites is 2.84 eV corresponding to the wavelength of 437 nm. Here, the used UV lamp has the mode wavelength of 365 nm, which is shorter than the bandgap. It means that the photon energy is adequate to excite electrons in the photocatalytic materials yielding the photocatalytic reaction. After 30 min, 77 % of ciprofloxacin was degraded in the presence of pristine TiO_2. The higher degradation of CIP of 80–90 % was achieved after 30 min, using the synthesized photocatalysts, 0.05 wt.%. This increased efficiency can be assigned to the presence of gold particles on the surface of the photocatalysts, confirmed by the TEM and EDX characterization (section 3.1). Quantitatively, the reaction rate was computed using the Langmuir-Hinshelwood kinetics (Eq. 3), Table 4.1. The apparent reaction rate constant k of the experiment with the bare TiO_2 was found to be 0.047 min^{-1}, while the decoration with gold particles improved the photocatalytic activity by 2–3 times. As predicted, in the presence of gold, the excited electrons of TiO_2 are scavenged by gold particles, reducing the electron-hole recombination rate and prolonging the lifetime of generated holes [59], [60]. As a consequence, the photocatalytic activity of the composites increases. Additionally, larger chloroauric acid concentrations might induce a larger number of gold particles distributed on the TiO_2 surface, increasing the number of electron absorption centers. This might account for the increase of k from 0.078 to 0.131 min^{-1} when increasing the Au loading

from 0.025 to 0.5 wt. %. However, the ongoing rise of the Au loading causes the decrease of k. These results can be addressed to the loss of photocatalytic active sites – on the surface of TiO_2 nanoparticles. Based on the TEM analysis, Figure 4.2, when the Au loading is very high both the amount and the size of Au nanoparticles over the surface of TiO_2 nanoparticles are large, which contributes to a reduction of TiO_2 sites for adsorption, may also affect the charge transfer process and probably reduces the radiation absorbance by the catalytic nanoparticles. Together, these limitations contribute to a reduction of the photocatalytic efficiency of the nanocomposite concerning the samples with lower Au loadings.

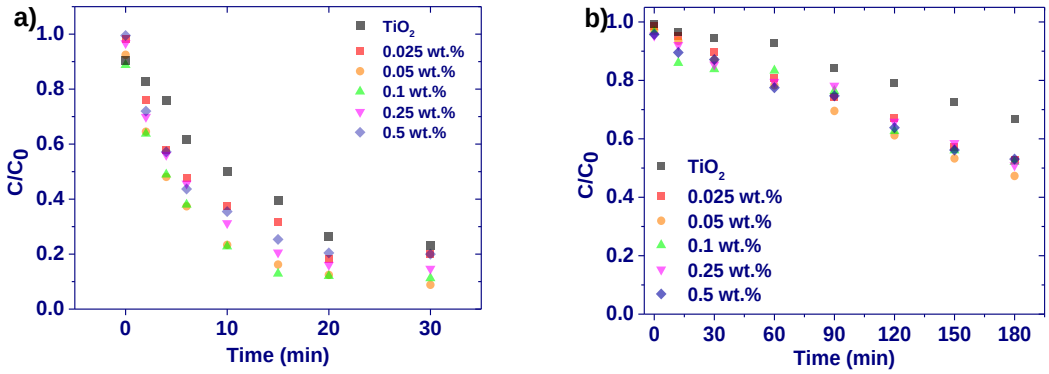

Figure 4.8. Photocatalytic degradation of ciprofloxacin (5 mg L^{-1}), with bare TiO_2 and Au/TiO_2 nanocomposite with different Au concentrations, under 30 and 180 minutes of UV (a) and visible (b) radiation.

The photocatalytic assays performed under simulated visible illumination are shown in Figure 8b. As a reference, two different blank essays were performed, without the presence of the catalyst and the radiation. In the first case, the CIP solution was exposed to the radiation for 180 min without catalyst, without any apparent degradation of CIP, proving its photostability under the experimental conditions. In the second case, the Au/TiO_2 nanocomposites were mixed to a CIP solution in the dark for 180 minutes, in this case, approximately 11% of CIP was removed from the solution by adsorption to the Au/TiO_2 nanocomposites.

Similarly, to the UV light experiments, the degradation rates of all produced nanocomposites were faster than that with the bare TiO_2. TiO_2 could remove ≈ 33% of CIP after 180 min of simulated visible irradiation. This significant CIP removal may be partially assigned to adsorption (11 %). Additionally, the sun simulator device has a small percentage (≈ 3%) of UV radiation (to mimic sunlight radiation), this radiation can induce

a low photocatalytic activity on bare TiO_2 (estimated to be 22 % in 180 minutes), which together with the adsorption of CIP, are responsible for its removal.

The decoration of gold particles on the TiO_2 surface resulted in the faster degradation rate of CIP under visible radiation. The bandgap of the composites was lowered, from 2.96 eV to 2,84 eV (section 4.1); thus, the materials could absorb the longer wavelength in the visible range (up to 437 nm). The reaction rates constant k increased from 0.073 h^{-1}, without Au, to 0.195–0.224 h^{-1}, with different Au loadings (Table 4.1).

Table 4.1. Apparent reaction rates (*k*) for photocatalytic degradation of CIP (5 mg L^{-1}) with bare TiO_2 and Au/ TiO_2 nanocomposite with different Au loadings, over 30 and 180 minutes of UV and simulated visible radiation, respectively.

Au loading (wt. %)	UV *k* (min^{-1})	Simulated visible *k* (h^{-1})
0	0.047	0.073
0.025	0.078	0.211
0.05	0.099	0.242
0.1	0.131	0.211
0.25	0.089	0.195
0.5	0.076	0.202

The obtained results, for UV and visible radiation, confirm that the photocatalytic efficiency of the TiO_2 nanoparticles is enhanced with the Au loading, until a specific *plateau*. When the Au loading is higher than 0.1 and 0.05 wt.%, respectively for UV and visible radiation, the gold nanoparticles can block the surface pores of TiO_2 nanoparticles, causing a decrease of surface area [61]. Furthermore, an excessive amount of Au nanoparticles can play as recombination centers for photoinduced electrons and holes. Both situations can contribute to a significant reduction of pollutant adsorption and consequently the photocatalytic efficiency [62]. The remaining assays of this study will be performed with an Au loading of 0.05 wt.%.

- *Effect of synthesis temperature*

The synthesis of the Au/TiO_2 nanocomposite is a chemical reaction thus it is a temperature-dependent process. Temperature can influence the surface charge and phenomenon and the dispersity of the TiO_2 particles in the solution during the synthesis.

It can also impact the nucleation as well as the growth of the gold particles on the TiO_2 surface. In this study, the syntheses were operated at 25, 60, and 80 °C, and the photocatalytic degradation of CIP, with the nanocomposites produced at different temperatures, was performed under UV and visible radiation (Figure 4.9 and Table 4.2).

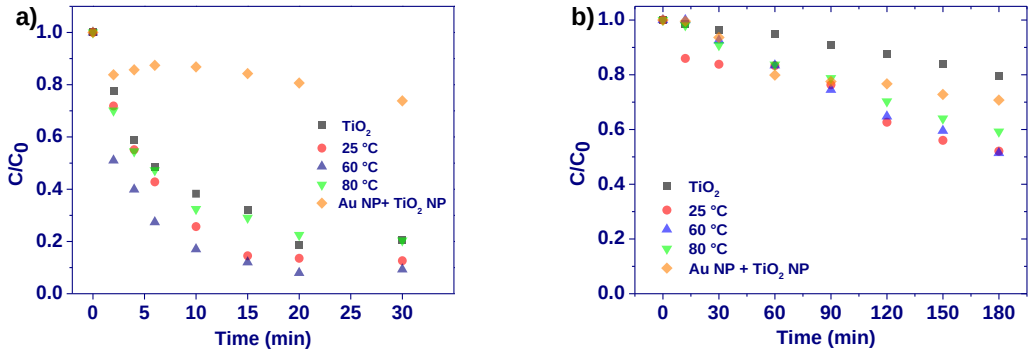

Figure 4.9. Photocatalytic degradation of ciprofloxacin (5 mg L^{-1}), with bare TiO_2 and Au/TiO_2 nanocomposites synthesized at different temperatures and Au loading of 0.05 wt. %, under 30 and 180 minutes of UV (a) and simulated visible light radiation, respectively.

Regardless of the synthesis temperature, the photocatalytic activity of the nanocomposites (Au loading = 0.05 wt.%) is higher than that of the bare TiO_2. Here, the syntheses at the room and medium temperatures (25 and 60° C) yielded the more efficient photocatalytic materials, for UV and visible radiation, towards higher temperature synthesis (80°C).
For both types of radiation, the sample obtained at 60° C presents higher degradation efficiencies (Table 2), 91% and 50% of CIP degradation under UV (30 min) and visible radiation (180 min), respectively. On the other hand, the synthesis performed at 80 °C reveal low degradations rates 80 and 40% for UV and visible radiation, correspondingly. Other works have reported that higher temperatures accelerate the reduction process and yield broader size distributions [63]. In this context, when the synthesis occurs at 80 °C, the size of Au nanoparticles produced is larger than the dimensions obtained with 25 and 60° C (in good agreement with STEM-HAADF micrographs Figure 2). Similarly, to what happens with the Au loading, when the amount of Au on the surface of TiO_2 is too high, the pores are blocked and the pollutant adsorption compromised.

For both types of radiation, the sample obtained at 60° C presents higher degradation efficiencies (Table 2), 91% and 49% of CIP degradation under UV (30 min) and visible radiation (180 min), respectively. Compared with bare TiO_2, these results correspond to a

degradation efficiency increase of approximately 14 and 170% for UV and visible radiation, respectively.

Table 4.2. Apparent reaction rates (*k*) for photocatalytic degradation of CIP (5 mg L^{-1}) with bare TiO_2 and Au/TiO_2 nanocomposite synthesized at different temperatures, over 30 and 180 minutes of UV and simulated visible radiation, respectively.

Temperature (°C)	UV		Simulated visible	
	k (min^{-1})	Degradation (%)	*k* (h^{-1})	Degradation (%)
TiO_2	0.660	80	0.073	20
25	0.131	88	0.221	48
60	0.117	91	0.226	49
80	0.047	80	0.176	41

Both under UV and visible radiation another control was performed. The very same amount of Au (corresponding to 0.05 wt.% obtained at 60 °C) and TiO_2 nanoparticles was added to the CIP solution. The solution was irradiated and the photocatalytic activity assessed. The results confirm that the photocatalytic efficiency obtained by the nanocomposites has to be due to the interface between Au and the TiO_2 surface.

- *Reproducibility test*

The reproducibility of the produced nanocomposites on the CIP degradation was explicitly measured. This involved three independent syntheses while all the parameters were kept unchanged. The produced samples were then used in the photocatalytic degradation of CIP under visible radiation Figure 4.10.

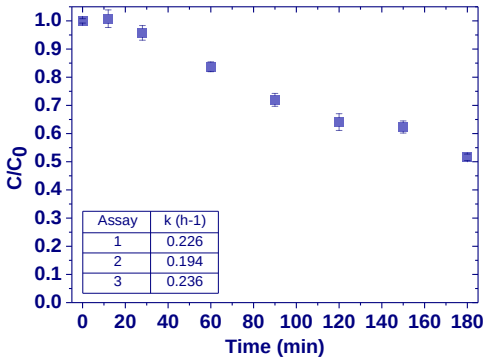

Figure 4.10. Photocatalytic degradation of ciprofloxacin (5 mg L^{-1}) a) with Au/TiO_2 nanocomposites, obtained in three batches using the same synthesis conditions (temperature = 60 °C and Au loading of 0.05 wt.%), over 180 minutes of simulated visible light irradiation.

The apparent reaction rate constant of three experiments fluctuated around the value of 0.219 ± 0.022 min^{-1}. The standard deviation of 10 % showed the good reproducibility of the method. Eventually, the proposed decoration of gold particles on the TiO_2 surface can be an interesting methodology to improve the photocatalytic activity of TiO_2 easily.

4.4. Conclusion

An Au/TiO_2 nanocomposite was produced, characterized and applied in the photocatalytic degradation of ciprofloxacin. The characterization results changing the synthesis conditions (temperature and Au loading) indicate that the synthesis performed at 60 °C with the Au loading of 0.05 wt. % yielded the most homogeneous distribution of Au nanoparticles (≈ 3 nm) over TiO_2 nanoparticles surface, after TEM inspection. Additionally, these samples absorb more radiation in the visible range (≈ 66% at 545 nm) and also present a lower band gap (2.84 eV *vs.* 2.96 eV from bare TiO_2). The photocatalytic results confirmed that all the manufactured nanocomposites possess higher photocatalytic efficiency in the UV and simulated visible radiation towards the pristine TiO_2. It was also possible to understand the impact of the synthesis parameters envisaging the optimal photocatalytic efficiency conditions. In this way, with the Au/TiO_2 nanocomposite, it was possible to enhance the photocatalytic degradation efficiency in 13 and 145 % under UV and simulated visible light radiation, respectively. As the photocatalytic efficiency was improved under both types of radiation, it is likely that two different processes take place on the nanocomposite. On the one hand, the efficient separation of an electron-hole pair, and on the other hand the surface plasmon of resonance can leverage the photocatalytic efficiency of the nanocomposite. The gold nanoislands play a paramount role, working as a sink of electrons and endowing the nanocomposite with the ability to absorb the visible radiation. Furthermore, it was proved the importance of the interface between TiO_2 and Au nanoparticles, by mixing TiO_2 and Au nanoparticles separately, obtaining low photocatalytic degradations of CIP (< 25%), under UV and Visible radiation. According to these results, the technique herein presented is straightforward and reproducible for photocatalytic applications.

4.5. References

1. An, T., et al., Mechanistic Considerations for the Advanced Oxidation Treatment of Fluoroquinolone Pharmaceutical Compounds using TiO_2 Heterogeneous Catalysis. The Journal of Physical Chemistry A, 2010. 114(7): p. 2569-2575.

2. Hapeshi, E., et al., Drugs degrading photocatalytically: Kinetics and mechanisms of ofloxacin and atenolol removal on titania suspensions. Water Research, 2010. 44(6): p. 1737-1746.

3. Mompelat, S., B. Le Bot, and O. Thomas, Occurrence and fate of pharmaceutical products and by-products, from resource to drinking water. Environment International, 2009. 35(5): p. 803-814.

4. Li, W.C., Occurrence, sources, and fate of pharmaceuticals in aquatic environment and soil. Environmental Pollution, 2014. 187: p. 193-201.

5. Zhao, J., et al., Facile fabrication of novel Mn2O3 nanocubes with superior light-harvesting for ciprofloxacin degradation. Catalysis Communications, 2017. 102: p. 5-8.

6. Ayati, A., et al., A review on catalytic applications of Au/TiO2 nanoparticles in the removal of water pollutant. Chemosphere, 2014. 107: p. 163-174.

7. Jiang, J.-Q. and S.M. Ashekuzzaman, Development of novel inorganic adsorbent for water treatment. Current Opinion in Chemical Engineering, 2012. 1(2): p. 191-199.

8. Khalid, N.R., et al., Cu-doped TiO_2 nanoparticles/graphene composites for efficient visible-light photocatalysis. Ceramics International, 2013. 39(6): p. 7107-7113.

9. Chong, M.N., et al., Recent developments in photocatalytic water treatment technology: A review. Water Research, 2010. 44(10): p. 2997-3027.

10. Lutic, D., et al., Mesoporous cerium-doped titania for the photocatalytic removal of persistent dyes. Catalysis Today, 2018. 306: p. 300-309.

11. Lu, S.-y., et al., Photocatalytic decomposition on nano-TiO_2: Destruction of chloroaromatic compounds. Chemosphere, 2011. 82(9): p. 1215-1224.

12. Khaki, M.R.D., et al., Application of doped photocatalysts for organic pollutant degradation - A review. Journal of Environmental Management, 2017. 198: p. 78-94.

13. Fabregat-Santiago, F., et al., High Carrier Density and Capacitance in TiO_2 Nanotube Arrays Induced by Electrochemical Doping. Journal of the American Chemical Society, 2008. 130(34): p. 11312-11316.

14. Hoffmann, M.R., et al., Environmental Applications of Semiconductor Photocatalysis. Chemical Reviews, 1995. 95(1): p. 69-96.

15. Vargas Hernández, J., et al., Effects of metal doping (Cu, Ag, Eu) on the electronic and optical behavior of nanostructured TiO2. Journal of Alloys and Compounds, 2017. 710: p. 355-363.

16. Shen, L., R. Liang, and L. Wu, Strategies for engineering metal-organic frameworks as efficient photocatalysts. Chinese Journal of Catalysis, 2015. 36(12): p. 2071-2088.

17. Ahmad, R., et al., Photocatalytic systems as an advanced environmental remediation: Recent developments, limitations and new avenues for applications. Journal of Environmental Chemical Engineering, 2016. 4(4, Part A): p. 4143-4164.

18. A. Barakat, M. and R. Kumar, Photocatalytic Activity Enhancement of Titanium Dioxide Nanoparticles Degradation of Pollutants in Wastewater. 2016.

19. Carneiro, J.T., et al., How Gold Deposition Affects Anatase Performance in the Photo-catalytic Oxidation of Cyclohexane. Catalysis Letters, 2009. 129(1): p. 12-19.

20. Momeni, M.M. and Y. Ghayeb, Preparation of cobalt coated TiO_2 and WO_3–TiO_2 nanotube films via photo-assisted deposition with enhanced photocatalytic activity under visible light illumination. Ceramics International, 2016. 42(6): p. 7014-7022.

21. Almeida, N.A., et al., TiO_2/graphene oxide immobilized in P(VDF-TrFE) electrospun membranes with enhanced visible-light-induced photocatalytic performance. Journal of Materials Science, 2016. 51(14): p. 6974-6986.

22. Martins, P.M., et al., Improving Photocatalytic Performance and Recyclability by Development of Er-Doped and Er/Pr-Codoped TiO_2/Poly(vinylidene difluoride)–Trifluoroethylene Composite Membranes. The Journal of Physical Chemistry C, 2014. 118(48): p. 27944-27953.

23. Li, X., et al., Novel ZnO-TiO_2 nanocomposite arrays on Ti fabric for enhanced photocatalytic application. Journal of Molecular Structure, 2017. 1148: p. 347-355.

24. Momeni, M.M. and Y. Ghayeb, Fabrication, characterization and photocatalytic properties of Au/TiO_2-WO_3 nanotubular composite synthesized by photo-assisted deposition and electrochemical anodizing methods. Journal of Molecular Catalysis A: Chemical, 2016. 417: p. 107-115.

25. Momeni, M.M. and Y. Ghayeb, Cobalt modified tungsten–titania nanotube composite photoanodes for photoelectrochemical solar water splitting. Journal of Materials Science: Materials in Electronics, 2016. 27(4): p. 3318-3327.

26. Momeni, M.M., Fabrication of copper decorated tungsten oxide–titanium oxide nanotubes by photochemical deposition technique and their photocatalytic application under visible light. Applied Surface Science, 2015. 357: p. 160-166.

27. Angkaew, S. and P. Limsuwan, Preparation of silver-titanium dioxide core-shell (Ag@TiO_2) nanoparticles: Effect of Ti-Ag mole ratio. Procedia Engineering, 2012. 32: p. 649-655.

28. Daskalaki, V.M., et al., Solar Light-Responsive Pt/CdS/TiO_2 Photocatalysts for Hydrogen Production and Simultaneous Degradation of Inorganic or Organic Sacrificial Agents in Wastewater. Environmental Science & Technology, 2010. 44(19): p. 7200-7205.

29. Bian, Z., et al., Superior Electron Transport and Photocatalytic Abilities of Metal-Nanoparticle-Loaded TiO_2 Superstructures. The Journal of Physical Chemistry C, 2012. 116(48): p. 25444-25453.

30. Tian, Y. and T. Tatsuma, Mechanisms and Applications of Plasmon-Induced Charge Separation at TiO_2 Films Loaded with Gold Nanoparticles. Journal of the American Chemical Society, 2005. 127(20): p. 7632-7637.

31. Wei, S.Z., et al., Janus Au-TiO_2 Photocatalysts with Strong Localization of Plasmonic Near-Fields for Efficient Visible-Light Hydrogen Generation. Advanced Materials, 2012. 24(17): p. 2310-2314.

32. Elahi, N., M. Kamali, and M.H. Baghersad, Recent biomedical applications of gold nanoparticles: A review. Talanta, 2018. 184: p. 537-556.

33. Al-Akraa, I.M., et al., Flower-shaped gold nanoparticles: Preparation, characterization, and electrocatalytic application. Arabian Journal of Chemistry, 2017. 10(6): p. 877-884.

34. Santhoshkumar, J., S. Rajeshkumar, and S. Venkat Kumar, Phyto-assisted synthesis, characterization and applications of gold nanoparticles – A review. Biochemistry and Biophysics Reports, 2017. 11: p. 46-57.

35. Gusmão, R., et al., Screen-printed carbon electrodes doped with TiO_2-Au nanocomposites with improved electrocatalytic performance. Materials Today Communications, 2017. 11: p. 11-17.

36. Haruta, M., Catalysis of Gold Nanoparticles Deposited on Metal Oxides. CATTECH, 2002. 6(3): p. 102-115.

37. Thompson, D.T., Using gold nanoparticles for catalysis. Nano Today, 2007. 2(4): p. 40-43.

38. Barakat, T., et al., Gold catalysts in environmental remediation and water-gas shift technologies. Energy & Environmental Science, 2013. 6(2): p. 371-391.

39. Okumura, M., et al., The reactivities of dimethylgold(III)β-diketone on the surface of TiO2: A novel preparation method for Au catalysts. Solid State Ionics, 1997. 95(1): p. 143-149.

40. Su, R., et al., Promotion of Phenol Photodecomposition over TiO_2 Using Au, Pd, and Au–Pd Nanoparticles. ACS Nano, 2012. 6(7): p. 6284-6292.

41. Haugen, A.B., et al., TiO_2, TiO_2/Ag and TiO_2/Au photocatalysts prepared by spray pyrolysis. Journal of the European Ceramic Society, 2011. 31(3): p. 291-298.

42. Chandrasekharan, N. and P.V. Kamat, Assembling Gold Nanoparticles as Nanostructured Films Using an Electrophoretic Approach. Nano Letters, 2001. 1(2): p. 67-70.

43. Zhang, Q.H., W.W. Yu, and H.Z. Wang, One-Pot Synthesis of Au Supported Titania Composite Photocatalyst and its Photocatalytic Activities for Dye Degradation. AMR Advanced Materials Research, 2012. 512-515: p. 2080-2083.

44. Zhu, H., et al., Mechanism of supported gold nanoparticles as photocatalysts under ultraviolet and visible light irradiation. Chemical Communications, 2009(48): p. 7524-7526.

45. Li, J. and H.C. Zeng, Preparation of Monodisperse Au/TiO_2 Nanocatalysts via Self-Assembly. Chemistry of Materials, 2006. 18(18): p. 4270-4277.

46. Sakthivel, S., et al., A fine route to tune the photocatalytic activity of TiO_2. Applied Catalysis B: Environmental, 2006. 63(1): p. 31-40.

47. Song, M., et al., Surface ζ potential and photocatalytic activity of rare earths doped TiO2. Journal of Rare Earths, 2008. 26(5): p. 693-699.

48. Carole, S., et al., Dispersion and stability of TiO_2 nanoparticles synthesized by laser pyrolysis in aqueous suspensions. Journal of Physics: Conference Series, 2009. 170(1): p. 012013.

49. Chen, W., J. Zhang, and W. Cai, Sonochemical preparation of Au, Ag, Pd/SiO_2 mesoporous nanocomposites. Scripta Materialia, 2003. 48(8): p. 1061-1066.

50. Kuge, K.i. and G. Calzaferri, Gold-loaded zeolite A. Microporous and Mesoporous Materials, 2003. 66(1): p. 15-20.

51. Mihai, S., et al., Morpho ierarhic TiO_2 with plasmonic gold decoration for highly active photocatalysis properties. Materials Letters, 2016. 162: p. 222-225.

52. Cojocaru, B., et al., Enhanced photo-degradation of bisphenol pollutants onto gold-modified photocatalysts. Catalysis Today, 2017. 284: p. 153-159.

53. Evgenidou, E., K. Fytianos, and I. Poulios, Semiconductor-sensitized photodegradation of dichlorvos in water using TiO_2 and ZnO as catalysts. Applied Catalysis B: Environmental, 2005. 59(1): p. 81-89.

54. Le, H.N., et al., Impact of ultrasonic dispersion on the photocatalytic activity of titania aggregates. Beilstein journal of nanotechnology, 2015. 6: p. 2423-30.

55. Behnajady, M.A., N. Modirshahla, and R. Hamzavi, Kinetic study on photocatalytic degradation of C.I. Acid Yellow 23 by ZnO photocatalyst. Journal of Hazardous Materials, 2006. 133(1): p. 226-232.

56. Emeline, A.V., V. Ryabchuk, and N. Serpone, Factors affecting the efficiency of a photocatalyzed process in aqueous metal-oxide dispersions: Prospect of distinguishing between two kinetic models. Journal of Photochemistry and Photobiology A: Chemistry, 2000. 133(1): p. 89-97.

57. Thakur, R.S., R. Chaudhary, and C. Singh, Fundamentals and applications of the photocatalytic treatment for the removal of industrial organic pollutants and effects of operational parameters: A review. Journal of Renewable and Sustainable Energy Journal of Renewable and Sustainable Energy, 2010. 2(4): p. 042701.

58. Ollis, D.F., Kinetics of Liquid Phase Photocatalyzed Reactions: An Illuminating Approach. The Journal of Physical Chemistry B, 2005. 109(6): p. 2439-2444.

59. Kumar, S.G. and L.G. Devi, Review on Modified TiO_2 Photocatalysis under UV/Visible Light: Selected Results and Related Mechanisms on Interfacial Charge Carrier Transfer Dynamics. The Journal of Physical Chemistry A, 2011. 115(46): p. 13211-13241.

60. Pichat, P., Photocatalysis and Water Purification: From Fundamentals to Recent Applications. 2013.

61. Wang, H., et al., Mesoporous Au/TiO_2 composites preparation, characterization, and photocatalytic properties. Materials Science and Engineering: B, 2012. 177(11): p. 913-919.

62. Wongwisate, P., et al., Effects of monometallic and bimetallic Au–Ag supported on sol–gel TiO2 on photocatalytic degradation of 4-chlorophenol and its intermediates. Desalination, 2011. 272(1): p. 154-163.

63. Scarabelli, L., et al., A "Tips and Tricks" Practical Guide to the Synthesis of Gold Nanorods. The Journal of Physical Chemistry Letters, 2015. 6(21): p. 4270-4279

5.TiO_2/graphene and TiO_2/graphene oxide nanocomposites for photocatalytic applications

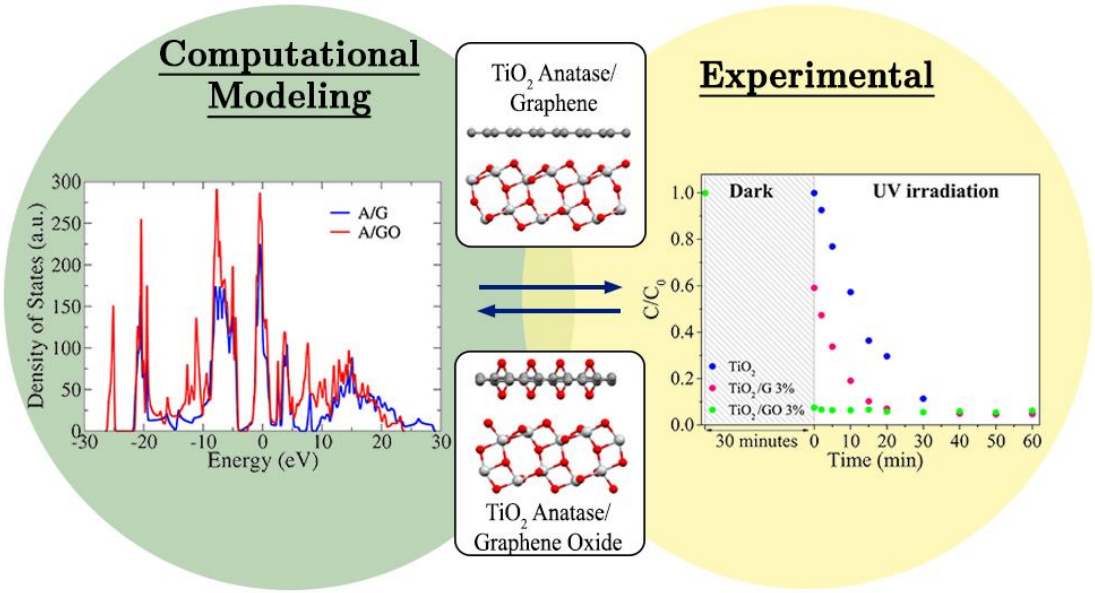

This work reports a computational study, focused on graphene (G) and graphene oxide (GO) interfaces with TiO_2, and an experimental assay on the photocatalytic activity of TiO_2/G and TiO_2/GO nanocomposites in the degradation of two different pollutants: methylene blue and ciprofloxacin. Additionally, GO was immobilized into a PVDF-TrFE matrix, the nanocomposite characterized and the photocatalytic activity evaluated.

This chapter is based on the following publications: Martins, P.M., et al., TiO2/graphene and TiO2/graphene oxide nanocomposites for photocatalytic applications: A computer modeling and experimental study. Composites Part B: Engineering, 2018. 145: p. 39-46;
Almeida, N.A., et al., TiO2/graphene oxide immobilized in P(VDF-TrFE) electrospun membranes with enhanced visible-light-induced photocatalytic performance. Journal of Materials Science, 2016. 51(14): p. 6974-6986.

5.1. Introduction

Water contamination is one of the most severe environmental issues, as many hazardous micropollutants, such as heavy metals, pharmaceuticals, dyes, fertilizers, and pesticides are increasingly being released into the watercourses [1, 3]. Since these pollutants present high toxicities and thus constitute a threat to fauna and flora, it is essential to develop efficient techniques for water decontamination [4, 5].

Semiconductor-based heterogeneous photocatalysis is one of the most promising processes for the treatment of contaminated water. Among the available catalysts, titanium dioxide (TiO_2) presents the most suitable properties: it is chemically and biologically inert, stable, non-toxic, cheap and easy to produce [6, 7] However, it has an energy band gap (3.2 eV for the anatase phase and 3.0 eV for the rutile phase) with photoexcitation in the ultraviolet (UV) range. This translates to a reduced spectral activation with natural light since UV radiation corresponds to just 5% of the solar spectrum.[4] Also, the recombination of photogenerated electron-hole pairs is high, which results in reduced photocatalytic efficiency [4, 8].

Several strategies have been attempted to tailor TiO_2 band gap and to reduce the electron-hole recombination to overcome these limitations, namely doping TiO_2 with metallic [9], no-metallic [10], and rare earth elements [4], and mixing TiO_2 with other nanomaterials [8]. One particularly promising approach lies on the mixing with graphene (G) and graphene oxide (GO) to develop TiO_2 nanocomposites (designated by TiO_2/G and TiO_2/GO, respectively), as these composite materials have been found to present improved electronic and optical properties for photocatalysis. For instance, the creation of Ti–O–C bonds can expand the light absorption to longer wavelengths [11]. Thus, the association of TiO_2 nanoparticles with graphene nanosheets offers a great opportunity to design TiO_2/graphene nanocomposite materials with improved visible-light photocatalytic activity.

TiO_2/G and TiO_2/GO nanocomposites have been produced by solvothermal [12], hydrothermal [13, 14], and one-step colloidal blending methods [15]. These nanocomposites have been assessed for the degradation of pollutants, namely: methylene blue (under UV and visible-light irradiation), [13,15] risperidone (using artificial sunlight and visible radiation) [14], naphthenic acids [12] methyl orange and dimethyl phthalate [16] (both under UV irradiation). In these studies, high photocatalytic efficiency was found was attributed to the increasing adsorption of the pollutants onto the nanoparticles

surface and to improved separation of charge carriers, which effectively inhibits recombination.

Computationally, DFT studies regarding the electronic properties of TiO_2/G interfaces have been reported addressing the interfaces of TiO_2 surfaces/slabs for the anatase [17, 18] and rutile crystal phases with one graphene adlayer. In all these studies, it was found that these interfaces show a reduced band gap and at the same time promote separation of charge carriers at the interfaces.

Few of the reported works to date relate the photocatalytic efficiency with the G/GO concentration, and none of them compares the performance of the TiO_2/G with the performance of the TiO_2/GO nanocomposites. Further, although the properties of TiO_2/G interfaces have been computationally calculated previously, the properties of TiO_2/GO interfaces are yet to be determined.

The recuperation of the catalyst is another widely-discussed issue related to photocatalytic materials. This is a relevant issue not only to allow the nanocatalyst reutilization/recycling, which is a time-consuming and expensive process but also to avoid secondary pollution – with loss of nanoparticles into the treated water. In this context, nanofiber membranes containing the catalyst prepared by electrospinning have been reported [19]. The electrospinning technique allows the fabrication of membranes with a high surface area, the product does not exhibit the aggregate effect and can be easily separated from liquid phases. TiO_2 based membranes produced using this technique have been reported as an efficient approach to immobilize the catalyst [20][21]. However, when a titanium precursor is added to the polymer solution, after the electrospinning process, the fiber mat needs to be calcined to crystallize the TiO_2 phase and remove the polymer. Although the methodology is appropriate to obtain photocatalytic active membranes, these inorganic membranes present poor mechanical properties - brittle and consequently difficult to handle. In chapter 2 it was reported the photocatalytic activity of rare earth metal doped (erbium, Er) and codoped (erbium and praseodymium, Er/Pr) TiO_2 nanoparticles immobilized in a poly(vinylidene difluoride-co−trifluoroethylene) (P(VDF−TrFE)) copolymer membrane prepared by solvent casting [4]. It was shown that P(VDF-TrFE) possesses a microporous structure suitable for TiO_2 nanoparticles immobilization. In this connection, the preparation of new P(VDF−TrFE) membranes containing previously prepared TiO_2/GO nanocomposites by electrospinning was tested in relation with this previous work, to further study the suitability of the P(VDF-TrFE) copolymer new morphology to act as porous support of a photocatalytic active

nanocomposite. P(VDF-TrFE) copolymers have attracted scientific and technological interest due to their chemical resistance, remarkable mechanical properties and excellent electroactive properties due to very stable C−F bonds. Additionally, they present excellent UV radiation resistance, making it suitable for photocatalytic applications [22]. The membrane preparation by electrospinning allows a high surface area exposure and increasing the photocatalytic performance.

Therefore, the present work comprises an experimental and theoretical investigation of the photocatalytic activity of TiO_2/G and TiO_2/GO nanocomposites with different contents of graphene and GO. These nanocomposites were used to degrade a dye (methylene blue - MB) and an antibiotic (ciprofloxacin – CIP), under UV and visible-light irradiation, to evaluate and compare their photocatalytic performance. Also, the fundamental electronic properties of TiO_2/G and TiO_2/GO interfaces were also computed through density functional tight-binding method to rationalize the results. Moreover, this is, to the best of our knowledge, the first study that uses these nanocomposites to degrade antibiotics, even though these represent a grave concern to the environment due to their toxicity and the increasing risk of new antibiotic-resistant microorganisms [3]. Moreover, the TiO_2/GO photocatalytic nanocomposite was immobilized in a PVDF-TrFE electrospun membrane, characterized and tested for MB photocatalytic degradation (also under UV and visible radiation).

5.2. Experimental methods

Computer model

Computations were performed with Self Consistent Charge Density Functional Tight Binding (SCC-DFTB) Hamiltonian, with the *tiorg* parameters set, using the software *DFTB+* (version 1.2.2) [23]. The DFTB Hamiltonian shows a higher computational efficiency than DFT methods and therefore is ideal for the study of large systems [24, 25].

The structure and electronic properties of the pristine materials and the TiO_2/G and TiO_2/GO interfaces were computed and compared. Interfaces between TiO_2 surface slabs and graphene/GO sheets were built using *Virtual NanoLab* software (version 2015.1) from *QuantumWise*. For the TiO_2 slabs, the most thermodynamically stable surfaces of anatase (101) and rutile (110) were computed with two atomic layers. Suitable

commensurate graphene and GO layers were cut and interfaced with the slabs. For simplicity, the GO model considered in this study assumed a full, two face, functionalization of the graphene with epoxy C-O functional groups with a ratio C:O of 2. Interfaces of anatase/graphene (A/G), rutile/graphene (R/G), anatase/GO (A/GO) and rutile/GO (R/GO) were studied. The number of atoms contained in TiO_2 slabs and graphene/GO layers, as well as the commensurate supercell dimensions and strains of the interfaces, are listed in Table For all cases, a vacuum slab of approximately 15 Å perpendicular to the interface was considered. The use of the DFTB Hamiltonian allowed the modelling of a larger system than those reported in the literature[16 - 18] with lower strain values, *i.e.*, higher commensurability.

Table 5.1. Number of atoms, supercell dimensions and strain considered in the construction of the interfaces.

Interface	TiO_2 atoms	G/GO atoms	Supercell dimensions	Strain
A/G	240	144	51.48×7.43×35 $Å^3$	0.80%
R/G	360	224	30.03×19.82×35 $Å^3$	0.11%
A/GO	312	264 (176 C)	10.36×49.33×35 $Å^3$	0.42%
R/GO	252	216 (144 C)	46.60×8.97×35 $Å^3$	0.80%

Geometry optimization of the interfaces was performed through the conjugate gradient method, considering a maximum force of 10^{-4} Ha/Bohr. The atoms of the bottom layer of the TiO_2 slab were fixed at the bulk positions. Two different Monkhorst-Pack meshes were used, one for the geometry optimization and a denser one to compute the electronic properties and the adhesion energy. The charge transfer isosurfaces were computed with the *waveplot* software (version 0.3.1). Details of the meshes used are presented in the supplementary information.

Materials

TiO_2 (P25 - AEROXIDE) nanoparticles were provided by *Evonik Industries AG*. Graphite flakes (99.99 %) and all the remaining chemicals were supplied by Sigma-Aldrich and used as received. The water used in all the photocatalytic experiments is ultra-pure (Millipore). Poly(vinylidene fluoride–trifluoroethylene), P(VDF–TrFE), 70/30 was purchased from Solvay (Belgium).

Preparation of TiO_2/G and TiO_2/GO nanocomposites

Graphene oxide (GO) was produced by the chemical exfoliation of graphite flakes, according to the method suggested by Hummers and Offeman [26], [27]. Briefly, 7 g of $KMnO_4$ was added to a suspension containing 50 mL of concentrated H_2SO_4 and 2 g of graphite. The resulting mixture was magnetically stirred for 2 hours and then treated with a solution of H_2O_2 (30 wt. % in water) until the gas evolution ceased. After that, the suspension was intensively washed, first with a diluted solution of HCl (0.1 mol/dm^3) and then with distilled water by filtration. Finally, the solution was centrifuged and dried by lyophilization to obtain the GO. The quality of the GO flakes was evaluated by AFM, Raman and SEM characterization (data not shown).

The graphene was obtained from the reduction of the GO, by adding 2 mL of NH_2OH (0.1 mol/dm^3) to 10 mL of a suspension of GO (0.5 mg/mL). After stirring for 30 minutes, the pH was adjusted to 12 by adding an aqueous solution of NaOH (0.1 mol/dm^3). Then the suspension was heated to 80 ºC for 1 hour and finally washed by centrifugation. The success of the GO flakes reduction was accessed by Raman spectroscopy (data not shown).

The synthesis of the TiO_2/G and TiO_2/GO nanocomposites was based on a one-step hydrothermal method described in previous studies [8, 12]. In short, the appropriate amount of graphene/GO (depending on the wt. % of the composites required – namely 0.5%, 1%, 1.5% and 3%) was dispersed in a mixture of 40 mL of deionized water and 20 mL of ethanol and stirred by ultrasonication for 1 hour. Subsequently, 100 mg of TiO_2 were added, and the resulting suspension was stirred for 2 hours to achieve a complete homogenization. After that, 15 mL of this suspension was placed in a Teflon lined autoclave, sealed and heated to 120 ºC during 3 hours. The resulting nanocomposites were then washed with deionized water and freeze-dried to avoid the agglomeration of the particles.

Preparation of TiO_2/GO/PVDF-TrFE nanocomposites

Different amounts of TiO_2/GO nanocomposites (0, 3, 5, 8 and 20%, w/w) were sonicated in ultrasonic bath (Bandelin, model Sonorex Super RK106) for 2 h to achieve a good dispersion, in a solution of polymer with N,N-Dimethylformamide / methyl ethyl ketone (85/15, vol/vol) to reach a final concentration of 15% (w/w) of P(VDF-TrFE). Later, the solution was magnetically stirred for 2 h until complete polymer dissolution.

Electrospinning process was performed according to the method described elsewhere [28]. Briefly, the solution was placed inside a glass syringe fitted with a metal needle with gauge 22. Electrospinning was conducted at 1.5 kV/cm using a voltage source from Glassmann (PS/FC30P04). A syringe pump (from Syringepump) was used to feed the polymer solution into the needle tip at 0.5 mL/h, and the electrospun fibers were collected in a grounded collecting plate kept at 15 cm from the needle tip. Hereafter, the produced fibers will be referred as P(VDF-TrFE)/TiO_2 for the fibers prepared with the polymer and the TiO_2 and P(VDF-TrFE)/TiO_2/GO for the fibers prepared with the polymer and the TiO_2/GO nanocomposites.

Materials characterization

SEM characterization was performed with an FEI *Quanta 650 FEG* microscope, equipped with an *INCA 350* spectrometer from *Oxford Instruments* for EDX. A small amount of powder was placed in copper tape and observed under 20 kV.

Electrospun membranes morphology was assessed by scanning electron microscopy (SEM) with a FEG-SEM Hitachi S4100 microscope operating at 25 kV. Before observation, samples were coated with a thin carbon layer by using a Fisons Instruments SC502 sputter coater.

The crystallinity of the samples was accessed through XRD using a *Philips PW 1710* diffractometer with a Cu source (K_α, λ=1.5045Å) operating at 40 kV and 30 mA, at room temperature.

To identify the vibrational modes of the nanocomposites, FTIR was performed in ATR mode, using a *PerkinElmer Spectrum Two IR* Spectrometer and considering 64 scans, with a resolution of 4 cm^{-1}. The FTIR of the PVDF-TrFE membranes were also performed at RT in an Alpha FTIR apparatus from Bruker in ATR mode from 4000 to 600 cm^{-1}. FTIR spectra were collected after 32 scans with a resolution of 4 cm^{-1}.

DRS was performed by a *Shimadzu UV-2501 PC* apparatus equipped with integrating spheres. These measurements allowed to estimate the band gap of the photocatalysts, by converting the reflectance spectra to absorption Kubelka-Munk units through Eq. [29]:

$$F(R_\infty) = \frac{(1 - R_\infty)^2}{2R_\infty} \tag{5.1}$$

where $F(R_\infty)$ is the Kubelka-Munk function and R_∞ is the absolute diffuse reflectance.

Photocatalytic experiments

- *Suspension assays*

The photocatalytic activity of TiO_2 composites with different G and GO content were evaluated through the degradation of methylene blue (MB) and ciprofloxacin (CIP) aqueous solutions (10^{-5} mol/dm^3) at pH ≈ 4, under UV and visible light. For this, 50 mg of the catalysts were added to 50 mL of solution and magnetically stirred in the dark for 30 minutes, to achieve the adsorption-desorption equilibrium. Afterward, the UV photocatalytic degradations were carried out using a home-made photoreactor equipped with six 8W mercurial fluorescent lamps, from *Philips*, with a flux of 1.6-1.7 mW/cm^2 and an excitation peak of 365 nm, placed at 10 cm above the solution. For the visible light experiments, an *Ingenieurburo Mencke & Tegtmeyer GmbH* sun simulator, with a flux of 9.8 mW/cm^2, was used. In this case, the light source was placed 21 cm above the solution. For both the experimental setups, the reaction rate and efficiency of the degradation were determined by monitoring the intensity of the main absorbance peaks of MB (664 nm) and CIP (276 nm), using a *Biotek Cytation3* spectrophotometer. The experiments revealed that the degradation of both solutions fitted to a pseudo-first-order reaction, Langmuir–Hinshelwood model, expressed by Eq. 2.3, in chapter 2 [30].

- *Immobilized assays*

UV photocatalytic activity assays were performed with 12 cm^2 of P(VDF-TrFE)/TiO_2 and P(VDF)-TrFE/TiO_2/GO. These nanocomposite membranes were immersed in a quartz cuvette (1 cm optical path) with 13 mL of methylene blue (MB) solution (10^{-5} mol/dm^3). The quartz cell was then irradiated with a high-power LED source (Thorlabs, 700 mA) with an excitation peak at 365 nm (UV-A). The incident radiation over the sample was measured with a Delta Ohm irradiance meter, and radiation of 4 mW·cm^{-2} was adjusted [32]. The absorbance of the MB was monitored at intervals of 2 min using a spectrophotometer (ScanSpec UV-Vis, ScanSci) in the range of 300–900 nm.

The photocatalytic activity of the nanocomposites, under visible radiation, was tested using samples of 9 cm in diameter were placed covering the bottom of a flat beaker and 50 mL of MB solution (10^{-5} mol/dm^3) was added. The flat beaker was placed in sun

simulator, manufactured by Ingenieurbüro Mencke & Tegtmeyer GmbH (Germany) and monitored with Susicontrol software (version 2.9.0), under radiation of 9.8 mW cm^{-2}.
For both the experimental setups, UV and visible, the rate of photocatalytic degradation of MB was analyzed by monitoring the intensity variation of the main absorption peak at 663 nm.
Similarly, to the assays performed in suspension, MB degradation (under UV and visible radiation) in aqueous solution fits a pseudo-first-order reaction, which can be expressed by the Eq.2.3.

5.3. Results

Computational modeling

Modeled structures of the interfaces A/G, A/GO, R/G, and R/GO are presented in Figure 5.1. Equilibrium distances measured between the top of the TiO_2 slabs and the graphene/GO layers are listed in Table 5.2. These distances ranged between 2.53 Å, for the A/GO interface, and 2.92 Å, for the R/GO one.
The interfacial adhesion energy, defined as the difference between the total energy of the interface and the sum of the energies of the TiO_2 slab and the graphene/GO layer, was calculated for all systems. The values obtained, per carbon atom, are also presented in Table 5.2. For all the interfaces, the adhesion energy was negative, which indicates that these are thermodynamically stable. Adhesion energies were three/four times larger for the TiO_2/G interfaces than for the TiO_2/GO ones, which is because graphene layers are perfectly flat and, therefore, TiO_2/G interfaces should be more stable thermodynamically.
The density of States (DOS) were computed in the optimized geometries, to characterize the electronic structure of the interfaces, and are presented in Figure 5.1b, e and k, for the A/G and A/GO systems, and in the supporting information. In both cases, the presence of the graphene/GO leads to significant changes in the DOS of the composites, with the introduction of new energy states inside the band gap of TiO_2. For the A/G interface, the energy gap, calculated as the energy difference between the lowest unoccupied orbital and the highest occupied orbital, is null as the graphene Fermi Energy matches the upper valence band of TiO_2.

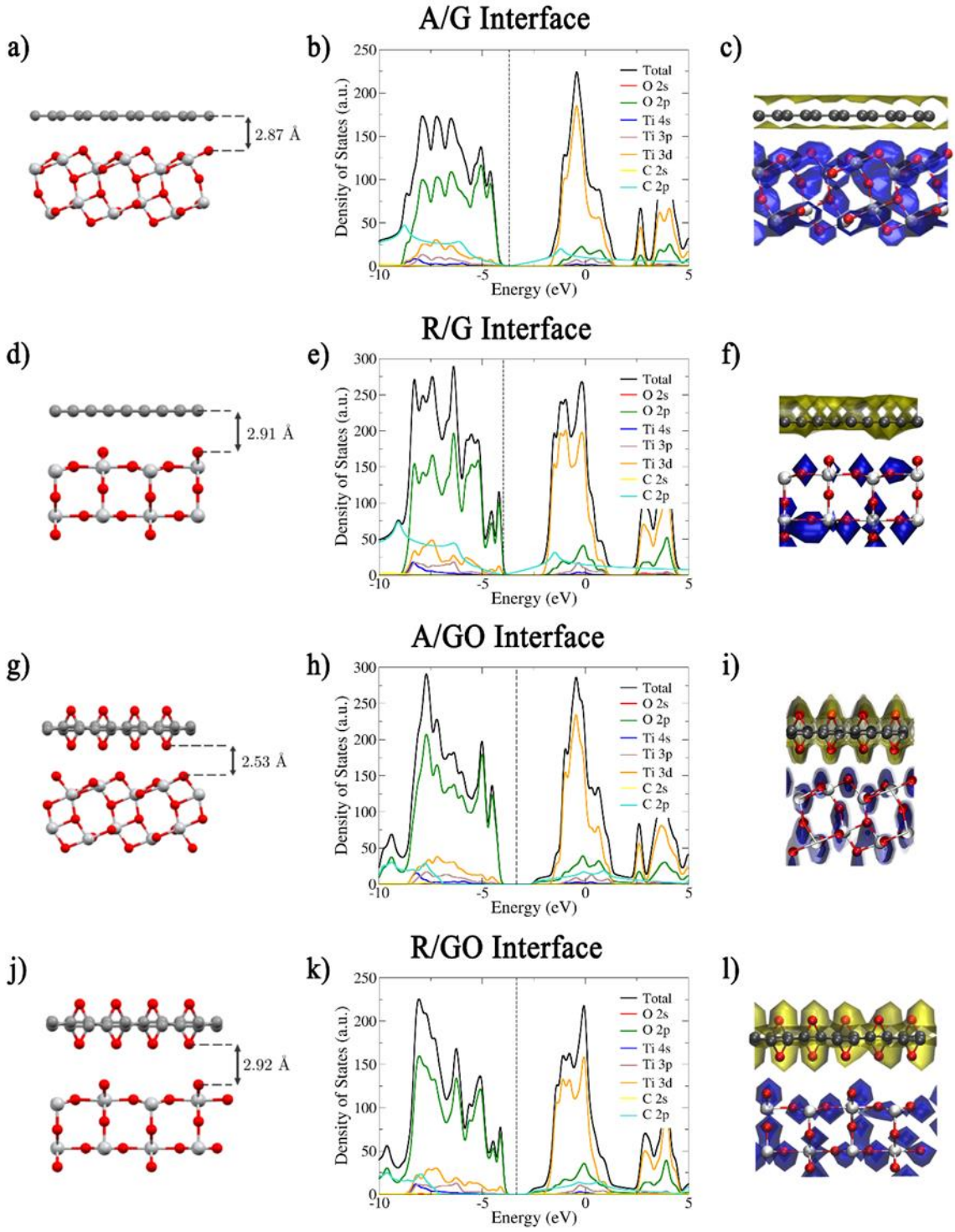

Figure 5.1. Optimized geometries (a), (d), (g), (j), total and partial density of states (b), (e), (h), (k) and charge density differences (c), (f), (i), (l) of the interfaces A/G (a)-(c), R/G (d)-(f), A/GO (g)-(i) and R/GO (j)-(l).

This band is composed mainly of O 2p and Ti 3d states of the TiO_2, whereas the lower conduction band consists of delocalized C 2p states of the graphene. Analogous results

were also obtained for the R/G interface (Figure 5.1d-f). On the other hand, the A/GO interface has a band gap of 1.79 eV, and in this case, the transitions are expected to occur from the O 2p and Ti 3d states of the TiO_2 to the C 2p and O 2p states of the GO. These results were analogous to the obtained for the interface R/GO (Figure 5.1j-l), with a lower gap of 1.31 eV.

Charge density difference maps of the interfaces A/G and A/GO are presented in Figure 5.1c and f), respectively (charge density maps for all the interfaces are presented as supporting information). The blue isosurfaces correspond to regions of charge accumulation, while the yellow isosurfaces represent spaces of charge depletion. For all interfaces, separation of charge carriers was observed, with an accumulation of electrons in the TiO_2 slab and of holes in the graphene/GO layers. The average charge transfer per adlayer atom to the TiO_2 surface slabs, for all the interfaces constructed, are listed in Table 5.2. The calculated values ranged between 8×10^{-7} e/atom, for the R/GO interface, and 7×10^{-4} e/atom, for the A/G one.

Table 5.2. Equilibrium distance, adhesion energy, gap energy and G/GO charge per atom calculated for all interfaces.

Interface	*Equilibrium distance (Å)*	*Adhesion energy (eV/C atom)*	*Gap energy (eV)*	*G/GO charge (e/atom)*
A/G	2.87	-0.028	0	7×10^{-4}
R/G	2.91	-0.021	0	2×10^{-5}
A/GO	2.53	-0.006	1.79	3×10^{-4}
R/GO	2.92	-0.008	1.31	8×10^{-7}

Materials characterization

-TiO_2*/G and* TiO_2*/GO nanocomposites*

SEM analysis of the samples TiO_2, TiO_2/G 1%, 3% and TiO_2/GO 1%, 3% was performed. The results obtained for the nanocomposites with 3% of graphene and GO are presented in Figure 5.2. These images show the presence of TiO_2 agglomerates, and due to the high amount of TiO_2 compared with the carbon nanosheets, the latter are less visible. Also, it is expected that during the hydrothermal treatment the TiO_2 nanoparticles completely adhere to their surfaces. Even so, it is also possible to identify some GO sheets for the TiO_2/GO 3% composite, amplified in the upper right corner of Figure 5.2b.

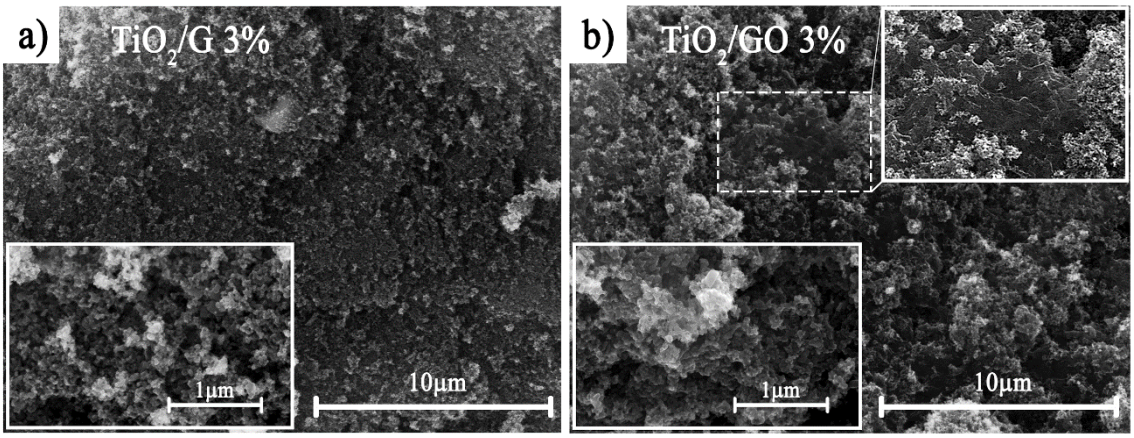

Figure 5.2. SEM micrographs, amplified 10 000 (background images) and 100 000 (insets in the lower left corner) times of TiO_2/G 3% (a) and TiO_2/GO 3% (b) nanocomposites.

The elemental composition of the TiO_2/G 3% and TiO_2/GO 3% nanocomposites was determined by EDX. The results, shown in Figure 5.3a, allowed to identify the presence of carbon (C), oxygen (O) and titanium (Ti), which can all be addressed to the nanocomposites.

XRD was performed to access their crystalline properties. Diffractograms obtained for pure TiO_2, TiO_2/G 3%, and TiO_2/GO 3% nanocomposites are shown in Figure 5.3b.

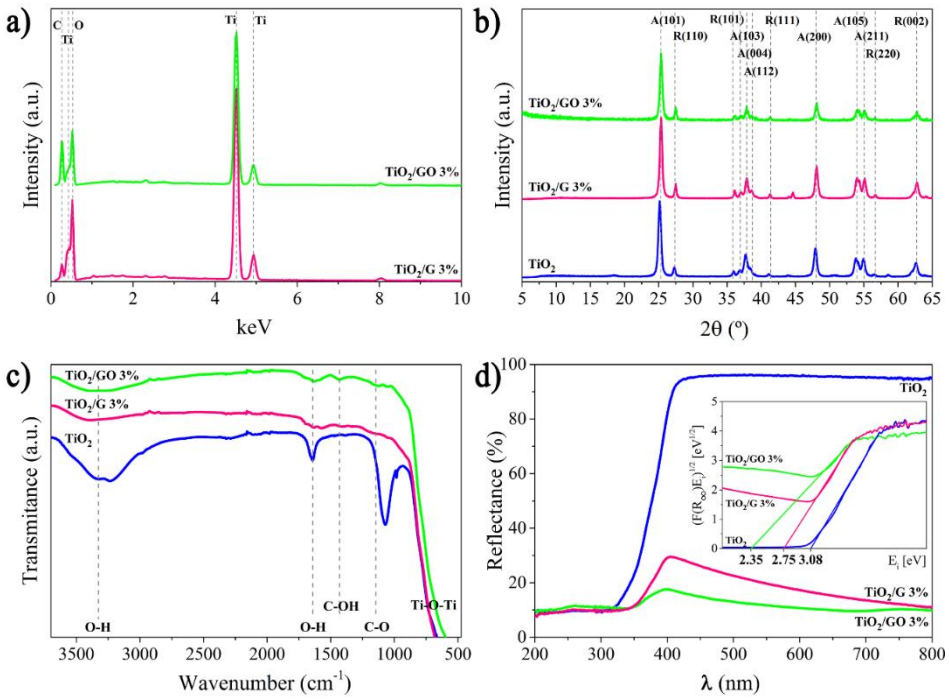

Figure 5.3. EDX spectra (a), XRD patterns (b), FTIR-ATR spectra (c) and DRS spectra (d) of pure TiO_2, TiO_2/G 3% and TiO_2/GO 3% composites.

All of them correspond to the characteristic TiO_2 crystal planes, in both anatase, A, (25º, 38º, and 48º peaks) and rutile, R, (the 27º peak) crystal phases (JCPDS cards 21-1272 and 21-1276, respectively[33]). The expected peaks of graphene (23º-24º) or GO (7º-12º) were not found,[33] probably due to their low concentration in the composites. Using *Match* software (version 1.10b), the weight ratio of anatase and rutile phases was estimated from XRD spectra. The results, listed in 3, indicate that the initial TiO_2 powder is composed of roughly 80% anatase and 20% rutile (in good agreement with the specifications values of the Aeroxide P25 particles. The produced nanocomposites present an anatase content ranging from 73.8% to 77.2% and a rutile content ranging between ≈ 23% and 26%.

FTIR-ATR measurements were performed to assess the chemical interactions within the composites. The spectra obtained for the TiO_2, TiO_2/G 3%, and TiO_2/GO 3% samples are shown in Figure 5.3c.

The most prominent absorption bands observed correspond to water O-H stretching modes (at 3350 cm^{-1} and 1640 cm^{-1}) and Ti-O-Ti bonds (the broad band at wavenumbers between 500 cm^{-1} and 900 cm^{-1}). Additionally, for the graphene/GO nanocomposites, it is also possible to identify the peaks corresponding to hydroxyl C-OH (1425 cm^{-1}) and epoxy C-O (1150 cm^{-1}) stretching modes [8, 35]. These bands are more intense for the TiO_2/GO composites but are also observed for the TiO_2/G ones, which may be due to the incomplete reduction of the GO during the synthesis of the graphene. The high transmittance band observed between 1000 and 450 cm^{-1} shifts to lower wavenumbers for the TiO_2/G 3% and TiO_2/GO 3% nanocomposites, which indicates the interaction between TiO_2 nanoparticles and G/GO, bonds Ti–O–Ti and Ti– O–C.

UV/Vis reflectance of all samples was accessed by DRS and the spectra obtained for pure TiO_2, and for TiO_2/G 3% and TiO_2/GO 3% composites are presented Figure 5.3d. The results show that all the samples reflect approximately 10% of the light when the incident radiation has a wavelength lower than 300 nm. For incident wavelengths in the range 400-800 nm, the reflectance of pure TiO_2 is higher than 90%, Further, for this range, TiO_2/G and TiO_2/GO composites present reflectance values below 30% and 40%, correspondingly. These observations are in good agreement with the dark gray color of the nanocomposites powders and suggest that the these might be photocatalytically active under visible radiation. The band gap of the samples, estimated from DRS spectra by converting the reflectance to Kubelka-Munk units through Eq. (5.1), are shown in the inset graph of Figure 5.3d.

Table 5.3. TiO_2 crystalline phases, estimated from XRD spectra, and gap energies, assessed from DRS spectra, of the produced samples.

Sample	TiO_2 *crystalline phases*		*Gap energy (eV)*
	%Anatase	*%Rutile*	
TiO_2	82	18	3.1
TiO_2/G 0.5%	76	24	2.9
TiO_2/G 1%	76	24	2.9
TiO_2/G 1.5%	76	24	2.9
TiO_2/G 3%	75	25	2.8
TiO_2/GO 0.5%	75	25	2.8
TiO_2/GO 1%	74	26	2.6
TiO_2/GO 1.5%	75	24	2.5
TiO_2/GO 3%	77	23	2.4

The values obtained for all the nanocomposites are listed in Table 5.3 and reveal that the energy gap decreases with increasing wt. % of graphene/GO in the composites. Furthermore, TiO_2/GO samples show a lower band gap (comprised between 2.35 eV and 2.80 eV, depending on the GO content) than the TiO_2/G ones (between 2.75 eV and 2.94 eV) and, in both cases, these values are inferior to pure TiO_2 (3.08 eV).

- *P(VDF-TrFE)/*TiO_2*/GO nanocomposites*

Polymer electrospun mats show smooth fibers with the presence of beads, which suggest that a lower solution viscosity and fully polymer chain entanglement was not achieved. Further, the addition of TiO_2/GO fillers probably leads to an increase of the solution electrical conductivity, and consequently to smaller fiber diameter due to the extra mechanical stretch promoted by the applied electrical field. Therefore, the number of beads presents in the membranes increases, giving origin to a necklace-like fiber structure (Figure 5.4).

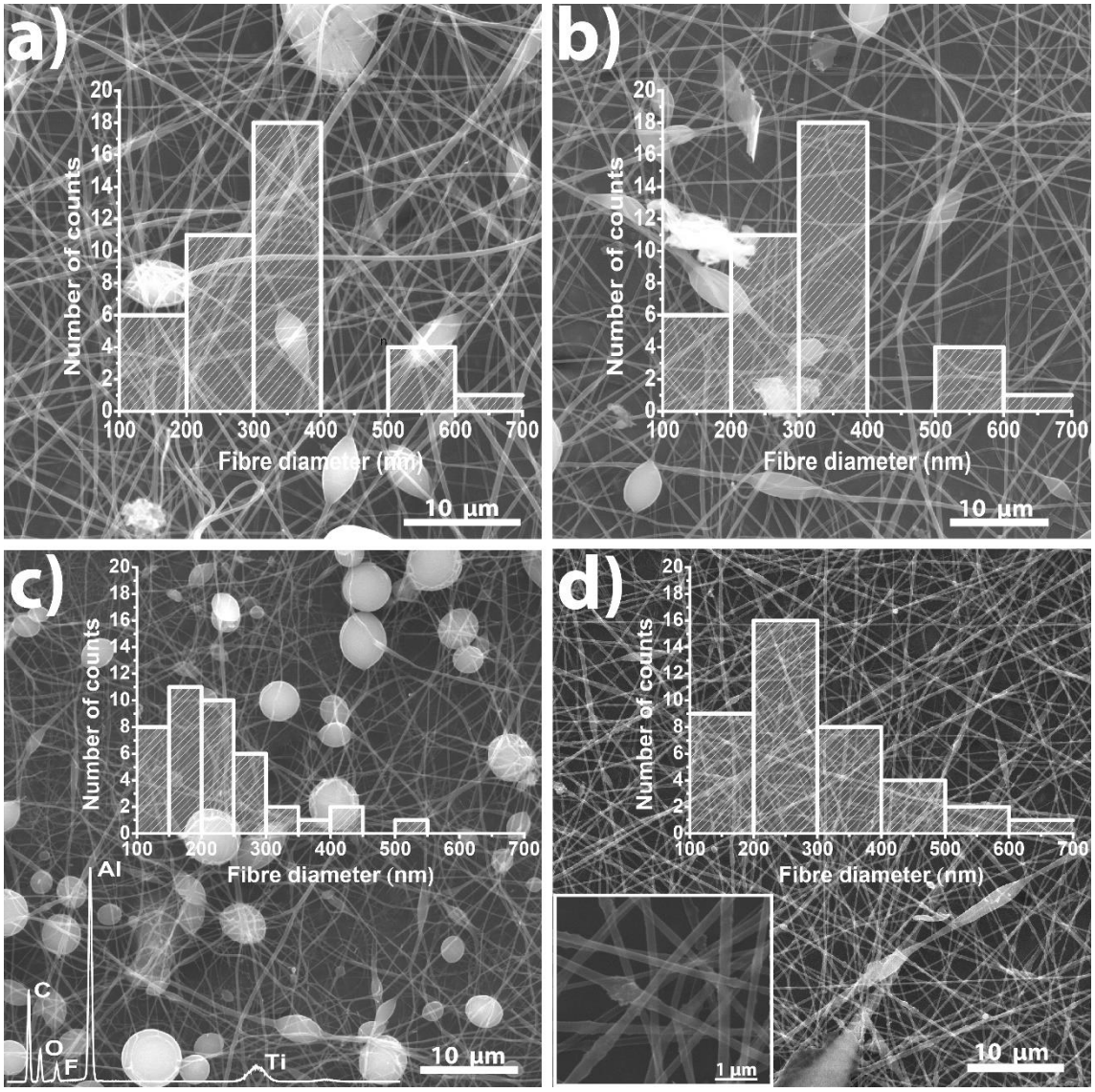

Figure 5.4. SEM micrographs of P(VDF-TrFE)/TiO_2/GO electrospun mats with 3 (a), 5 (b) 8 (c) and 20% (d) of GO/TiO_2. The inset in (c) corresponds to the EDS spectrum. Fiber diameter histograms for all the nanocomposite membranes are also inserted. The inset in (d) shows the fiber structure in detail.

Pristine fibers present an average fiber diameter ≈ 518 ± 119 nm [29], while nanocomposite mats showed a decrease of the average fiber diameter varying from 318 ± 126 down to ≈ 226 ± 93 nm, for the samples from 3 to 8 wt. % of TiO_2/GO. It was reported by Yu et al. [35] that the presence necklace-like fiber mats exhibit superior photocatalytic activity performances, when compared to the membranes made from smooth fiber membranes, for the degradation of organic contaminants under visible light irradiation, probably due to the increase of light scattering and surface area available.

Concerning EDX elemental analysis of the samples (inset in Figure 5.4c), the elemental peaks of C, O, Ti, and F can be identified. All these elements can be addressed to the nanocomposite fibers, C to the polymer and GO, F to the polymer, Ti, and O to the nanoparticles. The presence of a sharp peak of Al is caused by the aluminum foil.

FTIR-ATR analysis (Figure 5.5) confirms that the polymer crystallizes in the electroactive *β*-phase.

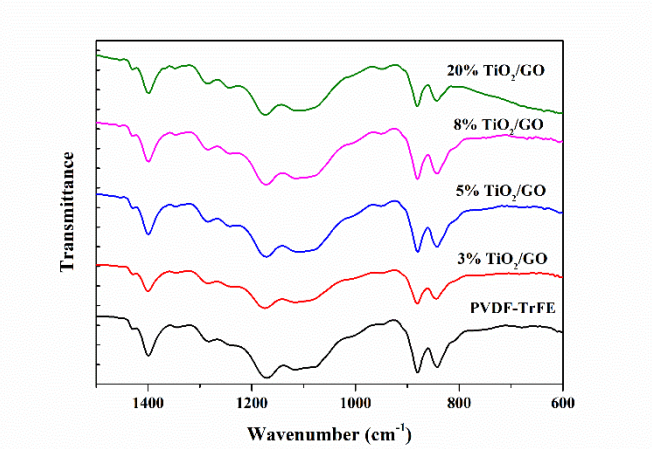

Figure 5.5. FTIR spectra of pristine P(VDF-TrFE) and P(VDF-TrFE)/TiO_2/GO electrospun mats.

Thus, the FTIR-ATR spectra are characterized by the absorption bands of the polymer β -phase (840 and 1279 cm^{-1}), and no trace of the nonpolar α-phase (766, 795 and 855 cm^{-1}) or γ-phase (810 and 833 cm^{-1}) [36] are found in the electrospun composite membranes. It is thus to notice that the presence of the filler does not influence the polymer phase. Further, no new bands, indicating specific filler-polymer bonding are observed.

Photocatalytic experiments

- *Suspension assays*

The investigation of the photocatalytic activity of composites TiO_2/G and TiO_2/GO under UV radiation through the degradation of MB and CIP aqueous solutions, at room temperature. The assessment of pollutants concentration by monitoring the values of the maximum UV-Vis absorbance peaks for 60 minutes. For both solutions, the results obtained using pure TiO_2 and different nanocomposites with G and GO are plotted in Figure 5.6. The apparent reaction rate (k), calculated from the slope of the exponential curve of the concentration plot, and the removal efficiency (both in the UV irradiation period) for all samples are listed in Table 5.4.

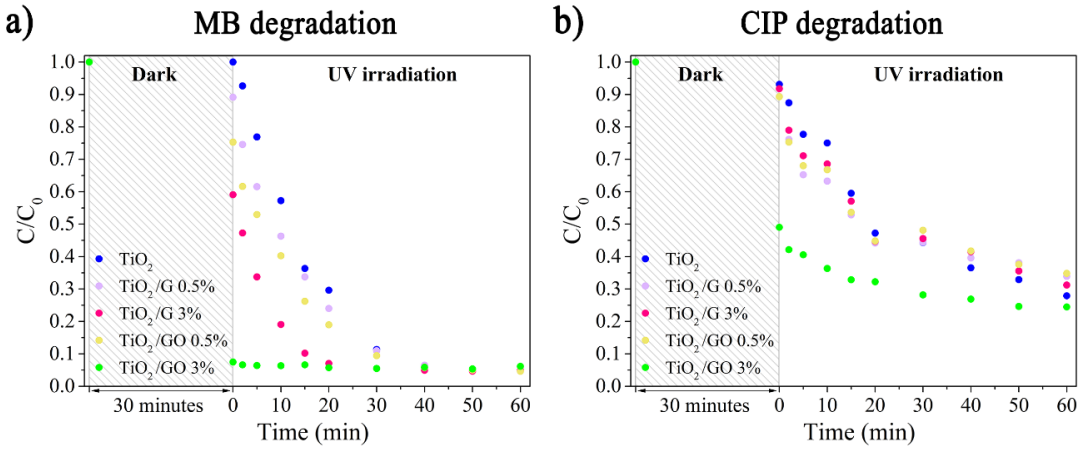

Figure 5.6. Photocatalytic degradation of (a) MB and (b) CIP under UV-light irradiation using pure TiO_2, TiO_2/G 0.5%, TiO_2/G 3%, TiO_2/GO 0.5% and TiO_2/GO 3% nanocomposites.

Before the photocatalytic activity tests, a systematic study was performed to the adsorption process (data not shown), confirming the complete saturation of the nanocomposites in the first ≈ 10 minutes in the dark with the MB solution, under mechanical agitation. For the photocatalytic assays, 30 minutes in the dark for adsorption-desorption were used to assure a complete saturation of the nanocomposites. Concerning the photocatalytic tests (Figure 5.6) a large adsorption of MB dye onto the nanoparticles surface was observed during these 30 minutes, for nanocomposites with higher concentrations of G and GO. Moreover, TiO_2/GO nanocomposites showed higher adsorption of MB than the TiO_2/G ones. For the TiO_2/GO 3% sample, most of the dye was adsorbed onto the catalyst in the equilibration step which prevented the measurement of its photocatalytic activity. The enhanced adsorption of MB is justified by the fact that it is a cationic dye and so it is positively charged in solution. In turn, the presence of carboxylic moieties on the GO surface will favor the electrostatic interaction between the dye and the catalyst surface. A similar but less marked behavior was observed with the CIP solution (Figure 5.6b, as CIP showed a lower affinity for the nanocomposites than the MB. This can be rationalized as CIP is also charged in solution but zwitterionic [37]. Regarding the degradation of MB, the period under UV irradiation (from 0 to 60 minutes), nanocomposites show a higher photocatalytic performance than pure TiO_2, with larger concentrations of G or GO contributing to a faster degradation of the dye (Table 5.5). The only exception was the TiO_2/GO 1% composite that presented the lowest rate of degradation (0.064 min^{-1}). For all the tested nanocomposites, MB was completely degraded after ≈ 30 min under UV irradiation.

Photocatalytic tests using CIP solution revealed that the tested nanocomposites are less efficient in degrading this pollutant than the powdered TiO_2 under UV irradiation. Furthermore, it was also observed that the degradation of the CIP was slower than that of the MB: after 60 minutes of exposure to light, a considerable amount of CIP (between 24% and 35% of the initial concentration) was still present. Moreover, the reaction rates and the photocatalytic degradation efficiencies measured for CIP were similar, irrespectively of the G and GO concentration present in the nanocomposites. The reaction rates of the composites range between 0.010 min^{-1} and 0.016 min^{-1}, and their removal efficiencies range from 50% to 67%.

Furthermore, photocatalytic degradation of the CIP solution was also studied under visible-light irradiation, considering the TiO_2/G and TiO_2/GO nanocomposites. The results obtained are plotted in Figure 5.7, and the corresponding values of the reaction rate and removal efficiency are listed in Table 5.4.

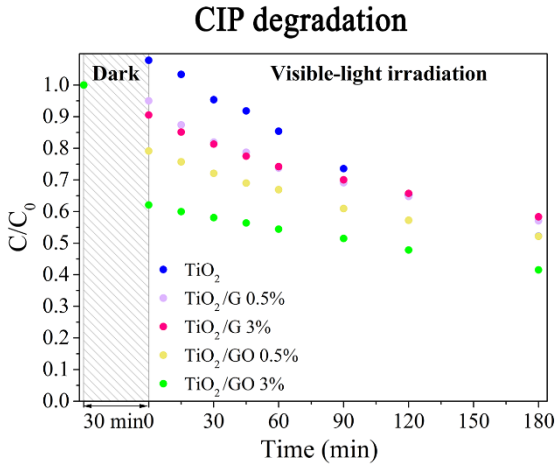

Figure 5.7. Photocatalytic degradation of CIP under visible-light irradiation using TiO_2/G and TiO_2/GO nanocomposites with different contents of G/GO.

Under these conditions, nanocomposites also present a lower photocatalytic activity than pure TiO_2. In fact, a large amount of CIP (between 32% and 59% of the initial concentration) was measured in the solution after 180 minutes of irradiation. The values of the reaction rates and removal efficiencies (alike with UV light) were low and similar for both composites studied (TiO_2/G and TiO_2/G) and did not vary significantly for different G and GO contents. In particular, reaction rates of the composites assumed values between 0.002 min^{-1} and 0.003 min^{-1}, while the removal efficiencies after 180 minutes were comprised between 32.51% and 42.99%.

Table 5.5. First-Order Reaction Rate Constants, *k*, and Photocatalytic Degradation Efficiencies of all the Samples, Determined After the Degradation Tests of MB and CIP Solutions, Carried Out Under 60 Minutes of UV Irradiation and 180 Minutes of Visible Light Irradiation.

	UV irradiation				***Visible light irradiation***	
Sample	***MB degradation***		***CIP degradation***		***CIP degradation***	
	k (min^{-1})	***%***	***k*** (min^{-1})	***%***	***k*** (min^{-1})	***%***
TiO_2	0.070	95.23	0.022	70.04	0.004	51.62
TiO_2/G 0.5%	0.088	94.38	0.014	58.66	0.003	39.94
TiO_2/G 1%	0.105	95.08	0.014	66.48	0.002	32.51
TiO_2/G 1.5%	0.121	94.79	0.015	63.22	0.003	36.37
TiO_2/G 3%	0.160	91.69	0.016	65.99	0.002	35.58
TiO_2/GO 0.5%	0.089	93.85	0.013	61.01	0.002	34.14
TiO_2/GO 1%	0.064	91.64	0.014	61.09	0.003	42.99
TiO_2/GO 1.5%	0.115	85.97	0.014	64.84	0.003	37.75
TiO_2/GO 3%	---	---	0.010	50.08	0.002	33.04

- *Immobilized assays*

The photocatalytic activity of P(VDF-TrFE)/TiO_2/GO fibers prepared with 3, 5, 8 and 20 wt. % filler content were used in the photocatalytic degradation of MB as model reaction under UV irradiation. The control samples of the pure polymer and the polymer membranes with 5 and 20 wt. % of TiO_2 without GO were also analyzed, and the results are shown in Figure 5.8.

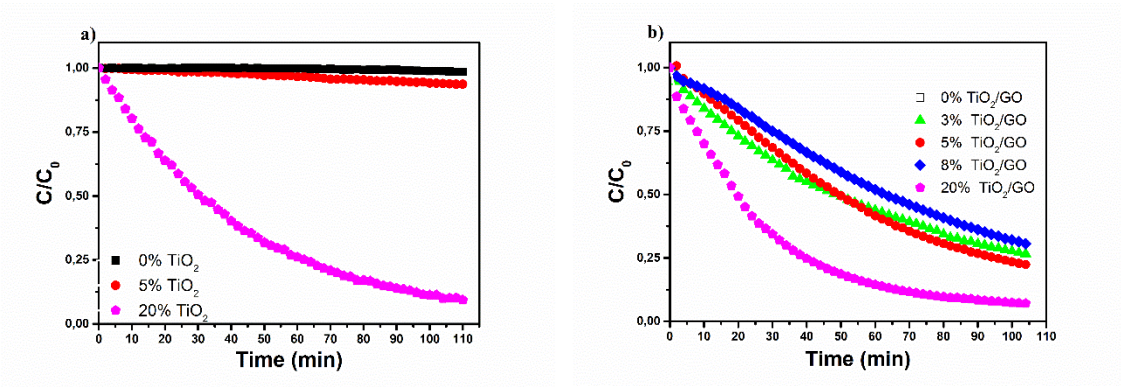

Figure 5.8. Photocatalytic degradation of MB under UV light for the P(VDF-TrFE) fibre membranes prepared with pure TiO_2 (a) and fiber membranes prepared with TiO_2/GO nanocomposite (b).

The photocatalytic degradation assays revealed that the pristine polymer membrane shows only a negligible (≈1%) photocatalytic activity (Figure 5.8a and Table 5.5), what can be attributed to the adsorption of the dye on the fiber mat sample, and thus not to a real degradation of the compound. The samples with 5 wt. % of TiO_2 nanoparticles, presented an MB removal efficiency of 15% and an estimated first-order rate constant (k) of 0.012 min^{-1}, after 90 minutes of UV irradiation. On the other hand, the incorporation of 20 wt. % TiO_2 yielded higher removal efficiency and reaction rate value, 92% and 0.022 min^{-1}, respectively, after the same period. These results are consistent with other works, showing that increasing amounts of immobilized TiO_2 P25 nanoparticles into a polymeric substrate of PA12 (polyamide 12) allowed higher rate constants and improved MB removal. Moreover, it was produced a sample containing 20 wt. % TiO_2 which took approximately 110 minutes to completely degrade the same concentration of MB used in this work, at an irradiance of 5 mW/cm^2 [38]. These results show the dependence of photocatalytic performance on the concentration of the used catalyst and also indicate that the immobilization substrate, in this case, the polymer, also plays a relevant role in the photocatalytic activity. The advantageous electrical characteristics of P(VDF-TrFE), such as high polarization and dielectric constant combined with the low dielectric loss [39], may favor the electron transfer process and consequently enhance the photocatalytic performance of the nanocomposite.

Table 5.6. First-order rate constant (k) and MB removal efficiency estimated values for all the tested P(VDF-TrFE) fiber mats, for 110 min under UV radiation.

Amount of TiO_2 or TiO_2/GO in the sample (wt. %)	**TiO_2**		**TiO_2/GO**	
	k **(min^{-1})**	**Removal (%)**	***k*** **(min^{-1})**	**Removal (%)**
3	-	-	0,013	63
5	0.012	15	0.015	77
8	-	-	0.012	65
20	0.022	92	0.028	93
0	0.0001		0.85	

Regarding the nanocomposites with GO doped TiO_2 (Figure 5.8b), results show that increasing amounts of these nanocomposites yielded removal efficiencies of 63, 77, 65 and 93% for 3, 5, 8 and 20 wt. % TiO_2/GO, respectively. The reaction rate estimated values have a similar trend, varying from 0.013 min^{-1} for the nanocomposite with 3 wt. % of TiO_2/GO up to 0.028 min^{-1} for 20 wt. % of TiO_2/GO. Thereby, a higher amount of TiO_2/GO contributes to faster and more efficient degradation of MB in solution.

However, it is important to notice that the sample with 8 wt. % of nanoparticles does not follow the trend, presenting lower reaction rates and removal efficiencies than the sample with only 5 wt. %. This situation may be caused by different thicknesses of the tested fiber mat sample or even due to a heterogeneous TiO_2/GO distribution over the sample tested. In good agreement, other works equally reported about enhanced photocatalytic degradation using GO nanocomposites towards pristine TiO_2 [40,41]. However, also in these works, when high loadings of GO were used, the photocatalytic efficiency decreased, owing to possible aggregation or scattering. In our study, such limitations were not noticed, the photocatalytic performance increased proportionally with GO concentration, with maximum performance for the sample containing 20 wt. % of TiO_2/GO.

Comparing the nanocomposites membranes with 5 and 20 wt. % of naked and GO doped TiO_2 nanoparticles, results indicate higher rate constants for both the samples with TiO_2/GO (values in Table 5.6). Additionally, the removal efficiency increased from ≈15% in samples with 5 wt. % TiO_2 to 77% in an equivalent sample with GO. These results denote that GO doping plays a more significant role in membranes with lower amounts of nanoparticles (3 and 5%), presenting removal efficiencies much higher than the ones shown by the correspondent fiber membranes with bare TiO_2. For the samples containing 20 wt. % of TiO_2 and TiO_2/GO, both performed an MB removal efficiency of 92 and 93%, for 90 minutes of UV irradiation and a similar rate constant.

To assess photocatalytic degradation under visible radiation the same control samples used for the UV assays were tested (Figure 5.9a).

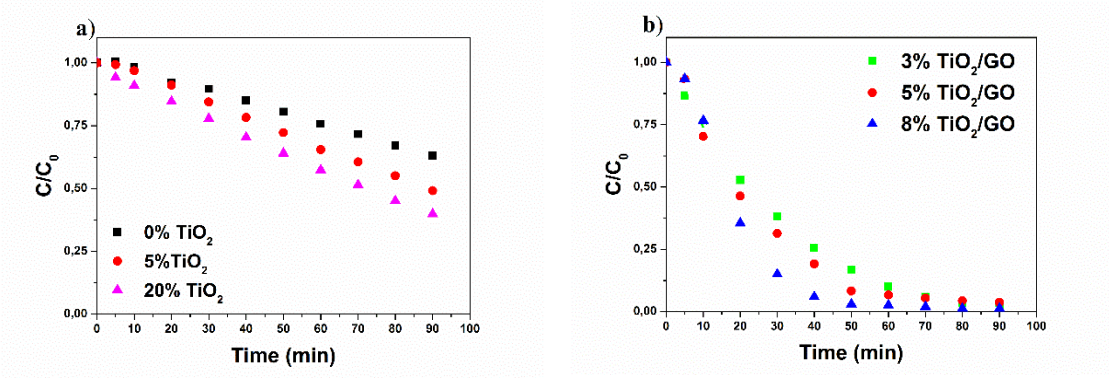

Figure 5.9. Photocatalytic degradation of MB under visible radiation for P(VDF-TrFE) fiber membranes prepared with pure TiO_2 (a) and membranes prepared with TiO_2/GO nanocomposite (b).

MB degradation by membranes prepared without nanoparticles (0 wt. %) removed about 38% of MB from the solution at a rate constant of 0.005 min^{-1} (Table 5.6). Since no

catalytic particles are present in this sample, such MB reduction must be addressed to MB photodegradation. When fibers with 5 and 20 wt. % of TiO_2 nanoparticles were tested, a slight increase in the rate constant to 0.007 and 0.009 min^{-1}, further an MB removal efficiency of 60 and 63% was achieved, respectively. Also, the MB removal should address the adsorption phenomena, which is even enhanced with the incorporation of TiO_2 nanoparticles, due to their porous surface. In this sense, a low photocatalytic activity occurs, which is consistent with the reduced ability of pristine TiO_2 to absorb visible radiation, shown by DRS measurements. The low photocatalytic degradation observed is due to the UVA presence in the visible radiation which corresponds to less than 5% of the visible spectrum.

Table 5.6. First-order rate constant (k) and MB removal efficiency estimated values for all the tested samples, for 90 min under visible radiation.

Amount of TiO_2 or TiO_2/GO in the sample (wt. %)	TiO_2		TiO_2/GO	
	k **(min^{-1})**	**Removal (%)**	***k*** **(min^{-1})**	**Removal (%)**
3	-	-	0.042	98
5	0.007	60	0.048	98
8	-	-	0.075	99
20	0.009	63	-	-
0	0.005		38	

Regarding the nanocomposites containing TiO_2/GO (Figure 5.9b), the MB removal efficiency is ≈98% for the samples with 3 and 5 wt. % of TiO_2/GO, and 99% for the sample containing 8 wt. %, for 90 minutes of visible radiation exposure. The major difference noticed between samples containing different amounts of TiO_2/GO nanoparticles lies on the rate constant, which was 0.075 min^{-1} for the sample with 8 wt. % and merely 0.042 and 0.048 min^{-1} for the samples with 3 and 5 wt. % TiO_2/GO, respectively. The sample with 20 wt. % TiO_2/GO was not tested as the one containing 8 wt. % revealed remarkable photocatalytic efficiency. These results proved that the addition of GO to the nanocomposite enabled photocatalytic activity under visible radiation, as it was expected from the DRS measurements and estimated band gap values previously presented; already pointed towards the potential photocatalytic activity of TiO_2/GO under visible radiation, therefore overcoming one of the handicaps of photocatalysis. [30,42] The beneficial effects of the presence of GO in photocatalysis have been reported by Calza et al., they studied risperidone degradation under artificial

solar light using TiO_2/GO nanocomposites and concluded that higher amounts of GO yielded enhanced photocatalytic activity [13]. Another study showed improved performance of TiO_2/GO nanocomposites regarding the TiO_2 P25 nanoparticles, indicating practically a total degradation and mineralization of pollutants achieved in ≈ 60 minutes, under UV/vis irradiation (6 mW/cm^2) [43].

The incorporation of GO into the nanocomposite has played a relevant role in the photocatalytic activity improvement, both under UVA and visible light radiation. Besides the already mentioned favorable optical properties, GO can act as a suppressor of electron-hole pairs recombination, increasing the formation of highly reactive species involved in the oxidation process [40]. Moreover, as a planar structure, GO provides a superior surface area for MB adsorption and contact interface with TiO_2 [44].

5.4. Discussion

In this study, complementary computational and experimental assays were performed to evaluate the photocatalytic efficiency of TiO_2/G and TiO_2/GO nanocomposites.

Through computational modeling, interfaces between a TiO_2 surface slab (both in anatase and in rutile crystal phases) and a G or GO layer were constructed, and their electronic properties were determined. Similar TiO_2/G interface models were previously studied using density functional theory (DFT) by Ferrighi et al.[17] and Li et al.[16] (interfaces between anatase (101) and graphene) and by Du et al.[18] (interfaces between rutile (110) and graphene). In contrast, the use of DFTB method in this work allowed the construction of larger interfaces than the reported by those authors, with a considerably higher number of atoms and, subsequently, being highly commensurable and presenting deficient strains. On the other hand, to the best of our knowledge, no studies have addressed the computational modeling of TiO_2/GO interfaces. In this case, it is important to note that there is no unique structure for GO, since the conditions and methods of production influence the number, type and distribution of the functional groups of GO [45, 46]. In this work, for simplicity, a model where graphene was utterly functionalized with epoxy C-O groups was considered to evaluate the effect of oxidation on the fundamental properties of TiO_2/GO interfaces.

For both A/G and R/G interfaces, the distances measured between the TiO_2 slab and the graphene sheet after geometry optimization agree well with the values reported. In particular, the separation calculated for the A/G interface was 2.87 Å, while the distances

obtained by the previous authors were comprised between 2.51 Å, using an LDA+U functional [16], and 2.84 Å, considering PBE-D2 and B3LYP-D functional [17]. For the R/G interface, the 2.91 Å separation determined in this work is slightly higher than the 2.75 Å measured by Du et al. [18] through LDA. The smallest separation, of 2.53 Å, was obtained for the A/GO interface, while the distance measured between the rutile and the GO in the R/GO interface was 2.92 Å.

Additionally, analysis of the DOS plots obtained for the A/G and R/G interfaces lead to the observation of new energy states, corresponding to C 2p orbitals of the graphene, inside the band gap of the TiO_2 in full accordance with the reported in the literature [16–19]. For these interfaces, transitions from the valence to the conduction bands occur directly from the O 2p and Ti 3d states of the TiO_2 to the C 2p states of the graphene. Similar results were obtained for the A/GO and R/GO interfaces, where the presence of the GO was responsible for the introduction of new C 2p and O 2p energy states immediately below the conduction band of the pure TiO_2. So, transitions between the O 2p and Ti 3d states of the TiO_2 to this new set of states of the GO could lower the excitation energy for these interfaces.

Due to the existence of additional energy states, the band gaps of the interfaces are lower than those of pure TiO_2. In particular, the gaps observed for the A/G and R/G systems were null, although like for graphene, there are a low number of states at the Fermi Energy. The energy gaps calculated for A/GO and R/GO interfaces were equal to 1.79 eV and 1.31 eV, respectively, which would correspond to visible and near-infrared radiation. This means that the photoexcitation of the electrons of the TiO_2/G and TiO_2/GO composites can be improved concerning the one of the TiO_2 under solar irradiation. Experimental measurements, performed by DRS, showed that the band gap of the nanocomposites is lower than the gap of pure TiO_2 but by a smaller factor. A decrease in the gap energy with the increase of the content of G and GO in the composites was also observed and is qualitatively in agreement with the computational calculations. However, the experimental band gap values of the TiO_2/G samples were higher than the gaps estimated for the TiO_2/GO composites, contrary to what derived from the computations. This apparently counter-intuitive observation might be rationalized considering that the graphene used in the composites was obtained by reduction of the GO and the existence of defects/holes in the carbon network structure is likely [47] and may lead to wide band gap opening.

Furthermore, the charge distribution at the interfaces was also analyzed with computer models which resulted in electrons accumulation in the TiO_2 and hole accumulation in the G and GO layers. This means that there is charge transfer between the TiO_2 slab and the G and GO, resulting in a separation of the charge carriers, which can potentially lead to a reduction of their recombination rate, thus enhancing the mechanism of heterogeneous photocatalysis.

In short, due to their electronic properties, it is expected that the TiO_2/G and TiO_2/GO nanocomposites will possess an enhanced photocatalytic activity, especially under visible-light irradiation, when compared with pure TiO_2. This improvement results from their lower energy gap which can allow the quantitative photoexcitation of electrons with solar radiation. Additionally, the separation of the charge carriers at the interfaces should reduce the electron-hole pair recombination rate, and thus should fundamentally enhance the photocatalytic performance of these materials when compared with pure TiO_2.

In the experimental assays, TiO_2/G and TiO_2/GO nanocomposites degraded MB more efficiently than TiO_2 under UV light, as previously observed by Zhang et al. [12] and Nguyen-Phan et al. [14]. The increase of the photodegradation reaction rates of MB occurred with the rise in G or GO content. For the same content of G and GO, these values were very similar for the TiO_2/G and TiO_2/GO composites. These results are in good agreement with those obtained by Nguyen-Phan et al.,[14] who observed that an increase in GO content from 1 to 10 wt. % yielded higher degradation rates of the MB. At the same time, these results are also in accordance with the computed electronic properties of these materials.

In contrast with the observations with MB, TiO_2/G and TiO_2/GO nanocomposites presented a lower photocatalytic activity under UV light for CIP degradation than pure TiO_2. Furthermore, for this pollutant, the values of the reaction rate constant and removal efficiency did not change significantly, regardless the different G and GO concentration tested. Analogous results were obtained when these photocatalysts were used to degrade the CIP solution under visible-light irradiation.

Computer modeling addresses the fundamental properties of TiO_2/G and TiO_2/GO interfaces, and the results indicate that the composites should have enhanced photocatalytic properties than pure TiO_2 nanoparticles due to their electronic properties. The experimental results have shown that the photocatalytic efficiency is also strongly dependent on the pollutant molecular properties and chemical structure. According to literature, the compound to degrade also influences the dependence of the photocatalytic

activity with the content of G/GO. For example, under UV-light irradiation TiO_2/GO nanocomposites, Nguyen-Phan et al.[14] observed an increase in the degradation rates of the MB with the increase of GO content from 1% to 10%. In contrast, Yadav et al.[48] reported that an increase in wt. % of GO from 0.25% to 2% lead to a decrease in the degradation rates of benzene gas.

The well-known adsorption properties of carbonaceous materials (like G or GO),[14], [49] our computational results and the efficient MB degradation indicate and support the enhanced photocatalytic properties of the nanocomposites compared with the pristine TiO_2. In this sense, the inefficient degradation of CIP is a consequence of the chemical and molecular properties of this compound, and not due to the catalyst the catalyst. The adsorption of MB and CIP after 30 minutes in the dark also mirror this idea; it is possible to observe that the adsorption occurred with MB is significantly higher than with CIP. The adsorption process is critical for photocatalysis efficiency, in this way, the low affinity of CIP molecules with the nanocomposites, compromises the adsorption of CIP into the nanocomposite surface and consequently reduces the photocatalytic efficiency. The described low adsorption is even more evident in the G nanocomposites (for MB and CIP degradation), as it becomes more hydrophobic than GO due to the loss of O groups [50].

These results corroborate the idea that the photocatalytic efficiency depends not only on the electronic properties of the used photocatalyst, but it is also highly dependent on the pollutant considered and of its interactions with the catalyst surface.

In spite of all the advantages above of immobilized photocatalytic systems, mass transfer limitation, surface area loss and a reduction of nanoparticles/nanocomposite exposure to radiation occurs, which leads to lower efficiencies when compared with nanoparticles in suspension. In this scope, the fiber nanocomposites herein proposed present a higher surface area than other nanocomposites, for instance, thin films or membranes, which allows mitigating the undesirable effect of nanoparticles surface area loss. Additionally, fiber mats promote scattering events between adjacent fibers, boosting the light absorption and utilization, thus favoring the photocatalytic process [35,51]. GO is also providing additional features which, once again, allow to minimize the hurdles of immobilization, namely the high conductivity which allows GO to act as an electron acceptor [46]. Moreover, the high adsorption properties of GO rendered by its π - conjugation plays a meaningful role in the overall enhanced photocatalytic activity of this nanocomposite [12].

Comparing the assays with TiO_2/GO in suspension and immobilized in PVDF-TrFE for MB degradation, it is possible to observe a significant reduction in the reaction rate constant, and consequently on time required to attain similar efficiencies. In suspension, after 60 min 91% of MB was degrade, on the other hand, the electrospun membrane required 110 min to degrade 93% of the dye. The membrane as the advantage of retaining the catalyst allowing its reuse and avoiding the secondary pollution (with released nanomaterials). However, the drawback is the mass transfer limitation, reduced surface area, reduction of available catalytic sites, reduced light harvesting. Depending on the application, both materials can be used, as the work proved that both present suitable properties and efficiencies.

5.5. Conclusions

A comprehensive work enclosing a computational study focused on TiO_2/G and TiO_2/GO interfaces, and the experimental photocatalytic performance of these nanocomposites with different contents of G and GO was carried out. Computational results of the fundamental electronic properties of the nanocomposites have shown that these are potentially more efficient than pure TiO_2, due to their lower energy gap and to the existence of a charge separation at the interfaces, which reduces the recombination of electron-hole pairs. The nanocomposites characterization, through SEM, and FTIR confirmed the interaction between TiO_2 nanoparticles and G or GO. Additionally, the reflectance measurements corroborate the computational results, with lower band gaps for the nanocomposites (ranging from 2.94 to 2.35 eV) compared with TiO_2 (3.08 eV). Experimental results revealed that the nanocomposites degrade more efficiently the MB than the TiO_2, but the opposite occurs for CIP. These results indicate that the photocatalytic efficiency depends not only on the properties of the catalyst but also on the compound to degrade and its favorable/unfavorable interactions with the catalytic surface. In this situation, CIP does not have an efficient interaction with the nanocomposite surface, which promotes low adsorption and adverse outcomes for the photocatalytic process. Therefore, further theoretical and experimental studies are required with different pollutants to fully elucidate the mechanism behind the observed behavior of these composites and to be able to accurately match photocatalyst properties with specific contaminants for an optimized degradation.

Finally, concerning the photocatalytic activity of the P(VDF-TrFE) electrospun nanocomposite, the results showed that GO incorporation improves MB adsorption, reaction rate, and removal efficiency, both under UV and visible radiation (similarly to the results obtained in suspension assays). Under UV radiation and 5% of TiO_2/GO, the MB removal increased about 80% comparatively to the correspondent sample without GO. Additionally, under simulated visible light radiation all the samples containing GO were able to remove ≈100% of MB in less than 90 minutes. The high surface area and porosity of the electrospun samples together with the advantageous electrical and structural properties of GO, especially avoiding electron-hole recombination and favoring adsorption, promote a notable photocatalytic performance. Thus, the proposed electrospun nanocomposite is a promising system to degrade organic pollutants in aqueous or gaseous systems.

5.6. References

1. Schwarzenbach, R.P., et al., The Challenge of Micropollutants in Aquatic Systems. Science, 2006. 313(5790): p. 1072-1077.

2. Muñoz, I., et al., Ranking potential impacts of priority and emerging pollutants in urban wastewater through life cycle impact assessment. Chemosphere, 2008. 74(1): p. 37-44.

3. Eckert, H., et al., Modeling of photocatalytic degradation of organic components in water by nanoparticle suspension. Chemical Engineering Journal, 2015. 261: p. 67-75.

4. Martins, P.M., et al., Improving Photocatalytic Performance and Recyclability by Development of Er-Doped and Er/Pr-Codoped TiO_2/Poly(vinylidene difluoride)–Trifluoroethylene Composite Membranes. The Journal of Physical Chemistry C, 2014. 118(48): p. 27944-27953.

5. Luo, Y., et al., A review on the occurrence of micropollutants in the aquatic environment and their fate and removal during wastewater treatment. Science of The Total Environment, 2014. 473-474: p. 619-641.

6. Mills, A. and S. Le Hunte, An overview of semiconductor photocatalysis. Journal of Photochemistry and Photobiology A: Chemistry, 1997. 108(1): p. 1-35.

7. Anandan, S., et al., Superhydrophilic Graphene-Loaded TiO_2 Thin Film for Self-Cleaning Applications. ACS Applied Materials & Interfaces, 2013. 5(1): p. 207-212.

8. Almeida, N.A., et al., TiO_2/graphene oxide immobilized in P(VDF-TrFE) electrospun membranes with enhanced visible-light-induced photocatalytic performance. Journal of Materials Science, 2016. 51(14): p. 6974-6986.

9. Kozlova, E.A. and A.V. Vorontsov, Noble metal and sulfuric acid modified TiO_2 photocatalysts: Mineralization of organophosphorous compounds. Applied Catalysis B: Environmental, 2006. 63(1): p. 114-123.

10. Marschall, R. and L. Wang, Non-metal doping of transition metal oxides for visible-light photocatalysis. Catalysis Today, 2014. 225: p. 111-135.

11. Liu, J., et al., Photocatalytic degradation of commercially sourced naphthenic acids by TiO2-graphene composite nanomaterial. Chemosphere, 2016. 149: p. 328-335.

12. Zhang, H., et al., P25-Graphene Composite as a High Performance Photocatalyst. ACS Nano, 2010. 4(1): p. 380-386.

13. Calza, P., et al., Photocatalytic transformation of the antipsychotic drug risperidone in aqueous media on reduced graphene oxide—TiO_2 composites. Applied Catalysis B: Environmental, 2016. 183: p. 96-106.

14. Nguyen-Phan, T.-D., et al., The role of graphene oxide content on the adsorption-enhanced photocatalysis of titanium dioxide/graphene oxide composites. Chemical Engineering Journal, 2011. 170(1): p. 226-232.

15. Wang, P., et al., Dye-Sensitization-Induced Visible-Light Reduction of Graphene Oxide for the Enhanced TiO2 Photocatalytic Performance. ACS Applied Materials & Interfaces, 2013. 5(8): p. 2924-2929.

16. Li, X., H. Gao, and G. Liu, A LDA+U study of the hybrid graphene/anatase TiO_2 nanocomposites: Interfacial properties and visible light response. Computational and Theoretical Chemistry, 2013. 1025: p. 30-34.

17. Lara, F., F. Gianluca, and V.C. Di, Charge Carriers Separation at the Graphene/(101) Anatase TiO_2 Interface. Advanced Materials Interfaces, 2016. 3(6): p. 1500624.

18. Du, A., et al., Hybrid Graphene/Titania Nanocomposite: Interface Charge Transfer, Hole Doping, and Sensitization for Visible Light Response. The Journal of Physical Chemistry Letters, 2011. 2(8): p. 894-899.

19. Shen, J., et al., Preparation of doped TiO_2 nanofiber membranes through electrospinning and their application for photocatalytic degradation of malachite green. Journal of Materials Science, 2014. 49(5): p. 2303-2314.

20. Zhu, P., et al., Facile Fabrication of TiO_2–Graphene Composite with Enhanced Photovoltaic and Photocatalytic Properties by Electrospinning. ACS Applied Materials & Interfaces, 2012. 4(2): p. 581-585.

21. Doh, S.J., et al., Development of photocatalytic TiO_2 nanofibers by electrospinning and its application to degradation of dye pollutants. Journal of Hazardous Materials, 2008. 154(1): p. 118-127.

22. Botelho, G., et al., Performance of electroactive poly(vinylidene fluoride) against UV radiation. Polymer Testing, 2008. 27(7): p. 818-822.

23. Aradi, B., B. Hourahine, and T. Frauenheim, DFTB+, a Sparse Matrix-Based Implementation of the DFTB Method. The Journal of Physical Chemistry A, 2007. 111(26): p. 5678-5684.

24. Koskinen, P. and V. Mäkinen, Density-functional tight-binding for beginners. Computational Materials Science, 2009. 47(1): p. 237-253.

25. Elstner, M. and G. Seifert, Density functional tight binding. Philosophical Transactions of the Royal Society A: Mathematical,
Physical and Engineering Sciences, 2014. 372(2011).

26. Hummers, W.S. and R.E. Offeman, Preparation of Graphitic Oxide. Journal of the American Chemical Society, 1958. 80(6): p. 1339-1339.

27. Goncalves, G., et al., Surface Modification of Graphene Nanosheets with Gold Nanoparticles: The Role of Oxygen Moieties at Graphene Surface on Gold Nucleation and Growth. Chemistry of Materials, 2009. 21(20): p. 4796-4802.

28. Sencadas, V., et al., Fiber average size and distribution dependence on the electrospinning parameters of poly(vinylidene fluoride–trifluoroethylene) membranes for biomedical applications. Applied Physics A, 2012. 109(3): p. 685-691.

29. Torrent, J. and V. Barron, Diffuse reflectance spectroscopy. Methods of soil analysis. Part, 2008. 5: p. 367-387.

30. Hoffmann, M.R., et al., Environmental Applications of Semiconductor Photocatalysis. Chemical Reviews, 1995. 95(1): p. 69-96.

31. Marques, J., et al., Release of Volatile Compounds from Polymeric Microcapsules Mediated by Photocatalytic Nanoparticles. International Journal of Photoenergy, 2013. 2013: p. 9.

32. Dufour, F., et al., Morphological control of TiO_2 anatase nanoparticles: What is the good surface property to obtain efficient photocatalysts? Applied Catalysis B: Environmental, 2015. 174-175: p. 350-360.

33. Blanton, T.N. and D. Majumdar, Characterization of X-ray irradiated graphene oxide coatings using X-ray diffraction, X-ray photoelectron spectroscopy, and atomic force microscopy. Powder Diffraction, 2013. 28(2): p. 68-71.

34. Wang, P., et al., One-step synthesis of easy-recycling TiO_2-rGO nanocomposite photocatalysts with enhanced photocatalytic activity. Applied Catalysis B: Environmental, 2013. 132-133: p. 452-459.

35. Yu, H., et al., Fabrication of Ag3PO4-PAN composite nanofibers for photocatalytic applications. CrystEngComm, 2013. 15(24): p. 4802-4805.

36. Martins, P., A.C. Lopes, and S. Lanceros-Mendez, Electroactive phases of poly(vinylidene fluoride): Determination, processing and applications. Progress in Polymer Science, 2014. 39(4): p. 683-706.

37. Garrido, J.M.P.J., et al., β–Cyclodextrin carbon nanotube-enhanced sensor for ciprofloxacin detection. Journal of Environmental Science and Health, Part A, 2017. 52(4): p. 313-319.

38. Cossich, E., et al., Development of electrospun photocatalytic TiO_2-polyamide-12 nanocomposites. Materials Chemistry and Physics, 2015. 164: p. 91-97.

39. Garcia-Gutierrez, M.-C., et al., Understanding crystallization features of P(VDF-TrFE) copolymers under confinement to optimize ferroelectricity in nanostructures. Nanoscale, 2013. 5(13): p. 6006-6012.

40. Adamu, H., P. Dubey, and J.A. Anderson, Probing the role of thermally reduced graphene oxide in enhancing performance of TiO_2 in photocatalytic phenol removal from aqueous environments. Chemical Engineering Journal, 2016. 284: p. 380-388.

41. Pant, H.R., et al., Immobilization of TiO_2 nanofibers on reduced graphene sheets: Novel strategy in electrospinning. Journal of Colloid and Interface Science, 2015. 457: p. 174-179.

42. Park, H., et al., Surface modification of TiO_2 photocatalyst for environmental applications. Journal of Photochemistry and Photobiology C: Photochemistry Reviews, 2013. 15: p. 1-20.

43. Pastrana-Martínez, L.M., et al., Advanced nanostructured photocatalysts based on reduced graphene oxide–TiO_2 composites for degradation of diphenhydramine pharmaceutical and methyl orange dye. Applied Catalysis B: Environmental, 2012. 123-124: p. 241-256.

44. Cao, Y.-C., et al., Reduced graphene oxide supported titanium dioxide nanomaterials for the photocatalysis with long cycling life. Applied Surface Science, 2015. 355: p. 1289-1294.

45. Nasehnia, F., et al., First principles study on optical response of graphene oxides: From reduced graphene oxide to the fully oxidized surface. Computational Materials Science, 2016. 114: p. 112-120.

46. Putri, L.K., et al., Graphene oxide: Exploiting its unique properties toward visible-light-driven photocatalysis. Applied Materials Today, 2016. 4: p. 9-16.

47. Bagri, A., et al., Structural evolution during the reduction of chemically derived graphene oxide. Nature Chemistry, 2010. 2: p. 581.

48. Yadav, H.M. and J.-S. Kim, Solvothermal synthesis of anatase TiO_2-graphene oxide nanocomposites and their photocatalytic performance. Journal of Alloys and Compounds, 2016. 688: p. 123-129.

49. Bai, H., et al., Enhanced adsorbability and photocatalytic activity of TiO_2-graphene composite for polycyclic aromatic hydrocarbons removal in aqueous phase. Colloids and Surfaces B: Biointerfaces, 2017. 150: p. 68-77.

50. Faraldos, M. and A. Bahamonde, Environmental applications of titania-graphene photocatalysts. Catalysis Today, 2017. 285: p. 13-28.

51. Anjusree, G.S., et al., Facile fabrication of TiO_2 nanoparticle–TiO_2 nanofiber composites by co-electrospinning–electrospraying for dye-sensitized solar cells. Journal of Energy Chemistry, 2015. 24(6): p. 762-769.

6. Reusable photocatalytic optical fibers for underground, deep-sea and turbid water remediation

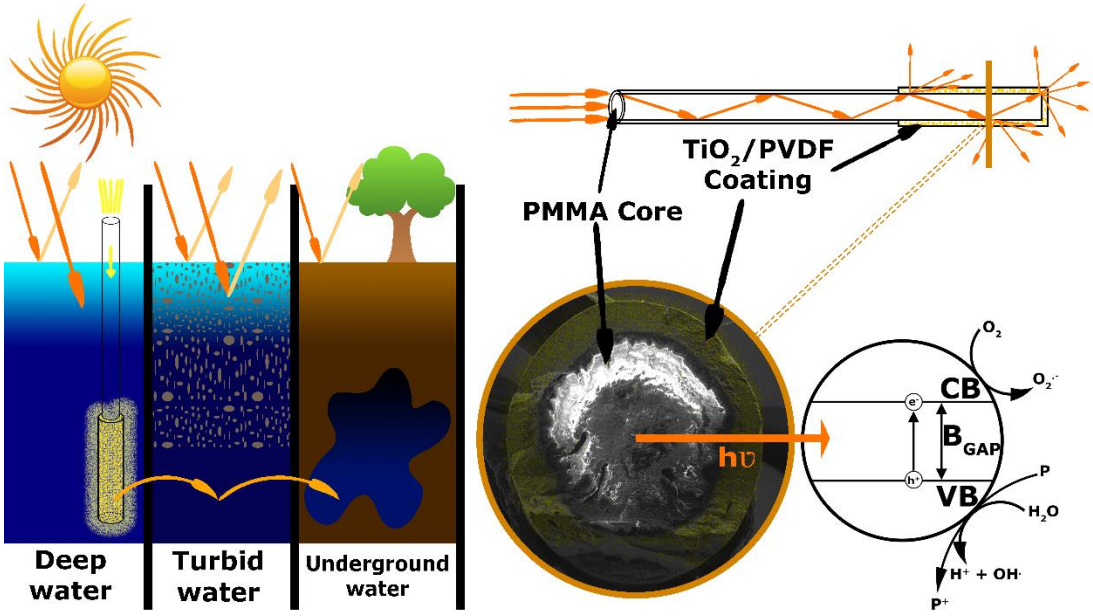

This work reports the development of a TiO_2/PVDF coating for polymeric optical fibers (POF). The hybrid material was characterized, and the degradation of ciprofloxacin under visible light and its reusability were here evaluated.

This chapter is based on the following publications: Teixeira, S., et al., *Reusable Photocatalytic Optical Fibers for Underground, Deep-Sea, and Turbid Water Remediation*. Global Challenges, 2018. 2(3): p. 1700124.

6.1. Introduction

AOP and adsorption have emerged as an effective alternative to conventional wastewater treatments to address environmental issues [1–3]. In spite of the simplicity and cost-effectiveness of adsorption, this method does not degrade the pollutant and may yield secondary pollution during disposal of adsorbent material [4,5]. Relatively to AOP's, it involves the generation of hydroxyl radicals that are highly reactive and oxidize the pollutants [6,7]. This process includes treatments, such as ozonation, Fenton oxidation, and photocatalysis [8,9]. The latter is an inexpensive technique because it only requires a source of radiation (UV or sunlight) and a photocatalyst, which is typically a semiconductor material [10,11]. Among photocatalysts, titanium dioxide (TiO_2) has shown to be effective in the removal of organic pollutants. Its remarkable photocatalytic activity and chemical/photo-stability are key properties to allow high efficiencies [12]. Additionally, studies focused on the environmental toxicity of different catalysts have shown that TiO_2 nanoparticles are less toxic than other catalysts [13], such as zinc oxide (ZnO) nanoparticles [14], In the last decades, many novel materials have been produced and investigated in the scope of photocatalysis. Most of these studies focus on overcoming the drawbacks of current photocatalysis limitations, such as the reduced spectral activation of TiO_2 (only active under UV radiation) and the difficulty in recovering and reusing the nanocatalyst used in slurry systems. In the former case, the approaches are doping catalytic materials [15, 18] or the production of nanocomposites [19, 20] with reduced band gap and enhanced photoactivation under visible radiation. Concerning the reusability, the nanocatalysts are typically immobilized on substrates that prevent their loss and allows reusability. In this sense, the expensive and time-consuming step for photocatalysts recovery becomes unnecessary [21,22]. Several substrates, such as glass [23,24], stainless steel [23,24], polymers [25,26], zeolites [27,28], silica [29,30] and magnetic particles [31], among others, have been used in the immobilization of photocatalytic materials.

Despite the significant and extensive research on the issues above mentioned, other relevant challenges still need to be addressed to apply photocatalysis to unexplored and highly important environments. For instance, the turbidity of the polluted water is one of the most important factors to consider in a photo-dependent reaction as photocatalysis [32,33]. The presence of particles in suspension (*e.g.*, solids, inorganic and fecal material)

can scatter the light or completely impede its penetration, leading to a reduction of the efficiency of the system [34,35]. Further, these suspended particles can act as active sites for the adsorption of microorganisms and contaminants, disabling the light-driven disinfection and pollutants degradation [36,37]. Additionally, in the photocatalytic slurry systems, increasing the concentration of the photocatalytic nanoparticles - to increase the photocatalytic efficiency - can cause undesirable turbidity that just like the pollutant particles will reduce the light penetration and thus the photocatalytic efficiency [38,39]. The removal of turbidity is a costly and time-consuming pre-treatment, such as coagulation-flocculation [40,41] and membrane filtration [37,42]. Moreover, the coagulants (iron and aluminum salts) used to change the polluted water pH, can be ecotoxic and generate large sludge volumes [43–45]. Concerning the filtration processes, membrane fouling is one of the major drawbacks [46,47].

Other challenges are two emerging environmental problems: the remediation of contaminated groundwater and deep-sea water (> 200 m). In the past, deep-sea water was considered an uncontaminated environment [48]. However, the intense research in this area indicates that both environments are affected by the increasing anthropogenic actions like agriculture, landfills, irrigation water, oil drilling, sea mining, and trawling [49, 50]. Recent studies indicate that deep-sea can accumulate contaminants like oil [51, 52] and other persistent organic pollutants [48]. Similarly, studies about groundwater pollution have revealed contamination with polycyclic aromatic hydrocarbons [53], fuel hydrocarbons, chlorinated ethylenes, and non-chlorinated solvents [54]. The existing technologies to remediate groundwater (*e.g.*, pump and treat, oxidation, biodegradation, and adsorption) are expensive and inefficient [55–57]. This lack of efficient technologies to remediate remote polluted water increases the demand for new materials and efficient technologies.

As a possible solution, the use of optical fibers as a substrate for photocatalyst immobilization can overcome the mentioned limitations, enabling the utilization of the photocatalytic process in turbid, ground or deep-sea polluted water. In this system, the optical fibers play a double role: 1) as photocatalyst support and 2) as an efficient light transmission tool. This approach avoids light loss caused by turbidity because the light directly reaches the photocatalyst immobilized on the surface of the optical fibers and since the photocatalyst is immobilized, it is possible to reuse the material, reducing the overall process costs [46]. Marinangeli and Ollis [58–60] firstly proposed the use of

quartz optical fibers with TiO_2 deposition for remote light transmission and as solid support for photocatalysts in the late 1970s. Later, Hofstadler et al. [61] designed a TiO_2-coated quartz fiber reactor and used it in the degradation of 4-chlorophenol in water. More recently, polymeric optical fibers (POF) of poly(methyl methacrylate) (PMMA) have been investigated, mainly due to their high mechanic flexibility, thermal stability, visible light transmission, simple handling and low cost [6, 62–65]. The practicability of the POF should be highlighted since quartz optical fibers are more expensive and fragile. The first photocatalytic application of PMMA optical fibers with immobilized TiO_2 nanoparticles on the surface was reported by Joo et al. [6]. Despite the promising results, the weak immobilization of the catalyst onto the POF surface did not allow efficient reuse of the material and leads to secondary pollution due to nanoparticle detachment from the POF surface.

The lack of reusable photocatalytic materials demands for new and robust coatings to efficiently immobilize the catalyst on the surface of the POF. In this sense, polymers as embedding matrices arise as an interesting approach, as they are chemically and mechanically stable, inexpensive, exhibit high durability and may display a porous microstructure, suitable for photocatalytic applications [66,67]. These features make polymers one of the most used coating materials [68, 70].

In this scope, the present paper reports on the first study on a reusable photocatalytic polymeric coating in POF employed for degrading organic pollutants. Poly(vinylidene difluoride) (PVDF) was used to immobilize TiO_2 P25 nanoparticles onto the surface of the PMMA-POF due to its high resistance and the possibility to tailor the degree of porosity and pore size [71]. Ciprofloxacin (CIP), a fluoroquinolone antibiotic, was used as a model pollutant to assess the photocatalytic efficiency and reusability of the produced materials.

6.2. Experimental Section

6.2.1. Coating of the Polymeric Optical Fibers

Firstly, according to the procedure used by Peill and Hoffmann [72], a coating solution consisting of an aqueous dispersion of 15% (w/w) TiO_2 nanoparticles (P25 – kindly provided by Evonik ®) was produced to assess the mechanical stability of the TiO_2 nanoparticles coating on PMMA-POF. According to the manufacturer, the TiO_2 P25

nanoparticles have 21 nm diameter, a surface area of 50 ± 15 m^2/g, and the anatase:rutile ratio is typically 70:30. The coating obtained with TiO_2 nanoparticles was further compared to the polymeric coatings. For this, different polymeric coating solutions were prepared to evaluate the mechanical stability of the coatings. Therefore, various amounts of PVDF (1010/1001, Solef) were dissolved in 9.7; 9.5; 9 and 8.5 mL of N, N-Dimethylacetamide (DMA, Sigma-Aldrich, purity ≥ 99.5 %) to reach final concentrations of 3, 5, 10 and 15 % (w/w) of PVDF, respectively. Mechanical stirring was applied until complete polymer dissolution.

To optimize the photocatalytic performance of the PVDF-based coatings, different amounts of TiO_2 (25, 40 and 50 w/w %) were dispersed in DMA using an ultrasonic bath for three hours. Afterward, the polymer was added to reach the final concentration of 15 % (w/w), and the solution was mechanically stirred until complete polymer dissolution.

The end tip (6 cm) of the 2-mm poly(methyl methacrylate) (PMMA) optical fibers (Conrad®) 60 cm long was roughened with a sandpaper nº 80 (Buehler). Acetone was used to eradicate the cladding debris. The 6 cm end tip of the POF was dip-coated with the selected coating solutions and withdrawn after ten seconds. The dipped fibers dried at room temperature for 12 hours. For different coating thicknesses, it was performed an increasing number (1, 2, 4 and 6) of consecutive dipping, repeating the dipping procedure.

6.2.2. Characterization of POF coated with TiO_2/PVDF

The morphological characterization was assessed by SEM, using an FEI Quanta 650 FEG microscope equipped with an INCA 350 spectrometer (Oxford Instruments) for EDX, for elemental and distribution analyses. To determine the coating thickness, microscopy (Optiphot-100 50 W from Nikon; camera model EC3 from Leica) was used and each sample was analyzed 20 times (Image J - version 1.48). The adhesion of the coating to the optical fiber was assessed placing a tape strip (7 cm) longitudinally to the fiber coating and removed after 1 minute, measuring the fiber weight before and after the test to estimate the coating mass loss. Optical microscopy was also used to evaluate the integrity of the coating. To assess the attenuation and to determine the amount of light absorbed by the coating, the difference between the input and the output of artificial sunlight was calculated. For that, the fibers (60 cm long) were stretched, one of the tips was placed next to the light source (9.8 mW/cm^2), and at the opposite end, the light output was

measured with a power detector (XLP12-3S-H2-D0, from GENTEC industries). These tests were performed in POF without cladding, with cladding, coating with PVDF and with a 50 % (w/w) TiO_2/PVDF coating.

6.2.3. Photocatalytic degradation experiments

The photocatalytic assays were carried out using a sun simulator (AM1.5, Ingenieurbüro Mencke & Tegtmeyer GmbH) with a light intensity of 9.8 mW/cm^2. A beaker with (80 mL) aqueous solution (5 mg L^{-1}) of CIP, purchased to Sigma-Aldrich, was used to test the photocatalytic activity of 20 POF with a 2-mm diameter POF bundle and 60 cm long - represented on Figure 6.1.

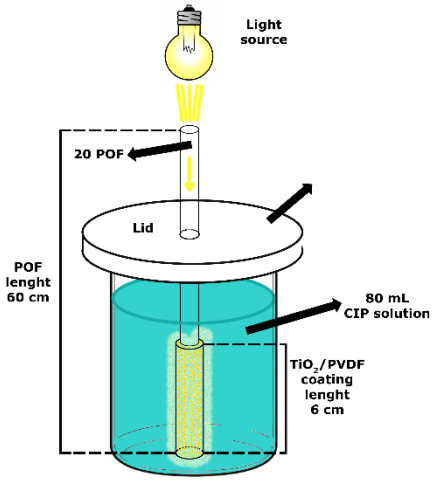

Figure 6.1. Schematic representation of the photocatalytic assays set up.

The POFs dipped once in the 50 w/w % TiO_2/PVDF solution were used for the photocatalytic assays. The light was focused at the top of the POF bundle and transmitted through the 60 cm of the fibers. The 6 cm of TiO_2/PVDF coating was wholly immersed in the CIP solution. Between the CIP solution and the irradiation source, it was placed a polystyrene lid with through holes for the fibers to pass. The spacing between the fibers prevented exfoliation of the photocatalytic coating and the cover completely covered the CIP solution to avoid the irradiation to reach the solution except by the optical fibers. Before illumination, the solution with the immersed POF coated part was stirred in the dark for 30 min to achieve the adsorption-desorption equilibrium of the antibiotic onto the photocatalytic coating. Later, the POF were exposed to artificial sunlight for 72 h under constant magnetic stirring. Aliquots of 2 mL were withdrawn every 24 hours. As controls, experiments were carried out in the absence of the photocatalytic coating. The

photocatalytic degradation was determined by analyzing the decrease of the absorption peak of ciprofloxacin with a maximum at 278 nm by UV-vis spectrophotometry (Varian CARY-100 UV-vis, Agilent). Three degradation cycles of 72 hours each were performed to study the reusability of the photocatalytic coating. The CIP degradation fits a pseudo-first order reaction, following the Langmuir-Hinshelwood model, represented by Eq. 2.3, in chapter 2 [8].

The degradation rate was calculated from the slope of the exponential curve of the concentration plot as a function of time.

6.3. Results and discussion

6.3.1. Characterization of the coating

To understand and improve previously reported approaches, SEM images (Figure 6.2) show a POF surface coated with TiO_2 dispersed in water in which cracks (Figure 6.a) and coating detachment (Figure 6.2b) were observed, and therefore, a smooth and stable coating layer was not obtained. The TiO_2 coating was delaminated when introduced in water caused by the water flow. Agglomeration of the TiO_2 particles and delamination of the coating were previously reported by Peil and Hoffman [72]. It is to notice that the detachment of the photocatalyst decreases the POF photocatalytic efficiency limiting its reusability. Further, nanoparticles detachment it is also the cause of undesirable secondary pollution.

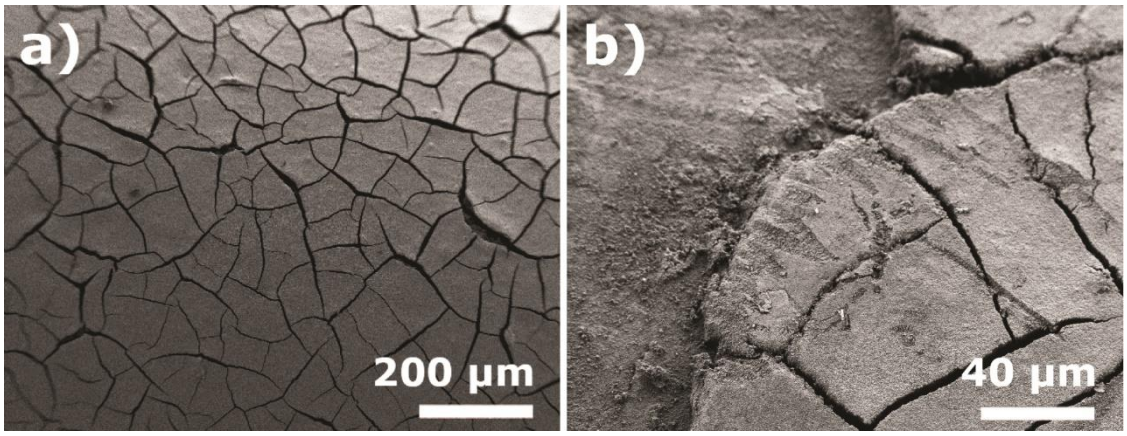

Figure 6.2. SEM micrographs of the surface of an aqueous TiO_2 solution coated on POF, 100x a) and 500x b).

Given the problems related to the aqueous TiO_2 coating, several TiO_2/PVDF coating solutions were then prepared. The optimization process of this coating addressed three

parameters: the concentration of the PVDF and the TiO_2 nanoparticles, as well as the thickness of the coating. First, it was tested the optimum PMMA-POF coating to posterior immobilize the TiO_2 nanoparticles. Therefore, different polymer concentrations (3, 5, 10 and 15 w/w %) were tested. Only the 15 % PVDF sample yielded a homogeneous and complete coating of the POF tip immersed within the PVDF solution. Hence, this polymer concentration was used to immobilize the TiO_2 nanoparticles on the POF.

The effect of the concentration of TiO_2 nanoparticles on the morphology and adhesion of the coating was assessed with 25, 40 and 50 w/w % TiO_2 in 15 w/w % of PVDF by the tape test. The coatings with the concentrations of 40 and 50 w/w % of TiO_2 exhibited the lowest coating weight losses, on the other hand, the coatings with a concentration of 25 w/w % of TiO_2 yielded the highest mass loss, 0.7 mg. Thus, the loadings of 50 w/w % of TiO_2 in 15 w/w % of PVDF was selected due to the highest concentration of catalyst and the higher stability of the coating.

To investigate the coating thickness 1, 2, 4 and 6 consecutive dips were performed and the cross-sections of the coated POF were inspected with an optical microscope, Figure 6.3.

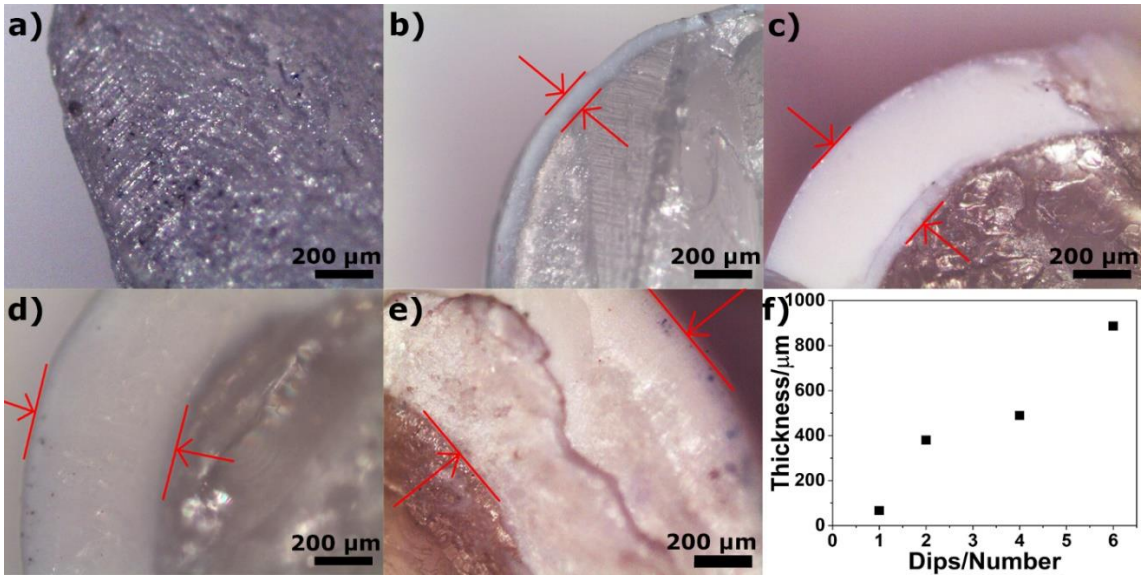

Figure 6.3. Microscope images (amplification of 50 X) of a commercial PMMA optical fiber a); coated with 50 % w/w TiO_2/PVDF by 1 dip b), 2 dips c), 4 dips d), and 6 dips e). The average thickness of the coating versus the number of dips is represented in f).

The coating thickness increases with the number of dips, Figure 6.3. Figure 6.3f summarized the average coating thickness approximately as 70, 390, 490 and 890 µm

for 1, 2, 4 and 6 dips, respectively (6.3b-e). The increase of the coating thickness by increasing the number of dips was previously reported [73–76]. The larger thickness found in the multi-coating tests are related to the withdraw velocity of the POF and the viscosity of the solutions [74,75]. The thickness of the coating is critical for photocatalytic applications, as thicker coatings represent a drawback because of the higher distance between the inner layers – where the visible radiation intensity is higher as it is closer to the PMMA core that transports the radiation – and the outer layers, in contact with the pollutant [76]. Therefore, the ideal thickness should provide a robust and lasting coating and allow the photocatalytic activation all along the photocatalytic coating. Taking this into account, two dips were used for the photocatalytic tests as it assures the best tradeoff between the thickness and light activation of the coating layers. The coatings obtained from 4 and 6 dips are too thick and the radiation is unable to cross all the coating. In this situation, the external layer is not activated and the hydrophilic behavior of the coating and consequently the photocatalytic process will be compromised.

The EDX spectrum and mapping images obtained from a cross-section of the 50 w/w % TiO_2/PVDF coated POF (2 dips) are shown in 6.4.

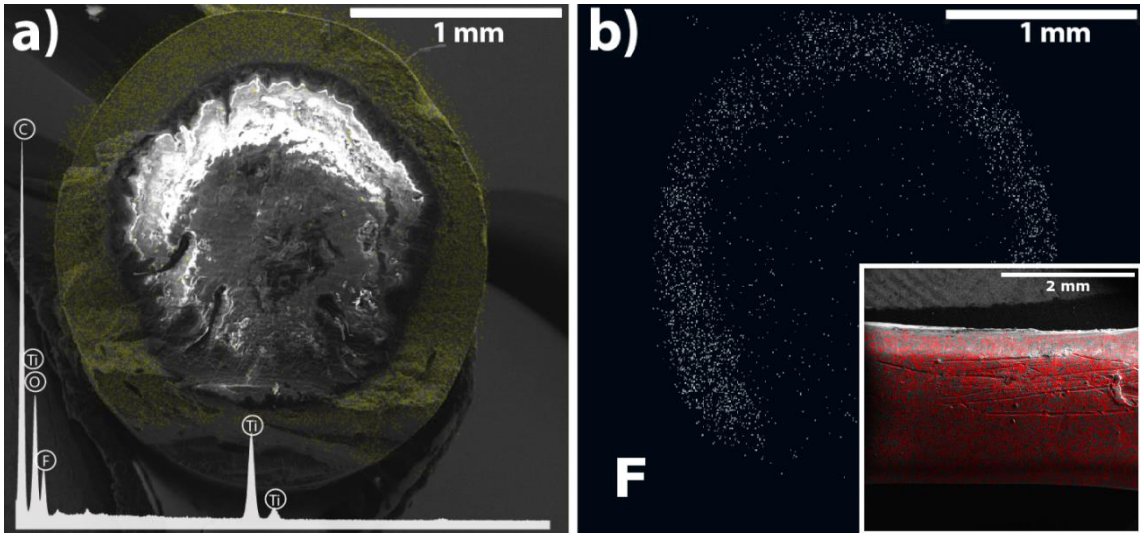

Figure 6.4. SEM-EDX mapping image showing the presence and distribution of Ti (yellow) in the PMMA-POF coating and inset of the EDX spectrum with the identification of the detected elements a); mapping EDX of fluorine (F) distribution over the TiO_2/PVDF coating, and surface SEM-EDX mapping of the 50 w/w % TiO2/PVDF POF - titanium (Ti) identified in red b).

The obtained coating has a constant thickness around the PMMA core, Figure 6.4a, which is in good agreement with the images obtained by optical microscopy. Additionally,

Figure 6.4a shows a good interface between the coating and the optical fiber (indicative of a good adhesion), as well as the homogeneous dispersion of the TiO_2 nanoparticles over the whole coating layer.

In the EDX spectra performed to the TiO_2/PVDF coating is cross section (Figure 6.4a), carbon (C, the concentration of 19.6 ± 1.6 %) and fluorine (F, the concentration of 35.4 ± 1.50 %), were identified. These elements are related to PVDF. Further, the presence of the TiO_2 nanoparticles is confirmed by the titanium (Ti) and oxygen (O) peaks, corresponding to a TiO_2 concentration of 45 ± 3 % (obtained from the sum of Ti and O). Also, by EDX mapping it was possible to observe a good dispersion of Ti (represented in yellow) without the evidence of nanoparticles cluster or agglomeration. The TiO_2 /PVDF weight ratio (45/55 %) estimated by the EDX is in good agreement with the experimental amount of TiO_2 and PVDF (50/50 %). Regarding Figure 6.4b, the white dots represent an SEM-EDX mapping of F, which also indicates the homogeneous and uniform distribution of the fluorinated coating (PVDF) around all the PMMA core.

6.3.2. Light output measurements

A detector measured the light transmission in a single POF, as a function of the different coatings at the 6 cm end tip, Figure 5.

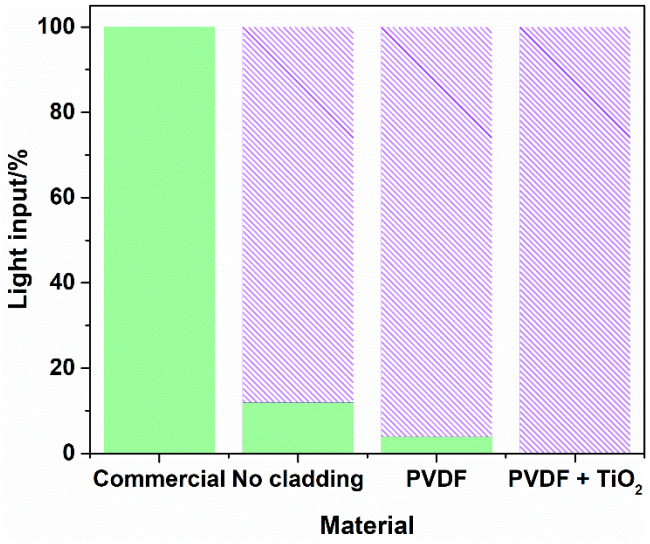

Figure 6.5. Artificial sunlight input (green) and loss of light (magenta pattern).

The measurements performed at the end tip of the fiber with different coatings allow estimating the reflected light propagated along the 60 cm of fiber until its end tip and the refracted/absorbed light. Before the cladding removal, the incident light (9.8 mW/cm^2) suffered total reflection inside the fiber, and it was transmitted to the end tip, where the detector was placed. For the sample without cladding, only 12 % of the incident light reached the end tip of the fiber, as 88 % of the total light input was refracted by the naked core surface. When the clad-free fiber was coated with PVDF, the transmitted light at the end of the tip decreased to 4 %, which means that 8 % of the light was absorbed by the PVDF coating, compared to the sample without cladding, as also confirmed by other works [21,68]. The incorporation of TiO_2 nanoparticles exhibited a total absorption of light, with no transmission of the light to the tip of the fiber. This complete absorption of the light by the photocatalytic coating was also reported by Peill and Hoffmann [77]. The light is propagated through the optical fiber due to total internal reflection because the core material (PMMA) possess a higher refractive index than the fluorinated polymer of the cladding. Since PMMA and PVDF exhibit a similar refractive index, 1.5 and 1.4, respectively, [78,79] the light propagated along the fiber is refracted when in contact with the PVDF coating. Also, as the refractive index of TiO_2 (2.4 – 2.8) is higher than that of the PMMA (1.5), it is likely that the total internal reflection would not take place when the PMMA optical fiber is coated with TiO_2 [79]. Therefore, the TiO_2/PVDF coating receives all the input visible radiation (totally refracted), which matches one of the most important characteristics of a photocatalytic system.

6.3.3. Photocatalytic results

The photocatalytic efficiency of the 50 w/w % TiO_2/PVDF coated (sample with one dip) polymeric optical fibers (POF) was assessed in the degradation of a solution of ciprofloxacin (CIP, 5 mg L^{-1}) under artificial sunlight. The absorption peak of CIP at 275 nm was monitored as a function of time (72 hours) with a UV-vis spectrophotometer. Additionally, the non-coated POF and the POF coated with PVDF (without TiO_2) were also tested as controls (6.6a).

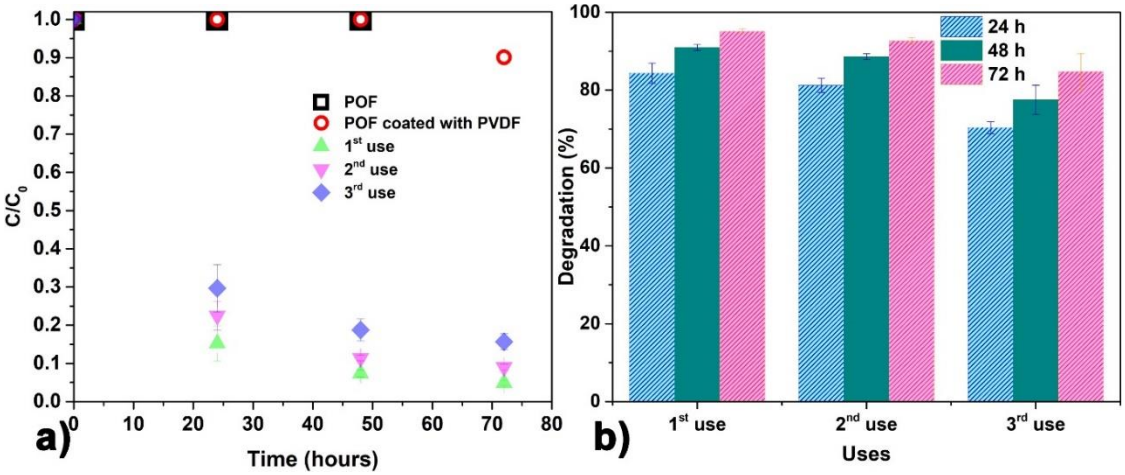

Figure 6.6. Photocatalytic degradation, C/C_0 vs. time a) and degradation efficiency vs. number of uses b), of 5 mg L^{-1} of CIP for 72 hours under artificial sunlight using the 50 w/w % TiO_2/PVDF coated polymeric optical fibers.

The results obtained with the controls (absence of nanocatalyst) show that the CIP solution is photo stable under artificial sunlight as no photolysis occurred. Additionally, CIP was not adsorbed by the uncoated POF, and only 10 % was adsorbed by the PVDF coated POF. These results show that the decrease of the CIP in solution is attributed to its degradation. Regarding the TiO_2/PVDF coated POFs, after 72 hours of irradiation 95 % of CIP in solution was degraded in the first use. In the third use and for the same irradiation time, 84% of CIP was degraded (corresponding to an efficiency loss of ≈11%), likewise the apparent reaction rate also decreased from 0.04 h^{-1} in the first use to 0.02 h^{-1} in the third use (Table 6.1).

Table 6.2. Degradation of CIP, calculated final concentration and the apparent reaction rate constant (*k*) after 72 hours of artificial sunlight.

Uses	**Degradation**		
	Degradation (%)	**Final concentration (mg L^{-1})**	***k*** **(h^{-1})**
1st use	95.1 ± 0.741	0.2	0.04
2nd use	91.0 ± 0.823	0.5	0.03
3rd use	84.3 ± 2.630	0.8	0.02

EDX spectra and mapping images were also performed to the surface of the TiO_2/PVDF/POF (inset of Figure 6.4b) to understand the efficiency loss. In the picture, it is possible to identify Ti (from TiO_2 nanoparticles) homogeneously present over all the

coating surface. The TiO_2 plays a double critical role. On the one hand, it promotes the photocatalytic, on the other hand, TiO_2 enhances the hydrophilicity [80] of the coating which promotes higher interaction between the pollutant and the photocatalytic nanoparticles, favoring the adsorption of CIP. In this context, the detachment of the poorly attached nanoparticles to the coating surface often contributes to a decrease in the photocatalytic efficiency, in good agreement with previous works [74–76]. Additionally, other works have reported the enhanced hydrophilicity of TiO_2/PVDF nanocomposites when compared with the pristine polymer [81,82]. The presence of TiO_2 nanoparticles increases the hydrophilicity of the nanocomposites [83,84], especially after light irradiation [85,86]. The changes in the wettability of the composites are related both to the topological and chemical structure of the surface [82]. Likewise, in the present work, the enhanced hydrophilicity is also caused by the increased roughness of the surface triggered by the TiO_2 nanoparticles and by the presence of hydrophilic functional groups like oxygen originated on the nanoparticles surface upon light irradiation [87].

6.4. Comparison with related systems

Until recently, not many research was devoted to optical fibers applied in photocatalysis and no report using polymeric coated POF or degrading CIP was found. Thus, the present results cannot be compared with the literature. Related works have reported on a solar-powered photocatalytic reactor (4.2 L), [77] in the degradation of 4-chlorophenol using 573 QOFs with 1 mm of diameter, and 1.30 m long coated with 15 wt. % TiO_2 (30 cm) under sunlight. The experiment was performed for two days with a sunlight exposure of 7 hours per day. However, the number and the length of TiO_2 coating over the quartz optical fibers (QOF) is much higher when compared with our work (only 20 fibers with a 6 cm TiO_2/PVDF coating). Additionally, this study did not provide any evaluation of the reusability of the TiO_2/QOF. Reusability assays were performed with 30 pieces of side-glow QOF, [22] using a 5 % Fe–TiO_2/Polyethylenimine coating in the degradation of rhodamine B. The durability of the coating was tested under UV with a decrease of efficiency of 82 % to 49 % after 42 h of operation. The inefficient attachment of the nanoparticles probably causes this 33 % of efficiency loss, in good agreement with our SEM results previously discussed (Figure 6.2).

Regarding the application of polymeric optical fibers in photocatalysis, 15 POFs with 1 mm of diameter were coated with a 5 % TiO_2 (40 cm) aqueous suspension [6] and tested under visible light in the photocatalytic degradation of trichloroethylene (reactor of 650 mL). The studied compound was completely degraded after ≈ 40 min under an intensity of 32 mW/cm^2 and 12 cm of photocatalytic coating. However, the authors did not assess the reusability of the material.

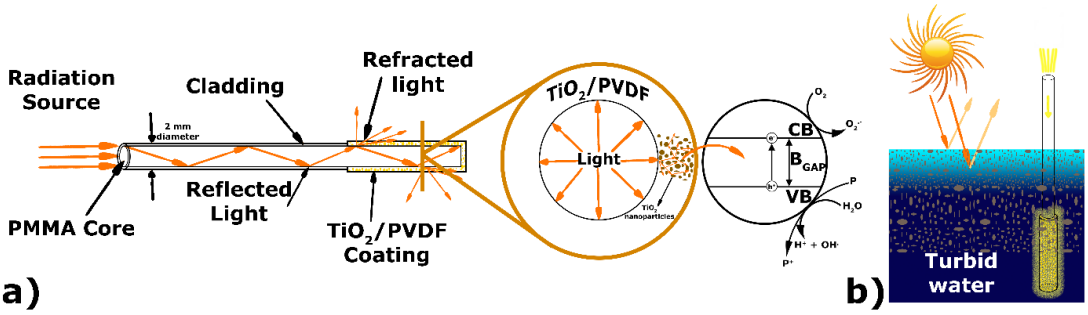

Figure 6.7. Conceptual representation of the PMMA optical fibers coated with TiO_2/PVDF and the different optical phenomena occurring during irradiation in photocatalytic applications a). Schematic representation of the application of POF in the photocatalytic treatment of turbid water b).

In the present study, a degradation of 95 % of CIP was reached within 72 hours under artificial sunlight using 20 POF with TiO_2 nanoparticles immobilized in PVDF. However, it is important to highlight that the immobilization of the nanoparticles into a substrate implies the loss of surface area and the reduction of active adsorption sites, as well as mass transfer limitations.

In the presented system, Figure 6.7, the radiation is transmitted throughout the PMMA core by reflection, and the refracted light (in the absence of the cladding) reaches the TiO_2 nanoparticles immobilized into the PVDF coating. In this way, regardless the turbidity or the remoteness of the polluted water, the photocatalytic process can take place because the TiO_2/PVDF coating is not irradiated from the outside (where the medium can be a limiting factor). In this case, the radiation is provided by the inner core of the POF that is in direct contact with the produced photocatalytic coating. Additionally, the radiation can be transported to deep water using bundles of TiO_2/PVDF coated POF. The system herein presented avoids the hindrances that a turbid medium may impose to the photocatalytic process and allows the degradation of pollutants in places where radiation does not penetrate, such as in ground and deep water.

6.5. Conclusion

In this work, a TiO_2/PVDF photocatalytic coating was successfully immobilized on the surface of PMMA optical fibers by dip coating, and the hybrid composite was characterized. The optimization process showed that 15 w/w % of PVDF and a TiO_2 concentration of 50 w/w % yielded the more uniform and robust coating. The coating thickness was also optimized obtaining a good homogeneity of the TiO_2/PVDF coating around the PMMA core and proper distribution of the TiO_2 along the coating and.

The total inputted radiation to the POF was delivered to the produced TiO_2/PVDF coating, which is paramount to ensure the photocatalytic efficiency of the coating. The photocatalytic tests confirm the excellent performance of the newly developed system, showing degradation of 95 % of CIP after 72 hours of irradiation and a re-utilization up to 3 times with an efficiency loss of ≈11 %, which indicates that the proposed material has interesting reusability properties.

Thus, the present investigation confirms the suitability of the TiO_2/PVDF coating for photocatalytic applications in water mediums with low or none radiation, opening a vast, new and needed area of applicability for water remediation.

6.6. References

1. Dewil, R., et al., New perspectives for Advanced Oxidation Processes. Journal of Environmental Management, 2017. 195: p. 93-99.

2. Di, J., et al., Controllable synthesis of $Bi_4O_5Br_2$ ultrathin nanosheets for photocatalytic removal of ciprofloxacin and mechanism insight. Journal of Materials Chemistry A, 2015. 3(29): p. 15108-15118.

3. Shi, S., Y. Fan, and Y. Huang, Facile Low Temperature Hydrothermal Synthesis of Magnetic Mesoporous Carbon Nanocomposite for Adsorption Removal of Ciprofloxacin Antibiotics. Industrial & Engineering Chemistry Research, 2013. 52(7): p. 2604-2612.

4. Nekouei, F., S. Nekouei, and H. Noorizadeh, Enhanced adsorption and catalytic oxidation of ciprofloxacin by an Ag/AgCl@N-doped activated carbon composite. Journal of Physics and Chemistry of Solids, 2018. 114: p. 36-44.

5. Li, X., H. Gao, and G. Liu, A LDA+U study of the hybrid graphene/anatase TiO_2 nanocomposites: Interfacial properties and visible light response. Computational and Theoretical Chemistry, 2013. 1025: p. 30-34.

6. Joo, H., et al., The use of plastic optical fibers in photocatalysis of trichloroethylene. Solar Energy Materials and Solar Cells, 2003. 79(1): p. 93-101.

7. Song, H., et al., The removal of natural organic matter with LiCl–TiO_2-doped PVDF membranes by integration of ultrafiltration with photocatalysis. Desalination, 2014. 344: p. 412-421.

8. Ahmed, S., et al., Influence of parameters on the heterogeneous photocatalytic degradation of pesticides and phenolic contaminants in wastewater: A short review. Journal of Environmental Management, 2011. 92(3): p. 311-330.

9. Molinari, A., et al., Degradation of emerging concern contaminants in water by heterogeneous photocatalysis with $Na_4W_{10}O_{32}$. Applied Catalysis B: Environmental, 2017. 203: p. 9-17.

10. Longobucco, G., et al., Photoelectrochemical mineralization of emerging contaminants at porous WO_3 interfaces. Applied Catalysis B: Environmental, 2017. 204: p. 273-282.

11. Anandan, S. and M. Miyauchi, Improved photocatalytic efficiency of a WO_3 system by an efficient visible-light induced hole transfer. Chemical Communications, 2012. 48(36): p. 4323-4325.

12. Hoffmann, M.R., et al., Environmental Applications of Semiconductor Photocatalysis. Chemical Reviews, 1995. 95(1): p. 69-96.

13. Kahru, A. and H.-C. Dubourguier, From ecotoxicology to nanoecotoxicology. Toxicology, 2010. 269(2): p. 105-119.

14. Silva, A.R., et al., Ciprofloxacin wastewater treated by UVA photocatalysis: contribution of irradiated TiO_2 and ZnO nanoparticles on the final toxicity as assessed by Vibrio fischeri. RSC Advances, 2016. 6(98): p. 95494-95503.

15. Rahimi, N., R.A. Pax, and E.M. Gray, Review of functional titanium oxides. I: TiO_2 and its modifications. Progress in Solid State Chemistry, 2016. 44(3): p. 86-105.

16. Khaki, M.R.D., et al., Application of doped photocatalysts for organic pollutant degradation - A review. Journal of Environmental Management, 2017. 198: p. 78-94.

17. Marschall, R. and L. Wang, Non-metal doping of transition metal oxides for visible-light photocatalysis. Catalysis Today, 2014. 225: p. 111-135.

18. Martins, P.M., et al., Improving Photocatalytic Performance and Recyclability by Development of Er-Doped and Er/Pr-Codoped TiO_2/Poly(vinylidene difluoride)–Trifluoroethylene Composite Membranes. The Journal of Physical Chemistry C, 2014. 118(48): p. 27944-27953.

19. Sudha, D. and P. Sivakumar, Review on the photocatalytic activity of various composite catalysts. Chemical Engineering and Processing: Process Intensification, 2015. 97: p. 112-133.

20. Faraldos, M. and A. Bahamonde, Environmental applications of titania-graphene photocatalysts. Catalysis Today, 2017. 285: p. 13-28.

21. Thakur, P., et al., In situ synthesis of $Ni(OH)_2$ nanobelt modified electroactive poly(vinylidene fluoride) thin films: remarkable improvement in dielectric properties. Physical Chemistry Chemical Physics, 2015. 17(19): p. 13082-13091.

22. Lin, L., et al., Enhanced photocatalysis using side-glowing optical fibers coated with Fe-doped TiO_2 nanocomposite thin films. Journal of Photochemistry and Photobiology A: Chemistry, 2015. 307-308: p. 88-98.

23. Matsuzawa, S., et al., Immobilization of TiO_2 nanoparticles on polymeric substrates by using electrostatic interaction in the aqueous phase. Applied Catalysis B: Environmental, 2008. 83(1): p. 39-45.

24. Lei, P., et al., Immobilization of TiO_2 nanoparticles in polymeric substrates by chemical bonding for multi-cycle photodegradation of organic pollutants. Journal of Hazardous Materials, 2012. 227-228: p. 185-194.

25. Teixeira, S., et al., Reusability of photocatalytic TiO_2 and ZnO nanoparticles immobilized in poly(vinylidene difluoride)-co-trifluoroethylene. Applied Surface Science, 2016. 384: p. 497-504.

26. Vild, A., et al., Orthogonal experimental design of titanium dioxide—Poly(methyl methacrylate) electrospun nanocomposite membranes for photocatalytic applications. Journal of Environmental Chemical Engineering, 2016. 4(3): p. 3151-3158.

27. Liu, Z., et al., Photocatalysis of two-dimensional honeycomb-like ZnO nanowalls on zeolite. Chemical Engineering Journal, 2014. 235: p. 257-263.

28. Salaeh, S., et al., Diclofenac removal by simulated solar assisted photocatalysis using TiO_2-based zeolite catalyst; mechanisms, pathways and environmental aspects. Chemical Engineering Journal, 2016. 304: p. 289-302.

29. Gude, K., V.M. Gun'ko, and J.P. Blitz, Adsorption and photocatalytic decomposition of methylene blue on surface modified silica and silica-titania. Colloids and Surfaces A: Physicochemical and Engineering Aspects, 2008. 325(1): p. 17-20.

30. Hussain, M., et al., VOCs photocatalytic abatement using nanostructured titania-silica catalysts. Journal of Environmental Chemical Engineering, 2017. 5(4): p. 3100-3107.

31. Teixeira, S., et al., Photocatalytic degradation of recalcitrant micropollutants by reusable $Fe_3O_4/SiO_2/TiO_2$ particles. Journal of Photochemistry and Photobiology A: Chemistry, 2017. 345: p. 27-35.

32. Islam, M.M., et al. Assessment of environmental impacts for textile dyeing industries in Bangladesh. in International Conference on Green technology and environmental Conservation (GTEC-2011). 2011.

33. López-López, C., et al., Combined treatment of textile wastewater by coagulation–flocculation and advanced oxidation processes. Desalination and Water Treatment, 2016. 57(30): p. 13987-13994.

34. Prado, J. and S. Esplugas, Comparison of Different Advanced Oxidation Processes Involving Ozone to Eliminate Atrazine. Ozone: Science & Engineering, 1999. 21(1): p. 39-52.

35. Azrague, K., et al., A new combination of a membrane and a photocatalytic reactor for the depollution of turbid water. Applied Catalysis B: Environmental, 2007. 72(3): p. 197-204.

36. Oladoja, N.A., et al., A new indigenous green option for turbidity removal from aqueous system. Separation and Purification Technology, 2017. 186: p. 166-174.

37. Giannakis, S., et al., Solar disinfection is an augmentable, in situ-generated photo-Fenton reaction—Part 1: A review of the mechanisms and the fundamental aspects of the process. Applied Catalysis B: Environmental, 2016. 199: p. 199-223.

38. Saien, J. and A.R. Soleymani, Feasibility of using a slurry falling film photo-reactor for individual and hybridized AOPs. Journal of Industrial and Engineering Chemistry, 2012. 18(5): p. 1683-1688.

39. Al-Dawery, S.K., Enhanced dynamics characterization of photocatalytic decolorization of hazardous dye Tartrazine using titanium dioxide. Desalination and Water Treatment, 2016. 57(19): p. 8851-8859.

40. Rodrigues, A.C., et al., Treatment of paper pulp and paper mill wastewater by coagulation–flocculation followed by heterogeneous photocatalysis. Journal of Photochemistry and Photobiology A: Chemistry, 2008. 194(1): p. 1-10.

41. Meriç, S., H. Selçuk, and V. Belgiorno, Acute toxicity removal in textile finishing wastewater by Fenton's oxidation, ozone and coagulation–flocculation processes. Water Research, 2005. 39(6): p. 1147-1153.

42. Rastogi, N.K., A. Cassano, and A. Basile, 4 - Water treatment by reverse and forward osmosis, in Advances in Membrane Technologies for Water Treatment. 2015, Woodhead Publishing: Oxford. p. 129-154.

43. Chen, X. and S.S. Mao, Titanium Dioxide Nanomaterials: Synthesis, Properties, Modifications, and Applications. Chemical Reviews, 2007. 107(7): p. 2891-2959.

44. Hassani, A., A. Khataee, and S. Karaca, Photocatalytic degradation of ciprofloxacin by synthesized TiO_2 nanoparticles on montmorillonite: Effect of operation

parameters and artificial neural network modeling. Journal of Molecular Catalysis A: Chemical, 2015. 409: p. 149-161.

45. Choy, S.Y., et al., Performance of conventional starches as natural coagulants for turbidity removal. Ecological Engineering, 2016. 94: p. 352-364.

46. Peill, N.J., L. Bourne, and M.R. Hoffmann, Iron(III)-doped Q-sized TiO_2 coatings in a fiber-optic cable photochemical reactor. Journal of Photochemistry and Photobiology A: Chemistry, 1997. 108(2): p. 221-228.

47. Aslam, M., et al., Membrane bioreactors for wastewater treatment: A review of mechanical cleaning by scouring agents to control membrane fouling. Chemical Engineering Journal, 2017. 307: p. 897-913.

48. Koenig, S., D. Huertas, and P. Fernández, Legacy and emergent persistent organic pollutants (POPs) in NW Mediterranean deep-sea organisms. Science of The Total Environment, 2013. 443: p. 358-366.

49. Hinderstein, L.M., et al., Theme section on "Mesophotic Coral Ecosystems: Characterization, Ecology, and Management". Coral Reefs, 2010. 29(2): p. 247-251.

50. Bongaerts, P., et al., Assessing the 'deep reef refugia' hypothesis: focus on Caribbean reefs. Coral Reefs, 2010. 29(2): p. 309-327.

51. Stout, S.A. and J.R. Payne, Macondo oil in deep-sea sediments: Part 1 – sub-sea weathering of oil deposited on the seafloor. Marine Pollution Bulletin, 2016. 111(1): p. 365-380.

52. Washburn, T., A.C.E. Rhodes, and P.A. Montagna, Benthic taxa as potential indicators of a deep-sea oil spill. Ecological Indicators, 2016. 71: p. 587-597.

53. Vela, N., et al., Removal of polycyclic aromatic hydrocarbons (PAHs) from groundwater by heterogeneous photocatalysis under natural sunlight. Journal of Photochemistry and Photobiology A: Chemistry, 2012. 232: p. 32-40.

54. Council, N.R., Alternatives for Ground Water Cleanup. 1994, Washington, DC: The National Academies Press. 336.

55. Swartjes, F.A. and P.F. Otte, A novel concept in ground water quality management: Towards function specific screening values. Water Research, 2017. 119: p. 187-200.

56. Zhang, S., et al., Groundwater remediation from the past to the future: A bibliometric analysis. Water Research, 2017. 119: p. 114-125.

57. Eckert, H., et al., Modeling of photocatalytic degradation of organic components in water by nanoparticle suspension. Chemical Engineering Journal, 2015. 261: p. 67-75.

58. Marinangeli Richard, E. and F. Ollis David, Photoassisted heterogeneous catalysis with optical fibers: I. Isolated single fiber. AIChE Journal, 1977. 23(4): p. 415-426.

59. E., M.R. and O.D. F., Photo-assisted heterogeneous catalysis with optical fibers II. Nonisothermal single fiber and fiber bundle. AIChE Journal, 1980. 26(6): p. 1000-1008.

60. E., M.R. and O.D. F., Photo-assisted heterogeneous catalysis with optical fibers. Part III: Photoelectrodes. AIChE Journal, 1982. 28(6): p. 945-955.

61. Hofstadler, K., et al., New Reactor Design for Photocatalytic Wastewater Treatment with TiO_2 Immobilized on Fused-Silica Glass Fibers: Photomineralization of 4-Chlorophenol. Environmental Science & Technology, 1994. 28(4): p. 670-674.

62. Kim, S., et al., Titania-coated plastic optical fiber fabrics for remote photocatalytic degradation of aqueous pollutants. Journal of Environmental Chemical Engineering, 2017. 5(2): p. 1899-1905.

63. Im, M.H., et al. Modification of Plastic Optical Fiber for Side-Illumination. in Human-Computer Interaction. Interaction Platforms and Techniques. 2007. Berlin, Heidelberg: Springer Berlin Heidelberg.

64. Zubia, J. and J. Arrue, Plastic Optical Fibers: An Introduction to Their Technological Processes and Applications. Optical Fiber Technology, 2001. 7(2): p. 101-140.

65. Selm, B., et al., Polymeric Optical Fiber Fabrics for Illumination and Sensorial Applications in Textiles. Journal of Intelligent Material Systems and Structures, 2010. 21(11): p. 1061-1071.

66. Gaya, U.I. and A.H. Abdullah, Heterogeneous photocatalytic degradation of organic contaminants over titanium dioxide: A review of fundamentals, progress and problems. Journal of Photochemistry and Photobiology C: Photochemistry Reviews, 2008. 9(1): p. 1-12.

67. Magalhães, F., F.C.C. Moura, and R.M. Lago, TiO2/LDPE composites: A new floating photocatalyst for solar degradation of organic contaminants. Desalination, 2011. 276(1): p. 266-271.

68. Li, D., L. Wang, and G. Zhang, A photocatalytic reactor derived from microstructured polymer optical fiber preform. Optics Communications, 2013. 286: p. 182-186.

69. Camara, R., et al., Evaluation of several commercial polymers as support for TiO_2 in photo-catalytic applications. 2014.

70. Mukherjee, D., S. Barghi, and A.K. Ray, Preparation and characterization of the TiO2 immobilized polymeric photocatalyst for degradation of aspirin under UV and solar light. Processes, 2013. 2(1): p. 12-23.

71. Martins, P.M., et al., Comparative efficiency of TiO_2 nanoparticles in suspension vs. immobilization into P(VDF-TrFE) porous membranes. RSC Advances, 2016. 6(15): p. 12708-12716.

72. Peill, N.J. and M.R. Hoffmann, Development and Optimization of a TiO_2-Coated Fiber-Optic Cable Reactor: Photocatalytic Degradation of 4-Chlorophenol. Environmental Science & Technology, 1995. 29(12): p. 2974-2981.

73. Catauro, M., et al., Modification of Ti_6Al_4V implant surfaces by biocompatible TiO_2/PCL hybrid layers prepared via sol-gel dip coating: Structural characterization, mechanical and corrosion behavior. Materials Science and Engineering: C, 2017. 74: p. 501-507.

74. Vital, A., et al., Morphology control in thin films of PS:PLA homopolymer blends by dip-coating deposition. Applied Surface Science, 2017. 393: p. 127-133.

75. Kohri, M., et al., Bright structural color films independent of background prepared by the dip-coating of biomimetic melanin-like particles having polydopamine shell layers. Colloids and Surfaces A: Physicochemical and Engineering Aspects, 2017. 532: p. 564-569.

76. Bouarioua, A. and M. Zerdaoui, Photocatalytic activities of TiO_2 layers immobilized on glass substrates by dip-coating technique toward the decolorization of methyl orange as a model organic pollutant. Journal of Environmental Chemical Engineering, 2017. 5(2): p. 1565-1574.

77. Peill, N.J. and M.R. Hoffmann, Solar-Powered Photocatalytic Fiber-Optic Cable Reactor for Waste Stream Remediation. Journal of Solar Energy Engineering, 1997. 119(3): p. 229-236.

78. Drobny, J.G., Technology of fluoropolymers. 2009.

79. Ray, A.K. and A.A.C.M. Beenackers, Development of a new photocatalytic reactor for water purification. Catalysis Today, 1998. 40(1): p. 73-83.

80. Méricq, J.P., et al., High performance PVDF-TiO_2 membranes for water treatment. Chemical Engineering Science, 2015. 123: p. 283-291.

81. Rahimpour, A., et al., Structural and performance properties of UV-assisted TiO_2 deposited nano-composite PVDF/SPES membranes. Desalination, 2012. 285: p. 31-38.

82. Shi, H., et al., A modified mussel-inspired method to fabricate TiO_2 decorated superhydrophilic PVDF membrane for oil/water separation. Journal of Membrane Science, 2016. 506: p. 60-70.

83. Emadzadeh, D., et al., A novel thin film composite forward osmosis membrane prepared from PSf–TiO_2 nanocomposite substrate for water desalination. Chemical Engineering Journal, 2014. 237: p. 70-80.

84. Yamashita, H., et al., Coating of TiO_2 photocatalysts on super-hydrophobic porous teflon membrane by an ion assisted deposition method and their self-cleaning performance. Nuclear Instruments and Methods in Physics Research Section B: Beam Interactions with Materials and Atoms, 2003. 206: p. 898-901.

85. Rahimpour, A., et al., Coupling TiO_2 nanoparticles with UV irradiation for modification of polyethersulfone ultrafiltration membranes. Journal of Membrane Science, 2008. 313(1): p. 158-169.

86. Wang, R., et al., Light-induced amphiphilic surfaces. Nature, 1997. 388: p. 431.

87. Jaleh, B. and N. Shahbazi, Surface properties of UV irradiated PC–TiO_2 nanocomposite film. Applied Surface Science, 2014. 313: p. 251-258.

7. Conclusions and future work

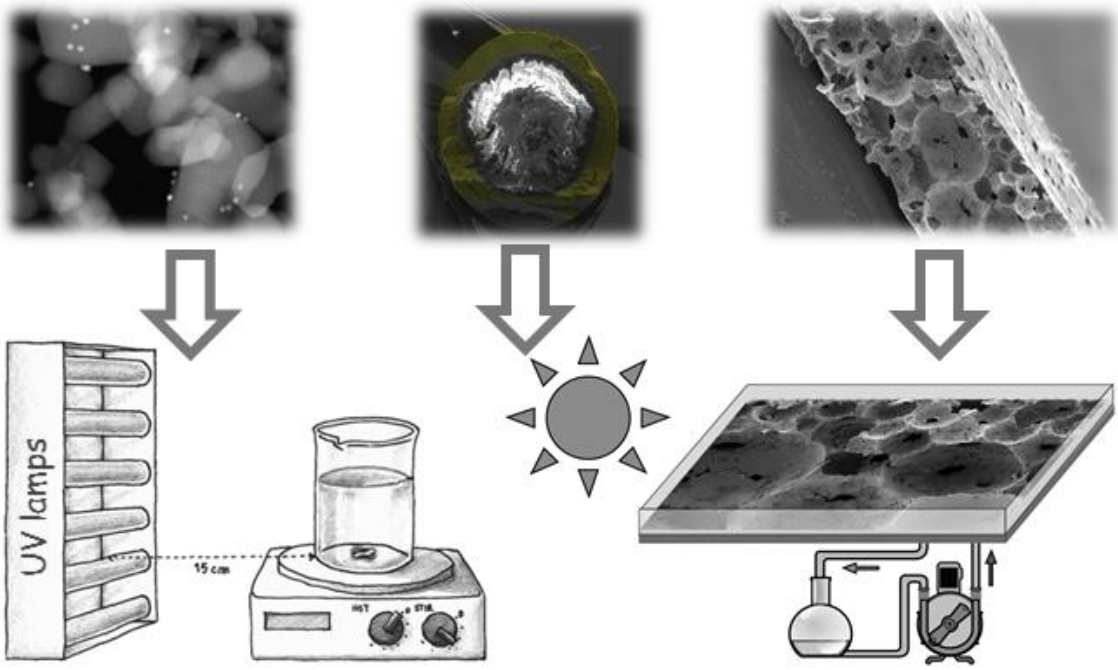

This chapter presents the main conclusions of the present work, which was mainly devoted to the development of new materials and immobilization strategies to overcome the typical limitations of photocatalytic materials. Moreover, a few suggestions for future works are also provided.

7.1. Conclusions

The application of photocatalysis to solve environmental issues has been widely explored in the last few decades. Photocatalysis consists in the use of radiation to generate highly oxidizing species, most often the hydroxyl radical (•OH), and destroy hazardous compounds into CO_2, and H_2O among others. This process requires a catalyst, and among many, titanium dioxide (TiO_2) nanoparticles stands out from the rest because of its significant oxidizing properties under UV irradiation, superhydrophilicity, chemical stability in a broad pH range, cheapness, and extended durability.

Despite the exciting features of the photocatalytic process and TiO_2 nanoparticles, as a part of the system, there are still some setbacks related to practical photocatalytic applications. The re-use/recycling of TiO_2 nanoparticles is time-consuming and requires costly separation/filtering processes. Further, another limitation is the reduced spectral activation of TiO_2, because it has a broad band gap (3.2 eV, for anatase), being only activated by UV radiation (< 387 nm), which corresponds to just 2 to 5% of the solar spectrum. Another major drawback is the fast recombination between electron-hole pairs, which significantly reduces the photocatalytic process efficiency.

The work herein presented, demonstrates a set of different approaches applied to surpass the obstacles mentioned above. In this way, the photocatalysts were immobilized in an in a PVDF-TrFE matrix with different morphologies, membranes, and fiber mats. Additionally, doped, co-doped and TiO_2 nanocomposites were produced. As a final stage, the TiO_2/PVDF-TrFE nanocomposite membrane was scaled up and tested in a solar photoreactor. The use of polymeric optical fibers with a photocatalytic polymeric coating is also presented as a new generation tool to broaden the application of photocatalysis to environments deprived of light.

It was demonstrated the suitability of TiO_2/PVDF-TrFE nanocomposite membranes for photocatalytic applications. All the produced nanocomposites presented a highly porous structure (> 73 %). The membrane with the best performance corresponded to an efficiency loss of 13 % regarding the experiment with nanoparticles in suspension. For the samples with zeolites (NaY), the results show that this material favors MB solution permeability and percolation through the interconnected porous structure. With this configuration, the efficiency loss was reduced to only 3 % regarding the best performance assay with suspended nanoparticles.

The scale-up process of a photocatalytic membrane was also a pursued goal, in this context a TiO_2/PVDF–TrFE nanocomposite membrane was produced and used in a solar photoreactor to degrade Tartrazine - a hazardous pollutant. The photocatalytic results have shown that after five hours of solar irradiation approximately 78 % of the contaminant was degraded. It was also demonstrated the ability of the system to operate under artificial UV light – despite the lower efficiency (≈ 37 % of tartrazine degradation). The reusability of the nanocomposite was tested and ultimately confirmed the efficient attachment of the TiO_2 nanoparticles on membrane pore walls.

Once the matrix to immobilize photocatalyst was experimentally validated, the focus of the research shifted to the nanocatalyst improvement. In this regard, erbium doped and erbium: praseodymium co-doped TiO_2 nanoparticles (≈10 nm diameter) were synthesized and characterized. The results show that the doped and co-doped nanoparticles possess a high surface area (273 m^2/g), the ability to absorb the radiation in the visible range, as well as a lower band-gap (ranging from 2.92 to 2.63 eV) when compared with the pristine TiO_2 (3.05 eV). Afterward, the produced nanoparticles were immobilized by a PVDF-TrFE matrix, and the Er-Pr codoped nanoparticles showed the highest photocatalytic activity in the degradation of MB. The high surface area and the efficient inhibition of the electron-hole pair recombination promoted by the dopant species are responsible for the enhanced efficiency. The proposed system not only addresses the reusability issue but also enables visible light utilization by engineered nanoparticles.

After doping the catalyst, the production of a photocatalytic nanocomposite arises as a different approach that can equally improve the photocatalytic properties of TiO_2 nanoparticles. Thus, Au/TiO_2 nanocomposites were produced - by nanoprecipitation, characterized and applied in the photocatalytic degradation of ciprofloxacin. The characterization results have shown that the presented method allows obtaining a nanocomposite with a homogeneous distribution of Au nanoparticles over the TiO_2 nanoparticles surface, with lower band gap and an enhanced absorbance of radiation in the visible range. Resulting in an enhanced photocatalytic degradation efficiency of CIP, 13 and 145 % under UV and simulated visible light radiation, respectively, when compared with pristine TiO_2 under the same conditions. Behind these results are gold nanoislands, which play a paramount role, working as electrons acceptors, preventing the electron-hole recombination and endowing the nanocomposite with the ability to

absorb more visible radiation. The presented method proved to be a simple and efficient approach to produce photocatalytic nanocomposites with enhaced catalytic properties.

Another strategy was used to improve TiO_2 photocatalytic efficiency, the production of G/TiO_2 (graphene) and GO/TiO_2 (graphene oxide) nanocomposites. The nanocomposites characterization revealed the interaction between TiO_2 nanoparticles and G/GO, as well as lower band gaps for the nanocomposites (ranging from 2.94 to 2.35 eV) compared with TiO_2 (3.08 eV). The photocatalytic results revealed that the as-produced nanocomposites degrade more efficiently the MB than the TiO_2 but regarding CIP degradation, the pure TiO_2 still presents a higher efficiency. The results suggest that CIP does not have an efficient interaction with the nanocomposite surface, which promotes low adsorption and reduced photocatalytic efficiency. Additionally, computational results confirm the experimental trend relative to the MB degradation, as the nanocomposites present smaller energy gap and interfacial charge separation, which decreases the electron-hole pairs recombination rate and consequently favors photocatalytic activity.

To explore new morphologies with P(VDF-TrFE), the TiO_2/GO nanocomposite, previously tested in suspension, was immobilized into fibers by electrospinning. The characterization results confirmed the above mentioned advantageous properties of GO/TiO_2 nanocomposite when compared with pure TiO_2. The photocatalytic activity of the electrospun nanocomposite increased with GO incorporation, similarly to what happened with GO/TiO_2 in suspension. Under UV radiation, MB removal increased about 80% comparatively to the sample with TiO_2. With simulated visible radiation, all the samples completely removed MB in less than 90 minutes. The high surface area and porosity of the fiber mat samples together with the advantageous electrical and structural properties of GO (already studied), especially avoiding electron-hole recombination and favoring adsorption, promoted a notable photocatalytic performance.

Another approach that photocatalysis reaches environments deprived of light was investigated. In this way, polymeric optical fibers (PMMA) were coated with TiO_2/PVDF. Characterization demonstrated the excellent TiO_2 nanoparticles distribution over the coating, as well as the ability to efficiently address the inputted radiation to the coating. The photocatalytic assays have shown remarkable efficiencies and reusability, with CIP degradations efficiencies of 95 and 84 % in the first and third uses, after 72 hours of radiation, respectively. This system indeed represents a new generation of materials as it allows to reach and remediate remote environments.

7.2. Future work

The work herein presented was mainly focused on the development of new materials that allow overcoming photocatalysis most significant limitations. First, new and more efficient catalysts were developed. Additionally, different systems to immobilize nanocatalysts were produced, a membrane and a coated polymeric optical fiber. In this context, it would be interesting to:

- ➔ Test the incorporation of catalysts active in the visible range (*e.g.*, Au/TiO_2 nanocomposite) in the porous membrane or optical fibers coating.
- ➔ Develop membranes incorporating two catalysts simultaneously to enlarge the range of radiation absorbance and increase photocatalytic activity.

All the herein produced materials presented advantages towards the traditional materials; however, despite the endowed improvements, the most efficient photocatalytic system for each pollutant has to be determined. In the photocatalytic process, the physical-chemical properties of the pollutnats also play a critical role on the process efficiency, which should be considered. In this context, the future works could also address:

- ➔ Development of new photocatalytic screening methodologies for the rapid and easy match between catalysts and pollutants;
- ➔ Test the developed materials for remediation of real wastewater effluents.